# Plasma enhanced pulsed laser deposition: A study of laser produced and radio frequency plasmas, and deposited films

## David Neil Meehan

Doctor of Philosophy

University of York

Physics

February 2019

*Dedicated to my Mum, Dad, and Sister*

# Abstract

Plasma enhanced pulsed laser deposition (PE-PLD), is a novel thin film deposition technique, which utilises both laser produced and radio frequency (RF) plasmas, in order to deposit semiconducting, metal oxide thin films. In PE-PLD, a pure metal target is ablated within the environment of a RF inductively coupled plasma, which generates reactive oxygen species that react with the laser produced plasma, forming oxides that deposit onto a substrate. Metal oxides of interest within this work are copper oxides (CuO, $Cu_2O$) and zinc oxide (ZnO), both of which are wide band-gap semiconductors, with applications in photovoltaics, electronic displays, batteries, and more. PE-PLD has shown promise in the deposition of metal oxides, with the RF plasma lending additional control over film growth, no need of substrate heating or film annealing, and the deposition of films on flexible plastic substrates.

Characterisation of both the laser ablated and RF plasmas will be presented in this work; laser ablation of metal and metal oxide targets has been modelled using the code POLLUX, showing that the compound nature of the oxide targets results in volatile ablation under the conditions used in PE-PLD. Whereas metal targets ablate in a much more stable and controlled manner.

Plus, gas temperature measurements of the RF plasma have been performed via complimentary diagnostic techniques, and the effect of pulsed operation on the gas temperature. Additionally simulations via the use of the code HPEM, have been used to characterise the importance of processes, such as heat transfer to reactor walls.

Lastly, analysis of films deposited by PE-PLD has been performed, showing ZnO, $Cu_2O$ and CuO films of uniform density across their entire depth, as well high density planes of ZnO, on both $SiO_2$ and Si substrates, and the successful deposition of $Al_2O_3$ films on steel substrates, and semiconducting films on polymer substrates.

# Contents

# List of Tables

# List of Figures

# Acknowledgments

Although my personal blood, sweat, tears, and even vinegar has been put into this work, and the process has shaped me as a person, it would not have been possible without those who have been part of both my life both in and out of the YPI, and here I wish to thank them all from the bottom of my heart.

First and foremost my supervisor. Erik, you have put up with me since those pokey summer days from even before my Masters, and I genuinely do not know how have done so. Your supportive and friendly, yet rigorous perfectionism has gotten me through this process. You have not only helped to produce this body of work, yet also instilled within me a work ethic and attitude that I will take with me where ever I go. I would use the dreaded term role model yet I don't want to inflate your ego too much! Thank you.

Plus all other staff at the YPI. Everyone from each member of academic staff who have been a great help and source of constant guidance, to the amazing admin staff who truly are the ones that keep the YPI running in the first place, let alone how smoothly they make it. To Kari N and Rich A in the labs, who have taught me skills I never even knew existed, and made literally everything work in the first place. Also to staff from other institutions I have had the pleasure of working with, including Jon B. and Leo L. or the Nanocentre, and Andy R. from Huddersfield, all of whom provided invaluable help. Thank you.

Also to all other PhD's of the YPI, all of whom have been great friends throughout this process. David S, to surviving the experiment literally melting down twice which I am still note sure how we did so, and your unique sense of humour. To Sudha R, who left me with a damn fine experiment to take over from. To Josh B, one of the best office mates an idiot like me could ask for. To Helen D, source of many a laugh and pictures of cute animals. To Scot D, a great conference travel buddy, but mate your puns are trash. To Sarah W, baker extraordinaire, and fellow victim of *that* code. To Joe B, master of having a good old moan. To James E, a damn fine ex-house mate, and a great sounding board about the state of the world. To Mike W, for being an amazing house mate and taking me in during this mental last few months. To Fred R, your special ways, and all the mud you track into the office. And to the amazing PostDoc's, Andrew G, Sandra S, and Jerome B, all of whom are a damn sight smarter than I will ever be and by a good stretch at that, and all the help they have gone out of their way to lend me. Instead of the following thesis I could go on and list more, plus the many more that have come and gone, yet sadly I wont get a doctorate that way. To name but a few, Mike M, Eduardo SM, Ben W, Damon F, Andy W, Andy H, Martin B, Ellie T, Phil D and of course David B. To all of you, thank you.

And of course, my friends around York and good old FragSoc. A source of great joy in my life, and dare I say it, just as much of an influence on me if not more than this PhD during my time at York. I have learnt skills and gained achievements whilst among your ranks I am eternally proud of, and hope that you will grow from strength to strength, and you continue to be a trendsetter in the coming years as I am finally forced to hang up the jersey (not really though, you're never totally getting rid of me). Again there is too many of you to thank each by name, but I must give a special shout out, not to the #sponsors, yet to Dhillan L, Jordan R, Rafee JJ, Rob T, Joe L, Jon LH, and the rest of you beautiful nerds. Thank you.

But also the friends made from York where not only the above counts, but to their further friendship. To James D, a great friend and maybe perhaps even a better drinking buddy. To David P, my favourite Hungarian, the friendliest man I know, and who has kept me sane much more so than you know. To Jo I, pub quiz music round genius. To Alex B and Sophie A, some of the best LAN buddies out there. And lastly but by no means least, Chris B, Alex S, and Gareth J, fantastic friends, adequate team mates, and although I may not have told you as much as I should have, the people who I would not have gotten through the past years without. Thank you.

Finally, my family. Mum, Dad, and my favourite little Big Sister. Your immense amount unwavering, unquestioning, and unending love, and support physically, financially, and emotionally is above all else, not only how I managed to complete this work, but have made me who I am. I have written 176 pages based on a load of physics nonsense, however I could write a thousand times more thanking you, but these following six words must suffice. Thank you, and I love you.

# Declaration

This thesis has not previously been accepted for any degree and is not being concurrently submitted in candidature for any degree other than Doctor of Philosophy of the University of York. This thesis is the result of my own investigations, except where otherwise stated. All other sources are acknowledged by explicit references.

Within this work some measurements of films were performed by Dr Jon Barnard and Dr Leonardo Lari of the York JOEL Nanocentre and by Dr Andrew Rossall of the University of Huddersfield, with input during measurements and further analysis being performed by myself. Where this data is presented, primarily in Chapter 6, it will be explicitly stated so. The latter of these two points lead to publication in NIM:B, again where results are presented within this work are taken from this publication, it will be explicitly stated so.

Additionally Chapter 4, plus Appendix A, presents work, performed of my own merit, alongside work from Dr Erik Wagenaars of the YPI, as well as Prof Mike Ashfold and Dr Hao Lui of the University of Bristol. This collaborative work has been accepted for publication within the Journal of Applied Physics. Where results taken from my input on said publication are presented within this work, it will be highlighted in detail.

# Chapter 1

# Introduction

## 1.1 Motivation

Modern electronic technologies are advancing at an increasingly rapid pace, in terms of smaller, more compact devices, an increasing range of applications, and more. This is in no small part due to the improvements in the understanding and creation of semiconductors, which are materials with conductivities between that of an insulator and conductor. Semiconductors have driven the technological revolution, being used in integrated circuits, and most importantly for this work, thin films. These are layers of materials on the order of magnitude of 10s of nanometres, to many microns thick. With semiconducting films being found to some extent in every piece of modern technology.

Manufacturing of semiconductor thin films is often achieved using plasma-based deposition techniques, with advancements in semiconductor technologies being driven in no small part by the advancement in plasmas physics. Colloquially referred to as the "fourth state of matter", plasmas are an ionised gas, formed when additional energy is imparted to a gas causing electrons to be liberated from their atoms. Of focus in this work will be two forms of plasmas commonly found in semiconductor manufacture and surface modification; Firstly laser produced plasmas, where a laser irradiates a target, ablating material from the surface and ionising it into a plasma. Secondly are radio frequency (RF) plasmas, where a gas is exposed to electromagnetic fields oscillating at an RF frequency, which excites electrons but not the heavier species, resulting in a plasma containing a variety of reactive species.

The semiconductor deposition technique explored in depth in this work combines both of these types of plasmas; plasma enhanced pulsed laser deposition (PE-PLD), ablates a pure metal (e.g. Cu, Zn) target within an RF oxygen plasma, where species in each plasma react to form an oxide, with material then depositing onto a substrate forming the film. This technique originally developed at the University of York, has been described computationally, and initial proof of concept via the deposition of copper oxide films in the following references [1, 2]. PE-PLD has shown great promise for the depositions of metal oxide films when compared to other deposition techniques, primarily in the fact that unlike many other techniques, PE-PLD does not require substrate heating during deposition, or annealing of deposited films in order to create a film of desired stoichiometry or crystal structure.

Of specific interest in this work will be two semiconductors that can be created by PE-PLD, with the use of a metal ablated laser plasma, and oxygen RF plasma. Firstly zinc oxide, ZnO, is a wide bad gap semiconductor with a direct band gap energy of 3.14 eV [3], which is above the visible spectrum. Also as it is transparent in colour when in the order of 10's of nanometres, ZnO finds use in many optical applications, such as electronic displays, plus in high density batteries [4]. Also, ZnO is currently touted as a replacement for the commonly used indium tin oxide (ITO), due to exhibiting very similar properties, and limitations in ITO film thickness and supply of materials. Secondly copper oxide, which can form two stable phases, being $Cu_2O$ and CuO. Uses of $Cu_2O$ films include photovoltaics, catalytic beds, and within toxic gas sensors [5–7]. Uses of CuO films include again catalytic applications, batteries, and photovoltaics [5, 8].

The work presented here delves deeper into key underpinning physical processes, vital to the understanding and operation of PE-PLD. This includes the behaviour of different target materials, chiefly metals and metal oxides, under nanosecond pulse laser ablation conditions within PE-PLD. Also the use of complimentary diagnostics to determine the gas temperature of the plasma, a parameter of key importance for plasma chemistry, plus how the gas temperature can be controlled by pulsed operation of the plasma. Lastly, films deposited by PE-PLD are analysed, in terms of their structure, and composition as a function of depth. This includes further analysis of previously deposited copper oxide films on quartz, yet additional films such as zinc oxides and the use of Si as a substrate. Additionally, in order to further highlight the versatility of PE-PLD, it is shown that flexible plastic substrates can be utilised, increasing the range of possible applications PE-PLD can be utilised for.

## 1.2 Thesis Outline

This thesis consists of the following chapters:

**Chapter 2** provides an overview of all the fundamental physics important for this entire work, including laser target interactions, radio frequency plasmas, and deposited films.

**Chapter 3** describes the PE-PLD apparatus in detail and methodology use to deposit thin films. Plus a detailed description of RF plasma and film diagnostics, and finally a description of the numerical codes used to simulate the laser produced and RF plasmas.

**Chapter 4** presents benchmarked simulations describing the differences between the nanosecond pulsed laser ablation of metal and metal oxide targets.

**Chapter 5** contains gas temperature measurements of the $O_2$ RF inductively coupled plasma under a range of pressures and powers, obtained by a variety of complimentary techniques. Plus an investigation into the affect of pulsed operation on the temperature, and simulations of the ICP.

**Chapter 6** provides analysis of copper oxide and zinc oxide films deposited on $SiO_2$ and Si substrates, characterising their structure, and composition as a function of depth. Plus the deposition of such films on flexible plastic substrates.

**Chapter 7** summarises the work presented here, providing key conclusions.

# Chapter 2

# Scientific background

*This initial chapter will cover all necessary background scientific knowledge that is relevant to the work presented in this thesis. This includes an introduction to PE-PLD and the current existing knowledge on this technique, and a description and highlighting of relevant areas of laser and plasma physics, deposition processes, and properties of deposited films.*

## 2.1 Plasma enhanced pulsed laser deposition fundamentals

Pulsed laser deposition (PLD) is a technique that is widely used for creating thin films [9–11], which are layers of material on the orders of 10's of nanometres to many microns thick [12]. PLD can be thought of as a three stage process: firstly a laser is incident on a target material, ablating material from the surface and ionising it into a plasma plume. Secondly this plume expands and cools due to collisions from both atoms and ions within the plume itself, and also from surrounding particles in its atmosphere, resulting in changes of the plumes kinetics and chemistry. Lastly this gaseous material is then incident onto a substrate where it deposits into the desired thin film; a rough schematic of PLD can be seen in Figure 2.1. Since its first description in the work of Smith and Turner in the 60's [13], PLD has become a technique utilised in the creation of films for photovoltaics [14, 15], cathodes in electronic devices [16, 17], and batteries [18, 19].

The work of this thesis will be focused around the novel deposition technique of plasma enhanced pulsed laser deposition (PE-PLD), which has been described conceptually with the use of simulations and with initial experimental works with the deposition of copper oxides in the following works from the York Plasma Institute [1, 2]. PE-PLD exploits the

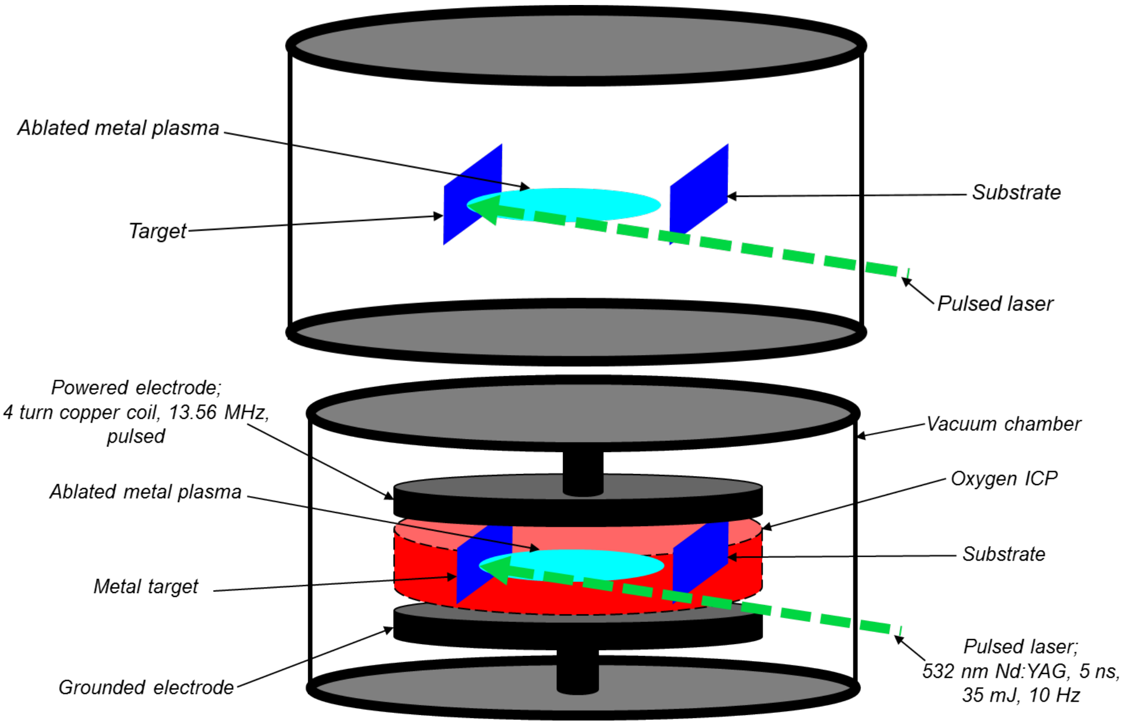

Figure 2.1: Basic schematics for, Top: Pulsed laser deposition. Bottom: Plasma enhanced-pulsed laser deposition

second phase of the PLD process, as what is already common practice in PLD is to use finely tuned background atmospheres of inert gases and even adding in such gases as oxygen to influence the plume expansion and film growth [20, 21]. PE-PLD takes this one step further and instead uses a radio frequency (RF) oxygen plasma to generate reactive oxygen species, that readily react with the ablated plasma plume.

By doing so PE-PLD has advantages over traditional PLD, in that pure metal targets can be used instead of the more experimentally challenging compound targets, and also there is no need for additional substrate heating or post deposition annealing in order to grow high quality films. It is also theorised that this technique can be more versatile, as additional gasses could be added instead of pure oxygen to grow a wide variety of films, such as nitrogen for either nitride or oxynitride films. Figure 2.1 also shows a basic description of the PE-PLD. As PE-PLD utilises many aspects of physics, all necessary aspects of key theory, from relevant laser-target interactions, plasma physics, film depositions and properties of desired films, will be discussed within this chapter.

## 2.2 Interaction of lasers with solids and plasmas

When considering energy absorption from a laser into a solid target or a plasma, there are a variety of aspects to consider, such as various parameters of the laser including wavelength and pulse duration, and certain physical aspects of the target medium itself:

### 2.2.1 Reflection, absorption and ablation of solid material

When first incident on a solid surface, a fraction of the laser's radiation is reflected with the remaining radiation being able to further interact with the target, with the amount of reflected radiation being dependant on three main factors. Firstly on the target material [22], which can also be dependant on temperature [23], and lastly the wavelength of incident photons [22, 24]. For any photons that are not reflected, it passes into the material and begins to decay based depending on the Beer-Lambert law [25]:

$$I(z) = I_0 e^{-\alpha z} \tag{2.1}$$

where $I$ is the intensity with $I_0$ being its initial value, $z$ the depth of penetration, and $\alpha$ the absorption coefficient. Note $\alpha$ is dependant on both temperature and wavelength, so for Equation 2.1 this is assumed to be constant. The final penetration depth of light into the material, $\delta$, can also be determined from $\alpha$ and can be seen in Equation 2.2. This is schematically shown in Figure 2.2.

$$\delta = \frac{1}{\alpha} \tag{2.2}$$

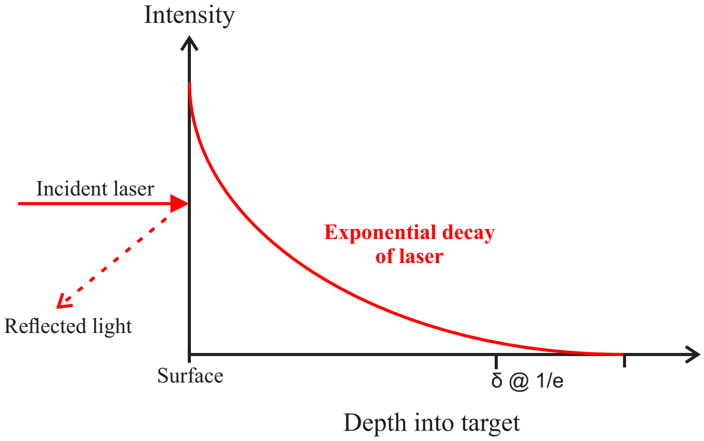

Figure 2.2: Decay of laser intensity during absorption into a target

In terms of how much energy is absorbed across this depth, the pulse duration has key importance, as the time scale for the interaction between hot electrons (i.e. electrons excited by the laser) and lattice phonons (i.e. the method of heat transfer through a lattice) of the target is on the order of $10^{-10}$ to $10^{-12}$ seconds for metals [26]. Therefore any laser of a longer interaction time than this, such as nanosecond (ns) lasers utilised in this work, can be assumed to impart their energy directly to heat as electronically excited sates with short life times can be ignored; such processes are commonly referred to as photo-thermal. Heat generated from photo-thermal processes then allow for "classical" phase changes within the target, with melting from solid to liquid and then further evaporation into a gas phase, which can then be ionised into a plasma. There are other processes that can result in ablation of a solid to a gas, being direct sublimation, however this is mostly observed with shorter pulse length lasers, such as picosecond (ps) and femtosecond (fs) lasers, where the pulse length of the laser is sufficiently small to consider phonon interactions [26–28].

### 2.2.2 Inverse-Bremsstrahlung absorption

There are two key mechanisms for the coupling energy of lasers into solids and other media; Firstly is Inverse-Bremsstrahlung (IB) absorption, prominent in cases where there are free electrons able to interact with the laser, such as a metal target or a plasma [29–31]. IB-absorption works by the electric component of the photon's electromagnetic field accelerating free electrons in the media it passes through. These free electrons are accelerated up to the frequency of oscillation of the electric field, yet are not bound to it by any means, and are therefore free to undergo collisions with their surrounding free electrons and nuclei. This imparts energy into the surroundings in terms of heat, and the coefficient for IB absorption, $K_{ib}$, is given as:

$$K_{ib} = 8\sqrt{\pi}\left(\frac{e^2}{4\pi\epsilon_0}\right)\frac{4}{3c^2}\frac{Z^2}{m_0^2}n_e n_Z\left(\frac{m_0}{2k_bT}\right)^{1/2}\frac{\pi^2c^2}{\hbar\omega^3}\left(1 - exp\left(-\frac{\hbar\omega}{k_bT}\right)\right) \tag{2.3}$$

Important to note in Equation 2.3 is that absorption of energy from IB absorption is strongly dependant on the laser wavelength ($\propto \omega^{-3}$ so $\propto \lambda^3$). Therefore IB absorption is often strongly observed within long wavelength and infra-red lasers, such as the commonly used 1064 nm Nd:YAG lasers, and far less of a prominent affect for shorter wavelengths.

### 2.2.3 Photo-ionisation

The second method of energy coupling is photo-ionisation of atoms within the target; single-photon ionisation occurs when the wavelength and, therefore, energy given by $E = hc/\lambda$, is sufficient when compared to the ionisation energy of a bound electron to cause an ionisation event during a collision. Typically this is observed with shorter wavelength lasers due to their higher photon energy, and more common with outer electrons within an atom due to their lower ionisation energies caused by shielding from the nuclei by the inner electrons [32]. In simple terms this is expressed in Equation 2.4 where X is a target element, $\gamma$ is a photon, and $e$ an electron.

$$X + \gamma \rightarrow X^{+} + e \tag{2.4}$$

However, atoms do not have to exclusively interact with one incident photon; In cases where there is a high photon flux, multiple laser photons can be incident on a bound electron simultaneously, and if the sum of $n$ photon's energies are higher than the ionisation energy then an ionisation event can occur, as shown in Equation 2.5. For instance a 532 nm Nd:YAG laser of photon energy 2.33 eV, then 4 photons would be required for the $1^{st}$ ionisation of Zinc at 9.39 eV. However, due to being a multi-body collision, the cross-section for such an event is much lower, and only occurs with high photon fluxes [33].

$$X + n\gamma \rightarrow X^{+} + e \tag{2.5}$$

Multi-photon ionisation can also occur within solids in a step wise manner, where electrons are instead excited to higher states by an initial electron, and then ionised by a second incident photon. However, this is much more common in ps and fs pulse length lasers, via the interaction with lattice phonons, and much less likely at longer pulse lengths lasers (e.g. ns) due to typically lower intensities [33, 34].

$$X + \gamma \rightarrow X^{*} + \gamma \rightarrow X^{+} + e \tag{2.6}$$

### 2.2.4 Gas-laser interaction, and the plasma frequency

For long pulse length lasers such as the nanosecond (ns) pulsed laser utilised in this work, material enters the gas phase through melting and evaporation whilst the laser is still incident onto the target. Lasers interact with gases in much the same way as they do with solids, so if the laser is of sufficient energy and flux, then single and multi-photon ionisation can occur, increasing the level of ionisation and electron density within the plasma (or indeed gas). And if any free electrons are present within the gas-phase material, then IB absorption can continue to occur, heating and ionising the plasma further also. However, as before when light could be reflected from the solid surface, now an additional effect must be considered; if there is a displacement of electrons within a plasma, they will be accelerated back towards the positive ions, however will "overshoot" due to inertia, causing an acceleration in the opposite direction. This effect continues to occur, and this oscillation is referred to as the plasma frequency, $\omega_p$, given in Equation 2.7 [35].

$$\omega_p = \sqrt{\frac{n_e e^2}{m \epsilon_0}} \tag{2.7}$$

Where $n_e$ is the electron density, $e$ the charge of an electron, $m$ mass of the species, and $\epsilon_0$ the permittivity of free space. It is interesting to note species of different masses, $m$, have different plasma frequencies, and therefore respond differently to a variety of external forces. For laser interactions this is important, as if the laser frequency is less than the plasma frequency, then electrons within the plasma are able to interact with and absorb energy from the laser. However if the laser frequency matches or is greater than the electrons' plasma frequency, then laser light will be reflected by the plasma, with this point being referred to as the critical frequency. The electron density of the plasma at this point, the critical density $n_c$, can be determined from the refractive index of the plasma, given by Equation 2.8, with $N$ being the refractive index.

$$N^2 = 1 - \frac{\omega_p^2}{\omega^2} \tag{2.8}$$

Therefore at the point of reflection of $N$ being 0, $n_c$, can be determined from the plasma frequency to be as shown in Equation 2.9 [36].

$$n_c = \frac{\epsilon_0 m}{e^2} \omega^2 \tag{2.9}$$

So it is apparent during the design of any laser-plasma system, be it a deposition system or perhaps any laser based diagnostic, that the plasma and critical frequencies are taken into account.

## 2.3 Expansion of a plasma plume

During laser ablation of a target, after solid material from the target has been sufficiently heated into a gas or a plasma, the interaction between this "plume" of material with its surroundings needs to be considered. However not only this, but also how species within the plasma plume itself interact needs to be considered, and in order to simplify the discussion here, this has been broken down into a few key stages. Firstly, during the removal of material from the surface, due to the high density of material being ablated and therefore high number of collisions, not all material is ablated away from the target, and some redeposits back onto the target. For the case of ns laser ablation this is best described as by Kelly and Miotello [37], where an "effusion like" behaviour occurs, where there is a build up of fluid on the surface before material enters the gas phase. This layer on the surface is highly collisional resulting in the re-deposition of some material back onto the target. This boundary at the target surface is referred to as the Knudsen Layer, with the velocity of material at this point defined in Equation 2.10.

$$v_k = \sqrt{\frac{\gamma k_b T_k}{m}} \tag{2.10}$$

Where $v_k$ is the minimum velocity at the Kundsen layer, $\gamma$ the surface energy, $T_k$ the temperature of species at the target during ablation, and $m$ the atoms mass. Any material with a velocity equal to or greater than $v_k$ can be assumed to have sufficient velocity to "successfully" ablate, whereas material slower than $v_k$ would lose too much of its velocity through collisions, and redeposit onto the target surface [38–40].

After material is ablated from the surface then its internal dynamics and interactions with its background can be considered. The most simplistic case for this is when the background environment is a vacuum, which can be described as an adiabatic expansion, i.e. there is no loss of energy or material to the environment, such as in the model of Anisimov et al [41], as outlined in Equation 2.11. This model describes how the velocity, $v$, density, $\rho$, and entropy, $S$, of the expanding plume develop over time.

$$
\begin{aligned}
\frac{\partial \rho}{\partial t} + \nabla(\rho v) = 0 \\
\frac{\partial v}{\partial t} + (v\nabla)v + \frac{1}{\rho}\nabla\rho = 0 \\
\frac{\partial S}{\partial t} + v\nabla S = 0
\end{aligned}
\tag{2.11}
$$

However recent literature has shown that such a model can be too simplistic, as although mass and energy can be assumed to not be lost, other parameters such as temperature and entropy need to be considered. Such that if these additional parameters are constant throughout the expansion, or if they are affected by processes within the plume, such as collisions, recombinations of ions and electrons etc. Such a model that takes these into account is the model of Stapleton et al [42], in Equation 2.12, where either an isothermal or isentropic assumption is made upon the initial conditions of the plume, defined by their initial distributions.

$$
X\frac{d^2X}{dt^2} = Y\frac{d^2Y}{dt^2} = Z\frac{d^2Z}{dt^2} = \omega\frac{E}{M}\left(\frac{X_0Y_0Z_0}{XYZ}\right)^{\gamma-1} \tag{2.12}
$$

where $M$ is the initial total mass of the plume, $E$ the total energy, $X, Y, Z$ are positions in 3-D space with subscript 0 corresponding to initial positions, $\gamma$ a constant of adiabatic expansion, and $\omega$ being a constant that varies based on either the isothermal or isentropic assumption.

This model has shown good comparison to experiment, however with some key assumptions, as an initial set of conditions of the plasma plume is required. Specifically that an initial distribution of densities and temperatures is required, whereas in the work where this model was first presented [42], this was artificially done so in order to fit experimental data. Therefore such models are not intrinsically predictive, and in reality initial assumptions made may not be valid in all cases, a concept that will be discussed within this work.

When treating the expansion of a plume within a background that is not a vacuum, such as a gas or a plasma, then not only must internal interactions be taken into account (as described above), but also the interactions with the background. This problem is best described by two key aspects, firstly being physical collisions affect the plume, and then also any chemical reactions that occur between the plume and the background. To first address the physical collisions and the effects they cause, this is best highlighted from the work of Harilal et al [43], and as shown in Figure 2.3, which investigated the laser ablation of a pure aluminium target within varying background pressures of inert argon. At the lower pressure of 150 mTorr (20 Pa), it can be seen that the plume travels in a much more dense fast moving front that passes out of view in approx 610 ns, where as the higher pressure of 10 Torr (1333 Pa) has a much more closely confined plume, that is still observable afer 2000 ns. This effect is caused by the physical collisions between the plume and background, with the denser, higher pressure case having a greater number of collisions and therefore reducing the plumes velocity.

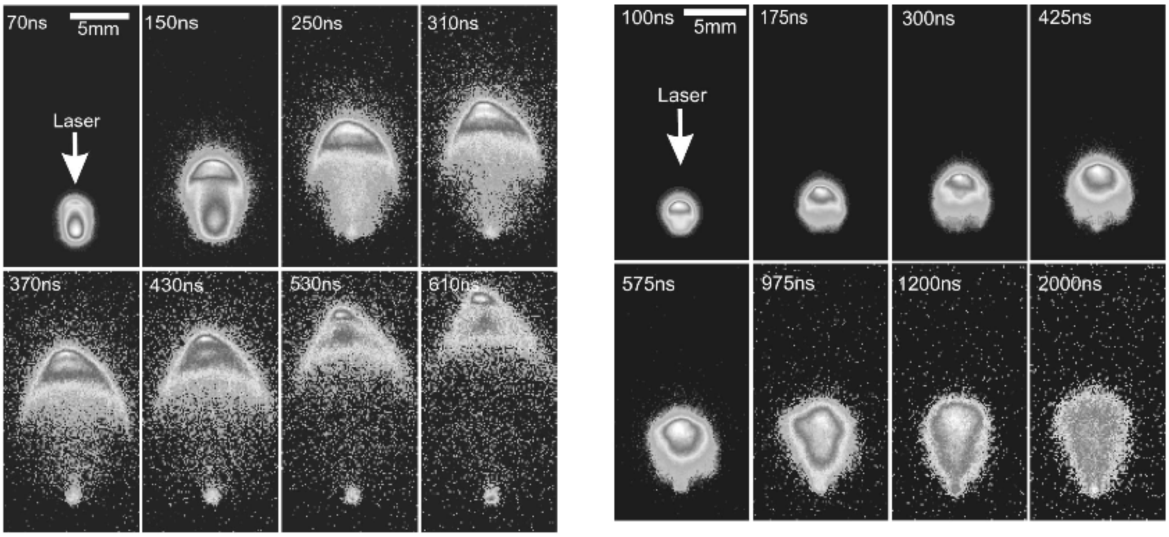

Figure 2.3: Expansion of a laser ablated plume from an Al target in different background pressures of Ar. Left: 150 mTorr (20 Pa). Right: 10 Torr (1333 Pa). [43]

The second affect to consider, being chemical reactions, is highlighted well within the work of Orsel et al [44] as shown in Figure 2.4, where a $LaAlO_3$ target is ablated within an atmosphere of $O_2$ and Ar. Here it is shown via laser induced fluorescence (LIF) that oxide species (AlO) are centred around the outer area of the plume (1b, 2a), whereas metallic Al exists more within the centre of the plume (1a), with both profiles being quite different to spontaneous emission of all species (2b). This shows that chemical reactions between the plume and background can indeed occur, affecting the chemical composition of the plume, and is more prominent around the edge of the plume where species will be in direct contact with the background.

It is control of the shape and velocity by background pressures, and composition of gasses to chemically react with the plume, that are commonly utilised within standard PLD in order to deposit films of a desired stoichiometry [32,45]. Yet it is this second point which PE-

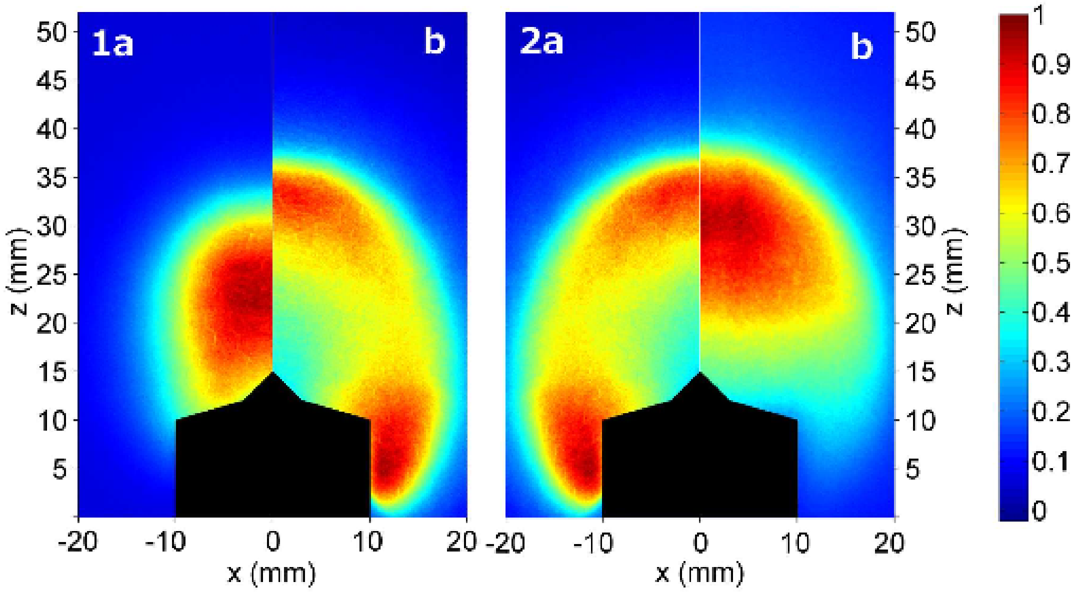

Figure 2.4: Expansion of a laser ablated plume from a $LaAlO_2$ target within an oxygen atmosphere. 1a LIF of Al, 1b,2a LIF of AlO, 2b spontaneous emission [44]

PLD exploits, via the use of reactive species generated by external plasmas (discussed shortly) instead of simple gases, in order to aid reactions with the plume to generate compound films.

## 2.4 Deposition onto a substrate

For PE-PLD, one also needs to consider how material deposits from a gas or plasma and grows a film, with a key aspect being the energies and densities of incident particles. Firstly, if the particle has too much kinetic energy, from being either a very heavy element and/or travelling at large speeds, then sputtering of substrate atoms can occur, which is a concept used in sputtering and etching processes yet not ideal for film growth. If the particle has suitable energies not to cause damage to the surface, then both their velocities and densities must be considered.

PE-PLD in its first description and proof of concept [2] was found to behave similar to standard PLD, in that deposition of films can be classified as being ”non-epitaxial”; i.e. the growth and structure of the film is *not* determined by the structure of the underlying substrate [9, 12]. This is because the laser ablated plume has sufficiently high densities for particles incident onto the substrate to begin depositing particles and forming clusters, before diffusion onto lattice sites of the substrate is a dominant affect. The full process of deposition

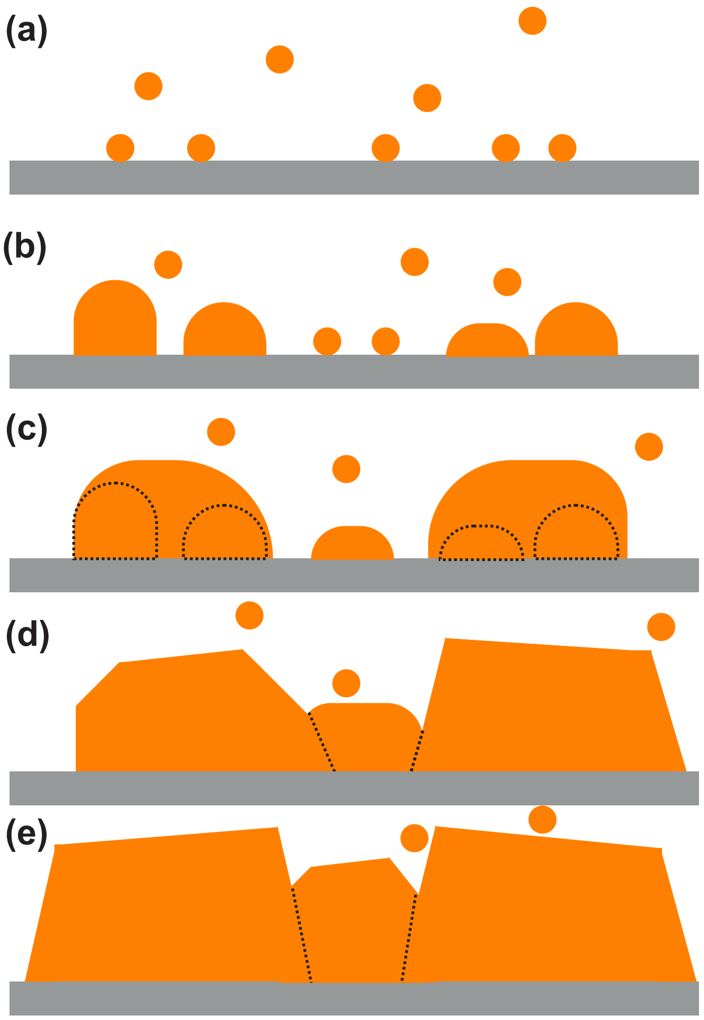

Figure 2.5: Illustration of fundamental process deposition onto a substrate and film growth. Processes are, (a) nucleation. (b) island growth. (c) island coalescence and grain formation (d) island coarsening and formation of polycrystalline grains (e) further development of grains and film frowth.

and film growth is shown schematically in Figure 2.5, taken from the descriptions of Petrov et al, and Brana et al [46, 47], which via in-situ analysis of film growth have described the process as occurring via multiple steps. Note, this describes the process of polycrystaline growth of films typical within PLD, and not layer-to-layer growth that may be observed in other techniques, or by control of substrate energies.

First atoms are incident onto the substrate, and begin to form groups or ”islands” on the surface. These islands, once large enough, begin to coalesce with each other and form larger grains, and it is typically around this stage that due to a combination of a sufficient number of atoms being present and sufficient time passing, for diffusion into lattice sites to occur and a crystalline structure forms, i.e. atoms arranged in an ordered lattice. This typically leads to a "coarsening" of these grains, yet each grain can form different crystalline structures, hence such a film being called "polycrystalline".

However it is important to note that in practice, the interfaces between substrate and film are not as instantaneous and sharp as shown in Figure 2.5, and there is a "transition layer" or region between these two layers. This arises from the bonding of the film to the substrate itself, which typically has a different structure to the polycrystalline film. The thickness of this layer is indicative of the difference between the lattice size of the substrate and the film [47]. In non-epitaxial growth techniques such as PLD, typically there is very little control over grain structure and transition layer thickness during film growth, and post-deposition techniques such as annealing are utilised in order to control the structures grown. Epitaxial techniques, for example molecular beam epitaxy [48], also utilise this but, also controlled "seeding" layers, which are substrates or other layers of films with pre-determined lattice constants in order to influence grains grown during deposition [47, 49].

## 2.5 Radio frequency plasmas

Laser produced plasmas are not the only form of plasma utilised in this work, and indeed radio frequency (RF) plasmas play a key role. RF plasmas work by exciting electrons within a gas by an external electric field operating at an RF frequency, typically at regulated frequencies such as 13.56 MHz and its harmonics as to not interfere with communications. These RF fields accelerate electrons within the plasma, but not ions due to their much greater masses and therefore lower mobility, not allowing them to be accelerated to high velocities within one RF cycle. This results in a plasma with high electron temperatures yet low ion temperatures, hence in some cases RF plasmas are referred to as "non-equilibrium plasmas" (see Section 2.6), or "low temperature plasmas" (LTP's) [50]. RF plasmas have a variety of chemically reactive species, due to the free electrons being able to undergo collisions and reactions with the cool, heavy species within the plasma. Due to this RF plasmas have found a variety of applications, from etching and deposition of electronics [51, 52], to biomedical applications [53], spacecraft propulsion [54] and more.

Before the specific forms of RF plasmas utilised in this work are discussed, a few important aspects of the plasmas will be highlighted. Firstly is the breakdown of a gas into a plasma, which occurs when free electrons within a gas, typically present due to influences such as solar radiation, are initially excited by an external influence. This causes them to collide with other heavy species in the gas, causing further ionisation and release of electrons. These electrons then repeat this process with heavy species causing further ionisation multiple times, resulting in what is commonly referred to as a "cascade" of electrons and breaking down the gas into a plasma. The nature of this breakdown was first described by Paschen in 1889 [55], and in much more detail since [56,57], yet what is key to note that the voltage required for a breakdown of a gas scales as a function of both the pressure of the gas $(p \cdot d)$, and the distance between the powered electrodes, as shown in Figure 2.6. Meaning low pressure RF plasmas such as the ones utilised here are able to cover much larger area and volume than higher pressure plasmas, hence their common use in large scale surface modification in industry and deposits such as in PE-PLD.

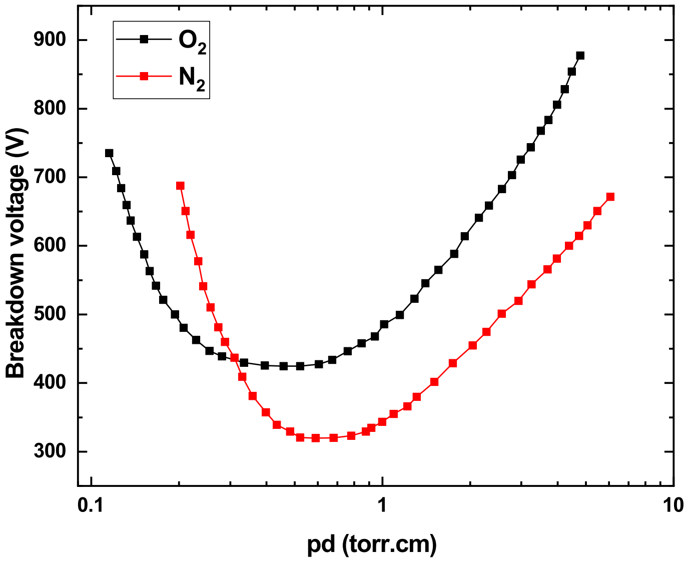

Figure 2.6: Example Paschen curve for $O_2$ and $N_2$. Data taken from [58]

Also of importance in RF plasmas is the "sheath", a region of net-positive charge between the plasma and its surrounding walls. A sheath is formed as although initially both electrons and heavy species are free to leave the plasma, electrons travel to the walls first due to their lighter mass and hence higher mobility. Due to these electrons leaving the plasma, a build up of negative charge is formed on the walls of the vessel surrounding the plasma, which in turns then repels electrons from within the plasma, resulting in a region of positive charge surrounding the plasma and electrons confined within the plasma bulk [50]. The thickness of this sheath, $s$, can be given as Equation 2.13:

$$s = \sqrt{\frac{2eV_0}{k_b T_e}} \cdot \lambda_d \tag{2.13}$$

With $e$ the charge of an electron, $V_0$ the voltage drop across the sheath, $k_b$ the Boltzmann constant, and $T_e$ the electron temperature. Also, $\lambda_d$ is the Debye length, given in Equation 2.14, where $\epsilon_0$ is the permittivity of free space. This is a characteristic parameter of plasmas, caused by the repulsion of like-charges within the plasma resulting in the screening of internal charges. When considering length scales shorter that $\lambda_d$ then internal electric fields within the plasma must be considered, yet for scales larger than $\lambda_d$ then said fields can be ignored. Therefore, plasmas with a higher electron density, $n_e$, have a shorter Debye length, resulting in a smaller sheath thickness, the effect of which will be discussed in the next section.

$$\lambda_d = \sqrt{\frac{\epsilon_0 k_b T_e}{n_e e^2}} \tag{2.14}$$

### 2.5.1 Capacitively and inductively coupled plasmas

There are two forms of low pressure RF plasmas important to the work presented in this thesis, both presented schematically in Figure 2.7. Firstly, a capacitively coupled plasma (CCP) is formed when a gas is in between a powered and grounded electrode, with the electric fields from these electrodes penetrating the gas, exciting electrons generating a plasma. For RF CCPs, sheath affects are of key importance for heating and energy coupling, as the acceleration along electric field results in species being accelerated either towards or away from the electrode, depending on the phase of the RF field [52]. This results in species such as heavy ions being accelerated through the sheath, that can aid processes such as sputtering of atoms from the surface, or through the release of secondary electrons from the surface to aid in heating of the plasma [35, 50].

Secondly are inductively coupled plasmas (ICP), created when the power is applied to a gas by an external coil instead of using a single plate electrode as with CCPs, with this coil acting as an antenna for the RF power [51, 52]. ICPs have two modes operation; E-mode ICPs are in fact very similar to CCPs, and occur when the ICP has low electron densities, i.e.

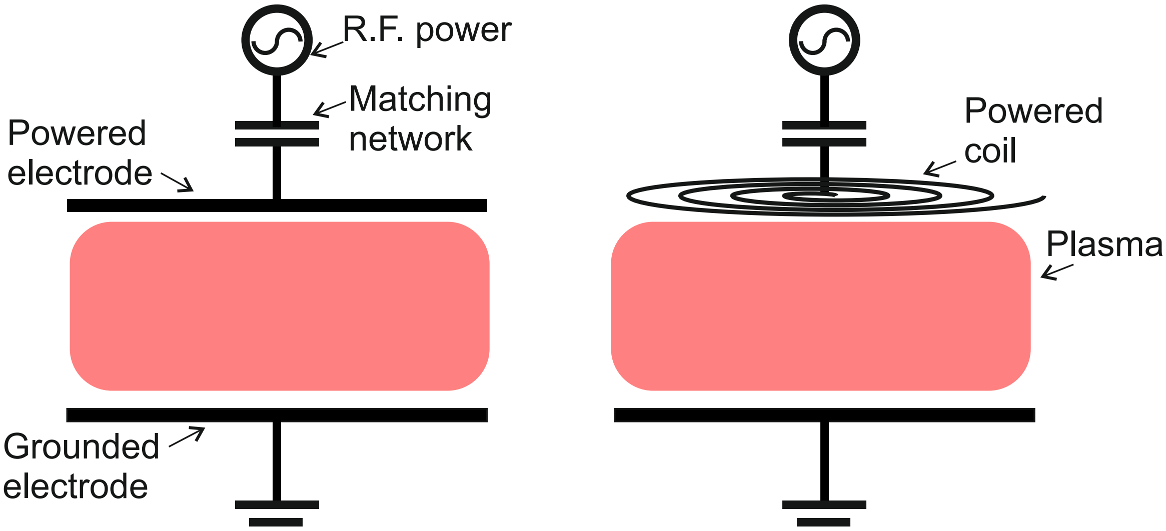

Figure 2.7: Typical configuration for low pressure RF plasma reactors. Left: CCP Right: ICP

at low pressures and powers, or during initial ignition of the plasma, where energy coupling is dominated by the effect of the capacitive fields generated by the coil. The most desirable form of an ICP is the H-mode, which occurs when the electron densities within the plasma are sufficiently high enough for the oscillating current within the coils to induce an electron current within the plasma, due to the coils fluctuating magnetic field and Faraday's law of induction [50].

H-mode ICPs typically operate at much higher plasma densities than E-mode ICP's and CCPs, and the transition to this mode of operation can clearly be seen via a significant change in various plasma parameters, such as electron and ion densities [59,60]. The H-mode of ICP's make them desirable in some cases over CCPs, as these high plasma densities are very beneficial for many applications. Plus as power is imparted to the plasma via magnetic coils and not via any form of sheath dynamics there is far less ion bombardment to the walls compared to CCPs. In addition to this, due to their higher densities and therefore smaller sheaths, combined with intrinsic higher plasma densities, H-mode ICPs can also be influenced by external biasing of targets in order to purposely create bombardment for highly efficient etching [51]. In terms of direct relevance for this work, a H-mode ICP has been chosen explicitly due to these two reasons, as high plasma densities can be beneficial for growth rates and interactions with the dense laser produced plasma, and the lack of ion bombardment meaning there is minimal interference and etching of the deposited film.

## 2.6 Equilibrium regimes

The last area of relevant background theory to detail is something that has been touched on above, such as within Section 2.5, this being the state of equilibrium within different forms of plasma. To be more specific, what is important is the state of equilibrium between the temperature of different plasma species, namely heavy ions/neutrals and the lighter electrons. As stated above RF plasmas are referred to as "non-equilibrium plasmas" due to the different temperatures of electrons and heavy species, caused by their different response to applied RF fields.

Laser produced plasmas however are quite different, as they are dense enough for sufficient collisions between electrons and heavy species for their temperatures to equilibrate, resulting in a plasma referred to as being in "Local Thermodynamic Equilibrium" (LTE) [61]; The condition required for this to be true is defined by the McWirther criterion, shown in Equation (2.15).

$$n_e > 1.6 \times 10^{12} T^{1/2} (\Delta E_{ij})^3 \tag{2.15}$$

Where $n_e$ is the electron density in $cm^{-3}$, T being the temperature of the system in K, and $\Delta E_{ij}$ being the energy difference between the i and j states within the atoms/ions in eV.

## 2.7 Metal oxide thin films

From the reactions between both the metal laser produced and RF oxygen plasma, PE-PLD is able to deposit metal oxide thin films, with two key types of metal oxides of interest within this thesis. Firstly is copper oxide, which is able to grow in two forms of stable compound; cuprous oxide ($Cu_2O$, copper(I) oxide) which has a band gap of 2.1 eV, comprising of Cu atoms within a FCC sub-lattice, and O atoms within a BCC sub-lattice, offset diagonally by one quarter of the cubic lattice constant, 4.684 Å [62,63]. $Cu_2O$ is chiefly of interest in the photovoltaic industry for use in solar cells [64, 65], but has also found uses in thin film transistors [66]. Secondly is cupric oxide (CuO, copper(II) oxide) has a narrower band gap of 1.2 eV, existing in a square planar monoclinic crystal of unit cell size 4.252 Å [63]. CuO has shown use in catalytic processes and gas sensors, as well as some uses in photovoltaics [62, 63]. The structure of both forms of copper oxide are shown within Figure 2.8.

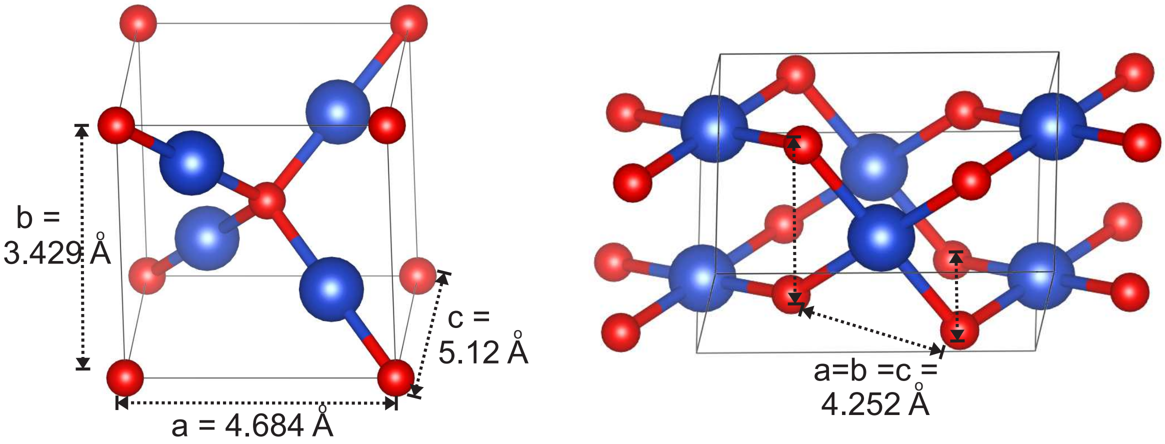

Figure 2.8: Lattice structure of unit cells for, Left: $Cu_2O$. Right: CuO. Blue atoms are Cu, red are O. Data obtained from COD [67], and plotted using VESTA [68].

Secondly of key interest in this work is zinc oxide (ZnO), as although elemental zinc is quite similar to copper, due to being direct neighbours on the periodic table, its oxide is quite different. ZnO primarily takes the form of a wurzite crystal structure, of base lattice parameters of 3.249 and 5.207Å [4, 62], as shown in Figure (2.9); although it is has been shown it is possible to grown ZnO in a zincblende structure, but only when using crystalline substrates of a cubic structure [69]. ZnO is classed as a "wide band gap" semiconductor, with a direct band gap of 3.1 eV, corresponding to a wavelength of 375 nm, putting it above the visible spectrum of light, which has a lower limit with violet at approximately 380 nm. Combined with the fact that thin films of ZnO on the order of 10's of nanometres thick are transparent, ZnO has great potential as a component in electronics in applications such as electrodes in displays [3, 70]

In particular ZnO is being highlighted as a replacement for the commonly used indium tin oxide (ITO), which is coming to the limits of its use due to such aspects as restriction on thickness due to sufficient levels of indium doping [71], and political issues regarding the access of indium. In addition to this, due to being a large band gap semiconductor, ZnO finds uses in higher energy applications of semiconductors, such as batteries [3, 70], and some specific phases and doped forms of ZnO are currently of interest in quantum communications, due to its high surface densities [72, 73]. Finally ZnO shows great promise in further applications such as again photovoltaics, and in piezoelectric applications, when either doped or used in conjunction with other thin film layers, such as the previously

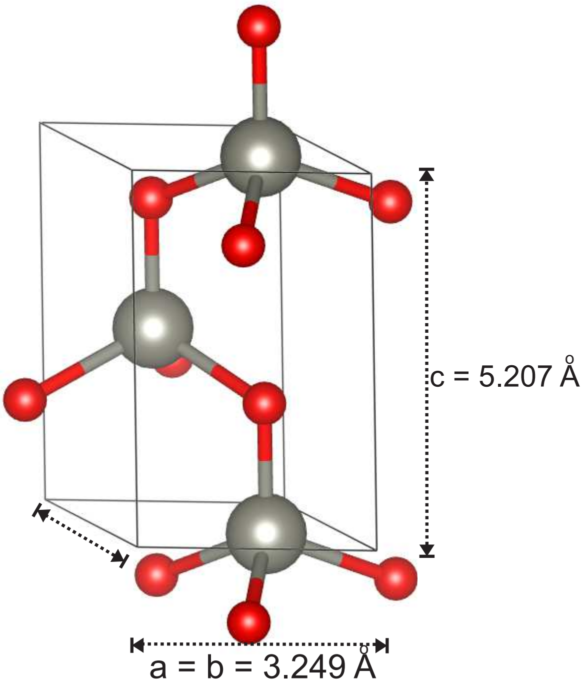

Figure 2.9: Lattice structure of wurzite unit cells for ZnO. Grey atoms are Zn, red are O. Data obtained from COD [67], and plotted using VESTA [68].

mentioned copper oxide films [3, 74].

Lastly to be discussed briefly in this work are aluminium oxide, $Al_2O_3$, films on steel substrates, which have been shown in recent times to be utilised as coatings for the steel under-layer, for uses and applications where high temperatures and physical or chemical corrosion need to be mitigated [75, 76]. Additionally, such films are also relevant for fusion-energy purposes, as $Al_2O_3$ is a suitable proxy for beryllium, Be [77]; Be deposits on steel are relevant to fusion as plasma facing mirrors on tokamaks are known to degrade over time, due to depositions of wall material onto said mirrors [78]. Therefore such $Al_2O_3$ films on steel can be used as an experimental proxy for these degraded mirrors, for means of the improvement of designs for cleaning processes [79, 80].

## 2.8 Comparison to other techniques and existing knowledge of PE-PLD

Currently there is a huge range of techniques that can be utilised to deposit thin films, however they generally all utilise the same key principle; this being the production of species to be deposited from a bulk material or precursor, which is then incident onto a substrate where the film is created. PLD is indeed one of these techniques and has been widely utilised since its inception [13], and is an attractive technique due to its competitive deposition rates and well documented good stoichiometry transfer from target to substrate . Although it does has some drawbacks, mainly being the need for substrate heating for successful film growth, control of particulates, which are commonly seen within PLD, need of carefully controlled backgrounds to influence the plume growth, and limited area of deposition [9, 11].

Other techniques for film deposition include, but indeed are not limited to: various forms of sputtering, where material is physically sputtered from the target by incident heavy atoms, which is widely utilised in modern industries due to being able to coat large areas of substrates. Again, sputtering has drawbacks similar to PLD in terms of needing to carefully control background species, and substrate heating control during deposition [81, 82]. And chemical vapour deposition (CVD), where chemical reactions break down precursors creating species to be deposited, is again a very widely used technique, perhaps mostly due to its versatility and range of applications [83]. CVD however has some significant disadvantages chiefly being the fact many chemical precursors used are highly toxic [84, 85].

A growing trend within such techniques in recent years has been the inclusion of various additions to improve the film growth, both in terms of deposition rate and film quality. Of most importance to this work is the utilisation of plasmas, where reactive species created from the plasma perform various processes during film deposition. For example the increased breakdown of precursors in PE-CVD [86], and magnetic fields used to increase electron and therefore plasma species used in HIPIMS [87]. Although this adds an additional level of complexity to the system, this has been off set by the improvements in film growth and the resulting applications and potential profits.

It is this logic that has now been applied to a PLD based technique to create PE-PLD. There has been some similar techniques reported in literature, yet they do not involve the exact same processes as the technique presented in this work. Examples are the use of titanium oxide and zinc oxide targets ablated in the presence of a CCP [88, 89], and the ablation of pure zinc targets with only the substrate being exposed to an oxygen ion beam [90, 91]. However still these works utilise processes such as substrate heating or post deposition annealing of the substrate, which were not needed to be used in the initial proof of concept for this form of PE-PLD [2], or in any of the depositions presented in this thesis. A summary of the key advantages and disadvantages of PE-PLD based on this knowledge, and some key points to be developed throughout this work, are shown below:

### 2.8.1 Advantages of PE-PLD

- Expansion and composition of the ablated plume can be influenced during its growth.
- Control of the RF produced oxygen plasma adds an additional level of control to the process.
- Use of metal targets, which are much more easily controlled than oxides, and much cheaper to manufacture than compound targets.
- Allows for additional gasses to be added into the system for a further variety of films (e.g. $N_2$ for nitrides)
- No need for post-deposition annealing, or heating of substrate during deposition.
- Low temperature environments allow for use of sensitive targets, such as polymers.

### 2.8.2 Disadvantages of PE-PLD

- Additional level of cost and complexity.
- Limited area of deposits.
- Still active area of research; Still not completely understood and described.

# Chapter 3

# Methodology

*This chapter presents the methodology used throughout this thesis, with an in depth description of the apparatus used in PE-PLD, alongside all diagnostic techniques used, both for plasmas and films. Lastly, numerical codes used to simulate various aspects of the plasma processes important to PE-PLD are described in appropriate detail.*

## 3.1 Experimental set-up

Figure 3.1 shows the internals of the deposition chamber, schematically and with photographs. The entire process occurs within a 6 arm vacuum chamber, with a vacuum achieved by two pumps, with deposition occurring under vacuum created by a scroll pump (Edwards nxDS 15i) able to maintain a base pressure of 1.5 Pa; with a further turbo pump (Pfeiffer TPU 170) used to achieve a lower base pressure of down to $5 \times 10^{-6}$ Pa. Pure oxygen gas (99.99% from BOC) is supplied to the chamber via mass flow controllers (MKS Instruments), operating typically at around 5 sccm to 10's of sccm, but additional gases may be added for spectroscopy or other reasons. Gas pressure is controlled during deposition by changing the flow rate of the gases, with additional fine control of the pressure by controlling screw valves leading to the vacuum pumps.

During deposition an ICP is created by supplying power to a 5 turn copper coil on the top side of the chamber which is separated from the gas by a 2.54 cm quartz barrier. Power comes from a 13.56 MHz RF power supply (Ceasar 1330), able to provide up to 1 kW, supplied through a Pi-type matching network (Meidan). This chamber is based upon the GEC reference cell [92], a device used within the global community for ease of comparison between experiments. The plasma may also be run as a CCP, by using the same power supply but applied to the bottom stainless steel electrode, via an Advanced Energy auto-matching network.

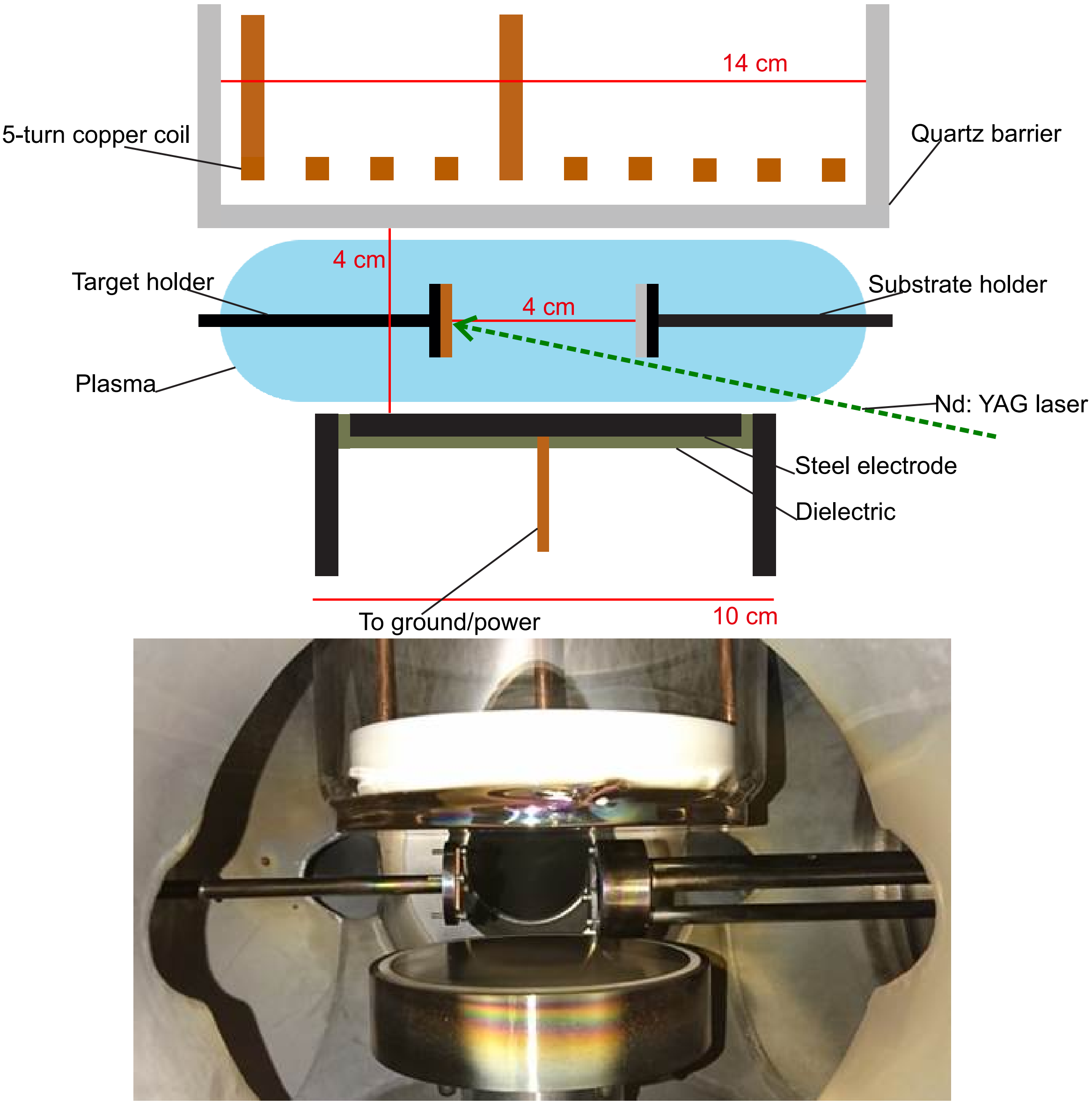

Figure 3.1: Top: Schematic of PE-PLD apparatus. Bottom: Picture of apparatus in YPI labs, from within vacuum chamber.

Targets (Zn, Cu etc.), which are 2.54 cm square in size, are held within the chamber on a manually rotatable stage which can be controlled from outside of the chamber, with the target held within the two electrodes, just off from the centre point of the chamber. Samples used are metals of at least 99.99% purity (from Testbourne), and are held in place via small screws around the outside of the target. Substrates are held in place on a stationary holder on the opposite flange to the target holder, with this substrate holder having the capability to be cooled from the external cooling system, which also manages to electrodes and vacuum pumps. Substrates are held in place via a series of screws around its circumference similar to the targets, and substrates used within this work are quartz ($SiO_2$), silicon (Si), stainless steel, and plastics. Target and substrate holders can hold targets of a 254 mm diameter. Before entering the chamber substrates are cleaned via treatment with acetone, then an ultrasonic bath of isopropanol at 40 to 50 $^o$C for at least 10 minutes to remove any blemishes and impurities on the surface.

The laser used is a Continuum Minilite laser, which is a frequency doubled Nd:YAG laser operating at 532 nm, with a pulse length of 5 ns, and total beam energy of 35 mJ per pulse, operating at a repetition rate of 10 Hz. The laser alignment is controlled by mirrors, and focused by a lens with a focal length of 50 cm, entering the chamber through a window with an anti-reflective coating for 532 nm, finally incident onto the target. The focal spot size of the laser on the target if it was normal to the laser is 1mm in diameter, however due to in practice being offset at an angle of 45$^o$, the spot size is not perfectly circular.

All components within the set-up are controlled by a digital delay generator (Stanford Instruments), with the timings as follows; Firstly the ICP coil is powered and the plasma

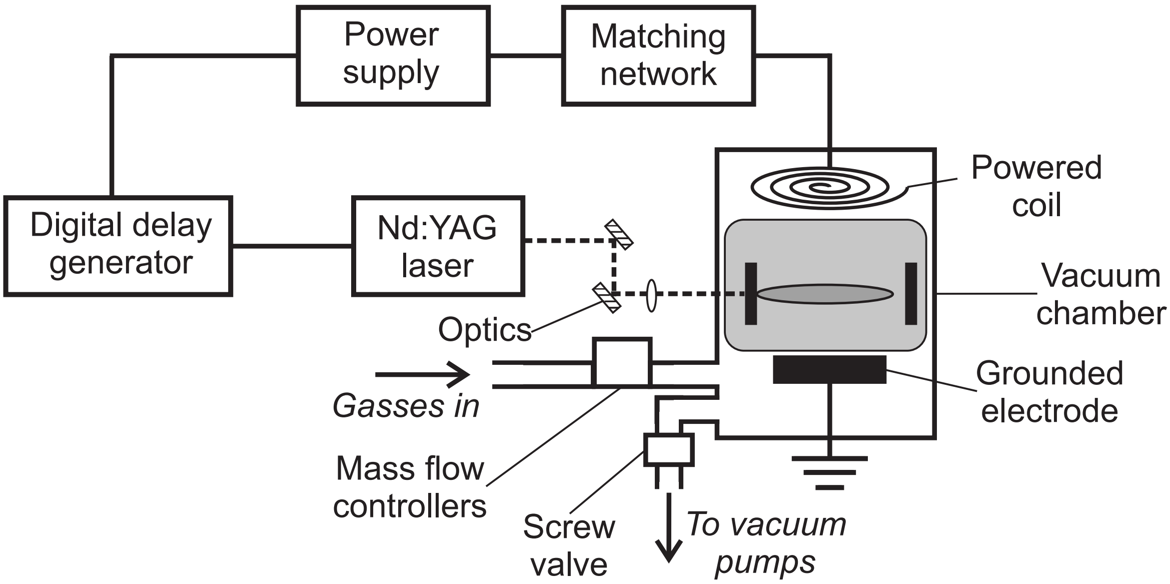

Figure 3.2: Representation of all apparatus used in PE-PLD.

is allowed to reach an equilibrium for 8 ms, with this point assumed as it is much longer than any process known to generate plasma species under such conditions. After this 8 ms the laser flash lamp is powered, generating gain within the lasing medium (Nd:YAG rods) which reaches its maximum at 150 $\mu$s, after which point the laser q-switch is triggered causing laser emission and ablation of target material into a plasma plume. This plume travels to the substrate, a distance of 4 cm, which from spectroscopy and simulations has been determined to take approximately 2 ms [2], and then after this total of 10 ms the power for the plasma is stopped. In order to be in line with the repetition rate of the laser, no power is applied to the system for a total of 90 ms which after said the point the cycle begins again; This gives the entire system a duty cycle of 10% [2]. A full representation of all apparatus used in PE-PLD can be seen in Figure 3.2.

## 3.2 Plasma diagnostics

In order to characterise the RF plasma used in this work, a range of diagnostics have been used, with the desired techniques being so called "passive", meaning that do not perturb the plasma. Such techniques are highly attractive across many plasma processes due to the lack of interference caused within the plasma. Also, many diagnostic techniques, such as electrical probes, cannot be used in many conditions, such as within PE-PLD, as the plasma can negatively effect said probe by corrosion or etching and deposition. Figure 3.3 shows how all diagnostics are situated on the PE-PLD chamber.

All diagnostics used in this work are utilised in order to determine the gas temperature of the plasma; this is a property of the plasma, which is well known to affect many processes, including collisional processes such as quenching, and therefore lifetimes of many species, interactions with surrounding walls, and the rate at which many chemical reactions occur [93–95]. However this being considered, gas temperatures are an aspects of plasmas that are yet to be fully understood, especially in low pressure $O_2$ RF ICPs such as the one utilised within this work. There has been some work within this field, such as measurements of gas temperatures within inductive RF plasmas containing $H_2$ [96] and $CF_4$ [97], and direct current discharges within $O_2$ [98], and simulations of $O_2$ RF ICPs [95], but experimental results of gas temperature measurements in such $O_2$ RF ICPs have yet to be reported. Therefore the range of techniques, as described in this following section, have been used

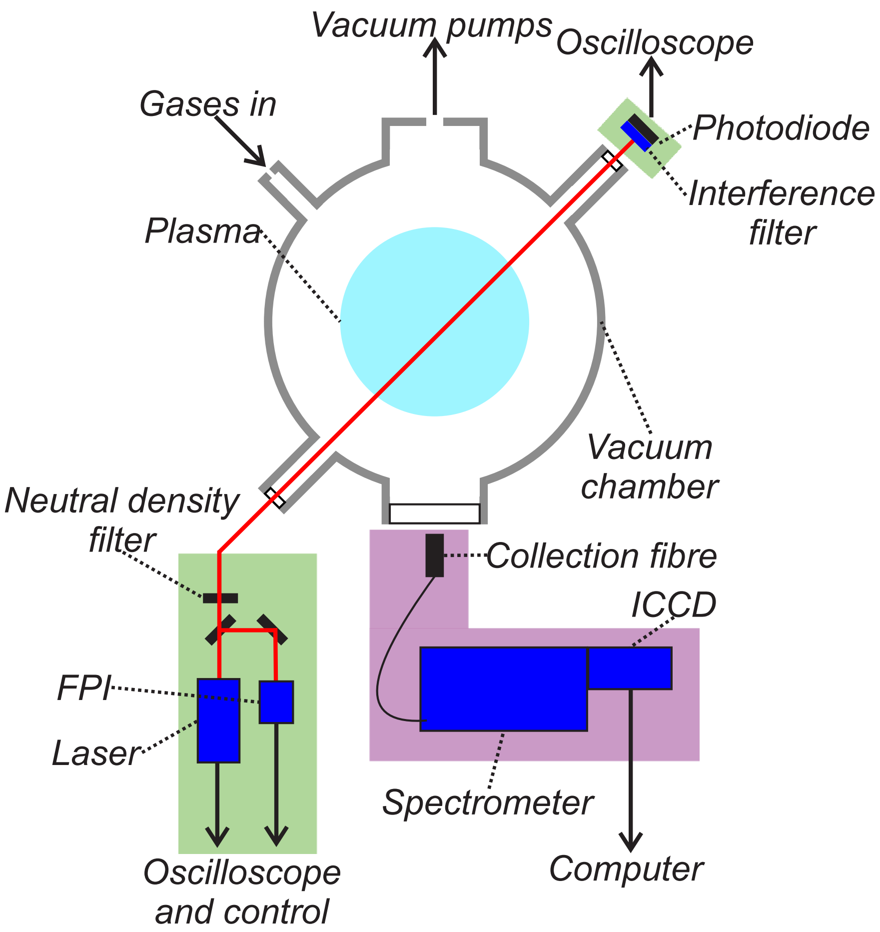

Figure 3.3: Top down view of the plasma diagnostic set-ups used. Equipment highlighted in green used for tunable diode laser absorption spectroscopy. Equipment highlighted in pink used for optical emission spectroscopy.

in order to determine the gas temperature and a comparison between all three method performed, for means of increasing the reliability of said results, and also an exploration into the applicability of each technique.

### 3.2.1 Optical emission spectroscopy fundamentals

Within a plasma there are processes that excite electrons to higher bound states within atoms or molecules, which then spontaneously decay to lower states emitting a photon of a specific energy corresponding to the species they are emitted from. Optical emission spectroscopy, OES, is a passive diagnostic technique that utilises these photons by detecting them and alongside the use of an appropriate model, is able to diagnose various aspects about the plasma, such as the gas temperature as desired in this work. During OES a device called a

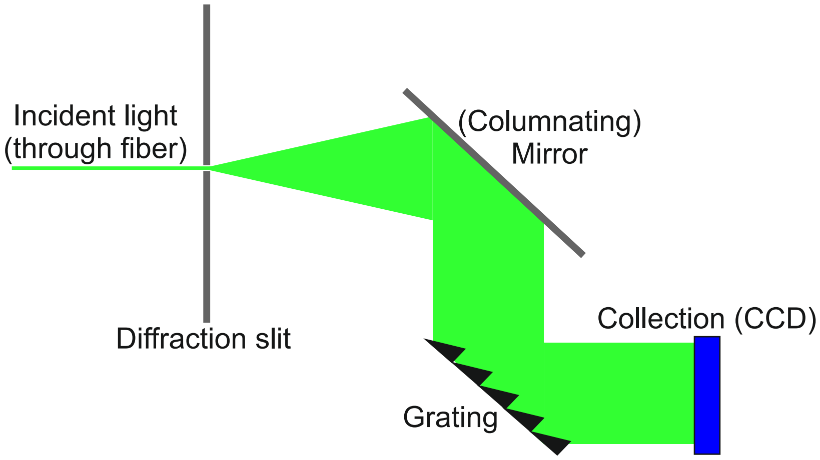

Figure 3.4: Schematic showing the basics of a spectrometer used during OES

spectrometer is utilised, the concept of which shown in Figure 3.4. Here collected photons are passed through a slit, and then typically incident on mirrors to direct and columnate the light, which is then incident on a diffraction grating. This is a component comprising of a series of angled surfaces, where photons of the same wavelengths that reflect off adjacent surfaces constructively interfere. Photons are then made incident onto a detector, which is typically some form of charge capture device (CCD), with photons of different wavelengths being observed at different spatial positions, which can then be analysed by various models [36].

In this work the spectrometer used is the Andor Shamrock 340i, which has a variety of different diffraction gratings allowing for further control of the signals spectral range and resolution, whilst also being able to be coupled to an intensified CCD (ICCD). An Andor iSeries 334T is used in this work, which uses a photo-cathode, multi-channel plate and phosphor screen to amplify signal allowing for analysis of much weaker spectral lines. This system is also able to be connected to the DDG that controls the timing of various processes within the PE-PLD system, allowing for time resolved measurements. When using such spectrometers, broadening effects need to be taken into account, which are processes increasing the width of observed emission lines. Indeed these are desired in some cases for means of diagnostics e.g. Doppler broadening of lines for temperature measurements, however certain unavoidable effects such as the experimental broadening need to be characterised. In this work this is done by a Ar plasma operating at similar conditions, chosen due to the well known and documented nature of various Ar species [22, 99], and discussed in detail in Chapter 5. The equipment used for all OES measurements during this work is shown in Figure 3.5, with how it is situated on the chamber during experiments having been shown previously in Figure 3.3.

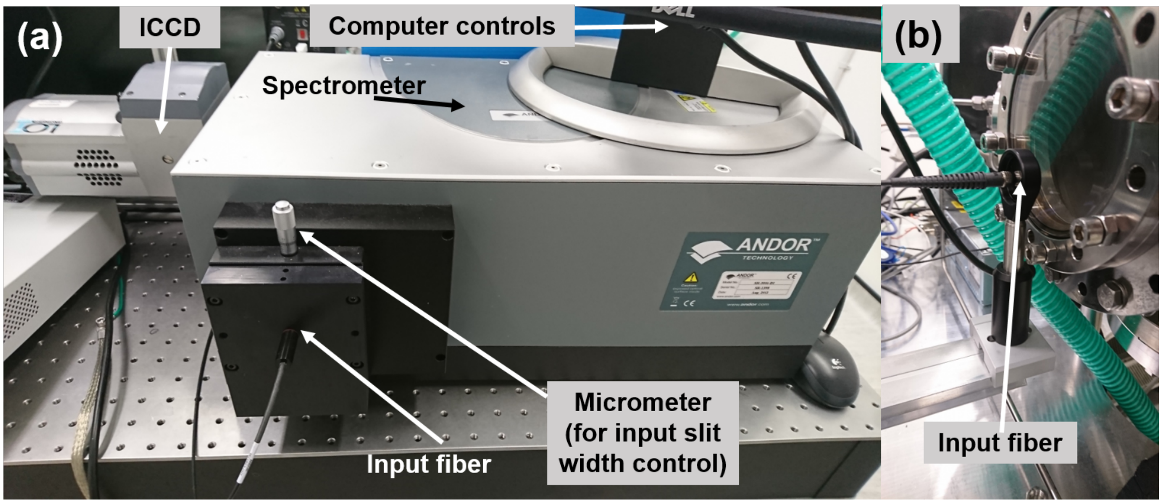

Figure 3.5: Apparatus used during OES experiments, (a) shows spectrometer, (b) shows fiber situated in front of plasma (see Figure 3.3).

### 3.2.2 OES: Molecular oxygen

Within this work two forms of OES are used, both on molecular species. The first technique is the most desirable, as it based purely on oxygen, which is the gas used within PE-PLD for the deposition of oxides. The molecular transition of interest is from the $O_2$(b) state, being a low energy, long lived metastable of oxygen, to the ground state of oxygen, $O_2$(X). This transition is shown in Equation 3.1.

$$O_2(b^1\Sigma_g^+, v' = 0) \rightarrow O_2(X^3\Sigma_g^-, v'' = 0) \tag{3.1}$$

This specific transition was first described from its detection in stellar and atmospheric physics in 1961 [100], and since has been used for the determination of gas temperatures in DC glow discharges through OES, in some cases down to pressures of 70 Pa (0.5 Torr) [101–103]. It has only yet been applied to a low pressure RF ICP in the work of Wegner at al [60], where measurements between 1 and 35 Pa were taken, however the technique used there was the more expensive and complicated microwave interferometry, and not passive OES as utilised here. From such a transition, a “molecular band” can be observed through OES, comprising of multiple peaks corresponding to different rotational transitions, each of which

Table 3.1: Höln-London factors for the four allowed branches of the magnetic dipole transition [105]

| **Branch** | $\Delta K$ | $\Delta J$ | $S^{J'}_{J''}$ |
|---|---|---|---|
| $^RR$ | +1 | +1 | $\frac{1}{2}J''$ |
| $^RQ$ | +1 | 0 | $\frac{1}{2}(J''+0.25)$ |
| $^PP$ | -1 | -1 | $\frac{1}{2}(J''+1)$ |
| $^PQ$ | -1 | 0 | $\frac{1}{2}(J''+0.75)$ |

has an intensity $I$, as described in Equation 3.2.

$$I^{J'}_{J''} = CS^{J'}_{J''}exp\Big(\frac{-F_{J'}hc}{k_bT_{rot}}\Big) \tag{3.2}$$

where:

$$F_{J'} = B_{v'=0}J'(J'+1) - D_{v'=0}(J'(J'+1)^2) \tag{3.3}$$

Where $J', J''$ are the rotational number of the upper and lower level respectively, $C$ a proportionality factor, $h$ Planck's constant, $c$ the speed of light, $k_b$ Boltzmann's constant, $B_{v'=0}$ and $D_{v'=0}$ being fine structure constants of 1.39138 $\text{cm}^{-1}$ and $5.486\times10^{-6}$ $\text{cm}^{-1}$ respectively, and $T_{rot}$ being the desired rotational temperature of the molecule. However this assumes the population of the upper state can be assumed to be proportional to that of the lower state, and described by a Boltzmann distribution, which requires a sufficient number of collisions between molecules for this to occur; perhaps a reason why this technique has yet to be utilised at low pressures as this cannot always assumed to be the case.

The factor $S^{J'}_{J''}$ in the equation above is the Höln-London factor [104], and given in Table 3.1. Where $\Delta K$ and $\Delta J$ are the change in the magnetic and rotational quantum number between the upper and lower states. This form of the Höln-London factors is used as this transition is electronically forbidden, as the selection rule for the primary quantum number, S, as shown in Equation 3.4 is broken; i.e. $\mathbf{^1}\Sigma_g^+ \rightarrow \mathbf{^3}\ \Sigma_g^-$.

$$S \equiv 0, \pm1 \tag{3.4}$$

Therefore this occurs via a magnetic dipole transition which is defined by four branches ($^RR$,$^RQ$,$^PP$, and $^PQ$), which conserve total angular momentum, as first described by Herzberg [104]. These four branches, each with a different combination of $\Delta K$ and $\Delta J$, as shown within Table 3.1 alongside the associated $S^{J'}_{J''}$.

Table 3.2: Diatomic constants of the upper and lower states of interest in the $O_2$ molecule [100]

| **Constant** | $O_2(X^3\Sigma_g^-, v=0)$ | $O_2(b^1\Sigma_g^+, v=0)$ |
|---|---|---|
| $B$, Rotational constant in equilibrium position ($cm^{-1}$) | 1.43 | 1.39127 |
| $\lambda_{ss}$, Spin-spin coupling constant | 1.985 | n/a |
| $\gamma$, Spin rotation coupling constant | $-8.4253\times10^{-3}$ | n/a |
| $D$, Quartic centrifugal distortion | $4.854\times10^{-6}$ | $5.486\times10^{-6}$ |

The wavelength of each emission line is determined by the difference in energy between the upper and lower states for different values of $J$. The energy of these states given by the Hamiltonian, H′, as shown in Equation 3.5. Where K and S are taken from Table 3.1, and other constants outlined in Table 3.2. But for the upper state, where **S** is 0, this equation can be simplified by ignoring the last term.

$$H^{'} = B\mathbf{K}^2 + \gamma(\mathbf{K}\cdot\mathbf{S}) + \lambda_{ss}\mathbf{S}^2 \tag{3.5}$$

However it is worth noting the diatomic constants outlined in Table 3.2 are known from experiment, so have some associated uncertainties in their accuracy. Therefore when simulating this spectra, there was disagreement between the spacing of the observed and simulated spectra; how this was accounted for will be discussed shortly. Due to this uncertainty in the precise values of these constants, much of the literature that has utilised this spectra at higher pressures do not solve the Hamiltonian for each state. Instead the wavelength positions for each line as presented in Babcock and Herzberg [104], taken from high resolution spectroscopy are utilised.

Experimentally observed spectra are compared to modelled spectra, and then the temperature within this model modified until a fit between the two spectra is reached. This modelling in practice is done here in two ways, both of which are utilised due to the aforementioned issues with exact precision of the wavelength position of each line. Firstly the freely available software PGOPHER is used [106], in combination with the diatomic constants of the upper and lower molecules in Table 3.2. PGOPHER uses an extensive database of various allowed forms of molecular transitions, such as the one highlighted here, in order to model the required spectra. However as mentioned the wavelength of simulated lines did not match those of experiment, with the central gap between the four branches being too large, being approximately 1 nm. However each half of the spectra, i.e. the $^{R}R$,$^{R}Q$ and the $^{P}P$, and $^{P}Q$, could independently match observed spectra, and therefore each half was fitted independently with an average of the fitted temperatures between the two being taken.

The second method was using a script written by Dr Kari Niemi of the YPI within LabView, which empirically solves equation 3.2, utilising the constants and theory as outlined above. Parameters, such as the gas temperature are then altered in an iterative manor until a best fit is performed, determined numerically by a chi-squared factor. This script has been used successfully for the determination of gas temperatures, within the work of Wijaikhum et al [107]. However, like with the use of PGOPHER, wavelength calibration issues were found with the central gap between the branches. The solution here was to artificially squeeze or stretch all observed lines till an agreement was met. A numerical compression factor of approximately 1.02 was found to match modelled data to experiments. This comes with the benefit of speed and the temperature of each branch matching, however some uncertainty in the magnitude in this squeezing is introduced. Figure 3.6 shows a simulation from PGOPHER modelling up to the 32$^{nd}$ $J$, exhibiting how raw emission lines for each transition look, alongside an example spectrum used for fitting where broadening of lines has been taken into account.

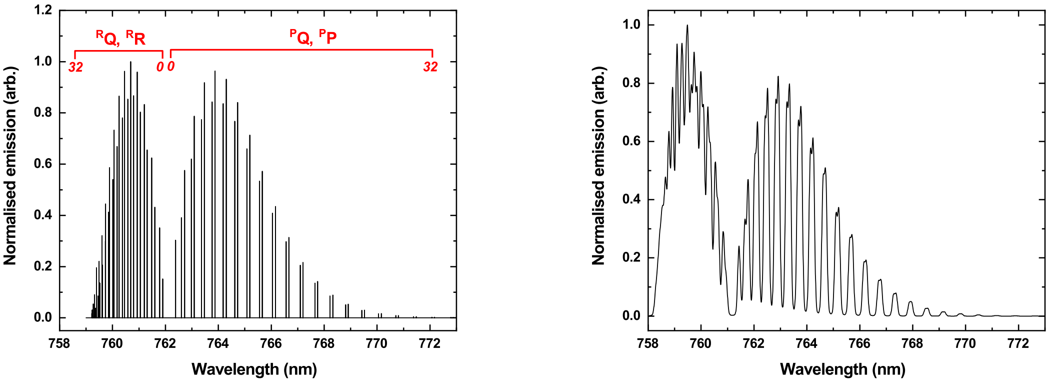

Figure 3.6: Example spectra of $O_2$ molecular transition of interest taken from PGOPHER simulation. Left: Raw intensity of each branch. Right: With broadening taken into account

### 3.2.3 OES: Molecular nitrogen

The second OES technique utilised is again based upon a molecular band, yet is performed with a small admixture of nitrogen, $N_2$. Here the transition is between two electronically excited states of $N_2$, being the $N_2$(C) and $N_2$(B) states, with the transition as outlined in Equation 3.6 observed.

$$N_2(C^3\Pi_u, v' = 0) \rightarrow N_2(B^3\Pi_g, v'' = 0) \tag{3.6}$$

This transition is commonly utilised within literature, and recently reviewed for means of gas temperature measurements by OES and other techniques in the work of Bruggeman et al [108]. Although this technique is mostly cited for use in higher pressure plasmas [109,110], though it has also been utilised in low pressure RF plasmas, including an ICP containing Chlorine in the work of Donnelly et al [111] operating at similar pressure and powers as studied in this work. Although an admixture of $N_2$ is required, it is discussed in the results (Chapter 5) that the amount used, being roughly 10%, does not perturb the oxygen to an observable degree. This transition is quite different to the $O_2$ one outlined in the previous section, as this is electronically allowed, and can therefore be described by the more classical description of molecular transition by Hund's cases, as outlined in the work of Herzberg [112]. However, Equation 3.6 is in fact quite a complicated transition, as both states within the molecule are relativity high in energy. In total there are 27 allowed transitions between the upper and lower $^3\Pi$ states, each of which with a different description of their intensity, instead of just the one used for the oxygen transition (Equation 3.2).

A rigorous treatment of each line within this transition will not be given here for brevities sake, but a detailed outline of this transition can be found in its first description by I. Kóvacs in 1965 [113], and A. Scahdee in 1975 [114]. Additionally S. Pellerin et al [115] shows a detailed description and empirical determination of each line for a similar transition within OES on $C_2$, observed during plasma cleaning of polluted gases. An important comment to make however, is due to there being no treatment of the magnetic quantum number, as there was with the $O_2$ transition, there is no "splitting" of the band into two distinct areas. Therefore the observed molecular band looks quite different, with an example simulated emission shown in Figure 3.7.

Fitting of observed spectra is performed via very similar means to $O_2$, with the use of

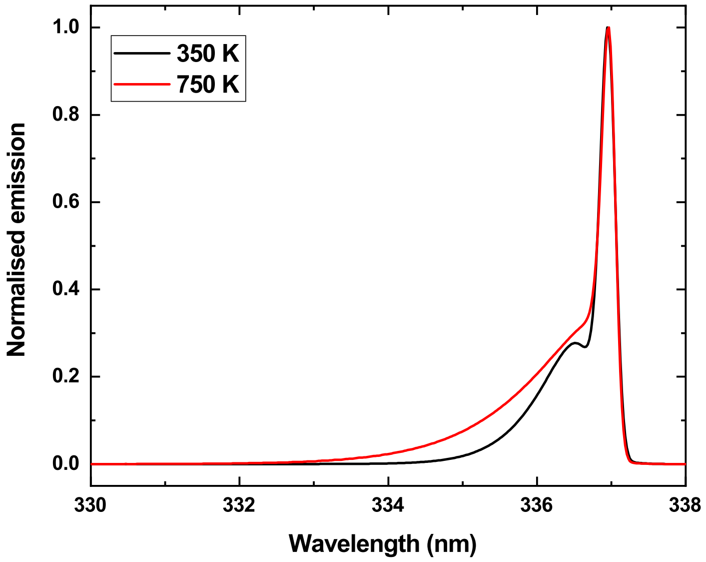

Figure 3.7: Example spectra of $N_2$ molecular transition of interest taken from LabView simulation at two different gas temperatures, with broadening affects applied.

LabView software developed by Dr K. Niemi, with this being used to produce Figure 3.7. This utilises the full treatment of all allowed transitions and their equations from Kóvacs [113], and has been successfully used for gas temperature fitting within an atmospheric pressure plasma jet in Wijaikum et al [107]. Said temperature is obtained as each of these transitions are dependant on the rational temperature of the molecule, quite similar to that as Equation 3.2, and therefore has the same assumptions of a Boltzmann distribution of electrons within states of the $N_2$ molecule.

### 3.2.4 Tunable diode laser absorption spectroscopy

Absorption spectroscopy differs strongly to the OES discussed above, as instead of passively analysing light emitted from the plasma itself, an external light source is used, with such sources typically being LEDs or lasers. Photons from these external sources interact with the plasma by imparting their energy to bound electrons, causing them to excite to higher states within the molecule or atom they are bound to, with the energy difference between these states corresponding to the incident photon's energy. From detection of photons that pass through the plasma, and use of an appropriate model, factors such as densities and temperatures of species within the plasma can be determined [116].

The specific form of absorption spectroscopy used in this work is tunable diode laser absorption spectroscopy (TDLAS) with an admixture of Argon, Ar. A tunable diode laser is a laser where the output wavelength can be altered by applying a different current to the diode from which photons are emitted, and in some cases by altering the path length of the lasing cavity by means such as piezo-electric motors. TDLAS of Ar for means of determination of gas temperatures is a well accepted technique within plasma physics, as been utilised in a range of conditions, including within low pressure inductive sources applicable to the source utilised in this work [117–119]. However to note in said works the gases used were pure Ar, not by means to diagnose $O_2$ dominate plasmas such as presented within this work. The laser used within this work is a Photonics TA Pro, controlled by a Photonics Laser Diode Pro Control Unit, as shown in Figure 3.8, alongside the other apparatus used, with how this is situated on the chamber shown previously in Figure 3.3

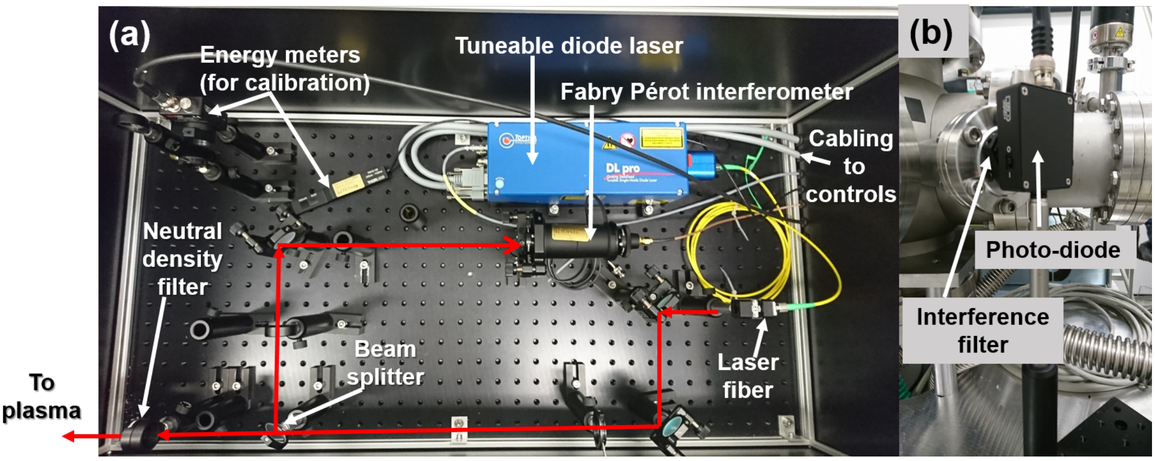

Figure 3.8: TDLAS apparatus utilised, (a) situated before laser light enters the chamber, (b) situated after laser light passed through plasma. (See Figure 3.3).

The laser has a continuous output of 150 mW, with to a central wavelength of 810.4 nm, which corresponds to the transition within Ar as outlined in Equation 3.7.

$$Ar(1s_4) + \gamma(810.4nm) \rightarrow Ar(2p_6) \tag{3.7}$$

This lower $1s_4$ state is a resonant state of Ar, and therefore known to have lower densities than other Ar species within RF plasmas [120], yet is present within the low pressure case used here, and shown to be present within low pressure cases in various works, such as Tian et al [121]. Figure 3.9 shows a spectrum taken with a Oceanoptics Maya spectrometer within

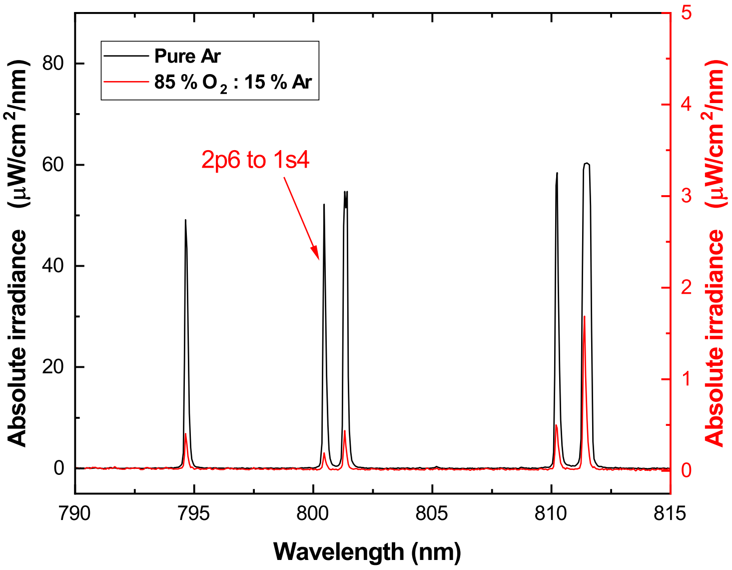

Figure 3.9: Example spectra of pure Ar and $O_2$:Ar ICP, operating 20 Pa, 700 W.

the PE-PLD chamber operating at 20 Pa, 700 W which is a typical case used throughout this work; both a pure Ar plasma is shown, alongside an $O_2$ plasma with an admixture of Ar used during TDLAS measurements, with this admixture being 15%. It can be seen that in the pure Ar case there is a strong signal corresponding to the decay from the $2p_6$ to the $1s_4$ state, with this emission still observed within the $O_2$ plasma, although much weaker due to affects such as Penning ionisation of the excited Ar. Similar to the admixture of $N_2$ used in the OES measurements, it is discussed within Chapter 5 that this 15% admixture of Ar did not perturb the oxygen chemistry; In addition it has been shown computationally in the work of Gudmundssson et al, that small admixtures of Ar does not affect the density of many oxygen states or their temperatures [122].

A gas temperature is determined via TDLAS by Equation 3.8, where $\lambda_0$ is the central wavelength of the peak, $k_b$ the Boltzmann constant, $M$ the mass of the species, and $T$ the temperature of interest. $\Delta\nu_D$ is the measured broadening of the peak determined from the full width half maximum (FWHM), which can be measured due to the tunable nature of the laser, as during measurements, the wavelength of the laser is scanned across a range of wavelengths close to the central wavelength.

$$\Delta\nu_D = \frac{2}{\lambda_0}\sqrt{2ln(2)\frac{k_b T}{M}} \tag{3.8}$$

The broadening of this signal is then assumed to come from Doppler broadening, i.e. the change in wavelength due to the motion of species within the plasma photons interact with, which is caused by the thermal motion of the species. Hence T being able to be determined from this observed absorbance signal, with other broadening effects such as pressure broadening are assumed to be negligible in magnitude compared to that caused by this thermal Doppler effect.

The intensity of the signal observed can be described by the Beer-Lambert law, Equation 2.1, yet written more explicitly for this case in Equation 3.9.

$$I = I_0 e^{-\sigma N l} \tag{3.9}$$

Where $I$ and $I_0$ are the observed and initial density as before, $N$ the density of absorbing species, and $l$ is the path length of the laser within the plasma to be considered; here $l$ is assumed to be 10 cm, the diameter of the electrodes.

The observed signal on the photo-diode, see Figure 3.3, comprises of photons that have passed through the plasma without being absorbed, with a reduction in intensity at a certain time, corresponding to when the wavelength of the scanning laser matches that of the transition in equation 3.7. In order to distinguish this absorbance "peak" from the rest of the observed signal, Equation 3.10 is utilised.

$$\frac{I_{P+L}(\nu) - I_P(\nu)}{I_L(\nu) - I_{BG}(\nu)} = e^{-\sigma N l} \tag{3.10}$$

Where subscripts $P, L$, and $BG$ corresponding to emission from plasma, laser, and background, respectively. This results in just the observed difference in intensity caused by absorbance of photons by the plasma. Within this work, signals were obtained in the following order; First the plasma was ignited and the signal of just the plasma obtained ($I_P$), the laser was then turned on and the signal of both ($I_{P+L}$) obtained. The plasma was then turned off, and just the laser signal ($I_L$) taken, and lastly the laser turned off the the background intensity taken ($I_{BG}$). This process reduced the amount of times both the laser and plasma were turned off and on, and therefore minimised any uncertainty caused from such sources as differences in matching of the plasma, or temperature deviation of the laser diode.

A wavelength calibration of the observed signal on the oscilloscope is performed by the following means; Before entering the plasma a beam-splitter is put in the path of the laser (ThorLabs, fused silica plate beam-splitter 9:1), to separate off a fraction of light, which is then passed into a Fabry-Pérot interferometer (FPI). In particular a confocal FPI (ThorLabs SA200-8B) is utilised, which comprises of two concave mirrors at a known distance, as shown in Figure 3.10. A wavelength calibration is achieved, as if the distance between mirrors is an integer multiple of the laser wavelength, constructive interference will occur, resulting in an increase in observed signal transmitted through the FPI. This signal takes the form of sharp peaks, each with a particular spacing between them. This spacing is known as the free spectral range (FSR), with the FPI used here having a FSR of 1.5 GHz. This can be quantified as in Equation 3.11.

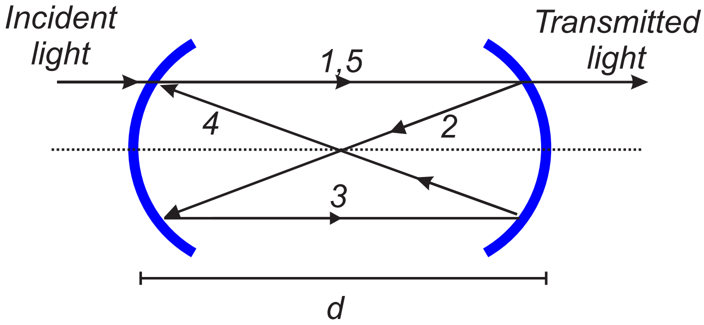

Figure 3.10: Schematic of a confocal FPI used for wavelength calibration of TDLAS signal.

$$FSR = \frac{c}{4d} \tag{3.11}$$

where $c$ is the speed of light, and $d$ is the distance between the mirrors. Note the denominator is a factor of 4 due to four reflections occurring during a photons path through the FPI. Therefore as the timebase of the oscilloscope used is known, and this distance between mirrors set, signals from the photo-diode can be calibrated to a wavelength.

## 3.3 Film diagnostics

### 3.3.1 Scanning electron microscopy

Scanning electron microscopy, SEM, is a well established technique, with its roots in the early 1900's [123, 124]; SEM is in principle very similar to optical microscopy yet instead of photons being used to irradiate the sample, a controlled beam of electrons is used as these can be accelerated to higher energies that are typical of white light photons, allowing for much higher resolution analysis. In practice electrons are produced by thermionic emission from a filament, and are then accelerated by an external electric field up to a known energy, commonly refereed to by the "acceleration energy" or "beam energy", which is typically in the order of keV. A series of magnetic lenses then focus the beam down to a known size to irradiate the sample, and some modern SEM machines, such as the *JOEL 7800F Prime* used here as shown in Figure 3.11, allow for further control of the magnetic lenses in order to account for any misalignment that may be caused by the electrons gyroscopic orbit within the magnetic field, and any astigmatism in the shape of the focal area [125].

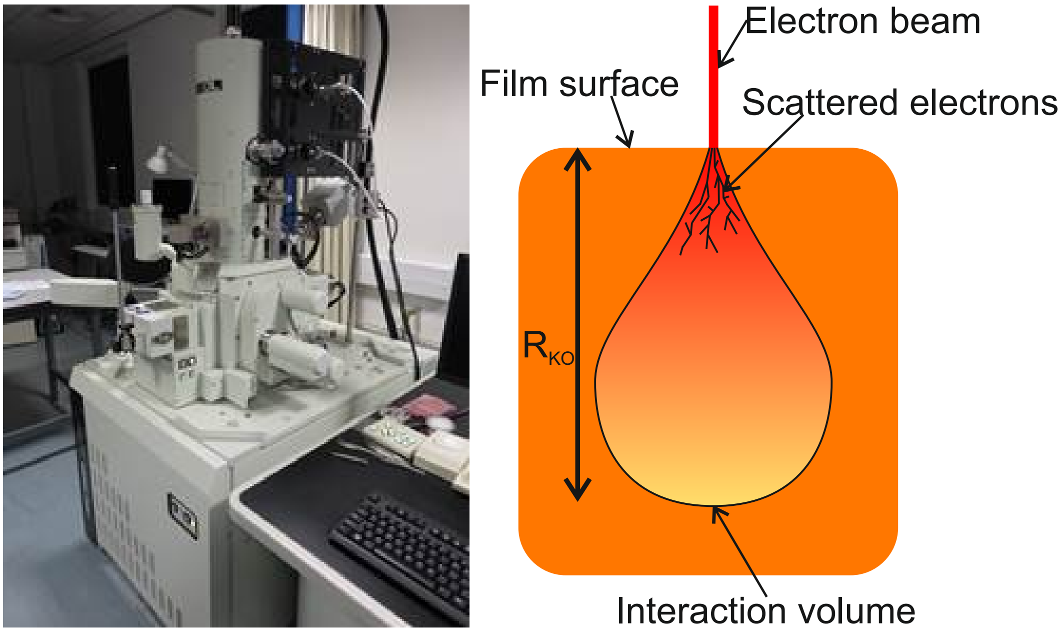

Figure 3.11: Left: SEM apparatus used. Right: Representation of tear-drop interaction of target

Incoming electrons penetrate the sample and begin to scatter off atoms and electrons in the sample, causing a typical tear-drop interaction volume which is also shown in Figure 3.11, with the means of calculating the depth shown in Equation 3.12, where $R_{KO}$ is the "range" of penetration named after Kanaya and Okayama who derived this relation in 1972 [126]. $A$ is the average atomic mass of the film, $E_0$ the beam energy of the SEM, and Z the average proton number of elements in the film. Based on the $Z$ numbers of the elements within the oxide films analysed in this work, and the beam energies utilised in order for EDX analysis (see next section) which was typically up to 5 keV, the $R_{KO}$ within the SEM within this work is on the order of a few hundred nanometres.

$$R_{KO} = \frac{2.76 \times 10^{-11} A E_0^{5/3}}{Z^{8/9}} \tag{3.12}$$

Electrons are reflected or scattered out of the sample from any point within this interaction volume, and subsequently detected. Within the JOEL SEM there is a variety of detectors each designed for different electrons, for example the lower electron detector (LED), placed close to the sample, which detects higher energy lowly scattered electrons. For films SEM can provide very high resolution images of the surface, by scanning the electron beam across the films surface. An example image taken from a ZnO film deposited by PE-PLD is shown in Figure 3.12. Such images are used to look at the morphology of the surface, i.e. to look for any particuates, if there are any observable large grain structures within the film etc. Yet it is used most within this work when used in tandem with other techniques, outlined below.

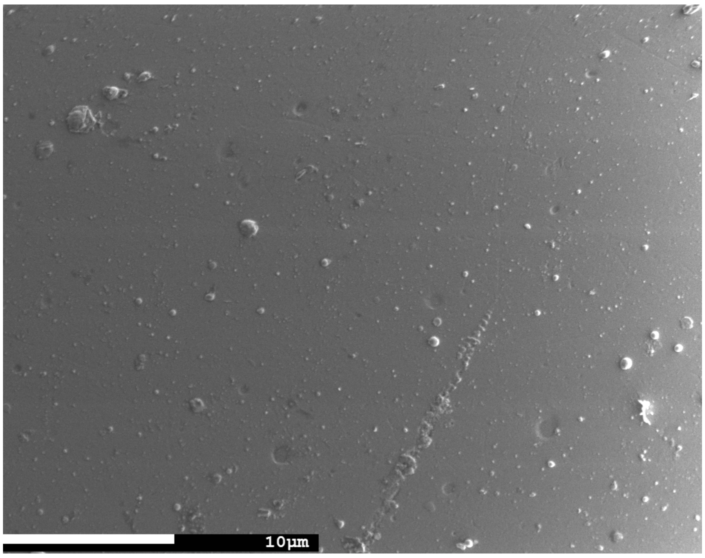

Figure 3.12: SEM image of the surface of a ZnO film deposited by PE-PLD. Some particulates seen on surface are from carbon sputtering onto the film to reduce charge build up of the sample.

### 3.3.2 Energy dispersive X-ray spectroscopy

Energy dispersive X-ray spectroscopy, EDX, is one such technique used in tandem with SEM, as it is not just electrons that can be detected within an SEM. Incident electrons are able to collide with and liberate bound electrons within inner levels of atoms in the sample, creating a “hole” in this lower level which is then filled by an electron from a higher level. It is this transition of the higher electron to a lower state that causes an emission of a photon, and is typically within the region of X-rays, which have an upper energy threshold matching that of the incident electron beam; These X-rays then leave the sample and can be detected for analysis, and can be used to determine the atomic composition of the film.

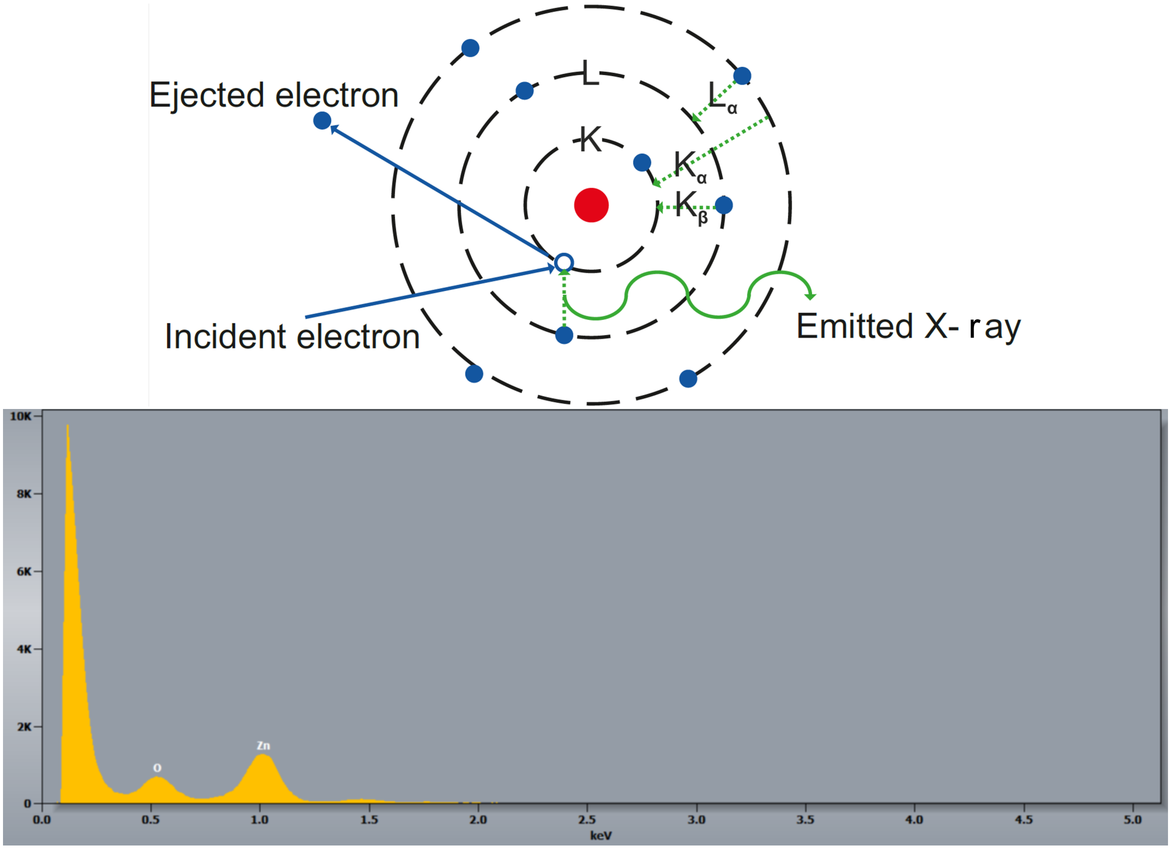

Figure 3.13: Top: Schematic of electron interaction with an atom during EDX and the known transitions. Bottom: Sample EDX spectra taken from ZnO film, with axes being observed counts against photon energy in KeV

This can be done as each electron transition within different elements have well known energies, given by the atoms size and which specific levels the electron travelled through. These levels, or “shells”, are sometimes referred to as K, L, and M levels, which leads to the naming of X-rays produced being $K_\alpha$, $L_\alpha$ and $L_\beta$, with $\alpha$ and $\beta$ referring to which upper state the electron decayed from. EDX allows for determination of atomic composition of the film by comparing the energy of detected X-rays to literature, and the average stoichiometry within the SEM interaction volume by comparing the relative counts of each of these X-rays [125]. A schematic of transitions and an example EDX spectra can be found in Figure 3.13, alongside an example spectrum obtained from a ZnO film deposited by PE-PLD.

### 3.3.3 Transmission Electron Microscopy

Transmission Electron Microscopy, TEM, is in essence quite similar to SEM, yet their are two key differences: Firstly, the electrons in the beam are of a much higher energy on the order of MeV, typically with wavelengths of picometers corresponding to radiation within the gamma range of the EM spectrum; specifically the JEOL 2200 FS aberration corrected TEM utilised here has a wavelength of approximately 2.5pm. This brings two advantages, firstly being higher resolution images due to the lower amount of diffraction, and higher penetration depths into the sample. The second advantage of TEM comes from this higher penetration as if the film is sufficiently thin then the electrons will pass through the entirety of the sample, and can be detected after fully transmitting through the film. This allows for high spatial resolution imaging, yet also additional analysis techniques such as investigating of the diffraction patterns of electrons caused by interaction with the crystal structures of the film.

However in order for a TEM to analyse a thin film across its depth, additional preparation must be performed on the sample. This was done with the use of a focused ion beam (FIB); The FIB used here utilises a beam of gallium, Ga, ions which are used to etch out a

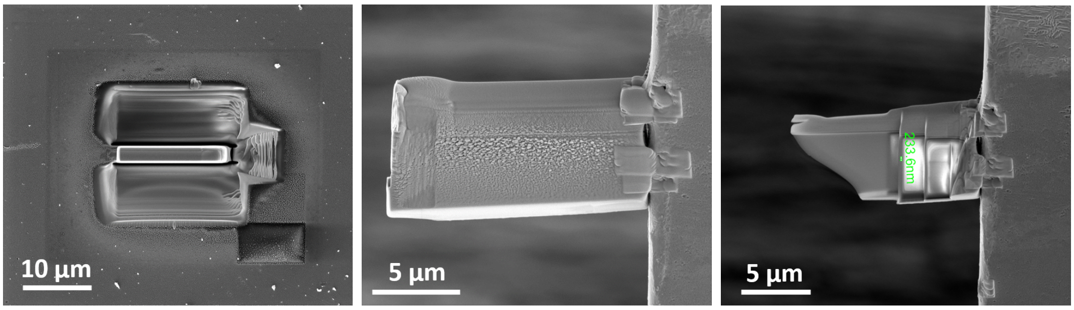

Figure 3.14: Left: Etched trenched around lamella after protective coating. Middle: Lamella mounted to central Cu mounting. Right: Polished lamella.

slice or "lamella" of the film, which can then be mounted sideways and used in the TEM. However, an effect to account for is although Ga can easily be used to etch out such a lamella due to being a large atom, a lot of kinetic energy is imparted into the sample which is converted into heat, which can then damage the film. So to mitigate this, films are typically covered in protective layers of elements such as platinum, which absorb a lot of the heat and protect the film [127]. An example of such a lamella is shown in Figure 3.14.

In practice there are a few different forms of TEM, here two are utilised, as shown in Figure 3.15, alongside an image of the TEM apparatus used within this work. Firstly standard diffraction based TEM is used, with the source electrons passing through the sample, and then focused onto a set of detection optics. Secondly is dark field imaging, where the central portion of light is blocked from the beam, with remaining light focused onto the sample. Further blockers are placed after the sample to stop any beams that pass straight through the sample, with the only signal incident on the detector being that from beams diffracted by the sample itself. Dark field analysis takes it name from the fact that the blocked signal results in a black image around the sample, and has further benefits over standard TEM as it allows for highly detailed images of the structure of the sample itself, yet can struggle in some cases due to low levels of light incident on the detector. Use of a TEM in such a way allows for determination of the films grain structure and size, and such lamellas can then undergo further analysis from such techniques as EDX for compositional analysis.

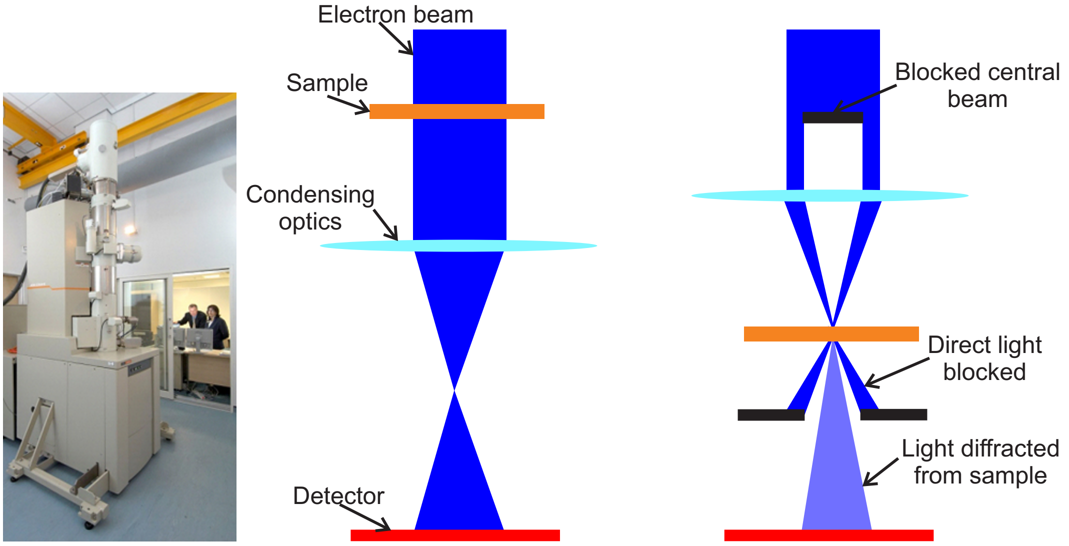

Figure 3.15: Left: The 1 Å Double Aberration Corrected In-situ TEM/STEMTEM at the York JOEL Nanocenter. Right: A schematic of TEM and darkfield imaging.

### 3.3.4 Medium Energy Ion Scattering

Medium Energy Ion Scattering, MEIS, utilises an ion beam of hydrogen or helium ions accelerated up to energies of 200 keV. These are then incident on the film, penetrating it, scattering off the constituent atoms causing the ions to lose energy and change direction. Some ions are reflected out of the target, losing more energy in this process, and are incident on a detector at a known angle; from this, a plot of the number of counts received as a function of the ions final energy is obtained. MEIS is mainly used in order to determine the composition of a film across its depth, which is obtained from further analysis of the scattered ions energy loss.

The depth profile analysis if done with custom scripts within IGOR PRO [128]: An initial assumption of the films thickness (typically done from prior knowledge of the deposition technique), is computationally subdivided into sections that are on the order of 0.1 nm.

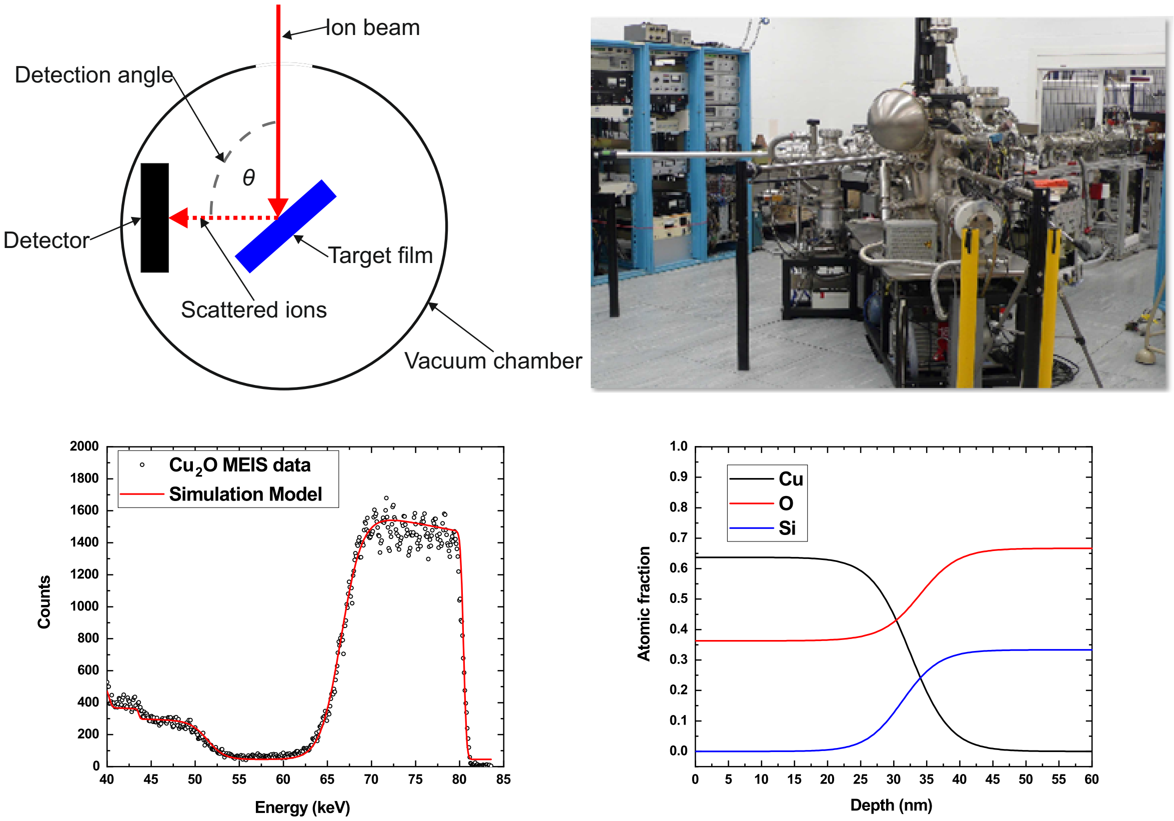

Figure 3.16: Top Left: Schematic of MEIS, Top Right: Picture of MEIS at the University of Huddersfield. Bottom Left: MEIS spectra of $Cu_2O$ on $SiO_2$. Bottom Right: Determined compostion of elements across depth for $Cu_2O$ on $SiO_2$.

Within each of these sections, inelastic energy loss is determined for each type of constituent element from the SRIM (the **S**topping and **R**ange of *I*ons in **M**atter) database [129]. The total energy loss and scattering loss in the film is calculated, and the composition of elements within each layer altered in order to best fit experimental data. This results in the relative composition of elements within the film as a function of depth. Additional assumptions can be made within MEIS, such as various broadening profiles used during analysis of transition layers, which are outlined in detail in literature [130–132]. Plus, there are some limitations on both depth and the ability to distinguish elements next to each other on the periodic table, due to their similarities in the SRIM database. MEIS is shown schematically in Figure 3.16, and some key assumptions discussed further in Chapter 6.

MEIS is an attractive technique due to effectively zero sample preparation time, as opposed to the aforementioned SEM and TEM, which can require signifcant time to prepare samples. Also as a consequence of this there is no damage to the sample which can in theory be used again for further testing. Other commonly utilised ion beam techniques that can also yield composition as function of depth, such as Rutherford Back Scattering (RBS) or Elastic Recoil Detection (ERD), which require much higher ion energies of at least a few MeV. This makes these techniques much more expensive experimentally, however do have some advantages over MEIS as they are able to probe deeper into the sample surface. Yet conversely this can be disadvantageous for thin films on the order of 10's of nm, such as films created in this work, as the larger energies typically have poorer resolution in their depth profiles, compare to the lower energy particles used in MEIS.

### 3.3.5 X-Ray Diffraction

X-Ray Diffraction, XRD, is utilised in order to determine the crystal structure of films deposited in this work. XRD uses a beam of X-rays incident on the sample with the angle of incidence, $\theta$, and the scattered X-rays then detected at a known angle. Due to the short wavelength of the X-rays most photons pass through the film without interaction however some do reflect off atoms in the film, and when the angle of incidence matches the Bragg angle, i.e. when the path difference between two reflected beams reflected off different planes in the crystal, are offset by an integer number of wavelengths, then constructive interference occurs. This is schematically shown in Figure 3.17, showing a lattice of spacing $d$ and two incoming X-ray photons at an angle $\theta$, with one photon being reflected off the top layer with the second photon reflected off the second layer, with its path distance given by $2dsin\theta$. Constructive interference between the detected photons occurs when the path difference is $n$ multiples of the wavelength, resulting in a peak in observed signal, at an angle corresponding to the angle of the detector [133]. Also shown in Figure 3.17, is the Rigaku High Resolution Smart Lab XRD device used in this work.

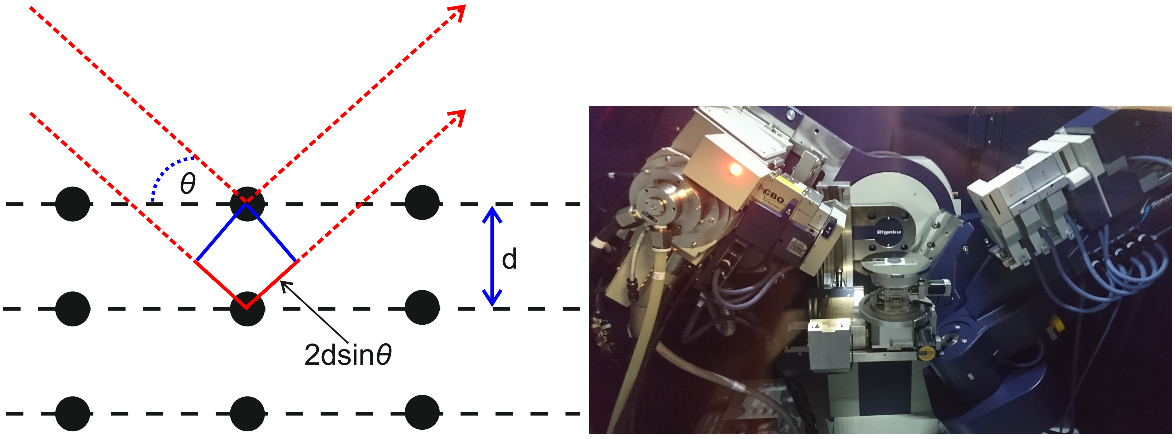

Figure 3.17: Left: Schematic of XRD, Right: Picture of Rigaku XRD device

There are different methods within XRD used in order to obtain a scan of different angles, here the $\theta/2\theta$ method is utilised. Where both the X-ray source (germanium) and detector are moved at the same time with the angle of incident $\theta$ being the same as the angle of reflection; this is analogous in geometry to another form of XRD where the sample is instead rotated and the reflected X-rays detected at an angle $2\theta$, hence the techniques name. XRD allows for determination of the films structure, as the peaks observed will correspond to a certain lattice spacing $d$ that can easily be determined from the relation in Equation 3.13, where $\lambda$ is the wavelength of X-rays utilised. Values of the angles where peaks are observed can be compared to literature or known databases of lattice properties of materials, such as the literature repository the Crystallography Open Database [67], or the database the International Center for Diffraction Data [134], in order to determine the structure of deposited films.

$$\lambda = 2dsin(\theta) \tag{3.13}$$

Also from XRD the grain size of the film can be determined, i.e. the physical size of areas within the film having the same crystal structure, see Section 2.4. This is done so by the Scherrer relation [135], Equation 3.14, where $\tau$ is the size of grains, $\omega$ the broadening of the observed peak (taken as the FWHM), and $K$ a dimensionless factor experimentally determined by Scherrer to be approx. 0.9. In essence it is the broadening of the peak that infers the size of the grains, as it is from scattering from the atoms within each structure that will cause the increased width of each peak which in theory should be a thin line positioned at the Bragg angle.

$$\tau = \frac{K\lambda}{\omega cos(\theta)} \tag{3.14}$$

## 3.4 POLLUX model

POLLUX is a code originally written by G. Pert [136–140], and since developed and maintained at the University of York [141], designed to model the irradiation of a target by a high intensity ($\geq 10^{10}$ Wcm$^{-2}$) laser, with the generation of a plasma plume which can then further interact with the laser. Here POLLUX has been used to simulate differences between the laser ablation of metal and metal oxide targets within Chapter 4, with this section describing the physical and mathematical models utilised within POLLUX. Figure 3.18 shows the steps and processes undertaken during a simulation within POLLUX, with important models utilised and additional information about the code described in detail below.

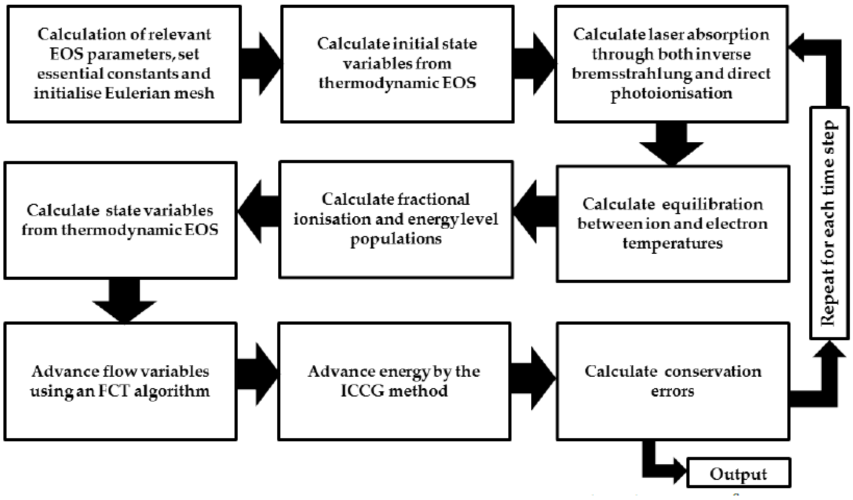

Figure 3.18: Algorithm for stages of a simulation within POLLUX [141]

### 3.4.1 Mesh

Simulations within POLLUX run on a 2-dimensional Eulerian mesh, with the term Eulerian referring to the mesh being fixed throughout the simulation, compared to a Lagrangian mesh, where it changes throughout the simulation whilst conserving mass. However from the work of Pert [142] there is a quasi-Lagrangian routine within POLLUX, used during the initial iterations of the code to adjust the size of cells close to the target surface for more efficient use of computation time, yet this does not continue during later time-steps, due to the complexity and therefore computation time it would add to the code. As mentioned the mesh is 2-dimensional, therefore assumptions have been made in order to model real systems that occur within 3-D space, with this being azimuthal symmetry around the z axis, the point through which the laser is incident onto the target, limiting POLLUX to lasers incident at a normal angle to the target. The geometry of the mesh used within POLLUX is shown schematically in Figure 3.19.

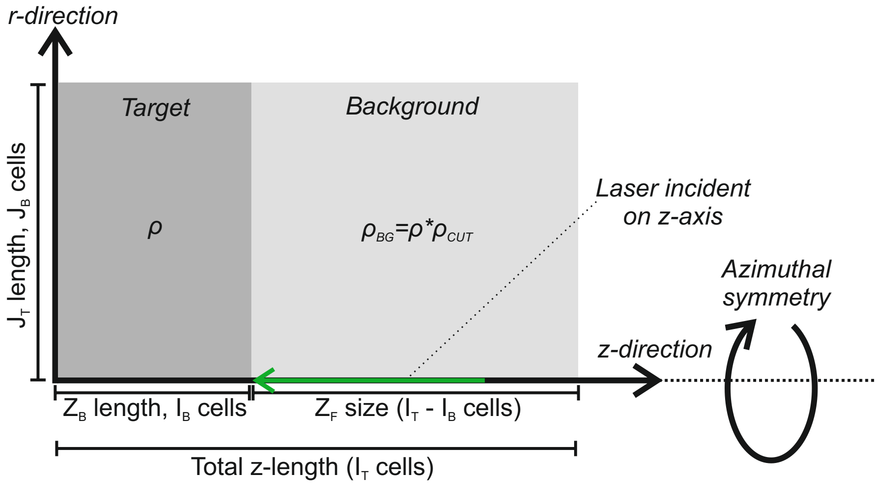

Figure 3.19: Description of geometry within a POLLUX simulation

The size of the mesh and resolution of constituent cells are controlled by the following means; first the physical size (in cm) in both the z and r directions, with a total length of $J_T$ in the r-direction and a length of $I_B$ (thickness of the target) plus $I_F$ (size of the background) in the z-direction. Each direction has a corresponding number of cells, resulting in a set number of cells within the mesh, each with a corresponding size. With the use of such a mesh there is a key mathematical assumption that must be maintained at all times, the Courant-Friedrich-Lewy (CFL) condition [143] which states that any material may not "skip" cells; As each cell within the mesh has a physical size, and the code having set time steps (both of which set by the user), if the velocity of material within a cell is such that it will travel a greater distance than 1 total cell within 1 time-step, numerical issues will occur. The CFL condition is given in Equation 3.15, where $C_{max}$ is the CFL parameter typically with an upper limit of 1, $\Delta t$ the time step of each itteration, $\Delta r$ & $\Delta z$ the size of one cell in each direction, and $u_r$ & $u_z$ the velocity of material within a cell in each direction.

$$C_{max} \gg \frac{u_r \Delta t}{\Delta r} + \frac{u_z \Delta t}{\Delta z} \tag{3.15}$$

The mesh and time-steps used within POLLUX simulations presented in this work are highly resolved, and are many orders of magnitude underneath the maximum limit of the CFL condition; meshes had a total physical size of 0.4 cm in z, and 0.25 cm in r, within a 900x90 grid. Time steps were $1\times10^{-12}$ seconds, and velocities of plume material typically on the order of $1\times10^{4}$ cm $s^{-1}$. This results in a CFL parameter many orders of magnitude under the maximum limit of $C_{max}$. Lastly, POLLUX is not able to simulate a complete vacuum, meaning cells cannot be totally void of any material (reasoning discussed shortly).Therefore a background material is generated based upon the target conditions; the density within the background cells $\rho_{BG}$ is set by multiplying the density of the target material $\rho$ but a numerical factor $\rho_{CUT}$. This results in a density, which when assuming the ideal gas law can be used to modify the pressure of the background.

### 3.4.2 Equation of State

An equation of state, EoS, is a term used within physics to describe a model that is used to characterise the key physical properties of a material or any given system. POLLUX utilises two different versions of an EoS, one for the thermodynamic and nuclear terms, and an additional one for electronic terms. Thermodynamic and nuclear terms are defined by the Chart-D EoS model, developed by Sandia National Labs [144], but more specifically the tabular version of this EoS is chosen. This requires the user to define an almost complete EoS of the target material prior to running, with all required parameters outlined in Table 3.3, with this chosen to reduce as many assumptions made within the code as possible. Upon the initial iteration, the Chart-D EoS routines within POLLUX use the parameters given within Table 3.3 to calculate various further important aspects of the EoS, namely factors vital for the Clausisus-Clapeyron relation [145], see Figure 3.20, which relates the current phase of a material to its pressure and temperature.

Table 3.3: Parameters required for the Chart-D EoS [144]

| Variable | Units |
|---|---|
| Number of elements in material | N/A |
| Physical assumptions | See Table (3.20) |
| Density | g $\text{cm}^{-3}$ |
| Bulk modulus | Barye |
| Gruneisen coefficient | Unit-less |
| Debye temperature | eV |
| Enthalpy of sublimation | ergs $\text{g}^{-1}$ |
| Melting temperature | eV |
| Thermal conductivity coefficient | ergs $\text{s}^{-1}$ $\text{cm}^{-1}$ $\text{eV}^{-1}$ |
| Atomic number of each element | Proton number |
| Fraction of each element in the material | Fraction |

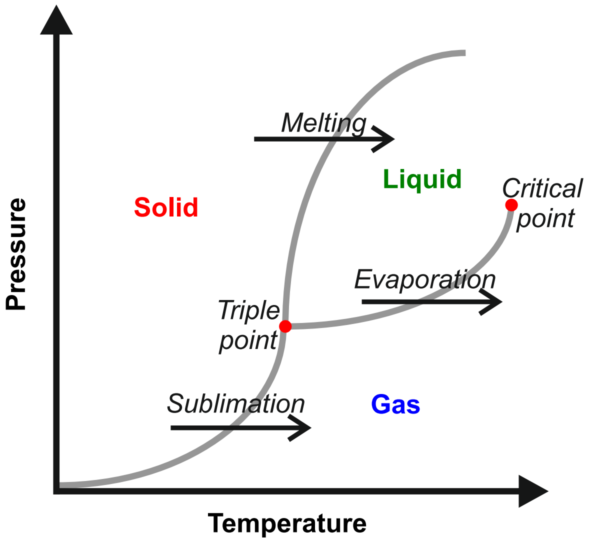

Figure 3.20: Classical description of a phase diagram based on the Clausis-Claperyron method of defining materials based upon pressure and temperature.

This is used to help describe the phase change within the target as it absorbs energy, and therefore increases in temperature, with some additional factors, such as the critical density being calculated by the EoS in order to properly determine the regions of phase change. On this point it is possible within POLLUX to use different assumptions of the Clausis-Claperyron based phase changes, as outlined within Table 3.4, where effectively different phases and corresponding changes are considered or not. Which can prove useful for simulations of different targets under a variety of laser and target conditions, as it was outlined in Section 2.2.1, yet also discussed again in more detail in Chapter 4.

Table 3.4: Allowed phase changes allowed within POLLUX

| **Number** | **Phase change** | **Assumptions** |
|---|---|---|
| 0 | Sublimation (no electronic terms) | Solid target that cannot undergo melting, with no TF model (see below) |
| 1 | Sublimation (with electronic terms) | Solid target that cannot undergo melting, with TF model |
| 2 | None | A dense, gaseous target where ablated material does not need to undergo a phase change |
| 3 | Full treatment (no electronic terms) | Solid target which can melt, with liquid material able to evaporate, no TF model |
| 4 | Full treatment (with electronic terms) | Solid target which can melt, with liquid material able to evaporate, with TF model |

Electronic terms within POLLUX are treated by a Thomas-Fermi (TF) model [146], where the properties of electrons are determined by the electric potential over a given volume. For this Poison's equation, given in Equation 3.16, is used to describe the charge density, $\rho$, across a potential, V, with a Fermi-Dirac distribution for the density of electrons.

$$\frac{1}{r^2}\frac{d}{dr}\left[r^2\frac{dV}{dr}\right] = 4\pi e\rho(r) \tag{3.16}$$

In order to simplify the solution of equation 3.16, the normalised parameters defined by Latter in 1955 [147] are introduced, which assumes a perfectly spherical system. These comprise of three factors, first being the electric field, $\phi$, in equation 3.17, where $\eta$ is the chemical potential determined from the Fermi-Dirac distribution, $e$ the fundamental charge of an electron, $V$ the electric potential, $r$ the radial dimension, $k$ Boltzmann constant, and $T$ the temperature of the ion or electron.

$$\phi(x) = \frac{[\eta + eV(r)]r}{r_1 kT} \tag{3.17}$$

Secondly to describe the dimensions of the system is equation 3.18, where $r$ is the same as above, and $x$ the axial dimension.

$$x = \frac{r}{r_1} \tag{3.18}$$

Laslty is a numerical term, $a$, as described in equation 3.19, where terms are the same as above, along with $m$ being the mass of the ion, and $h$ being Planck's constant.

$$a = (4\pi e)^2 (2m)^{3/2} (kT)^{1/2} \frac{r_1^2}{h^3} \tag{3.19}$$

When equations 3.17 - 3.19 are combined within 3.16, equation 3.20 is obtained:

$$\frac{d^2\phi}{dx^2} = axI_\eta \left( \frac{\phi(x)}{x} \right) \tag{3.20}$$

where $I_\eta$ the is Fermi-Dirac function, i.e. the probability of occupancy of energy levels of a fermion, computationally described by McDougall and Stoner [148], ans as shown in equation 3.21:

$$I_\eta = \int_0^\infty [exp(y-\eta)+1]^{-1} y^n dy \tag{3.21}$$

where $\eta$ is the checmical potential of the atom from which the electron is bound to. However within Pert's model [146], $\eta$ is empirically defined, and therefore this Fermi-Dirac function $I_\eta$ and its relation to this known $\eta$, are therefore utilised in Equation 3.20 in order to determine the total electric potential, and corresponding degree of ionisation of the material.

### 3.4.3 Energy absorption

As can be seen in Figure 3.18, the first stage of the iterations that are looped through within POLLUX is calculation of energy absorption, by inverse-Bremsstrahlung absorption. The physical aspects of this process have been previously outlined in Section 2.2.1, but it is important to highlight that this is the only method of energy absorption within POLLUX. This is a valid assumption for the work performed here, as the Nd:YAG laser's dominant energy absorption technique is indeed IB-absorption due to its relatively long wavelength. So the photon energies at such wavelengths are lower than the ionisation energies of elements used, for photon-ionisation to occur, and therefore insufficient for single photon-ionisation to occur. Multi-photon ionisation is not considered also, as it was also discussed previously that the required number of photons to be incident simultaneously would result in such a small cross section, that is assumed to be negligible.

### 3.4.4 Ion and electron temperatures

As seen the next stage is to equilibrate the ion and electron temperatures, as POLLUX is limited to LTE, the concept of which described in section 2.6. This limitation is due to rules within the TF model requiring high enough electron densities to create a sufficient electric potential. However, there is a wealth of literature describing such laser ablated plasma plumes being within LTE shortly after ablation, including experimental work in the original description of PE-PLD [2, 32], therefore this is a valid assumption in the conditions presented here; as will be shown in Chapter 4. Equilibration of these temperatures is done via the Spitzer-Harm model [149], which describes the electrical conductivity of a highly ionised gas, and how it is effected by the collisions between electrons and ions, given by a collision frequency $\nu_{ei}$. The Spitzer-Harm conductivity, $\sigma_{SH}$, is given in Equation 3.22, and is used to quantify the effective conductivities of the plasma and therefore equilibrate the ion and electron temperatures via modification of this collision frequency.

$$\sigma_{SH} = 3\frac{\sqrt{\pi}}{2}\frac{e^2 n}{m_e \nu_{ei}} \tag{3.22}$$

Where $e$ is the charge of an electron, $n$ the number density of species within the plasma, and $m_e$ the electron mass.

### 3.4.5 Mass transport and the FCT model

Within POLLUX there are two different techniques used for transport of variables between cells from one iteration to the next, here the method used for transport of mass will be discussed. Initially the problem to be solved is based in hydrodynamics, with the key equations to solve being that for the fluids velocities, momentum, and energy; within this the assumption is made that there must be a continuity of both mass and energy, as stated in Equation 3.23, where $X, Y$ are the total distance in the X and Y planes respectively, $z$ a small change in the $Z$ plane (similar logic applies to $x, y$ later), $m$ being the unit mass encompassed within the volume caused by $z$, and $\rho_0$ the initial density of the system.

$$\begin{gathered} \frac{\partial m}{\partial t} + \frac{\partial}{\partial z}(mv) = 0 \\ \rho_0 = \frac{m}{XY} \end{gathered} \tag{3.23}$$

Note, this equation and those to follow are for an Eulerian system, as used in POL-

LUX. Within the work of Pert in 1983 [140], it has been summarised that the required hydrodynamic equations for such a system, and are given here in Equation 3.24. This shows the equations of motion in the $X$ and $Y$ planes, with $U, V$ being the scale velocities of the system (i.e. $\partial X/\partial T$ and $\partial Y/\partial T$ respectively).

$$\begin{aligned} \frac{\partial X}{\partial t} + w\frac{\partial X}{\partial z} &= U \\ \frac{\partial V}{\partial t} + w\frac{\partial Y}{\partial z} &= V \end{aligned} \tag{3.24}$$

Equation 3.25 then states the equations of momentum for the system, with $p_0$ being the initial pressure within the system.

$$\begin{aligned} \frac{\partial U}{\partial t} + w\frac{\partial U}{\partial z} &= \frac{2}{X}\frac{p_0}{\rho_0} \\ \frac{\partial V}{\partial t} + w\frac{\partial V}{\partial z} &= \frac{2}{Y}\frac{p_0}{\rho_0} \\ \frac{\partial w}{\partial t} + w\frac{\partial w}{\partial z} &= -\frac{1}{m}\frac{\partial}{\partial z}(XYp_0) \end{aligned} \tag{3.25}$$

Lastly this leads to the energy conservation Equation 3.26, where $W$ is the energy deposited into the cell, of a conductivity $Q$.

$$\frac{\partial}{\partial t}(mE) + \frac{\partial}{\partial Z}\left(m\left[E + \frac{p_0}{\rho_0}\right]\right) = m\left(W - \frac{\partial Q}{\partial z}\right) \tag{3.26}$$

It is from Equations 3.24 to 3.26 that allows for calculation of velocities and transport of mass within POLLUX, as the required $W$ for energy absorption into the cell is pre-calculated in the previous step, either from IB-radiation of the laser or indeed loss of energy from collisional conductivity during the Spitzer-Harm equilibration. However these equations can only determine how fast each cell of density is travelling, yet there is nothing intrinsic within these equations that allows for computation of how to move variables from said unit cells into the appropriate neighbour.

In order to do this, alongside the hydrodynamic model described above, the Flux Corrected Transport (FCT) model of Boris and Book [150] is used for mathematically handling variables. This has a rich description in literature and has been utilised within many codes [151, 152], however the salient points will be described here. Essentially the FCT method is a technique for solving any standard diffusion equation, such as the one shown in Equation 3.27, where many parameters such as position, $X$, density, $\rho$, etc. evolve over time. The FCT takes the approach similar to that of performing a Taylor expansion of this equation, yet when doing so there is no mathematical guarantee that the latter terms in the expansion could converge to zero, introducing errors.

$$\frac{\partial \rho}{\partial t} + \mathbf{v} \cdot \nabla \rho = -\rho \nabla \cdot \mathbf{v} + s(X, \rho, etc...) \tag{3.27}$$

Therefore, an additional set of assumptions is made within the FCT model, which can easily be argued to be physically true for the conditions within this work. First there must be no non-positive values (i.e. there can be no negative or zero value masses), although this does limit POLLUX from not being able to simulate a vacuum. Secondly the transport between cells is monotonic (i.e. cannot have the gradient change order). As mentioned there are many different applications of the FCT model, yet specifically used here is the SHASTA algorithm, (or SHarp And Smooth Transport Algorithm) which comprises of two phases, namely the transport and the anti-diffusion phases. The initial transport phase is as shown in Equation 3.28, which is a highly diffusive assumption on the above dispersion Equation 3.27, where the left hand term is the transport term, and the right hand term in the bracket is assumed to encompass all errors in the expansion of the equation.

$$\widetilde{\rho_j}(t+\delta t) = \rho_j(t) + \delta t \dot{\rho_j}(t+\frac{\delta t}{2}) + \left\{ \nu_{j+(1/2)} \left[ \rho_{j+1}(t) - \rho_j(t) \right] - \nu_{j-(1/2)} \left[ \rho_j(t) - \rho_{j-1}(t) \right] \right\} \tag{3.28}$$

In order to then remove this diffusive error term, an assumption of the fluxes is then created, as shown in Equation 3.29, with $\Phi$ being the flux into the next cell, and $\nu$ the mass in said cells velocity, with this being calculated from the above hydrodynamics equations.

$$\widetilde{\Phi}_{j+(1/2)} = \nu_{j+(1/2)} \left[ \widetilde{\rho}_{j+1}(t+\delta t) - \widetilde{\rho_j}(t+\delta t) \right] \tag{3.29}$$

Using these fluxes in order to eliminate the diffusion term in Equation 3.29), we are left with the final equation from the FCT used within POLLUX in order to transport mass, and is shown within equation 3.30.

$$\rho_j(t+\delta t) = \widetilde{\rho_j}(t+\delta t) - \Phi_{j+(1/2)} + \Phi_{j-(1/2)} \tag{3.30}$$

### 3.4.6 Energy transport and the ICCG method

Energy is advanced within POLLUX by a combination of two different means; Initially after any energy absorption from the laser, or change in equilibrium temperature from collisions as done by the Spitzer-Harm calculation, the TF model is then used to determine how much this increase or loss in energy will affect the magnitude of the volume within the TF model. This change in volume is then compared to the set volume of each cell, and appropriate energy outside of this set volume transported into the corresponding surrounding cells, and described as a vector form within the z and the r directions. However in order to achieve full accuracy the Incomplete Cholesky-Conjugate Gradient (ICCG) method is also utilised; this technique uses the assumption that any matrix, $M$, can be described as a combination of its lower triangular matrix, and this sub matrices transpose, as shown in Equation 3.31.

$$M = LL^T \tag{3.31}$$

However for the ICCG to be valid, it is assumed that $M$ must be a positive-definite matrix, i.e. all diagonal cells are non-zero. Then if attempting to solve the basic vector multiplication as shown in Equation 3.32:

$$Mx = y \tag{3.32}$$

it can instead be stated as:

$$[L^{-1}M(L^T)^{-1}](L^Tx) = (L^{-1})y \tag{3.33}$$

The benefit for doing this is two fold; firstly if one was to solve 3.32 without knowing either vector $x$ or $y$, as is sometimes required when solving a system of linear equations, then 3.33 can be solved for either vector via an iterative means from a series of equations, outlined in Equation 3.34.

$$\begin{gathered}
a_i = (r_i, (LL^T)^{-1}r_i)/(p_i, Mp_i) \\
b_i = (r_{i+1}, (LL^T)^{-1}r(i+1)/(r_i, (LL^T)^{-1}r_i) \\
r_{(i+1)} = r_i - a_iMp_i \\
p_{(i+1)} = (LL^T)^{-1}r_{(i+1)} + b_ip_i \\
x_{(i+1)} = x_i + a_ip_i
\end{gathered} \tag{3.34}$$

The second benefit can also be tied to this iterative process, as if this definite-positive assumption holds true, then the ICCG method has shown to be a very rapid method of computing Equation 3.32 with an unknown vector, both via direct calculation and iterative means; This is shown in Figure 3.21 where the ICCG was initially applied to the laser fusion code LASNEX on two different forms of equations whilst being compared to other codes of a similar nature. This clearly shows the benefits as to using the ICCG in such a condition, as for an Eulerian condition, such as within POLLUX, this method converged many hundreds of iterations quicker than the other techniques.

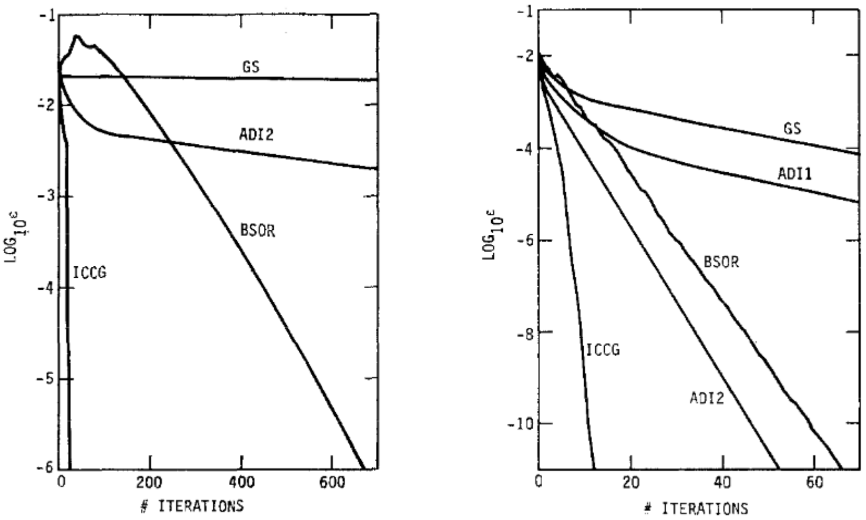

Figure 3.21: Comparison of the ICCG compared to other methods when applied to LASNEX, showing the convergence of parameters within the code against number of iterations; Left: Eulerian set of equations. Right: A laplacian set of equations [153]

How the ICCG is explicitly utilised alongside the TF model is a compliment to it; as stated the initial calculations of the changes in potential volume required for the TF is done via different means, yet this is then passed into the ICCG algorithm. This is initially solved via the TF model, however then the ICCG is used in an iterative means, until further conversion is reached.

### 3.4.7 Outputs from POLLUX

Data that is generated from POLLUX is outlined in Table 3.5. Each of these parameters are provided for each cell within the Eulerian mesh, at each iteration of the simulation, and therefore some high resolution meshes can become quite large and memory intensive. Due to this, it is possible within POLLUX to define which timings are desired for analysis. For

Table 3.5: Parameters outputted from POLLUX and associated units.

| **Parameter** | **Units** |
|---|---|
| Axial position | cm |
| Radial position | cm |
| Mass density | g $cm^{-3}$ |
| Axial velocity | cm $s^{-1}$ |
| Radial velocity | cm $s^{-1}$ |
| Ion temperature | eV |
| Electron temperature | eV |
| Average ionisation state | 1 = neutral, 2 = $1^+$, 3 = $2^+$ etc. |

example, each nanosecond if the expansion over time is desired, or instead just the final iteration if this is not of importance for the application. These outputs are stored in files that can be imported into other codes or data handling packages; here further analysis of outputs was performed within Matlab, due to its speed and efficiency of handling large datasets, and with some open source packages that proved useful for visualisation.

## 3.5 Hybrid plasma equipment model

In order to simulate the RF ICP used to generate the reactive background in PE-PLD, and specifically explore the nature of gas temperature within the system, the Hybrid Plasma Equipment Model (HPEM), written by Prof. M. Kushner [154] was utilised. As its name suggests, HPEM utilises a hybrid approach to plasma modelling, treating various species within the plasma by different means. However, as HPEM is a much more recent code when compared to POLLUX, a much more rigorous description of each module can be found within literature [154], and therefore, here only key concepts relevant to this work will be discussed; also as the specific use of this code used here has been adapted from the work of Gibson et al [95], where gas temperature within an $O_2$ RF ICP was explored. However in the work of Gibson, there was no comparison to experimental data, and conditions utilised are different to those used here, with a much large reactor geometry, and lower pressures explored, with a maximum of 5 Pa reported.

### 3.5.1 Modules

HPEM takes a modular structure, where various processes are handled within separate modules, allowing for the inclusion or exclusion of desired physics. Here a somewhat simplistic form of HPEM is used, with only four modules: the electromagnetic module (EMM), the fluid kinetic Poisson module (FKPM), the electron Monte Carlo Simulation (eMCS), and the plasma chemistry Monte Carlo module (PCMCM). These are called in a an iterative manner as described by Figure 3.22, and described below.

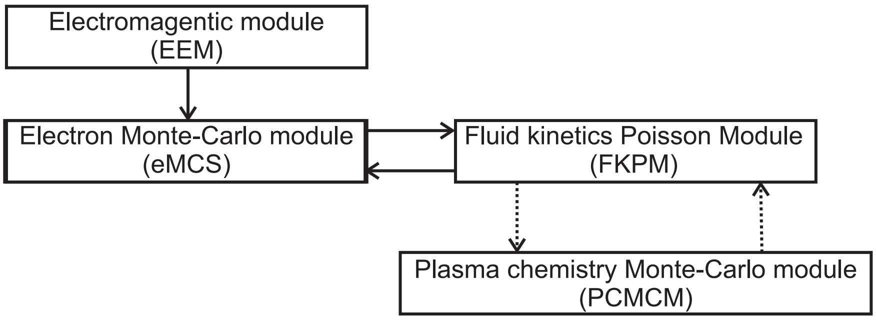

Figure 3.22: Representation of the order in which modules are utilised in HPEM. Dashed lines refer to pathways being active after the point of convergence.

The EMM is the first module used, and solves Maxwell's equations in order to determine electric and magnetic fields generated by the inductive coil, with the current within the coil adjusted in order to reach the desired power. The FKPM handles all heavy species separately (e.g. $O_2$, $O_2^+$ O etc.), solving the continuity, momentum and energy equations, alongside Poisson's equation for the electric potential. Electrons are handled by the eMCS, based upon electric fields from the EMM and electron pseudo-particles (i.e. large particles assumed to comprise of many constituent electrons), which generates the electron energy distribution function (EEDF) at all points in the simulation. These are then used as inputs within the FKPM in the next iteration, with this process repeated until densities of species converge to a steady state. After this point of convergence the PCMCM is utilised to handle ion and heavy species interaction with the walls, with pseudo-particles of initial position and trajectory obtained from the FKPM. Pseudo-particles motions in the PCMCM are integrated through time and space dependant fields from the FKPM, with information about all species incident on the wall stored for use in various modules, which is where the focus of the use of HPEM in this work is found.

One of these wall processes highly relevant to this work is the transfer of heat to the walls, handled in HPEM by the thermal accommodation coefficient $\alpha_E$. The work of Gibson et al [95] explicitly highlighted this parameter as heavily influencing both the gas temperature of the plasma, and the density of various species such as atomic oxygen. $\alpha_E$ can be thought of as an efficiency of heat transfer to the wall, and classically described, as shown in Equation 3.35.

$$\alpha_E = \frac{T_i - T_r}{T_i - T_s} \tag{3.35}$$

Where T is the temperature of incident (i) and reflected (r) plasma species ,and the surface (s), respectively. This concept is used within HPEM by the model of Lofthouse et al [155], by helping to define an effective gradient of temperature between the wall and plasma, $\Delta S$, which is then in turn used to modify the gas temperature $T_g$, as stated in Equation 3.36.

$$\frac{dT_g}{dx} = \frac{T_g - T_s}{\Delta S} \tag{3.36}$$

where:

$$\Delta S = \left[\frac{2 - \alpha_E}{\alpha_E} \cdot \frac{2\gamma}{(\gamma + 1)P_r}\lambda_{mfp}\right] \tag{3.37}$$

and $\gamma$ is the ratio of specific heats of species, $\lambda_{mfp}$ the collisional mean free path of species in the plasma, and $P_r$ the Prandtl number [156]. This in then implemented within HPEM by defining that the heat flux to the surface must remain constant, and therefore altering the thermal conductivity $\kappa$, of cells next to walls to an effective conductivity, $\kappa_{eff}$, as shown in Equation 3.38:

$$\kappa_{eff} = \frac{\kappa}{1 + \frac{\Delta S}{\Delta x}} \tag{3.38}$$

### 3.5.2 Mesh

Simulations within HPEM take the form of a mesh, in a somewhat similar manner to POLLUX as described above, with the mesh used shown in Figure 3.23; this mesh assumes azimuthal symmetry around the z axis in order to simulate the reactor used within PE-PLD, with the overall geometry is a square of 11.8 cm in both the z and r direction, comprising of 60 cells in both directions. This geometry is chosen as due to the numerical methods used to handle surfaces within HPEM, cheifly that many calculations are done on the vertex of cells, HPEM favours geometries that are as close to square as possible [154]. This mesh has been adapted from works based upon the chamber used in PE-PLD [1,80].

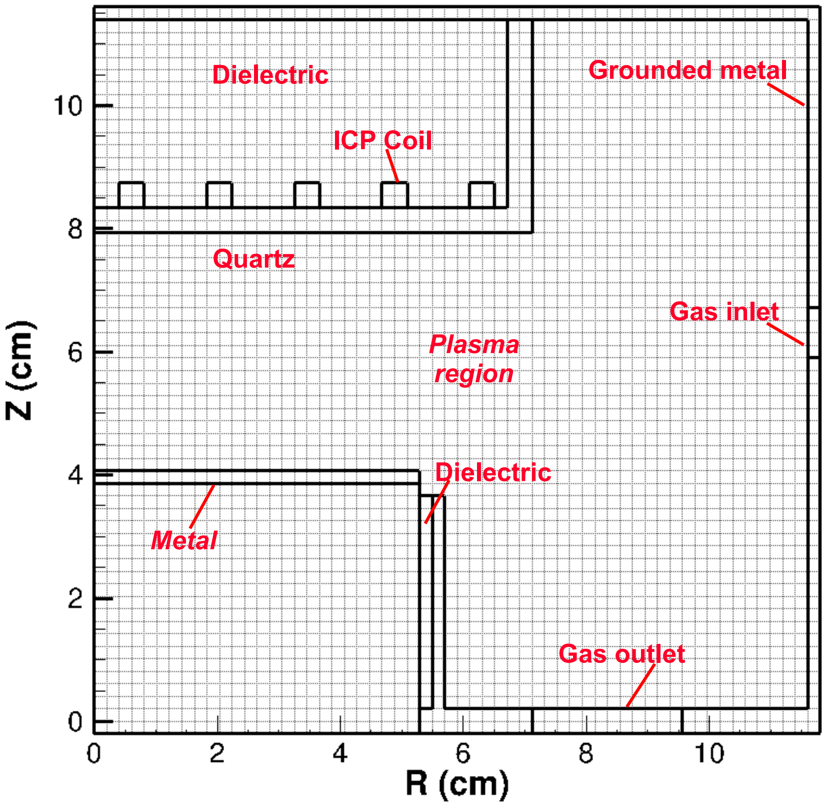

Figure 3.23: Mesh used for HPEM simulations

### 3.5.3 Chemistry

The chemistry set used in simulation here comprises of species as outlined in Table 3.6, and all reactions outlined in Table 3.7. This reaction set was compiled from previously known chemistry sets in the following references [157–159], taking into account dominant

Table 3.6: Species within the chemistry set utilised

| **Symbol** | **Species** |
|---|---|
| $e$ | Electrons |
| $O_2(X^3\Sigma_g^-)$ | Ground state molecular oxygen |
| $O_2(a^1\Delta_g)$ | $1^{st}$ metastable of molecular oxygen |
| $O_2(b^1\Sigma_g^+)$ | $2^{nd}$ metastable of molecular oxygen |
| $O(^3P)$ | Ground state atomic oxygen |
| $O(^1D)$ | Atomic oxygen metastables |
| $O_2^+$ | Molecular oxygen positive ions |
| $O^+$ | Atomic oxygen positive ions |
| $O^-$ | Atomic oxygen negative ions |

reactions between all charged and neutral species relevant under the low pressure conditions utilised here. Gas temperature is effected by this chemistry set, by the exothermicity of each reaction, determined from the enthalpy of formation of each species, and for electron impact dissociation values are taken from measurements by Cosby et al [160].

Table 3.7: Chemistry set used within HPEM

| **Reaction** | **Rate coefficient**$^{a,b}$ | **Ref.** |
|---|---|---|
| $e + O_2(X^3\Sigma_g^-) \rightarrow e + O_2(X^3\Sigma_g^-)$ | $f(\epsilon)$ | [161,162] |
| $e + O_2(a^1\Delta_g) \rightarrow e + O_2(a^1\Delta_g)$ | $f(\epsilon)$ | [163] |
| $e + O_2(b^1\Sigma_g^+) \rightarrow e + O_2(b^1\Sigma_g^+)$ | $f(\epsilon)$ | [163] |
| $e + O(^3P) \rightarrow e + O(^3P)$ | $f(\epsilon)$ | [164] |
| $e + O(^1D) \rightarrow e + O(^1D)$ | $f(\epsilon)$ | c |
| $e + O_2(X^3\Sigma_g^-) \rightarrow e + O_2(a^1\Delta_g)$ | $f(\epsilon)$ | [161,162] |
| $e + O_2(X^3\Sigma_g^-) \rightarrow e + O_2(b^1\Sigma_g^+)$ | $f(\epsilon)$ | [161,162] |
| $e + O_2(a^1\Delta_g) \rightarrow e + O_2(b^1\Sigma_g^+)$ | $f(\epsilon)$ | [165] |
| $e + O_2(b^1\Sigma_g^+) \rightarrow O_2(a^1\Delta_g) + e$ | $f(\epsilon)$ | d |
| $e + O_2(a^1\Delta_g) \rightarrow O_2(X^3\Sigma_g^-) + e$ | $f(\epsilon)$ | d |
| $e + O_2(b^1\Sigma_g^+) \rightarrow O_2(X^3\Sigma_g^-) + e$ | $f(\epsilon)$ | d |
| $e + O_2(X^3\Sigma_g^-) \rightarrow O_2^+ + e + e$ | $f(\epsilon)$ | [161,162] |
| $e + O_2(a^1\Delta_g) \rightarrow O_2^+ + e + e$ | $f(\epsilon)$ | e |
| $e + O_2(b^1\Sigma_g^+) \rightarrow O_2^+ + e + e$ | $f(\epsilon)$ | e |
| $e + O_2(X^3\Sigma_g^-) \rightarrow O(^3P) + O^-$ | $f(\epsilon)$ | [161,162] |
| $e + O_2(a^1\Delta_g) \rightarrow O(^3P) + O^-$ | $f(\epsilon)$ | [166] |
| $e + O_2(b^1\Sigma_g^+) \rightarrow O(^3P) + O^-$ | $f(\epsilon)$ | f |
| $e + O_2(X^3\Sigma_g^-) \rightarrow O(^3P) + O(^3P) + e$ | $f(\epsilon)$ | [161,162] |
| $e + O_2(a^1\Delta_g) \rightarrow O(^3P) + O(^3P) + e$ | $f(\epsilon)$ | e |
| $e + O_2(b^1\Sigma_g^+) \rightarrow O(^3P) + O(^3P) + e$ | $f(\epsilon)$ | e |
| $e + O_2(X^3\Sigma_g^-) \rightarrow O(^3P) + O(^1D) + e$ | $f(\epsilon)$ | [161,162] |
| $e + O_2(a^1\Delta_g) \rightarrow O(^3P) + O(^1D) + e$ | $f(\epsilon)$ | e |
| $e + O_2(b^1\Sigma_g^+) \rightarrow O(^3P) + O(^1D) + e$ | $f(\epsilon)$ | e |
| $e + O(^3P) \rightarrow e + O(^1D)$ | $f(\epsilon)$ | [167] |
| $e + O(^1D) \rightarrow e + O(^3P)$ | $f(\epsilon)$ | d |

| | | |
|---|---|---|
| $e + O(^3P) \rightarrow O^+ + e + e$ | $f(\epsilon)$ | [167] |
| $e + O(^1D) \rightarrow O^+ + e + e$ | $f(\epsilon)$ | e |
| $e + O^- \rightarrow O(^3P) + e + e$ | $f(\epsilon)$ | [168] |
| $e + O_2^+ \rightarrow O(^3P) + O(^3P)$ | $3.72 \times 10^{-9} T_e^{-0.7}$ | [169, 170] |
| $e + O_2^+ \rightarrow O(^3P) + O(^1D)$ | $7.44 \times 10^{-9} T_e^{-0.7}$ | [169, 170] |
| $e + O_2^+ \rightarrow O(^1D) + O(^1D)$ | $7.44 \times 10^{-9} T_e^{-0.7}$ | [169, 170] |
| $O_2^+ + O^- \rightarrow O_2(X^3\Sigma_g^-) + O(^3P)$ | $2.60 \times 10^{-8} T_0^{-0.44}$ | [171] |
| $O_2^+ + O^- \rightarrow O(^3P) + O(^3P) + O(^3P)$ | $2.60 \times 10^{-8} T_0^{-0.44}$ | [171] |
| $O^+ + O^- \rightarrow O(^3P) + O(^3P)$ | $4.00 \times 10^{-8} T_0^{-0.43}$ | [171] |
| $O(^3P) + O^- \rightarrow O_2(X^3\Sigma_g^-) + e$ | $1.50 \times 10^{-10} T_0^{-1.30}$ | [172] |
| $O_2(a^1\Delta_g) + O^- \rightarrow O_2(X^3\Sigma_g^-) + O(^3P) + e$ | $1.10 \times 10^{-10}$ | [173],g |
| $O_2(b^1\Sigma_g^+) + O^- \rightarrow O_2(X^3\Sigma_g^-) + O(^3P) + e$ | $6.90 \times 10^{-10}$ | [174] |
| $O^+ + O_2(X^3\Sigma_g^-) \rightarrow O_2^+ + O(^3P)$ | $2.30 \times 10^{-11}$ | [175] |
| $O^+ + O_2(a^1\Delta_g) \rightarrow O_2^+ + O(^3P)$ | $1.00 \times 10^{-11}$ | [175] |
| $O^+ + O_2(b^1\Sigma_g^+) \rightarrow O_2^+ + O(^3P)$ | $1.00 \times 10^{-11}$ | h |
| $O_2^+ + O_2(X^3\Sigma_g^-) \rightarrow O_2(X^3\Sigma_g^-) + O_2^+$ | $4.00 \times 10^{-10}$ | [176] |
| $O_2^+ + O_2(a^1\Delta_g) \rightarrow O_2(X^3\Sigma_g^-) + O_2^+$ | $2.00 \times 10^{-10}$ | i |
| $O_2^+ + O_2(b^1\Sigma_g^+) \rightarrow O_2(X^3\Sigma_g^-) + O_2^+$ | $2.00 \times 10^{-10}$ | i |
| $O(^3P) + O(^1D) \rightarrow O(^3P) + O(^3P)$ | $8.00 \times 10^{-12}$ | [177] |
| $O_2(X^3\Sigma_g^-) + O(^1D) \rightarrow O_2(X^3\Sigma_g^-) + O(^3P)$ | $0.32 \times 10^{-11} exp(67/T_g)$ | [178–180] |
| $O_2(X^3\Sigma_g^-) + O(^1D) \rightarrow O_2(a^1\Delta_g) + O(^3P)$ | $0.32 \times 10^{-11} exp(67/T_g)$ | [178–180] |
| $O_2(X^3\Sigma_g^-) + O(^1D) \rightarrow O_2(b^1\Sigma_g^+) + O(^3P)$ | $2.56 \times 10^{-11} exp(67/T_g)$ | [178–180] |
| $O_2(a^1\Delta_g) + O(^3P) \rightarrow O_2(X^3\Sigma_g^-) + O(^3P)$ | $2.00 \times 10^{-16}$ | [181, 182] |
| $O_2(a^1\Delta_g) + O_2(X^3\Sigma_g^-) \rightarrow O_2(X^3\Sigma_g^-) + O_2(X^3\Sigma_g^-)$ | $3.60 \times 10^{-18} exp(220/T_g)$ | [182] |
| $O_2(a^1\Delta_g) + O_2(a^1)\Delta_g) \rightarrow O_2(X^3\Sigma_g^-) + O_2(b^1\Sigma_g^+)$ | $1.81 \times 10^{-18} T_0^{3.8} exp(700/T_g)$ | [183] |
| $O_2(b^1\Sigma_g^+) + O(^3P) \rightarrow O_2(X^3\Sigma_g^-) + O(^3P))$ | $8.00 \times 10^{-14}$ | [182] |
| $O_2(b^1\Sigma_g^+) + O_2(X^3\Sigma_g^-) \rightarrow O_2(a^1)\Delta_g) + O_2(X^3\Sigma_g^-)$ | $3.90 \times 10^{-17}$ | [182] |

---

$a$: Units: rate coefficients in $cm^3s^{-1}$. $T_0 = T_g/300$. $T_g$ in K, $T_e$ in eV

**b**: $f(\epsilon)$ means rate coefficients are determined from the EEDF obtained from the eMCS module. Electron impact excitation of $O_2$ into rotationally, vibrationally and electronic sates, and of $O(^3P)$ into electronically excited states according to known cross sections from [161, 162, 167] is accounted for in the eMCS to properly simulate electron energy loses.

$c$: Assumed to be the same as $O(^3P)$

$d$: Superelastic cross section obtained by detailed balance from the corresponding excitation process.

$e$: Cross section estimated by shifting and scaling the corresponding cross section for the ground state by the excitation threshold of the metastable.

$f$: Cross section estimated by shifting and scaling the corresponding cross section for $O_2(a^1\Delta_g)$.

$g$: In reality occurs through the production of $O_3$, yet this is neglected here for simplicity due to low pressures.

$h$: Assumed the same as for the $O_2(a^1\Delta_g)$ state.

$i$: Lower rate assumed for collisions of $O_2^+$ with metastable molecules based on observations of from Ziolkowski et al [175], for the case of $O^+$.

# Chapter 4

# Laser ablation of metal and metal oxide targets.

*Results in this chapter focus around the first key stage of PE-PLD, being the laser ablation of the target material. Explicitly this chapter will be based around the use of the code POLLUX, for means of characterising this event computationally and comparisons between target materials, with benchmarking the validity of these simulations against experimentally obtained data.*

## 4.1 Comparison of metals and metal oxides.

As mentioned within Chapter 2, PE-PLD utilises a pure metal target instead of an oxide target, such as is common within standard PLD. Yet the behaviour and underpinning physics between the differences in the nanosecond laser ablation of metals and metal-oxides is not well understood. There is indeed a known difference in behaviour, assumed to arise from properties of each material being quite different, such as oxides having large melting temperatures and lower conductivities, however this has not been described in detail. Instead the differences are attempted to be mitigated experimentally, via some deal of trial and error, which such techniques as carefully tuned environments, and target or substrate heating to reduce particulates formation [9, 10]. There has been some relevant work analysing the ablation of oxide targets such as $Al_2O_3$ and MgO in the works of Ihlemann et al [184], and Hoon Kim et al [185]. But these were not compared to their metal counterparts, as the area of research was the effect of laser pulse length on ablation for means of micro-machining.

Table 4.1: Constructed tabular Chart-D EoS for Zn, ZnO, Cu, and $Cu_2O$

| **Chart-D Variable** | **Zinc, Zn** | **Zinc Oxide, ZnO** | **Copper, Cu** | **Copper Oxide, $Cu_2O$** |
|---|---|---|---|---|
| Density (g $cm^{-3}$) | 7.14 [187] | 5.61 [188] | 8.94 [189] | 6.31 [188] |
| Bulk Modulus (Barye) | 7x10x$10^{11}$ [190] | 1.583x$10^{12}$ [3] | 1.3x$107^{12}$ [190] | 1.037x$10^{12}$ [188] |
| Gruneisen coefficient | 1.93 [191] | 2.615 [190, 192] | 2.02 [191] | 1.16 [188, 193] |
| Debye Temperature (eV) | 4.396x$10^{-2}$ [191] | 3.792x$10^{-2}$ [187] | 5.025x$10^{-2}$ [191] | 1.56x$10^{-2}$ [194] |
| Sublimation enthalpy (ergs $g^{-1}$) | 1.986x$10^{10}$ [195] | 4.728x$10^{10}$ [189] | 5.3x$10^{10}$ [196] | 5.944x$10^{10}$ [197] |
| Melting temperature (eV) | 5.97x$10^{-2}$ [190] | 1.937x$10^{-1}$ [191] | 1.17x$10^{-1}$ [191] | 1.378x$10^{-1}$ [191] |
| Thermal conductivity coefficient (ergs $cm^{-1}$ $eV^{-1}$) | 1.345x$10^{11}$ [191] | 2.436x$10^{9}$ [187] | 4.65x$10^{11}$ [191] | 3.983x$10^{11}$ [198] |

Here this behaviour has been explored in detail via the use of the code POLLUX, as described in Section 3.4, which in the past has shown good experimental comparison for electron density within a generated plasma plume during the ablation of Mg by a ns pulse length laser in the work of Qaisar et al [186]. However, POLLUX has yet to be utilised for the modelling of a compound target, with all reported work solely based around targets comprising of a single element. It is possible, however, to model a compound material target within POLLUX, given an understanding of two modules and some key assumptions. Firstly the tabular form of the Chart-D EoS, in principle, can simulate any material given that various parameters are known, which for Zn, Cu, and their oxides, have been compiled from literature and shown within Table 4.1.

However, one key assumption made within the EoS is that there is no way to model different types of atoms within the target, say the way a molecular dynamics code would, and instead the fluid modelled has to be assumed to comprise of a singular type of "atom" with properties corresponding to the EoS. Therefore, effects such as different bond strengths between different types of atoms, and how the different masses of atoms will affect their kinetic energy and velocity cannot be considered. Secondly, the TF model has been utilised with slight modifications based upon this assumption, being that the TF model is calculated for both types of atom within the fluid based on their known chemical potentials, then a weighted average calculated based upon the ratio of atoms within the compound; e.g. for $Cu_2O$ the TF model is solved for Cu and O, then a 2:1 weighted resulted between the two is determined to represent a $Cu_2O$ “atom”. The parameters of the laser used, in order to match that in PE-PLD were: 532 nm wavelength, 35 mJ energy per pulse, 5 ns pulse width, focal spot of 1 mm diameter.

It terms of characterising the nature between these materials for means of film depositions in PE-PLD, two key parameters are investigated. Firstly, the mass ablated from the target per laser pulse, as the amount of ablated material directly corresponds to the deposition rate of the film; an important factor for the technique’s competitiveness in industry. Secondly, the ablated material’s temperature, which has been shown to affect the film quality as it relates to the atom’s ability to successfully diffuse into lattice sites. Especially in the case of metal-oxide deposits where it has been shown in the work of Blackwell et al [199] via molecular dynamic modelling of ZnO depositions from PECVD conditions, that O and Zn atoms require approximately 0.1 and between 0.2 to 0.44eV respectively for diffusion onto a lattice site to form a crystalline film. Temperatures greater than this damaged the film, and temperatures lower than this resulted in amorphous films. Also of interest in said work is that it was shown for these ZnO films that post annealing made very little affect on the lattice structure, and the deposition conditions were the dominating factors.

### 4.1.1 Experimental masses

Ablated masses are obtained from experiment by analysing the craters produced on the target after ablation. Experiments were set up in order to replicate conditions in POLLUX as closely as possible, most importantly the fact that POLLUX cannot model a vacuum and instead uses an inert background of a set pressure; in experiments this pressure is set to 20 Pa. Plus, due to simulations having no chemical reactions between the ablated material and the background, the gas used during the ablation of craters was argon. This also has the benefit of not having any chemical interactions with the target which could affect the craters formation. As POLLUX can only model a single laser ”shot”, whereas experimentally a single shot created practically no visible crater (at least not one that can be reliably measured), multiple shots were used to ablate a larger volume. From this the ablated mass from a single shot was determined from the appropriate fraction of the total volume, and the known density of the target. Volumes of each crater were measured by a Filmetrics Ltd. [200] Profilm 3D White Light Profilometery tool, which is able to create a 3-D map of the crater with a depth resolution of 0.05 $\mu$m. Other techniques such as Atomic Force Microscopy can result in higher depth resolution, however these techniques are limited to very small areas, not suitable for the 1 mm diameter craters produced here.

A histogram is created corresponding to the height profile of the crater, with the ablated volume determined from the area of this histogram, with any material above the crater discarded with this highlighted on the plots in dark red. Interesting physics can also be learnt from the structure of the crater itself, therefore Figures 4.1 & 4.2 shows both the crater and the associated histogram for each material. Line profiles of cross sections from each crater can also be seen in Figure 4.3.

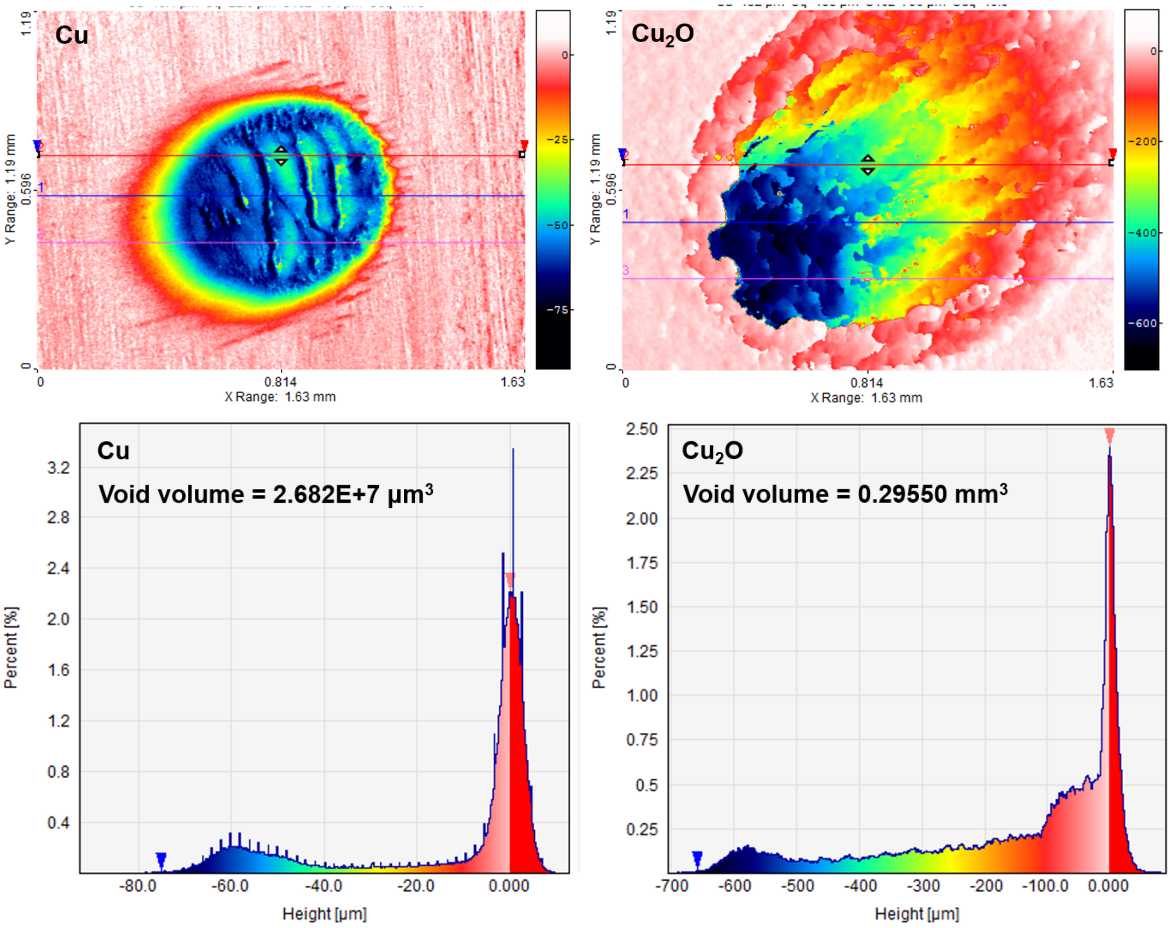

Figure 4.1: Cu (left) and $Cu_2O$ (right) craters after approximately 6000 laser shots, and associated histograms of hight profiles.

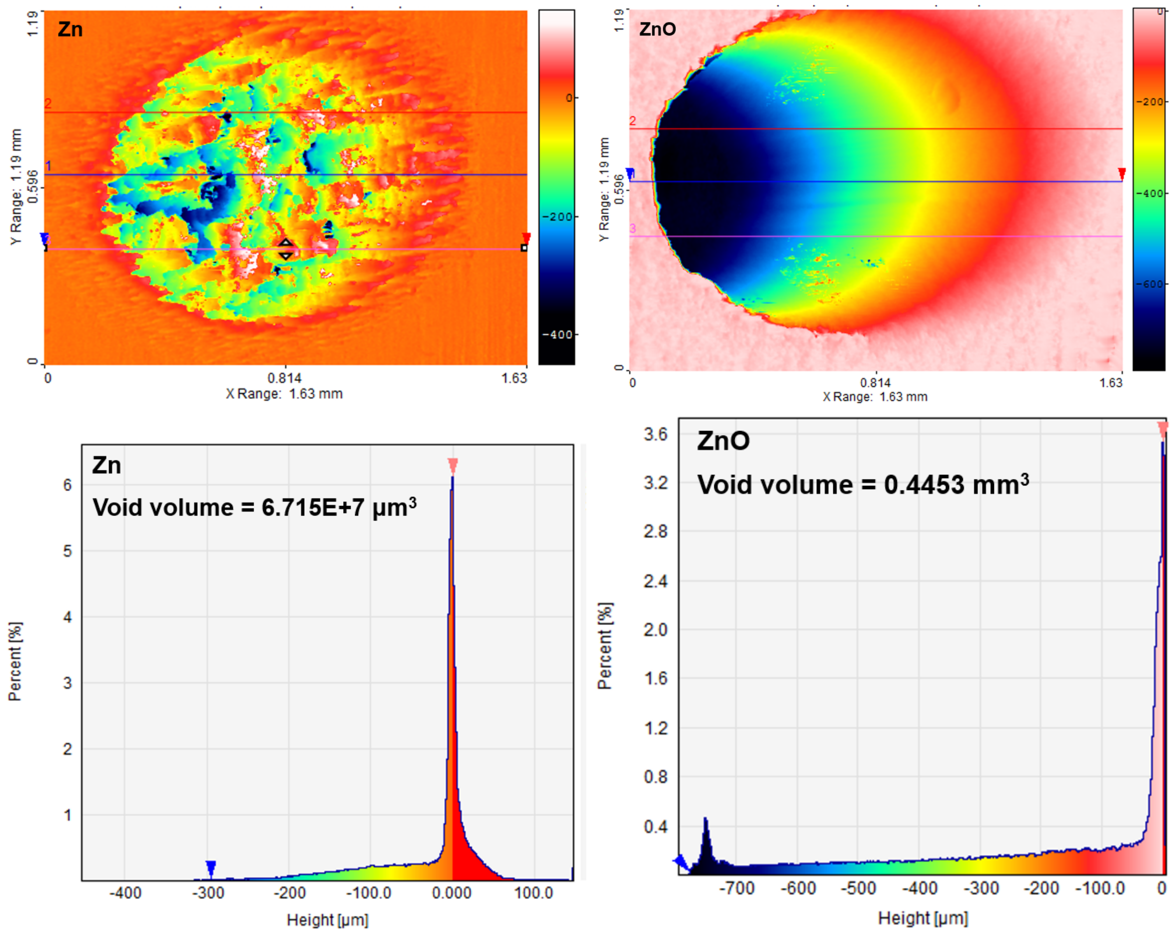

Figure 4.2: Zn (left) and ZnO (right) craters after approximately 6000 laser shots, and associated histograms of hight profiles.

The first clear difference seen in Figures 4.1 & 4.2 between the metals and oxides is the structure of the crater, with both metal Zn and Cu targets showing a rippling effect, whereas both Cu$_2$O and ZnO targets are smoother, which is also visible within Figure 4.3. The rippling effect is a result of the long pulse length of the laser, as when the pulse length of the laser is longer than the interaction time of phonon's within the material ($10^{-10}$ to $10^{-12}$ seconds), then classical phase change transitions occur within the target. This involves the melting of target material into a liquid which is then evaporated by the laser into a gas. Once the laser is no longer incident on the target and no further energy is imparted into the material, it is able to cool and re-solidify into this ripple pattern, an affect seen previously during the exploration of different pulse length lasers on metal targets [184]. However although one would think that this would also occur within the oxides due to being

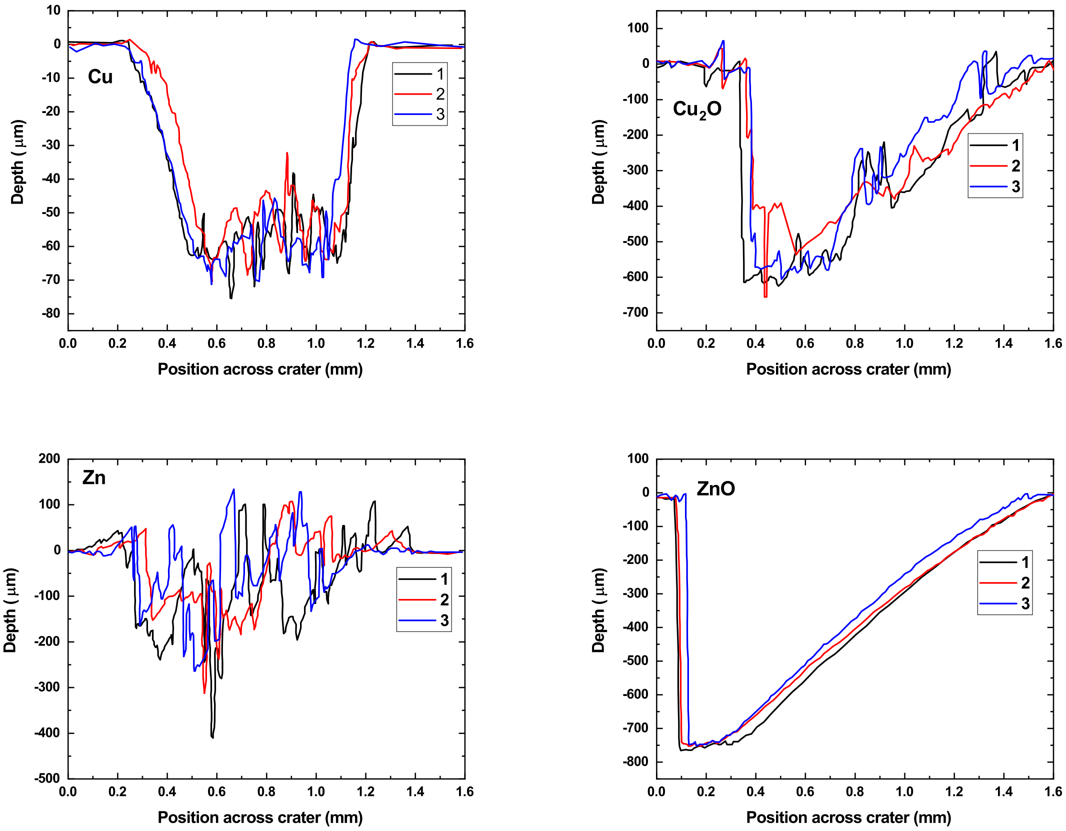

Figure 4.3: Line profiles of craters after laser ablation. Top left: Cu, Top Right: $Cu_2O$. Bottom Left: Zn. Bottom right: ZnO. Numbers in legend correspond to lines on craters as seen in Figs. 4.1 & 4.2

exposed to identical laser conditions, the underlying properties of the target material itself are very different; when looking at all of the relevant properties of the material, see the EoS table created for use in POLLUX (Table 4.1), various thermodynamic properties of the oxides important for classical phase changes are significantly different for the metals, such as the much higher melting point and lower thermal conductivities.

It is in fact that these targets are a compound of various elements which needs to be considered, as unlike the pure metal where one can assume the target will behave homogeneously, the compound targets cannot behave in the same ways due to various different internal properties within the material due to two key aspects. Firstly the different bond strengths between the metals atoms and oxygen atoms , i.e. $Cu-Cu$, $Cu-O$, $Zn-Zn$ and $Zn-O$, are quite different with both metal-metal bonds being quite weaker than the metal-

Table 4.2: Physical size of each ablated creater for metal and metal oxide tragets

| Target | Void volume (mm$^3$) | Number of shots |
|---|---|---|
| Copper | $2.6407\times10^{-2}$ | 5992 |
| | $2.8433\times10^{-2}$ | 6018 |
| | $2.6832\times10^{-2}$ | 6018 |
| | $2.8441\times10^{-2}$ | 6024 |
| Copper Oxide | 0.30651 | 6037 |
| | 0.30842 | 6354 |
| | 0.2955 | 6028 |
| | 0.31121 | 6052 |
| Zinc | $5.9766\times10^{-2}$ | 6020 |
| | $6.715\times10^{-2}$ | 6043 |
| | $6.1694\times10^{-2}$ | 6070 |
| Zinc Oxide | 0.4553 | 6203 |
| | 0.42887 | 6045 |
| | 0.41707 | 6034 |
| | 0.4411 | 6040 |

oxygen bonds [201]. One also needs to consider that the metal atoms are approximately 4 times heavier than the oxygen atoms, meaning that, although bonds between metals are easier to break within the target, oxygen atoms require far less energy to ablate from the surface.

This process of phase change is referred to as decomposition, an effect that can occur within compound materials when heated to their melting temperature. When this temperature is reached bonds begin to break within the target, with lighter elements (e.g. oxygen) effectively sublimating from the target, and accelerated easier than the metals due to their lighter mass. This leaves behind a target solely of heavier atoms (e.g. Cu, Zn), which either are ejected from their lattice sites via sublimation, due to the many broken bonds within their lattice, or to either melt and undergo classical phase changes if there are sufficient bonds between these heavier atoms [4, 63]. This volatile nature of oxygen and resulting decomposition within the film corresponds to the deeper craters observed, and can also explain the films created by S. Rajendrian who deposited films from the ablation of a copper oxide target [2]; These films were observed to be amorphous, and consisting of large grains of very inconstant sizes, implying that the target ablation was a much more irregular process.

However so far only the structure of the craters has been commented on. When looking at the histograms in Figures 4.1 & 4.2, and the associated volumes and masses in Tables

4.2 & 4.3, it can be seen that the ablated masses are larger for the oxides. Copper oxide ablates 7.6 times as much as pure copper, and zinc oxide 5.4 times as much as pure zinc, due to these metal-oxide target decomposing, an affect that overall requires less energy to be imparted from the laser and, therefore, allowing for a greater mass to be ablated. This affect is quantified with POLLUX in the following section. To note, each crater was ablated for 10 minutes, corresponding to roughly 6000 shots due to the 10 Hz rep. rate of the laser. Calculated masses per shot were determined from the crater volume, appropriate density of the material, and number of shots, with the uncertainty quoted being the standard deviation from the average of three or four craters. These masses and observed trends are what will be used to compare to POLLUX simulations in the following section.

Table 4.3: Calculated ablated mass per each laser shot, of each metal and metal-oxide target.

| **Target** | **Mass ablated per shot (kg)** | **Error** |
|---|---|---|
| Copper | $4.10\times10^{-11}$ | $0.2\times10^{-11}$ |
| Copper Oxide | $3.15\times10^{-10}$ | $0.1\times10^{-10}$ |
| Zinc | $7.43\times10^{-11}$ | $0.4\times10^{-11}$ |
| Zinc Oxide | $4.02\times10^{-10}$ | $0.1\times10^{-10}$ |

### 4.1.2 Masses from POLLUX, and comparison to experiment

Ablated masses are determined from POLLUX simulations by the following means; first the material that has been ablated into the gas phase and will successfully travel away from the target (see Section 2.3) has been determined by the Knudsen velocity, $u_k$, Equation 2.10. An example for a Zn target is described here; The temperature of material close to the target was determined from POLLUX to have a mean value of 5.01 eV, and the surface energy of 0.065 J m$^{-2}$ was taken from Billow et al [202]. This results in a $u_k$ of 6.9 $\times10^4$ ms$^{-1}$, and therefore any material with an axial velocity less than this value was discounted from the analysis; this resulted in an ablated plume as shown in see Figure 4.4. Then the density of any material within cells with sufficient velocity was used to determine the ablated mass, as each cell had a known corresponding area as this was pre-set within the simulation, and by its known radius from the axis of symmetry. To note, Figure 4.5 shows the determined ablated mass when using a cut-off position at varying axial velocities compared against the mean velocity at each cut-off point. It can be seen at the point where the mean velocity equals this determined $u_k$ there is a discontinuity in velocity, and a steep change in mass,

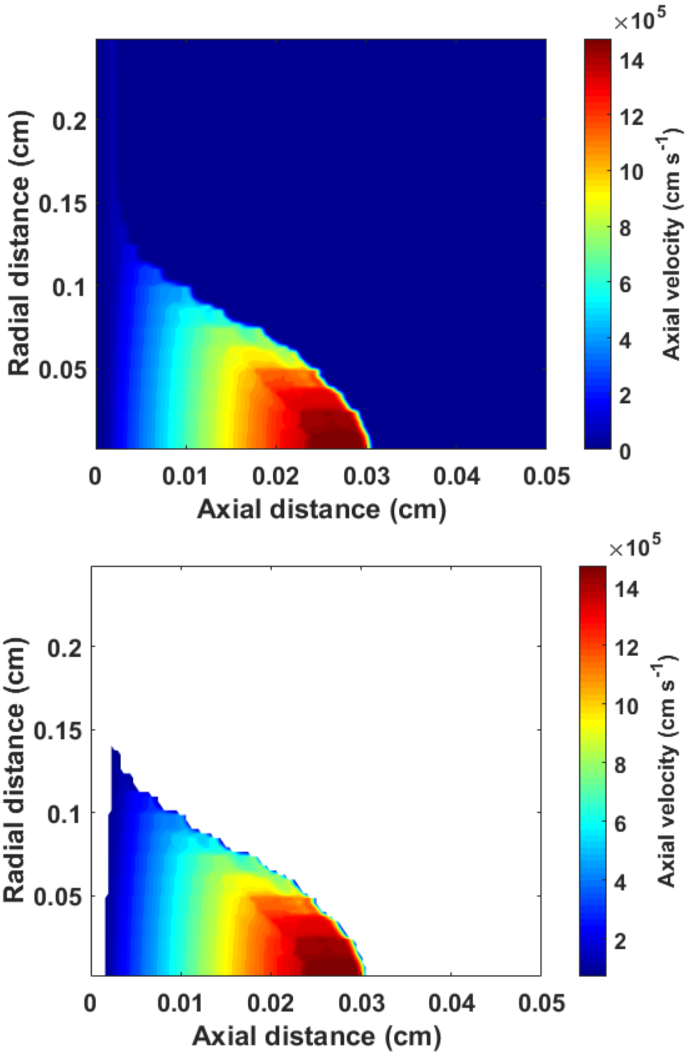

Figure 4.4: Top: Axial velocity of Zn plume within POLLUX after 20 ns. Bottom: All velocities under $u_k$ discounted.

thus showing a match between this calculated Knudsen velocity, and material entering the gas phase.

This has been performed for all four target materials, and additionally for various phase change assumptions, as was discussed in the previous section that it was seen experimentally the behaviour of oxides was different under nanosecond laser ablation than the metals. Therefore two different assumptions have been tested from Table 3.4, being the “full treatment” model, i.e. solid material melts to a liquid which then can evaporate, and the gaseous target model, which has been used based upon the nature of the oxides as discussed above. Masses for each case can be seen in Figure 4.6.

The first observation to discuss from Figure 4.6 is that for the case of the full treatment

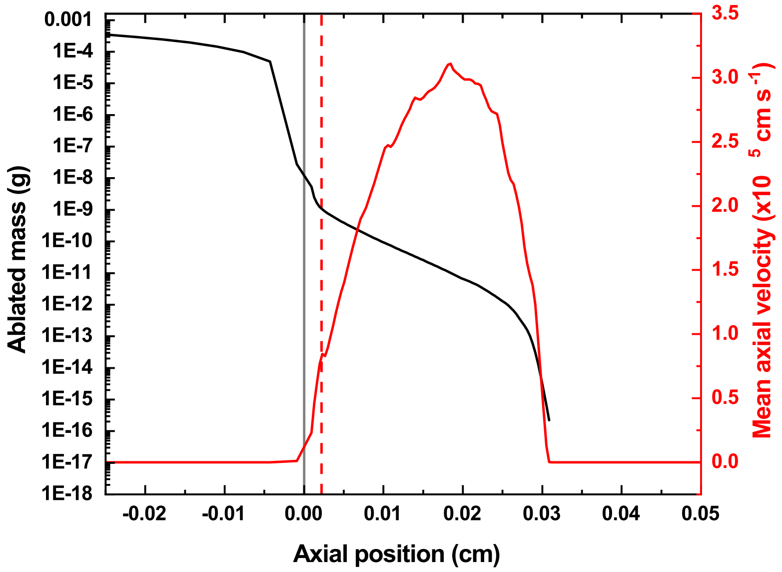

Figure 4.5: Ablated mass as a function of distance from target surface, alongside mean axial velocity, for a Zn target after 20 ns. Solid grey line corresponds to target surface, and dashed red line calculated Knudsen velocity.

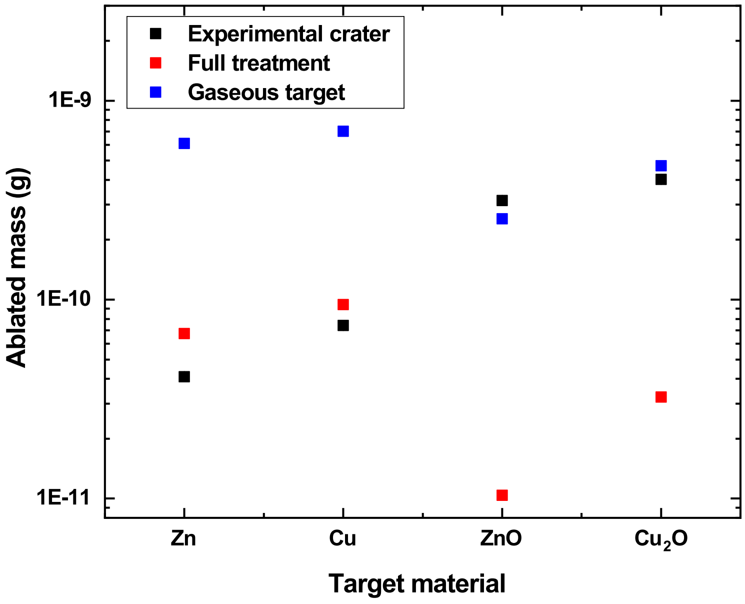

Figure 4.6: Determined ablated masses from POLLUX for all for target materials, and mass from experimental craters.

model when used for the metallic targets (Zn, Cu), that the masses from POLLUX match closely to those from experiment, with Zn and Cu matching within 35% and 22% respectively. But when comparing this trend to the full treatment model when used for the oxides, there is a difference of 300% for ZnO, and 120% for $Cu_2O$. Yet, when using the gaseous target model for the oxide targets, the determined masses match strongly, with ZnO matching by 19%, and $Cu_2O$ within 17%. This shows that POLLUX can accurately predict the behaviour of both metals and metal oxides under nanosecond laser ablation, as when using the phase changes that make the physical behaviour for target ablation (i.e. full treatment for metals and gaseous for oxides), the masses match experiment to a degree of a reduced order of magnitude, relative to the incorrect assumptions (i.e. gaseous metals and full treatment oxides).

This slight disparity in masses could be considered to arise from assumptions in the laser energy for two key reasons. First in POLLUX it is assumed the laser is incident at an angle normal to the target, whereas in experiment this is not the case and there is a $45^o$ angle offset. Thus causing the intensity of the laser across the spot-size to not be evenly distributed as it is in simulation. Also in experiment it was observed that not only the target, but also the target holder, heated up during ablation, meaning some laser energy has been lost. This factor is not considered within POLLUX which has no consideration of heat loss to surroundings, and all energy is assumed to be either absorbed, or reflected based upon the critical density of the plasma. This effect can be shown within Figure 4.7, where a laser of 15% less energy lead to a closer match to experiment for the ablated Zn plume, matching to 5%.

It could also be considered that the approximation of the Knudsen layer is incorrect in this case, however Figure 4.8 shows the rough approximation for the Knudsen layer for the case of Zn shown above (Figure 4.5), but with an additional mark for where the Knudsen layer must approximately be to match the experimental mass. It can be seen that for the Knudsen layer to result in an ablated mass that matches experiment, then the majority of the plume must be discounted, and therefore this is highly unlikely to be the main source of the difference to the experimental results.

Further insight into oxide ablation can be gained, when a direct sublimation of a solid to a gas of oxide targets is considered. This is shown in Figure 4.9, where it can be clearly seen that no observable plume is created the oxide target. This results from the fact that

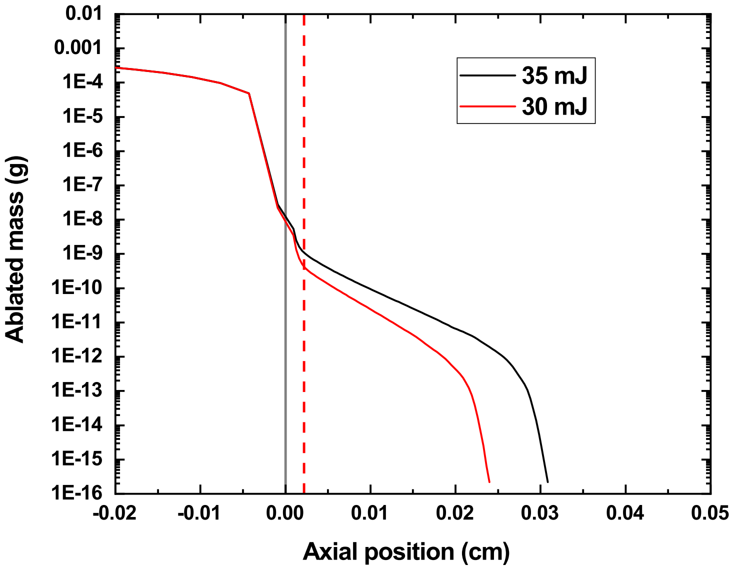

Figure 4.7: Ablated mass of Zn at 20 ns for a laser of 15% less energy per pulse. Grey line is target surface, dashed red line is calculated Knudsen velocity.

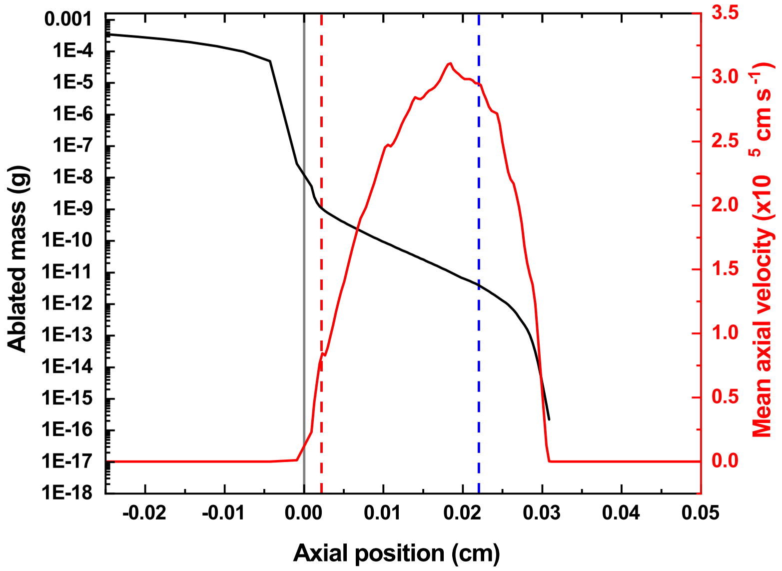

Figure 4.8: Ablated mass for Zn at 20 ns as a function of cut off distance. Grey line is target surface, dashed red line is calculated Knudsen velocity, dashed blue is is Knudsen velocity required for mass to match experiment.

even though the target is heated, the energy required for direct sublimation as determined by the Clausius-Clapeyron relation (Figure 3.20) is too high. The proper treatment of decomposition is not handled within POLLUX, due to limitations in the lack of treatment of atomic bonding within the target. Therefore, when considering the gaseous target model, which can be argued to be closest to the nature of decomposition of oxide targets due to the nature of oxygen within the film, but without any modelling of atomic bonding, that the experimental masses matched closely to that from the gaseous target model.

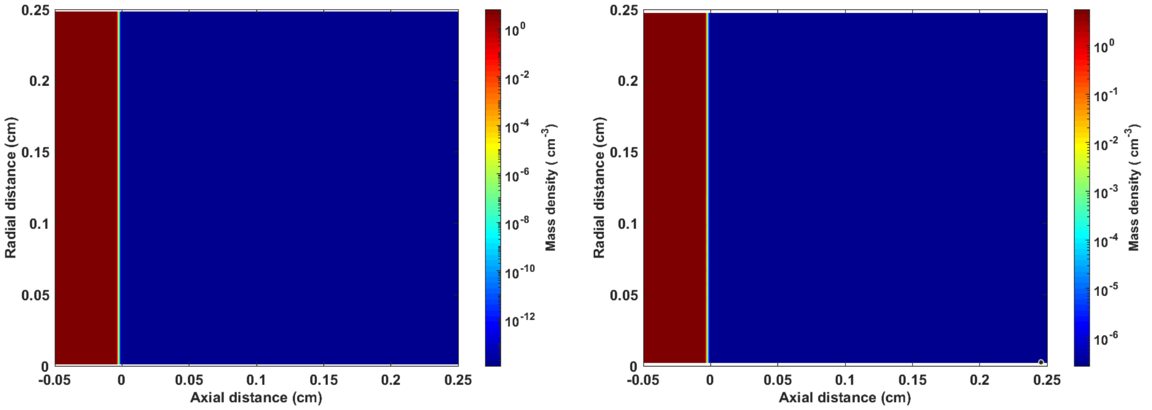

Figure 4.9: Ablated plumes, or indeed lack there of, from $Cu_2O$ (left) and ZnO (right) targets after 20 ns, when using pure sublimation assumptions

The amount of energy utilised from such phase changes within the target can also be determined by POLLUX, from the treatment of metallic targets (Zn, Cu) by the gaseous model, which are also shown in Figure 4.6. Comparing the internal thermal energy, $Q$, of the material determined for each different assumption made on the phase change of the target. $Q$ is given by Equation 4.1, where $m$ is the ablated mass, $k_b$ is the Boltzmann constant, and $T$ the mean temperature of the ablated plume, determined from POLLUX. This is also compared to the kinetic energy of ablated material, given by $1/2 \cdot mv^2$. These energies are shown in Table 4.4, where the energies determined are shown both in terms of Joules, and the total percentage of the applied laser energy, 35 mJ.

$$Q = mkT \tag{4.1}$$

Table 4.4 shows that the internal thermal energies of the plume in each case are minimal when compared to the laser energy, yet for the gaseous target it is larger by an order of

Table 4.4: Internal thermal and kinetic of Zn and Cu plumes for different phase change assumptions.

| **Material** | **Thermal energy (mJ)** | **Thermal energy (% of laser)** | **Kinetic energy (mJ)** | **Kinetic energy (% of laser)** |
|---|---|---|---|---|
| Zn (full treatment) | $1.14\times10^{-4}$ | $3\times10^{-4}$ | 2.35 | 6.9 |
| Zn (gaseous target) | $1.81\times10^{-3}$ | $5\times10^{-3}$ | 26.9 | 77 |
| Cu (full treatment) | $3.58\times10^{-4}$ | $9\times10^{-4}$ | 2.45 | 7 |
| Cu (gaseous target) | $2.21\times10^{-3}$ | $6\times10^{-3}$ | 29.8 | 86 |

magnitude. A great affect is seen in the kinetic energies, where approximately 7% of the laser energy has been converted to kinetic energy, whereas for the oxides it is an approximately 80%. This comes as a result of less energy being required in the gaseous targets for the target to begin expanding, as there is no energy expended in the phase change of the target; whereas it is clearly apparent for the metal targets that at least 50% of the laser energy is expended in this process. This again highlights the importance of understanding the phase changes that occur within targets during ablation conditions such as these, for applications in processes such as PE-PLD.

To conclude on the topic of ablated masses, POLLUX has successfully used in the modelling of ablation of both metal and metal oxide targets in two key aspects. One is the absolute values of masses of ablated material that can be obtained from POLLUX, yet also from the trends observed between different target materials, and how these can be modelled via understanding of the important phase changes that underpin the targets ablation; with metallic targets undergoing melting and evaporation, and oxide targets undergoing a decomposition, which although not able to be modelled within POLLUX, matches closely to an assumption of a gaseous target that undergoes no changes, similar to how oxygen behaves within the lattice.

## 4.2 Plume electron temperatures

Experimental measurements of electron temperatures within the laser ablated plasma used within PE-PLD, obtained by laser induced breakdown spectroscopy (LIBS), have been

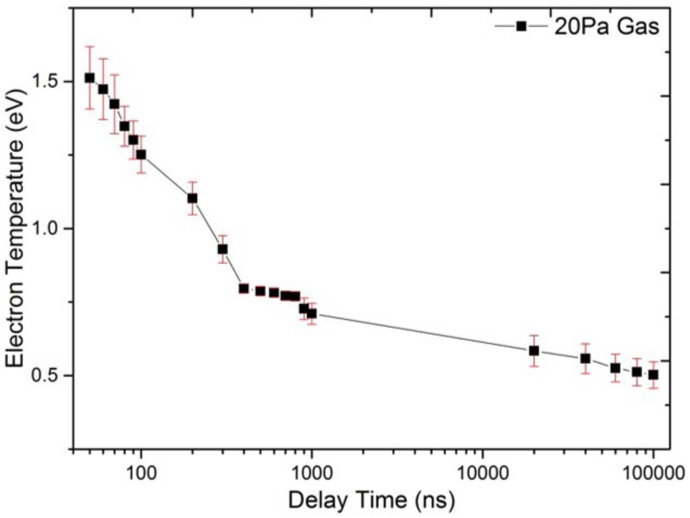

Figure 4.10: Measured electron temperatures within an ablated Cu copper plume under PE-PLD relevant conditions [2].

reported in the thesis of S Rajendiran, and shown in Figure (4.10) [2]; temporally resolved optical spectroscopy of the produced plume showed the observed electron temperature of the plume at approximately 50 ns to be 1.5 eV, which decreases to 0.5 eV after 1 $\mu$s, at which point it is fairly level. Electron temperatures from POLLUX simulations matching these conditions have been investigated, with Figure 4.11 showing the electron temperature of the plume 50 and 100 ns after ablation. The initial observation from these figures is that the temperature of the plume is much hotter (up to an order of magnitude) at the leading front, with a cooler bulk of the plume. In order to compare directly to the experiment, which although it was very well temporally resolved, performed spatially integrated measurements, and therefore a simple average of the entire plume is taken without weighting to any volume or species density; results of which shown in Figure 4.12.

Figure 4.12 shows a comparison between simulation and experiment at 50 ns, with an reasonable agreement overall; with the trend reproduced and the absolute values matching within 30%. One issue worth investigating however is the thin, hot region at the leading edge of the plume. With the main question being is if this is physical or an artefact of the code resulting from any models utilised.

Temperatures in POLLUX are calculated by the TF model (see Section 3.4.6), where plume volume and the electric field determined from the degree of ionisation of the material. So corresponding degrees of ionisation of the plume can be seen in Figure 4.13, where it is seen that the more highly ionised material is in the front, leading edge of the plume; an expected behaviour due to this material having absorbed more energy from the plasma and therefore has a higher thermal velocity as well as charge state [9]. But most importantly there is no clear higher region of ionisation matching that of the electron temperature observed as in Figure 4.11.

So if this leading hot edge does not intrinsically come from the TF model, then the only models that handle temperature and energy with POLLUX are the Spitzer-Harm model for LTE, and the ICCG method of handling energy transport. Firstly to ensure the Spitzer-Harm model is valid, the plasma must indeed be in LTE, which can be assumed from the McWirther criterion, as shown in Figure 4.14. This figure shows the electron density from POLLUX determined from the charge state and mass density, alongside the McWirther criterion (Equation 2.15), obtained using the electron temperature in $K$, and the difference in energy levels of Cu obtained from NIST [203]. It can be seen, even within the leading super hot front, that the plumes electron density is orders of magnitudes greater than the McWirther criterion. Thus the plume should certainly be in LTE and the Spitzer-Harm model valid, meaning this deviation in temperatures must come as a result of another effect.

In fact if one is to compare the profile of electron temperatures and densities, i.e. Figures 4.11 and 4.14, there is a clear difference in distribution and profiles of these parameters. Temperatures seem to behave as if a shock front, whereas densities have a more diffuse profile, and this is where the source of these lower temperatures arise. It is well known from high power laser plasma physics for ICF and astrophysical purposes, that shocks such as what is being observed here always correspond to not only a spike in temperature, yet *also*

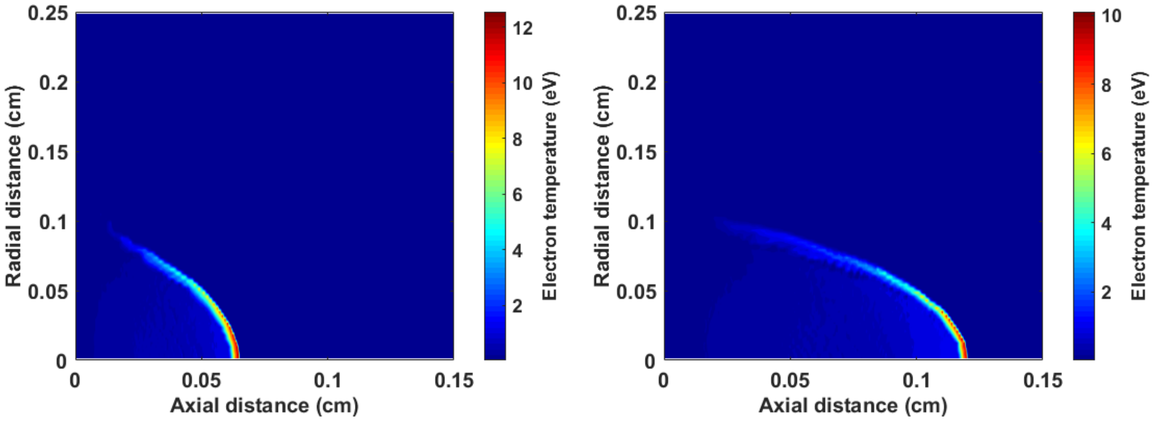

Figure 4.11: Electron temperatures of ablated plume after left: 50 ns. Right: 100 ns.

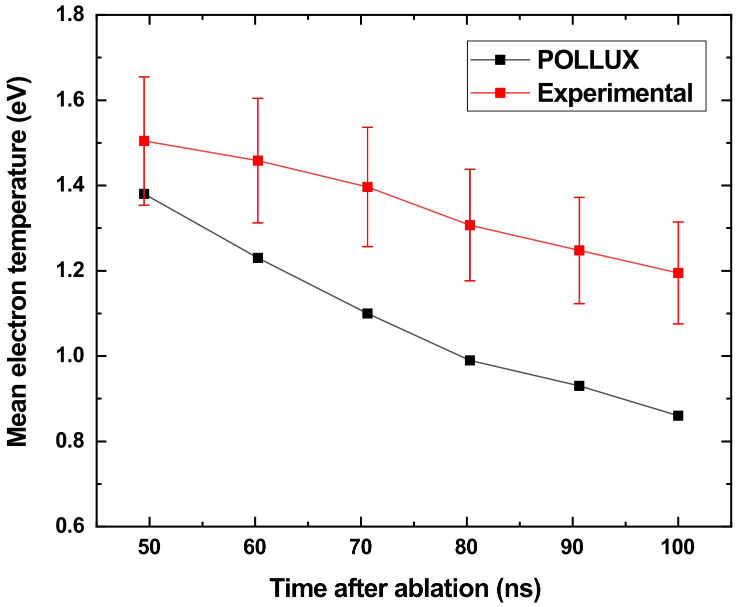

Figure 4.12: Mean electron temperatures obtained from POLLUX and experiment between 50 and 100 ns.

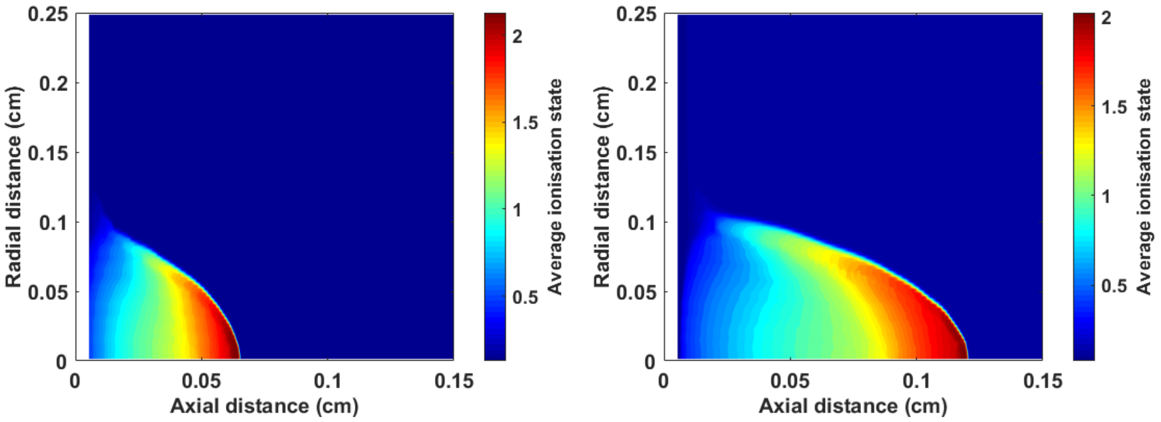

Figure 4.13: Average ionisation state of an ablated plume of Cu at two time times after ablation. Left: 50 ns. Right: 100 ns.

an increase in density as energy transports through the material [204]; This implies this shock front style spike in temperature is a mathematical artefact within the code. It is perhaps worth noting now that although POLLUX is a well used and referenced code, all literature based on POLLUX is for the use of exploration of densities, and although temperature effects have been area of interest it has always been either the temperature at the target surface,

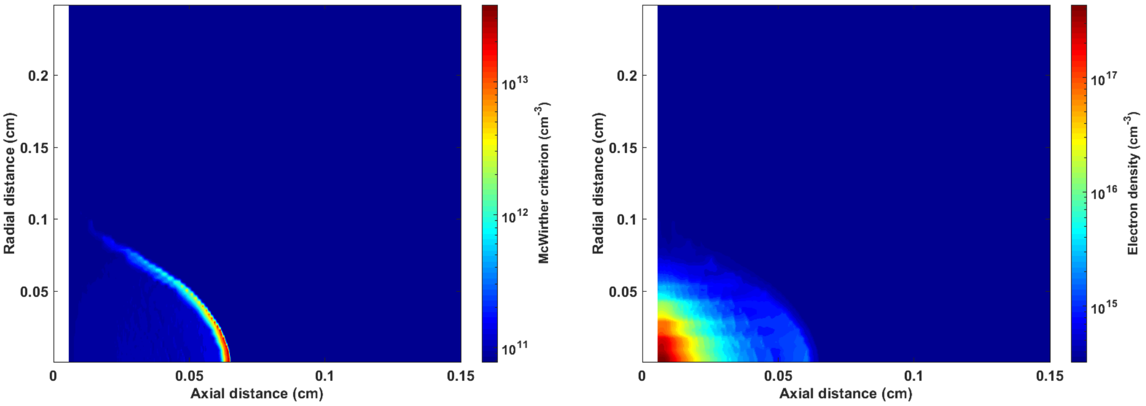

Figure 4.14: Calculated McWirther criterion (left) and electron density (right) for ablation of Cu after 50 ns

or after extremely short times after the ablation event such as in the works of Qaisar [186] and Rossall [205].

In terms of where this "shock front" of temperatures arises from, this is due to the handling of material by to the FCT and ICCG models utilised by POLLUX. Although the use of these models result in rapid speed of simulation, they are indeed limited, this being that as there is no explicit method of defining what is plume material and background. So when material is transported from one cell to another, *all* neighbouring cells are treated equally. Therefore background material will be used in various calculations, such as the determination of temperatures during the TF and Spitzer-Harm models. So seeing as this dense plume is made to equilibrate with this less dense background, there will be a sharp decrease in collisionality, and therefore increase in temperature. This leads to this artificial temperature spike at the plume edge, whereas temperatures within the plume have a more diffuse profile, matching that of the densities. So some form of model would be needed to be applied to the plume expansion, or some method of defining which cells are to be considered in each iteration, for a full and rigorous treatment of plume expansion over many nanoseconds.

Thus one needs to look into how a plume expands and travels over such time periods, which is in itself a highly complex area of physics and still an active area of research. This topic is perhaps best summarised in the work of Bogaerts et al [206], which presents a review of many different models that are used in past years and the complexity of this area due to the sheer number of considerations and assumptions. These include, but indeed are not limited to, how hydrodynamic flow is handled, if the system is adiabatic, or if anything is lost to the environment, and if so which parameters are to be conserved. Many models in literature have rigorous treatments using various assumptions, however these assumptions limit them to precise conditions such as early or late time-steps, or specific background pressures. POLLUX lacks such a rigorous model for plume expansion, with the only equations for fluid motion are those as outlined in Equation 3.24, and the only form of collisionality handled by the Spitzer-Harm model.

However this is not to say the results are not valid under certain conditions, as it can be seen that the ablated mass in Figure 4.6 match in trend, and are close in magnitude to experiment, and temperatures in early timesteps in Figure 4.12 are a match within error. Therefore the argument can be made that POLLUX has much more rigorous handling of phase changes and target conditions, and is well suited for characterising material directly after ablation , a concept that is further explored in the next section.

## 4.3 Silicon ablation in a vacuum

In an addition to the works with metals and metal oxides, POLLUX has been used in collaboration with Dr Hao Liu and Prof. Mike Ashfold of the Univeristy of Bristol. With results presented here, alongside others, recently being accepted to the Journal of Applied Physics [207]. The goal of these simulations were to characterise the laser ablation of a pure silicon, Si, target by both 532 and 1064 nm lasers within a vacuum, where highly spatially and temporally resolved spectroscopy was used to observe the ablated plume. Within this work I performed modelling and analysis of the laser ablation of Si with POLLUX, then used in further modelling and experiments by the collaborators listed above.

Table 4.5: Constructed tabular Chart-D EoS for Si

| **Chart-D EoS Variable** | **Value** |
|---|---|
| Density (g cm$^{-3}$) | 2.32 [189] |
| Bulk Modulus (Barye) | $9.76\times10^{11}$ [189] |
| Gruneisen coefficient | 0.455 [189, 208] |
| Debye Temperature (eV) | $5.966\times10^{-2}$ [208] |
| Sublimation enthalpy (ergs g$^{-1}$) | $1.705\times10^{11}$ [208] |
| Melting temperature (eV) | $1.455\times10^{-1}$ [208] |
| Thermal conductivity coefficient (ergs cm$^{-1}$ eV$^{-1}$) | $8.355\times10^{10}$ [191] |

The constructed EoS is shown in Table 4.5, and the laser conditions are as follows; both 532 and 1064 nm wavelengths were modelled, both with a pulse length of 18 ns, pulse energy of 80 mJ, and focal radius of 0.1 mm. However, as stated before, POLLUX cannot simulate a pure vacuum due to limitations set on the code by the FCT model (i.e. no cell can be void, see section 3.4). Therefore the initial tests performed were to reduce the background pressure by sequential values, and exploring the affects this had on the plume growth; this was done in order to determine the lowest possible background pressure that could be utilised within POLLUX, whilst avoiding numerical issues within the simulation. The parameter that was used in order to determine this lower limit was the electron and ion temperatures ($T_e$ & $T_i$ respectively), as POLLUX is only reliable when modelling LTE, any deviation in these would mean that the simulations would not be physical. Figure 4.15 shows these temperatures at various pressures.

It can clearly be seen from in Figure 4.15 that the plumes do exhibit LTE, in all cases with matching $\mathrm{T}_i$ and $\mathrm{T}_e$, yet a different affect is observed. Similar to the results with the metal and oxide work presented above, there is a leading hotter edge to the plume, yet the effect is dramatically different at the lower pressures. Higher pressures such as 100 & 10 Pa still have this leading edge, yet are not that different in magnitude, spiking at around 25 eV, although the shape is much more pronounced for 10 Pa. However when dropping by a further order of magnitude to 1 Pa then these temperatures increase by approx 50 eV, and at even lower pressures a significant change in profile is observed. This gives further evidence to the argument put forward with the previous section, being that plume expansion is not handled with explicit detail in POLLUX.

However unlike the Cu spectroscopy, the only measurements in this experiment to compare to were after much longer time steps, with the shortest being at 80 ns, far after any assumption within POLLUX can be trusted. Therefore these outputs from POLLUX have been used in an additional model, being the model of adiabatic plume expansion from Stapleton et al [42], see Section 2.3. This model requires as an input the total mass, internal energy, and velocity of the ablated plume, all of which can be obtained from POLLUX. So the expansion of a plume within POLLUX was explored over time in detail, with the results showing the electron temperatures shown in Figure 4.16, within a background pressure of 20 Pa.

Within times during the pulse in Figure 4.16, it can be seen that the plume begins to

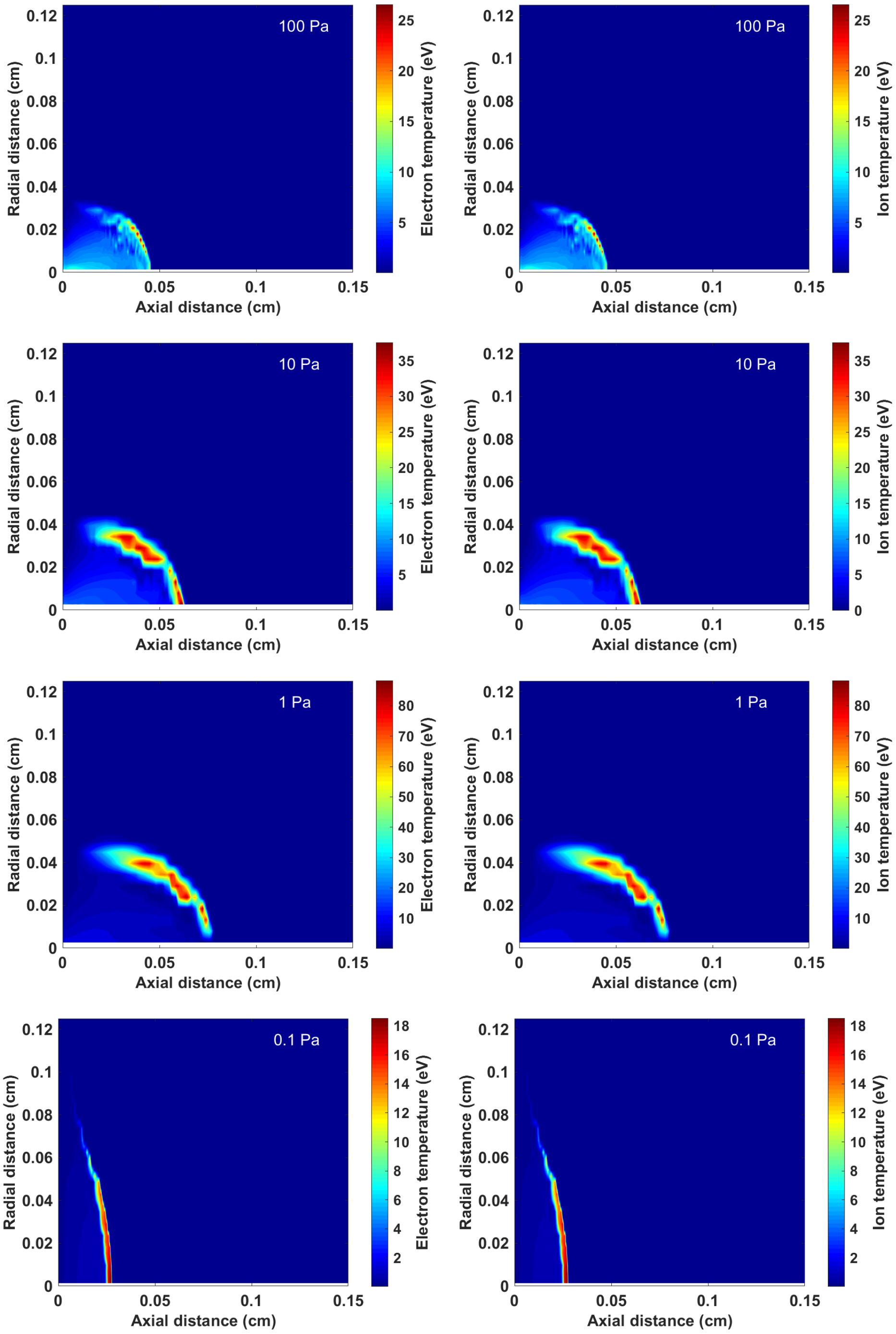

Figure 4.15: $T_e$ and $T_i$ in an ablated Si plume, in pressures from 100 to 0.1 Pa, after 20 ns.

expand and continues to heat up, then after the laser is no longer incident, begins to cool and expand due to the initial velocity of the plume and internal collision, however after approximately 25 ns the hot leading edge artefact beings to appear. This effect is seen at roughly this time-step as this is significantly after the laser stops heating the plasma, so

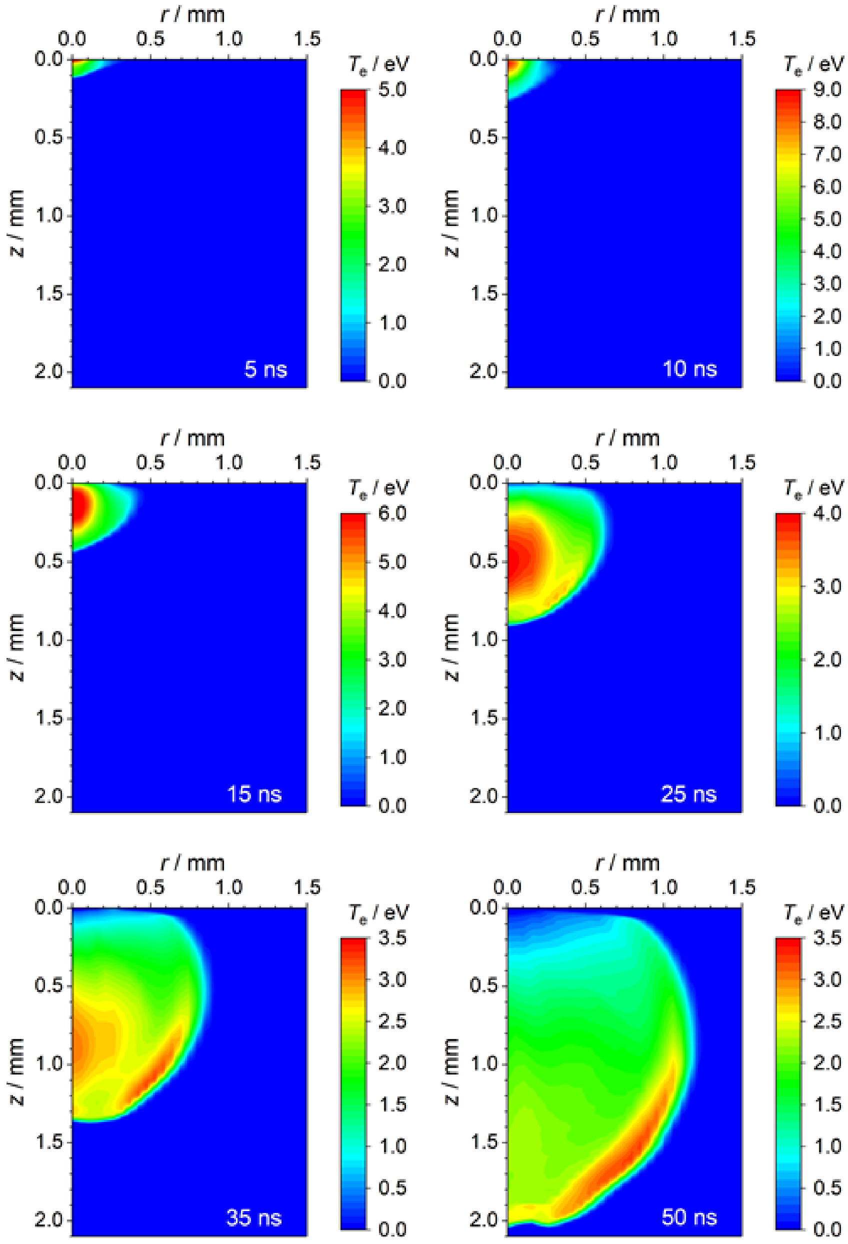

Figure 4.16: Evolution of T$_e$ in an ablated Si plume over time, in a pressure of 20 Pa.

all dynamics are not influenced by an external source. Also, the plume starts to significant expand in size from this point forward, meaning there is a larger area at the leading edge of the plume to be exposed to the background material, resulting in this artificial plume-background interaction occurring.

So data from these POLLUX simulations at 20 ns, close to the end of the laser pulse, were used as inputs for the aforementioned model of Stapleton; As this process was performed by Dr. E. Wagenaars therefore details are shown within Appendix A, however yet some key concepts will be discussed here. The model of Stapleton uses assumptions on the profile of density and temperature, as an input to the adiabtic expansion which is then a self consistent model. Exact profiles are dependant on the assumptions being made, with isothermal models assuming a constant temperature and half-Gaussian density profile, and isentropic models assuming an elliptical distribution of temperature and density.

It is clearly apparent from POLLUX simulations, that profiles of density and temperature within the observed plumes are neither half-Gaussian, elliptical, or constant in nature. In fact these assumptions used within the Stapleton model are effectively used in order to force a fit in the initial conditions observed in their initial work [42]. Therefore, the results from POLLUX, once allowed to expand adiabatically, do not match to that of the experiments of Hao and Ashfold. In some cases there are some trends that agree, such as the isothermal approach predicting electron density, and the electron temperatures in the isentropic case; yet there are still some clear disparities, such as temperatures in the isothermal case.

POLLUX can be argued to model phase changes of targets well, both in terms of ablated mass and temperatures at early time-steps, as discussed within the previous section. Such data is not utilised as inputs in the model of Stapleton, or indeed others in literature such as Singh or Anisimov [41, 209]. Therefore these findings highlight the issues and limitations within the modelling of such processes. My use of POLLUX here within this work has begun to highlight how complex an area laser ablation of targets can be, as if one is to use a model to treat the ablation phase and formation of a plume as rigorously as required, then existing models do not successfully handle the expansion of this material, due to their initial assumptions being no longer valid.

## 4.4 Conclusion

Results in this chapter have shown the successful modification of the code POLLUX for use with a compound target, and from this an exploration of the differences between metal and metal oxide targets under nanosecond pulse length laser ablation. Simulations of metallic targets, Zn and Cu, within POLLUX matching that of experimental data, with ablated masses matching within 35%, compared to that from masses obtained from target craters. Only a slight deviation is observed which can be described by assumptions used when comparing energy of the lasers.

Oxide targets within POLLUX, although again not matching experiment exactly, match up to experiment closely, within 20%, when using an assumption of a gaseous target, which can effectively model the decomposition of the targets when heated to high temperatures; a full treatment of decomposition cannot be made due to lack of modelling of atomic bonding within POLLUX. This clearly shows a matching trend between target materials within POLLUX, when matched to experiment. Plus a determination of the internal thermal and kinetic energies of the ablated plume for metallic targets has been performed, showing that under different phase changes of targets the thermal energy of the plume is slightly different although minimal. Yet kinetic energies are much higher for both solid targets, and even higher still in the case of gaseous targets, due to the lack of energy expended to undergo phase changes. Highlighting the importance of the understanding of the required phase changes of targets, in applications such as PE-PLD.

POLLUX has also been used as a input to additional models in order to compare to other experimental results of ablation of Si in a vacuum. Here it has been highlighted how, if a rigorous model is used to determine the plumes initial conditions, removing the assumptions made by models accepted within literature, that existing models do not accurately describe the expansion of the plume. Such key aspects being the initial magnitude and distribution of plume parameters, such as temperature and density. From the work on the metal and metal oxides, POLLUX has been shown to match experiment at early time-steps, so it can be argued that POLLUX provides a much more robust description for these initial conditions compared to those used in literature. Yet when used alongside further modelling, it is clear that existing models in literature make assumptions that can be argued to not be valid in cases.

# Chapter 5

# Gas temperature measurements in a RF, low pressure $O_2$ ICP

*This chapter will present comprehensive measurements of gas temperature within the low pressure $O_2$ RF ICP utilised during PE-PLD, with a comparison between novel and conventional diagnostics for means of both characterisation of the plasma, as well a means of benchmarking the validity of each diagnostic under various conditions. Alongside this further investigation of the ICP's gas temperatures has been performed via measurements during pulsed operation, and simulations.*

## 5.1 Calibration of diagnostics

### 5.1.1 OES calibration

The diagnostics utilised within the chapter have been described previously within Section 3.2, and as stated during said description, certain aspects of this apparatus needed to be calibrated before any measurements of gas temperature could be taken; being the wavelength (i.e. spectral) calibration, and the intrinsic line broadening of the system. Firstly to note the settings used on the spectrometer were as follows: a grating of 1199 lines/nm and a blaze of 500 nm, incident onto a 1024 pixel ICCD, able to view 21.31 nm per spectrum and therefore a resolution of 0.02 nm per pixel. Calibration has been performed by operating the ICP at a low pressure (5 Pa) of pure Ar at 500 W, a case close to the deposition conditions of PE-PLD. Spectral calibration was performed with four well known emission lines of Ar

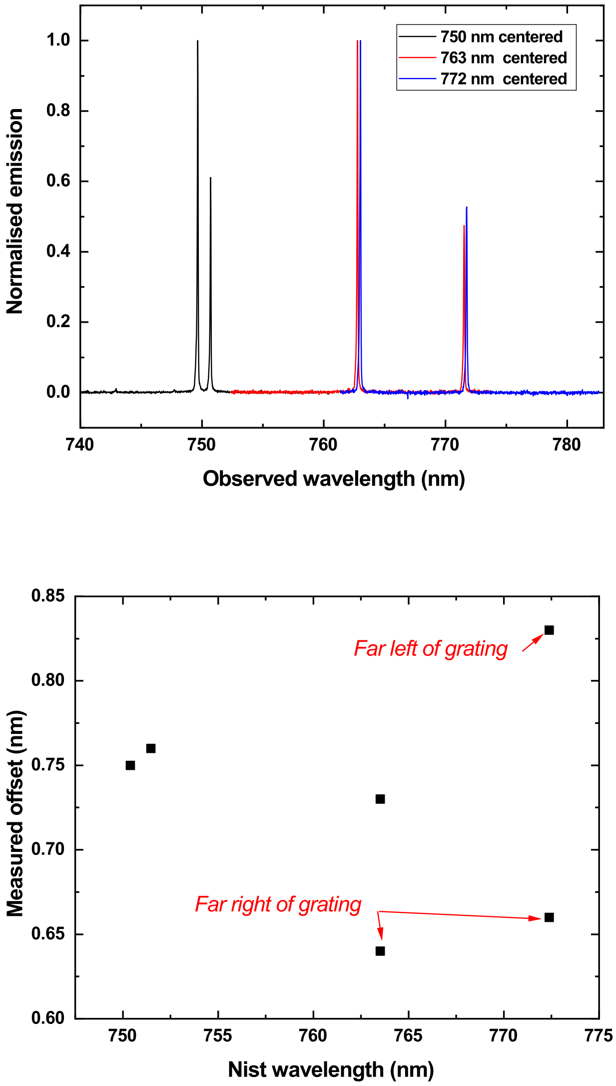

Figure 5.1: Top: Observed Ar lines used for wavelength calibration, centred around different areas of the ICCD. Bottom: Determined shift for each line, as shown top, as compared to true positions taken from NIST [210].

close to the transition of $O_2$ being investigated, being the 750, 751, 763 and 772 nm lines, with each of these four lines observed with the spectrometer at various positions across the ICCD whilst still keeping the desired area of the $O_2$ spectra within the range of view, as shown in Figure 5.1.

It can be seen that as lines are observed to the left of the ICCD, there is a shift of approx +0.85 nm shift from the reference position, and when to the far right a shift of

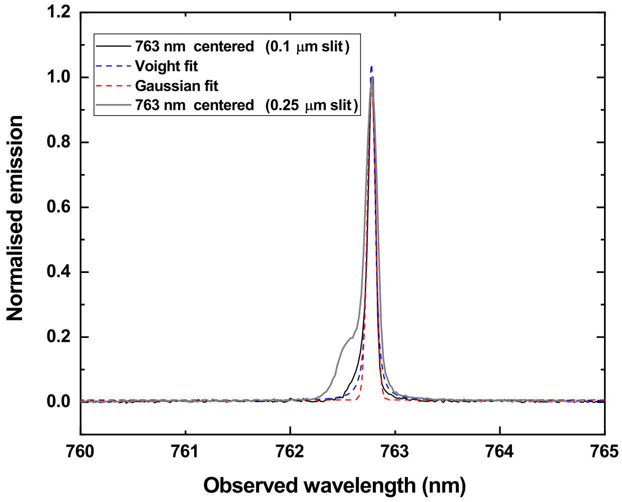

Figure 5.2: Broadening of signal determined by fitting to Ar 763 nm line, with Gaussian and Voight fits. Plus, same line observed however with larger slit opening (0.25 $\mu$m) and effect on the left tail.

+0.65 nm. This non-linear spectral calibration is a common effect with such devices [22], yet unfortunate seeing how the molecular bands of interest span approximately 10 nanometres. In order to account for this effect all emission of interest was centred as far right as possible, to minimise the magnitude of the shift.

Broadening of observed lines was calibrated with the closest line of Ar to the $O_2$ transition of interest (see section 3.2), this being the 763 nm of atomic Ar. For broadening of such lines there are two forms of broadening to consider, first being the broadening of the line from experimental equipment which is typically Gaussian in nature, and secondly the pressure broadening of lines from within the plasma typically Lorentzian in nature [22]. Fits to this line can be seen in Figure 5.2. Best fits were obtained with a Voight function, which is a convolution of both effects, implying that both instrumental and gas pressure broadening are effects important to this system. Final values of the broadening via a Voight function were $0.047 \pm 0.008$ and $0.053 \pm 0.007$ nm for the Gaussian and Lorentzian profiles respectively, which have been used throughout all fitting of molecular lines. However, worth noting is that the peak observed was not symmetric, with the left tail being wider than the right side, which was determined to come from the entrance slit of the spectrometer, as can also be seen in Figure 5.2, where a larger diffraction slit was used and this left tail become much more prominent in structure; the slit width used for measurements going forwards was $0.1\mu m$

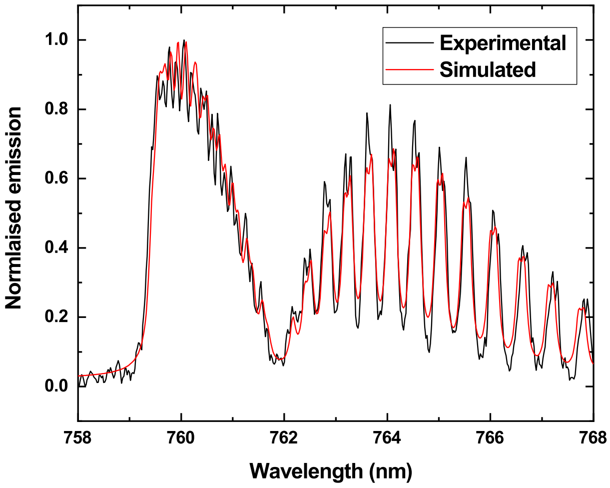

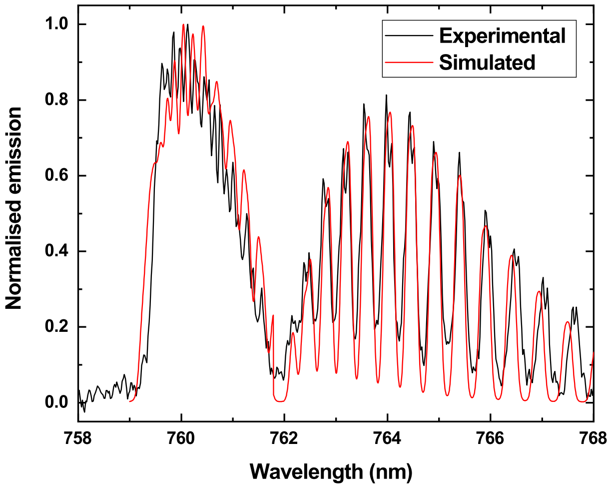

Figure 5.3: Example spectra and fit of the $O_2$ molecular band taken at 50 Pa, 300 W. Top: LabView method. Bottom: PGOPHER method.

Figure 5.3 shows an example fit of an obtained OES spectrum, using both methods of simulation, when using the above line broadening and wavelength calibration. To note for $O_2$, two methods of fitting were used due to difficulties in simmulating spectra which arrises from uncertainties in diatomic molecules (see section 3.2). A good fit can be seen in both cases, with the PGOPHER method deviating slightly at the highest and lowest wavelegnths, yet both with a suitable treatment of the gap between the two branches.

Figure 5.4 shows an example spectra of the $N_2$ molecular transition of interest, when compared to a simulated spectra, again when taking the above wavelength calibration and

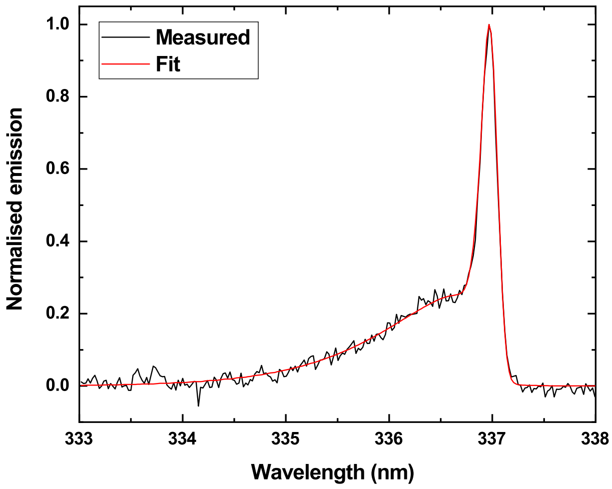

Figure 5.4: Example spectra and fit of the $N_2$ molecular band 50 Pa, 300 W.

broadening effects taken into account. Again, a good fit can be seen, with the higher wavelength spike matching very well, and the fit of the tail matching well within the noise.

Also to consider is the amount of $N_2$ (and Ar for TDLAS, see next section) to be added into the system, which was required to be sufficient enough for diagnostic purposes yet not to interfere with the $O_2$ plasmas dynamics or chemistry. The final amount of each gas used was 10% of $N_2$ as this was the smallest, stable flow of $N_2$ achievable with the use of the mass

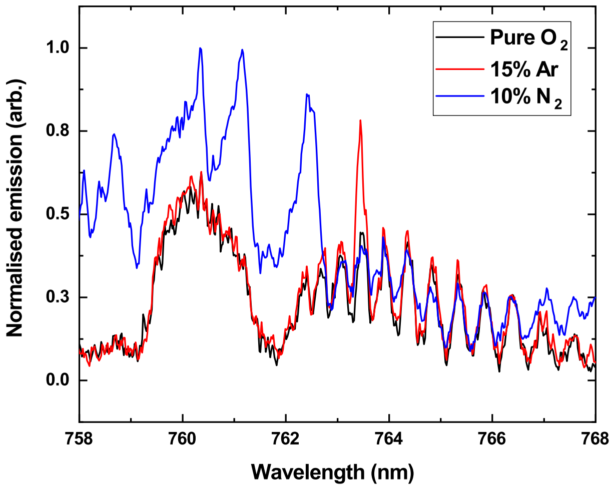

Figure 5.5: Admixtures of tracer gasses used, an the effect on the $O_2$ molecular transition

flow controllers used, and 15% of Ar as lower percentages in some lower pressure cases (e.g. 5 Pa) did not result in a distinguishable absorbance signal; the cause of this is believed to be Penning ionisation between the Ar metastable and molecular oxygen, Equation 5.1 [122].

### 5.1.2 Ar TDLAS calibration

Before use of the TDLAS, over-saturation of the photo-diode needed to be avoided. This was done by using a variety of neutral density, ND, filters of increasing strength, placed before the laser entered the plasma (see Figure 3.3), and the point at which the saturation broadening of the signal levelled. This variation can be seen in Figure 5.6, where it can clearly be seen that at an ND value of approximately 4, that the width of the observed peak become constant. Therefore for all TDLAS measurements performed on this $O_2$ ICP utilised an ND filter value of 4.5. An example of an observed TDLAS signal on the oscilloscope, alongside the determined absorption peak from Equation 3.10 can be seen in Figure 5.7.

$$Ar^* + O_2 \rightarrow Ar + 2O \tag{5.1}$$

In order to investigate if these admixtures would affect the plasma chemistry, in either $O_2$ state of interest, emission of the $O_2$ transition was observed in each case, as shown in Figure 5.5. It can clearly be seen that the Ar admixture did not affect the emission in any case,

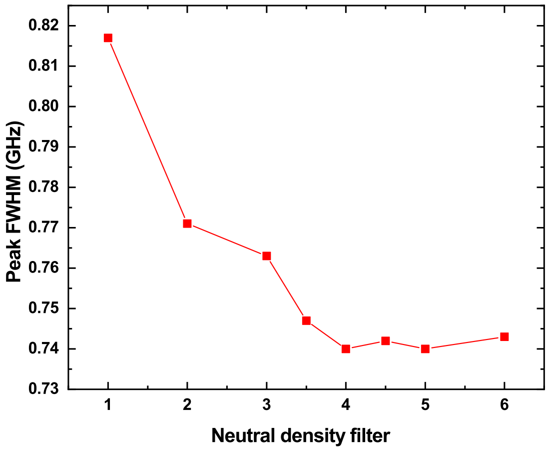

Figure 5.6: Observed peak FWHM with different neutral density filters, for a 50 Pa, 600 W plasma.

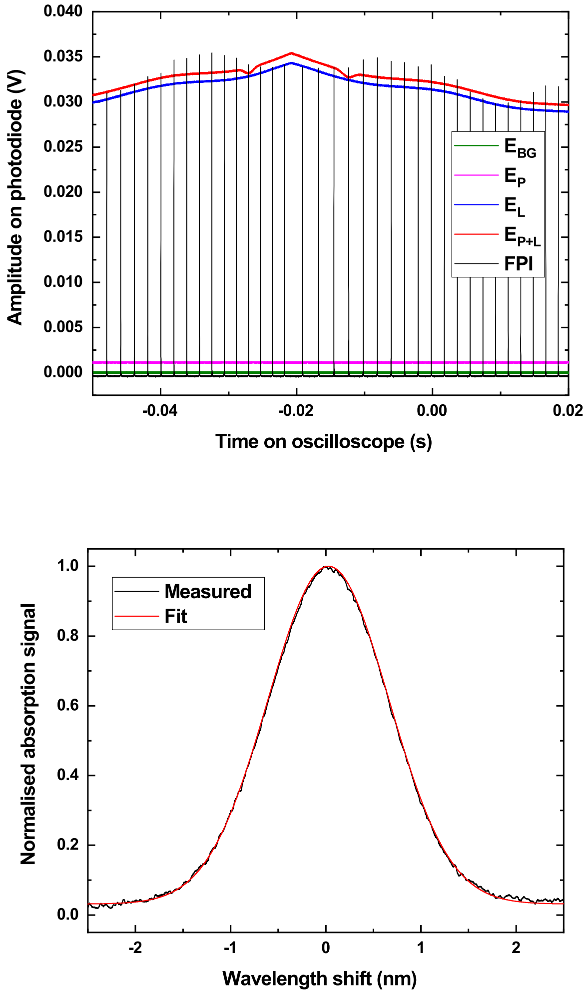

Figure 5.7: Example of observed TDLAS signals with determined fit, at 50 Pa, 600 W.

with only the atomic Ar line at 763 nm observed, and line ratios of the oxygen band not effected, indicating the gas temperature is the same in each case. Although it is harder to distinguish in the $N_2$ case as the left band was encompassed by an $N_2$ emission band, it can be seen that the line ratios between the peaks in the right hand band match that to the case of the pure $O_2$.

## 5.2 Experimental measurements

### 5.2.1 Pressure and power variations

Gas temperature measurements using all techniques outlined above have been performed at 5, 10, 20 and 50 Pa, at powers ranging from 100 to 900 W. The results of which can be seen in Figure 5.8. A thorough discussion on the application of each technique, across all power and pressures investigated, is presented in the next subsection.

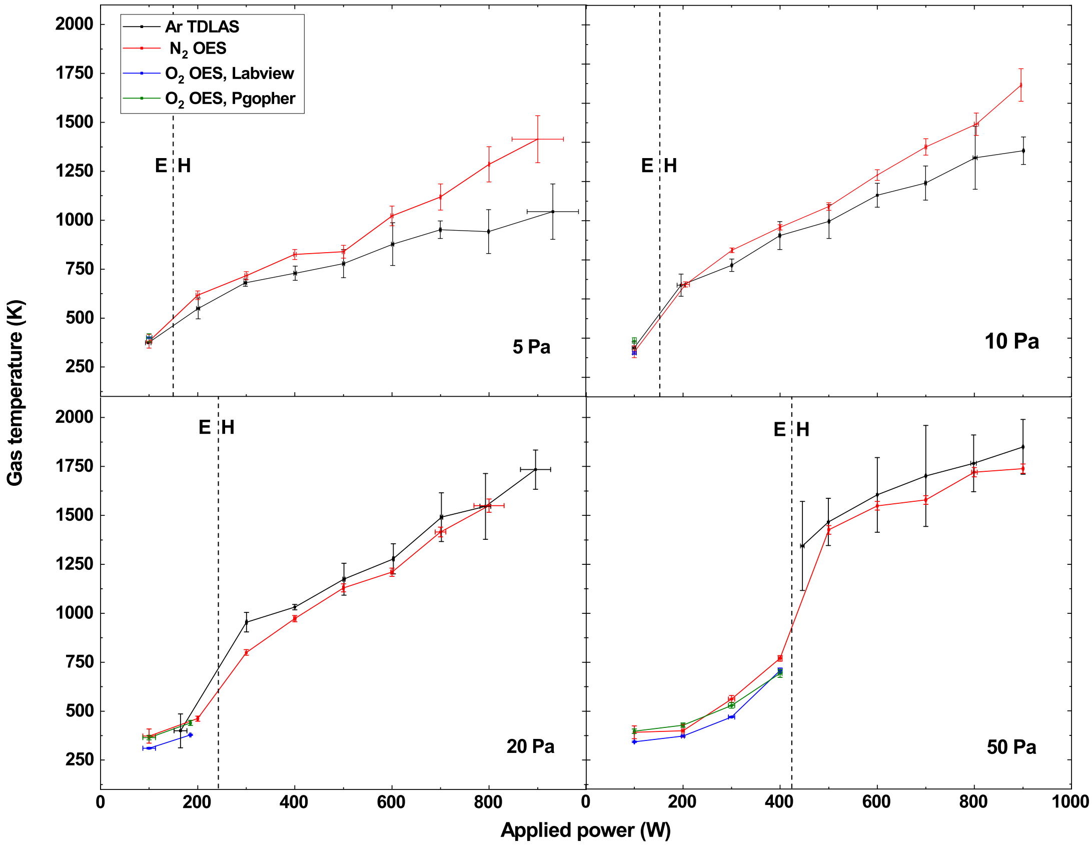

Figure 5.8: Gas temperature as a function of pressure and power determined by all four diagnostic techniques. Vertical dashed line corresponds to observed point of E-H transition of ICP. From top left clockwise: 5, 10, 20, 50 Pa.

It can be seen that the higher pressures reach higher gas temperatures when compared to lower pressures at the same power, with two regions of roughly linear increase in each case, with a large jump between the two regions. This sharp jump, occurring at around 100 to 500 W for different pressures corresponds to the transition between E and H mode of operation, which was observed experimentally by two means, both shown in Figure 5.9. Firstly as the matching unit utilised is tuned best for H-mode operation the magnitude of reflected power dropped dramatically across this transition. Secondly the plasma was visually dramatically different, with the E-mode showing a more pronounced sheath region around the entire top electrode, typical of capacitive coupling; whereas the H-mode was a much brighter, confined region underneath the top electrode typical of inductive coupling.

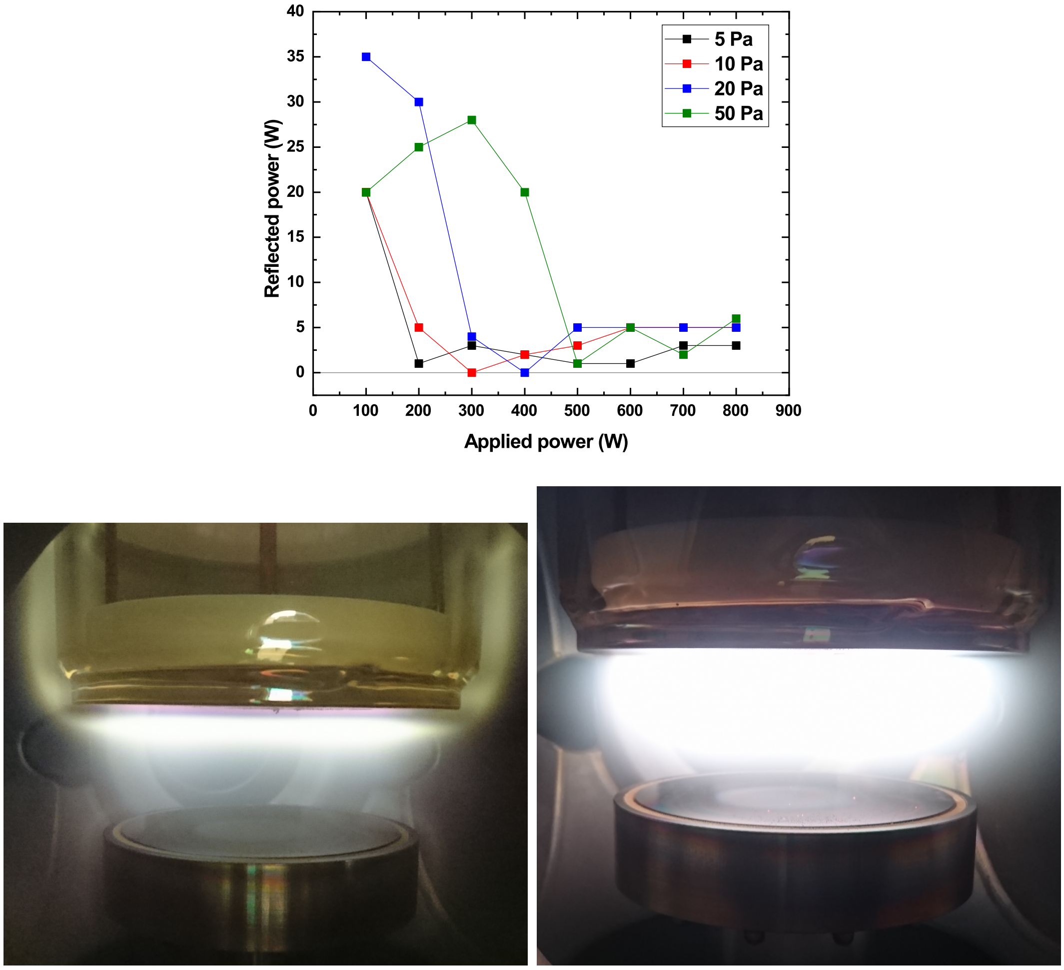

Figure 5.9: Matching and optical characteristics across the E-H transition. Top: Reflected vs applied power. Bottom left: E mode ICP (50 Pa 400 W). Bottom right: H mode ICP (50 Pa 500 W)

In order to understand the trends observed in Figure 5.8 it is important to understand the mechanisms of heating within the plasma, of which there are two. Firstly there is Ohmic heating which occurs due to physical collisions between heavy species, and the second effect comes from the diatomic nature of the gas, and dissociation of the bond between the oxygen molecules which releases thermal energy in correspondence with the dissociation enthalpy of the molecule. Table 3.7 outlines many such processes, including direct dissociation of the ground state molecule, yet also many forms of excitation of higher energy states that then dissociate into various ionic and neutral forms of atomic oxygen.

The power absorbed by the plasma through Ohmic heating, $P_\Omega$, is given in Equation 5.2, where $\sigma_{SH}$ is the conductivity of the plasma given by the Spitzer-Harm model in Equation 3.22, and $E$ is the external electric field applied to the plasma [50].

$$P_\Omega = \frac{1}{\sigma_{SH}} E^2 \tag{5.2}$$

As $\sigma_{SH}$ increases linearly with plasma densities, i.e. higher electron densities leading to a more conductive plasma, it can be determined that the effect of Ohmic heating is reduced at these higher density conditions, due to the relation shown in Equation 5.2.

Therefore as the plasma pressure and power is increased as shown in Figure 5.8, it can be argued that Ohmic heating becomes less effective, leading to lower gas temperatures. Thus the observed increasing trend indicates the dominant heating effect must be the dissociative heating. This also helps to explain the jump in temperatures as the plasma transitions into H-mode, as it is a well known that within ICP's containing molecular gases such as $O_2$, there is a sharp increases in dissociation degree of said molecules within the H-mode [60]. In some cases, such as the works of Zaplotnik et al [211] this increase in density of atomic oxygen was a factor of 2 within the H-mode, with the jump in temperatures observed here are also a factor of 2. Indeed, this may be a too simplistic of a comparison, as the density of other species must be considered, but it helps to provide further evidence that the nature of the temperatures observed here are of a suitable order of magnitude.

### 5.2.2 Comparison of diagnostics

Also of important note within Figure 5.8 are the trends observed between the diagnostic techniques. Before these are discussed uncertainties on these measurements will be clarified; the Ar TDLAS measurements have somewhat significant uncertainties of up to approximately 15% at the higher powers (i.e. around 500W and above), obtained from the standard deviation of repeat measurements (between 3 to 5). This is due to the individual measurements having a very small uncertainty on each value (approximately 0.5%), obtained from the wavelength calibration of the Doppler broadening, in turn determined from the resolution of the FPI which was 7.5 MHz out of a free spectral range of 1.5 GHZ (see section 3.2). Said uncertainties were far smaller than the deviation of repeat measurements, and therefore multiple measurements were taken. Deviations on each measurement resulting from a combination of the line integrated volume viewed by the laser, in combination with the unknown distribution of Ar species throughout the plasma during each measurement. Uncertainties on OES measurements are much smaller than the TDLAS standard deviation, as these are the uncertainties on a single fit, as the measurements were much more reproducible with deviations being insignificant compared to the errors on a fit, which is as a result from the OES seeing the entire plasma bulk.

When using the $O_2$ OES to determine the gas temperature, it can be seen that the data could not be collected within the H-mode regime. This is due to the signal reducing dramatically within H-mode, and was indistinguishable from the noise at the much higher powers. Reasoning for this is that the upper state, $O_2$(b), is believed to be heavily quenched by atomic oxygen [212–214], see Equation 5.3, taken from Table 3.7. The significant increase in atomic oxygen density that has been observed in $O_2$ ICP's would therefore result in a decrease in population of this upper state, therefore reducing the observed signal of the natural decay to the ground state as desired.

$$O_2(b^1\Sigma_g) + O(^3P) \rightarrow O_2(a^1\Delta_g) + O(^3P) \qquad k = 8 \times 10^{-14} cm^3 s^{-1} \tag{5.3}$$

It was considered that this loss of signal may also be due to dissociation of the $O_2$ molecules due to heat, however based on the enthalpy required and for each pressure and temperature, only approximately 3.5% of the molecules will have dissociated due to heat, which is insufficient to solely explain the complete loss of signal. There have been reports of analysis of the $O_2$(b) metastable within the H-mode of an $O_2$ ICP [60], yet the diagnostic used was a highly sensitive microwave interferometry setup, being able to detect lower densities due to actively probing the plasma, plus the chamber used was fairly different in geometry to the GEC reference cell used here, and measurements reported also barely enter the H-mode of operation. In the E-mode regime, the $O_2$ OES matched up almost within error to the $N_2$ OES and the Ar TDLAS, with this slight discrepancy most likely due to the poorer matching of the plasma in in E-mode conditions.

Within the H-mode there is a strong agreement between the $N_2$ OES and Ar TDLAS at the higher pressures (20 and 50 Pa), whereas in the lower pressures (5 and 10 Pa) there is an increasing deviation between the two techniques, which is likely due to a combination of two effects. Firstly, it is known that there is likely to be a spatial variation of the temperature vertically between the electrodes [95] (also discussed in the next section), which could affect the difference between the line integrated volume observed by the laser and the overall volume average of the OES between pressures. It can be seen in Figure 5.10 that in the lower power E-mode, the plasma was focused more around the top electrode just above the incident line of the laser. At the higher powers, where there was a stronger deviation, the plasma was more concentrated within the chambers centre, however in both cases clearly covering the lasers path. It is unknown and hard to quantify what the distribution of the Ar species throughout the chamber is, and therefore this affect cannot simply be ignored. Secondly what is also likely to be playing a role is the aforementioned assumption that the population distribution of electrons within states of the molecule, which as stated in Section 3.2 is required for the

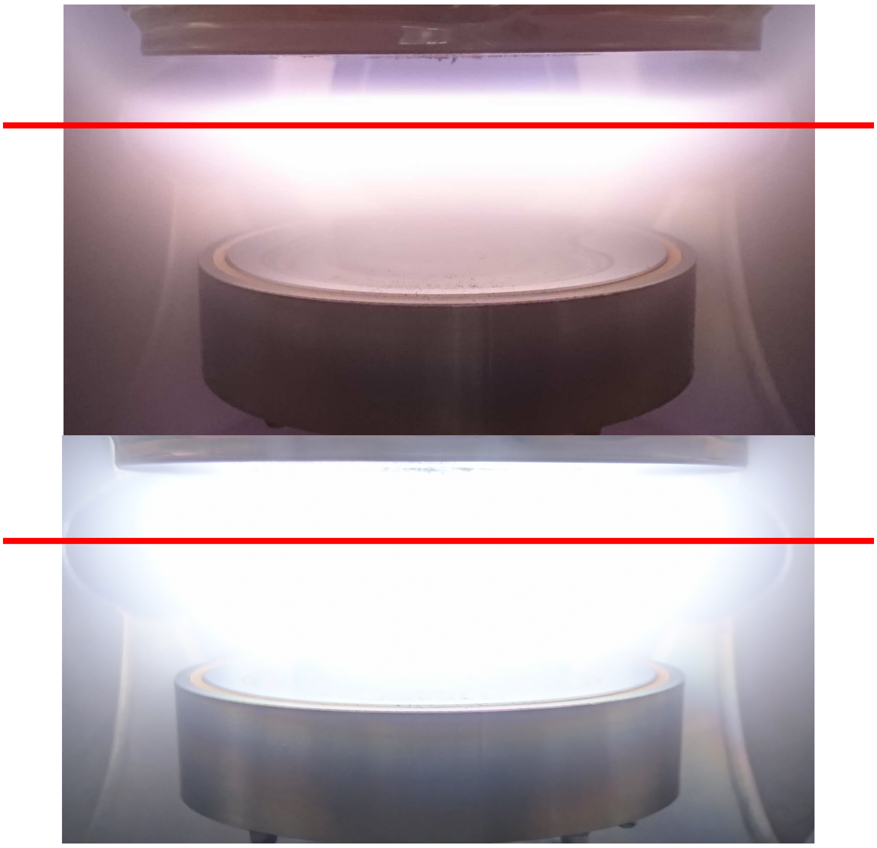

Figure 5.10: Approximate line through with TDLAS was incident within various plasma conditions; Top: 10 Pa 100W, Bottom: 10 Pa 700 W.

equations through which $T_{rot}$ is obtained. This may not be valid in these low pressure cases due to this distribution requiring a sufficient number of collisions not present at the lower gas pressures, which in turn comes from a sufficiently high density of heavy species, perhaps not the case at these lower pressures.

In conclusion it can be seen that each diagnostic used is best suited for different plasma conditions. The $O_2$ based OES, being the most desirable technique due to no admixtures of any gases being required, works well within the E-mode case yet it not suited for the H-mode cases, where increased density of species such as atomic oxygen quench the upper state of interest. OES on $N_2$ was the only technique that provided a signal distinguishable from noise in all conditions. However in the lower pressure, higher power cases, deviation from the Ar TDLAS was seen. Indeed the Ar TDLAS could be the technique that is deviating from the true value, however this is most likely due to the assumptions of the distribution of upper states within $N_2$ not being valid at these low pressure conditions. Ar TDLAS was not suitable in the highest pressure, lower power cases, due to reduction in the signal from Penning reactions with the $O_2$ molecules. So it can be argued that, although possible, great care in choice of diagnostic must be taken when performing gas temperature measurements under such plasma conditions, something that has yet to be quantified within literature.

## 5.3 Pulsed operation

In addition to the conditions measured experimentally in the previous section, temporally resolved measurements of the gas temperature have been performed, in order to further characterise the gas heating of the plasma in pulsed operation used during PE-PLD. As during its initial development the plasma was pulsed in order to reduce the overall temperatures that were high enough to melt the pure copper target [2]. However this effect of the pulsing was not fully quantified, and also can be of interest to other applications of ICPs, commonly used throughout industry. These measurements have been performed via the $N_2$ OES method, as this worked throughout both modes of the ICP, and was experimentally much easier to synchronise than the TDLAS. It is assumed that this technique is valid in pulsed cases used here as the natural lifetime of the upper $N_2(C^3\Pi_u, v' = 0)$ state is 36.6 ns [215], and the shortest pulse time measured here being 100 ns, and therefore an assumed sufficient population of the upper state. Results of this can be seen in Figure 5.11.

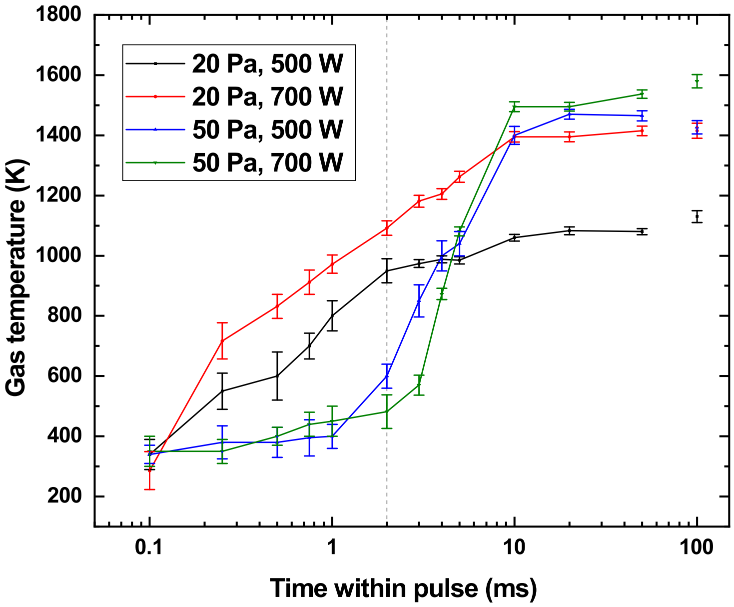

Figure 5.11: Gas temperature for a variety of conditions, as a function of time within the pulse, determined via the $N_2$ OES technique. Dashed line corresponds to limit of pulsed matching.

In Figure 5.11 it can be seen that there is a clear trend between the pressures; the lower pressure 20 Pa has one spike in temperature of approx 400 to 600 K (dependant on power) almost instantaneously at approximately 200 ns, upon which there is a linear increase up to the 10 ms point where equilibrium is reached. The higher pressure case of 50 Pa however take a much longer time, approx. 1 ms, to spike up to the point of equilibrium, with this increase again being somewhat linear, however of a much steeper gradient. What is being observed here is, similar to Figure 5.8, an E-H transition within the plasma; it is known that for an ICP to transition into H-mode, a high enough electron density much be present for sufficient current to be induced within the plasma; this electron density not being present at the instantaneous start up of the plasma [50].

In all cases the plasma was pulsed at a rate of 10 Hz, as done within PE-PLD, yet to experimentally obtain Figure 5.11 there are two regimes, indicated by the vertical dotted line at 2 ms.To the right of the line, e.g. at longer time steps, matching the pulsed plasma was not an issue so results at these longer time steps were taken with a plasma on time of that shown, with the emission collected throughout the entire pulse collected, i.e. on for 10 ms, off for 90 ms. Below 2 ms matching the plasma was not possible, therefore the plasma was pulsed for 2 ms (off for 98 ms), with the light collected from the beginning of the pulse for the required amount of time, i.e. on for 2 ms with the first 1 ms detected, then off for 98 ms. Timing was controlled by the external DDG to trigger the plasma and the camera, with the exposure time controlled by the internal Andor software and set to the values used within Figure 5.11. The data point at 100 ms corresponds to the continuous operation, taken from Figure 5.8.

As discussed when describing Figure 5.8, the increase in measured gas temperature corresponds to the H-mode of the plasma. Therefore this increased time taken for the temperature to rise to its equilibrium in H-mode for the 50 Pa case, is based upon the longer time required for a sufficient electron density to be produced during the capacitive E-mode, to allow for this transition into H-mode. Yet this effect could also have arisen from the response time of the matching network, the effect of which is currently of key interest in the design and control of matching networks. This is due to the matching network used being optimised for H-mode operation, and therefore at early stages within the pulse where plasma parameters are quite different (e.g. lower temperatures and electron densities), it is likely inefficient matching leads to poor energy coupling at the start of the pulse in the 50 Pa case. This could not experimentally quantified, due to the matching unit being wired directly into the powered coil, and therefore no method of analysing reflected power over short time steps could be used, e.g. a current probe in series with the cabling attached to a high speed oscilloscope.

This affect of matching within pulses has to date only been presented within work of simulations and electron temperature measurements within $Cl_2$ based plasmas [216, 217]; and yet to be described by such an observable effect such as gas temperature as shown here. Temporally resolved measurements of oxygen plasma gas temperatures have so far only been reported in glow discharge tubes at approx 100 Pa, in the works of Macko et al [218], and Hubner et al [219], where a rapid increase was seen followed by an equilibrium, somewhat similar to the what is seen here, yet indeed without any indication of a mode transition based on the experimental set-up.

What can also be inferred from these results is that the gas temperature of the plasma is able to return to (approximately) the initial temperature, even within the cases of longer pulse time and short off time. An affect that will be discussed in terms of applications in the next chapter where although the temperatures reached are very high, various sensitive materials such as polymers can survive the deposition environment.

## 5.4 Gas temperature simulations

The same conditions of continuous operation have been simulated within HPEM (Section 3.5), with Figure 5.12 showing the spatial profile of gas temperature within the chamber for 300, 600 and 900 W at 5 Pa, and an example 10 Pa 600 W. It can be seen that there is a hot central structure between the electrodes, that varies quite steeply vertically, but is quite constant horizontally until the edge of the electrodes. This profile does not change dramatically in shape with power, however with increasing pressure becomes more concentrated within the centre of the electrodes, due to the increased number of collisions confining the

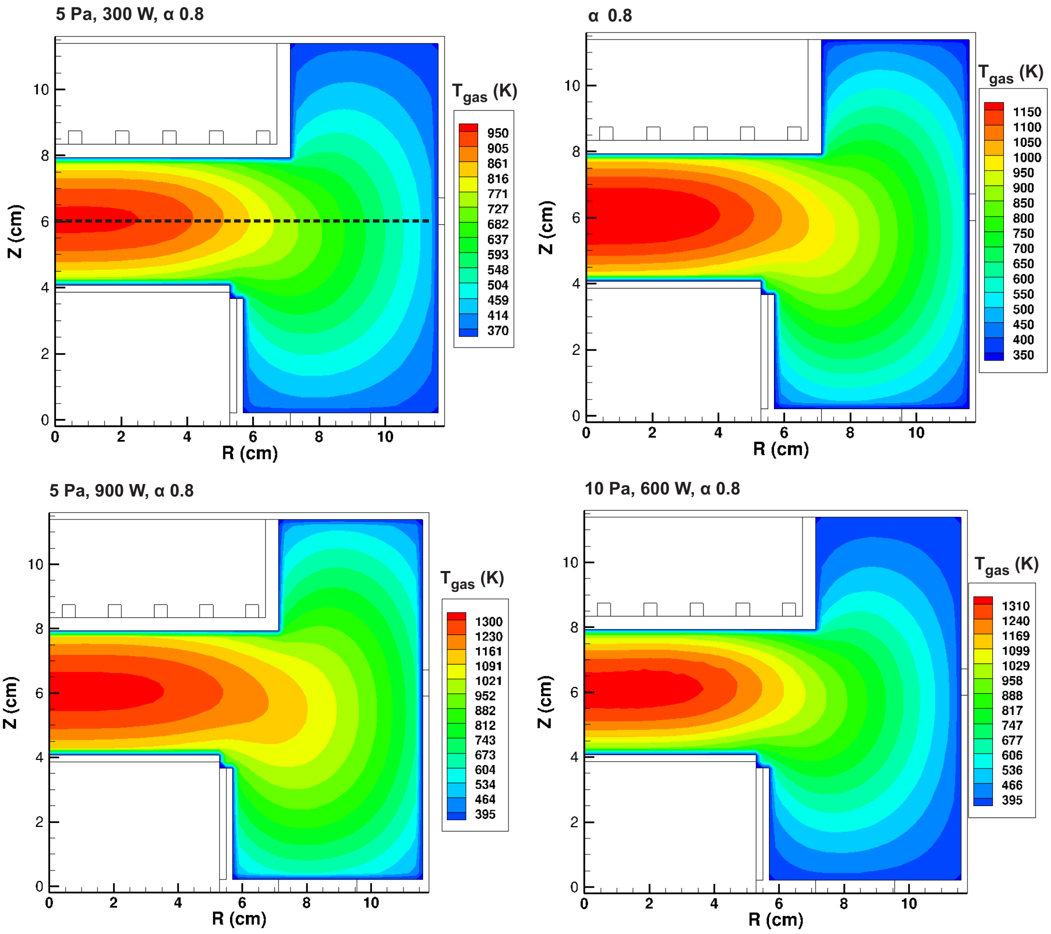

Figure 5.12: 2-D profiles of $T_{gas}$ from a power and pressure variation from HPEM for a 5 Pa $O_2$ RF ICP.

plasma and the shorter mean free path of plasma species [50].

For comparison to the TDLAS experiments, a cross section of the simulation comparative to the line integrated volume seen by the laser is used. This line out is demonstrated by the dotted line in the case shown in Figure 5.12, with these profiles shown in Figure 5.13. An average of these entire profiles has been performed in order to compare to experimental results, and also shown within Figure 5.13. It could be argued that a simple average may not be the correct method of further analysing these results, and instead some form of weighting performed to the density profile of Ar species, however this was not considered as the chemistry set utilised here was pure $O_2$. Also as shown in Figure 5.5, the gas chemistry was

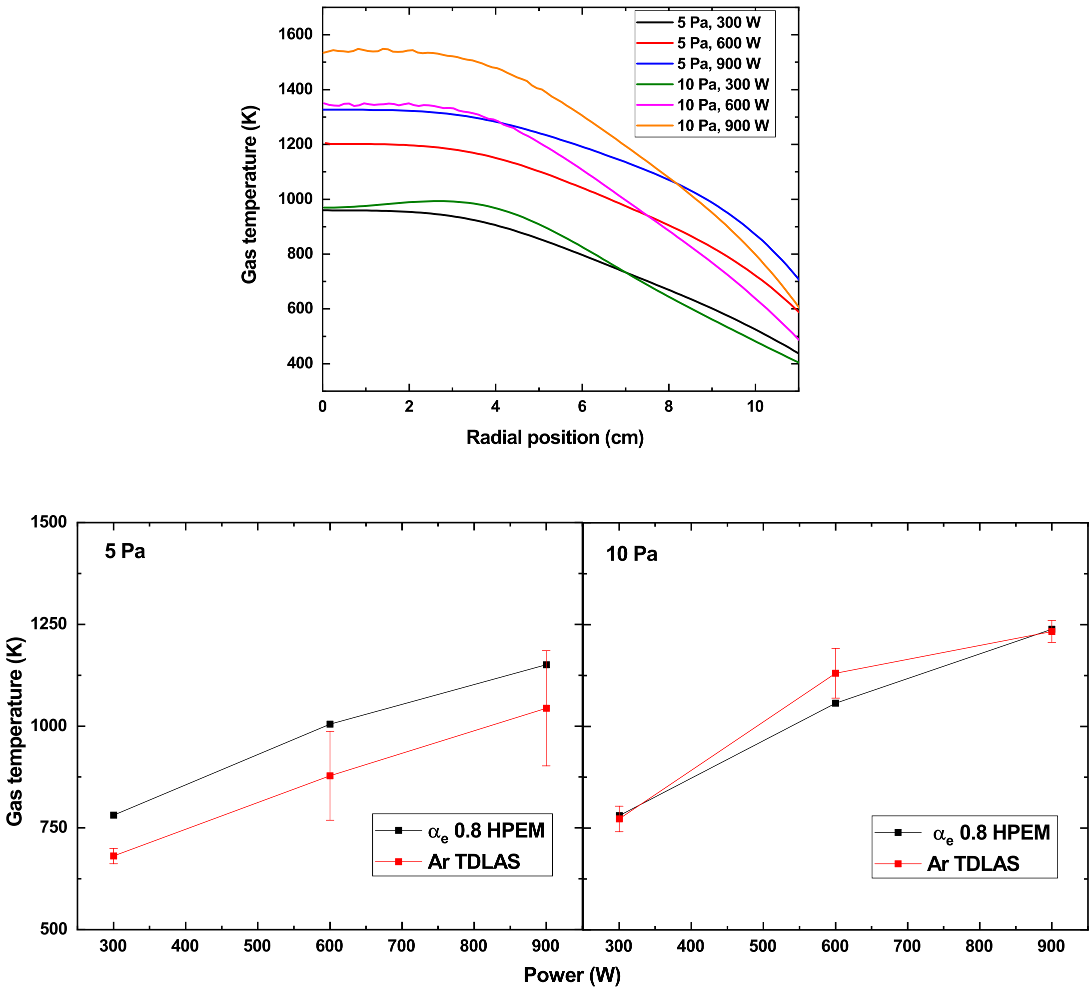

Figure 5.13: Line outs and determined averages of $T_{gas}$ from HPEM

not influenced heavily by these admixtures and therefore assumed to play a negligible effect in these profiles.

Within Figure 5.13 in the 10 Pa case there is a very close agreement between the HPEM values and the TDLAS measurements, whereas for the 5 Pa case there is a match at higher powers, with a small deviation at 300 W. Therefore simulations can be argued to have successfully modelled the system over the range tested, however it is clear that there is a different aspect also affecting the temperature, other than the pressure and power. This is the aforementioned thermal accommodation coefficient, $\alpha_E$. The simulations presented above use a value of $\alpha_E$=0.8, i.e. a fairly efficient transfer of heat to the walls, chosen as it is shown in the works of Gibson et al [95], that under similar plasma conditions to the ones presented, here that $\alpha_E$ varied strongly between 0.1 and 0.5, yet began to level off at

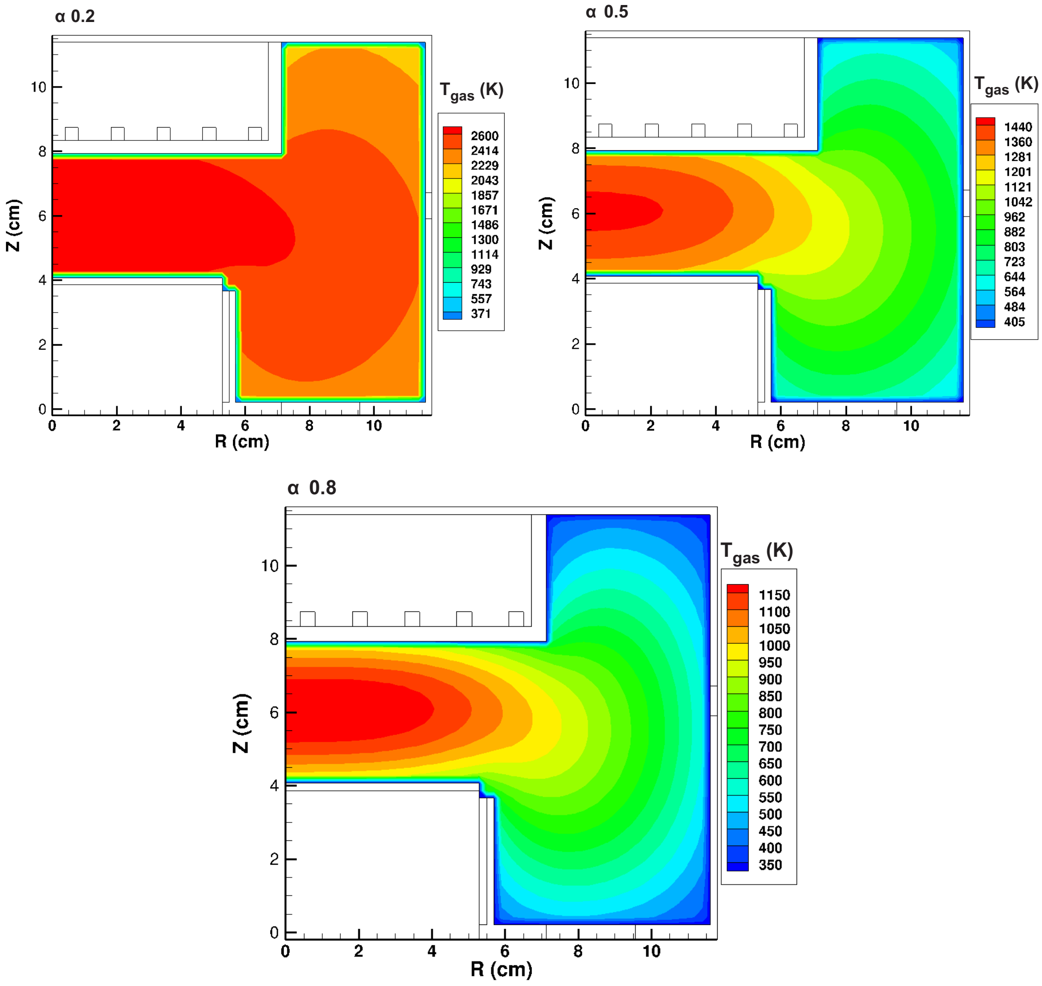

Figure 5.14: Gas temperature from a variation of $\alpha_e$ for 5 Pa 600 W.

values higher than this, so 0.8 was chosen as to lay within this regime where $\alpha_E$ was initially believed to not vary significantly. A variation on this affect for a 5 Pa, 600 W case is seen in Figure 5.14.

It can be seen that a lower value of $\alpha_E$ leads to a few key effects; Firstly is that as it was mentioned in Section 3.5, $\alpha_E$ affects the thermal conductivity of the nearest cell to the plasma wall. So it can be seen in Figure 3.5, especially between the electrodes, there is a much steeper gradient of gas temperature immediately at the walls. This leads to a much hotter gas temperature throughout the chamber, and it is this profile that is perhaps the most important affect. When analysis the mean gas temperature of the entire chamber, done so as it is shown $\alpha_E$ affects the overall profile of the plasma, clear differences can be seen, as shown in Figure 5.15.

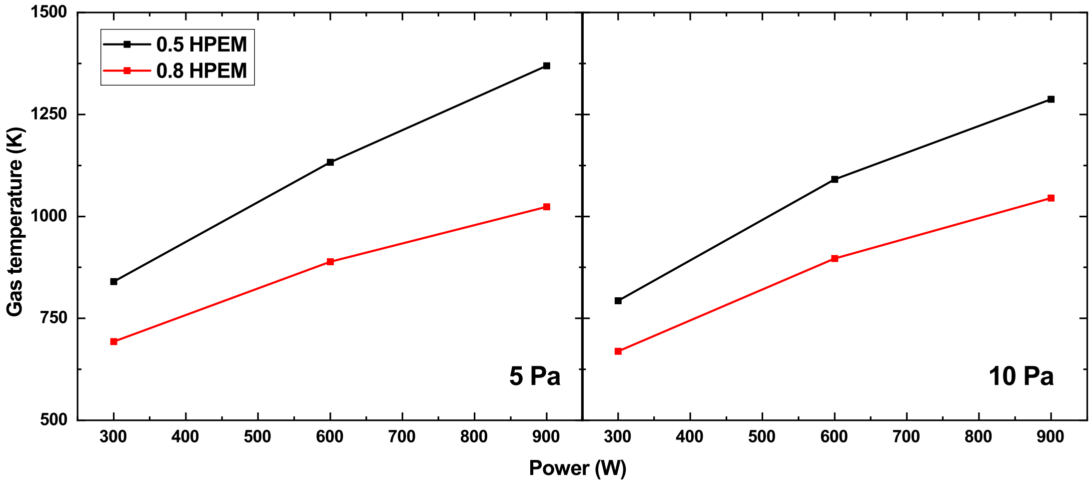

Figure 5.15: $T_{gas}$ as determined from the total reactor average from HPEM, with varying values of $\alpha_E$ for 5 and 10 Pa.

Figure 5.15 shows that between pressures, when using the same assumption of the thermal accommodation coefficient, that the temperature does not change to a significant degree. However when using a different assumption for alpha at a higher pressures, the simulated temperatures begin to deviate, as they do in experiment. Specifically when a value of 0.5, i.e. a more inefficient transfer of heat to the walls, is used for the higher pressure of 10 Pa. This indicates that although in higher pressure cases with a increased density of plasma species, there is a less efficient heat transfer of heat to the walls.

Reasoning for this is complex; It has been shown via various analytical models that within oxygen plasmas, effects such as heat transfer to the walls is much more efficient on walls where additional oxygen species are also present [220–222], an effect also seen in works

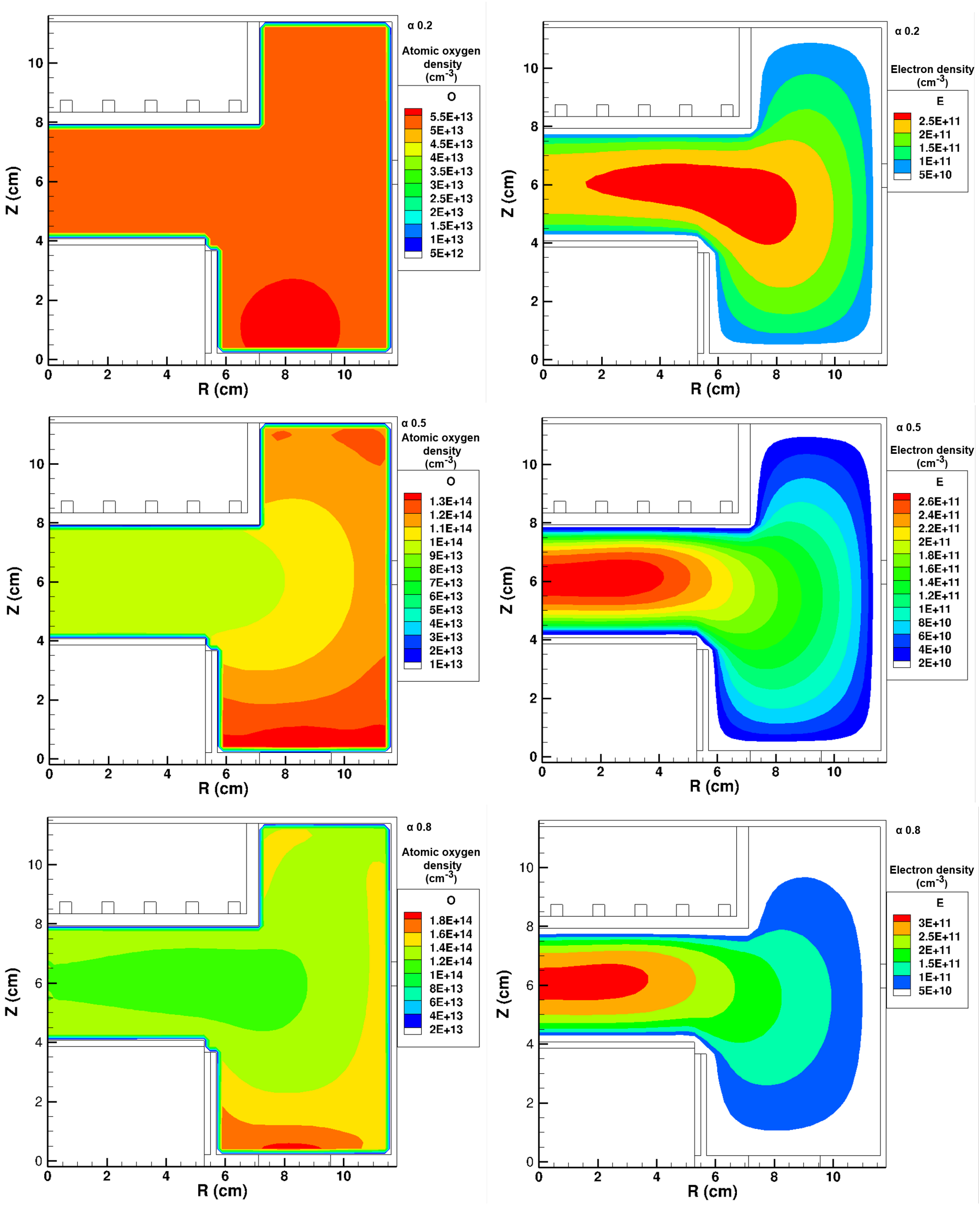

Figure 5.16: 2-D profiles of left: $O$ and right: $e$ densities for varying $\alpha_E$ a 5 Pa $O_2$ ICP within HPEM. Values of $\alpha_E$: Top 0.2, middle 0.5, bottom 0.8.

with other gasses, where its direct relevance to $\alpha_E$ is investigated [223, 224]. An increase in these additional species typically occurs at higher pressure plasmas where more species would be present in order to travel to the walls, and from this one would assume that a higher pressure case would be more efficient at transferring heat to the walls, which is the opposite to what is observed here. Plus one needs to look as to how $\alpha_E$ is defined, such as in Equation 3.36, where the mean free path, $\lambda_{mfp}$, is used to define $\alpha_E$. Yet from this equation a shorter $\lambda_{mfp}$, which occurs at higher pressures, assuming the gradient defined at the walls is constant, would still lead to a larger and more efficient $\alpha_E$.

Therefore additional aspects need to be considered, firstly is that some works within literature show that $\alpha_E$ is not only *not* constant as shown here, yet is indeed dependant on the gas temperature [225–227]. Plus, this varying $\alpha_E$ may in fact have something to do with how $\alpha_E$ is observed to affect the densities and profiles of various species within the plasma, as shown in Figure 5.16. Here it is seen that such reactive species important for wall reactions such as atomic oxygen, O, and the electron density, varies strongly with $\alpha_E$, both in terms of profile and overall magnitude. Therefore perhaps what is needed to implicitly predict and model gas temperatures in all cases of such an $O_2$ ICP is spatially resolved measurements of such reactive species, in order to reduce the degrees of freedom within the model, to help to correctly model an $\alpha_E$ that is dependant on position within the chamber, and perhaps how this would need to change per iteration as the density of species converged; instead of a simple dependence on pressure as shown here.

## 5.5 Conclusion

This chapter has presented absolute, benchmarked gas temperature measurements of a low pressure $O_2$ RF ICP, relevant to PE-PLD yet also other industrial processes. Temperatures were seen to have a linear increase in temperature within the E-mode of the plasma, reaching a maximum of 600 K in the highest pressure cases, but then a jump of approximately a factor of 2 into the H-mode regime, reaching maximum temperatures between 1200 and 2000 K dependant on pressure. This jump in temperatures across the mode transition has been related to the dissociative heating of the plasma, with the effects of ohmic heating being reduced due to the plasmas increased conductivities.

The most desirable diagnostic technique, due to no need of admixtures, being the OES of the $O_2$ metastable was found to break down in the H-mode regime of the ICP operation, due to heavy quenching of the upper metastable state with atomic oxygen, yet within the E-mode of operation did match OES of the $\mathrm{N}_2$ admixture or TDLAS of Ar. Said other techniques matched each other well throughout the E-mode, and within the higher pressures (20 and 50 Pa) a match was also seen in H-mode as well, yet a lower pressures there was a deviation between the $N_2$ OES and Ar TDLAS, most likely due to the assumptions of population distribution breaking down due to lack of collisions in these lower pressures within the case of the $N_2$ OES.

Temporally resolved measurements of gas temperatures have also been presented, performed within the same plasma conditions yet with power supplied via pulses, at a rate of 10 Hz. All conditions were found to reach a point of equilibrium after approximately 10 ms, yet the time taken to reach this point varying strongly on gas pressure, due to the increased electron density required to transition into a H-mode at the higher pressures. It was seen that 20 Pa transitioned to H-mode almost instantly, at 100 $\mu$ s and had a fairly constant increase of temperature over time, whereas the 50 Pa case took much longer, taking up to 1 ms, at which point the temperature spiked to its maximum almost instantly.

Also simulations have been presented, which can be seen to match the measured temperatures at the lower pressures of 5 and 10 Pa. Also the importance of the effect of wall interactions, particularly the efficiency of heat transfer to the walls affects not only the temperatures reached, yet also the density profile of many species within the plasma.

# Chapter 6

# Analysis of films deposited by PE-PLD

*Results presented in this chapter focus on analysis of films deposited by PE-PLD, including ZnO,* $Cu_2O$*, and* $Al_2O_3$ *on substrates including Si,* $SiO_2$*, steel, and plastics, in terms of parameters such as composition as a function of depth, and crystal structure. This is not only to further the understanding of the physical processes with PE-PLD, but also to explore its versatility and range of applications.*

## 6.1 Zinc Oxide films

Motivation behind the desire to create zinc oxide films has been discussed within Section 2.7, however it is important to reiterate one key fact. Although Zn is chemically similar to Cu, due to being next to it on the periodic table, Zn has a more restrictive limits in forms of compounds that can be deposited, as there is only one form of chemically stable compound, which is ZnO. Conditions for the deposition of ZnO films were initially assumed to be similar to that of the previously deposited Cu films, with the analysis of these films presented in the following section.

### 6.1.1 Composition

A pure Zn target was ablated within a range of oxygen ICP conditions, with the results from EDX being shown in Figure 6.1, along with the results from $Al_2O_3$ (discussed shortly), results for the copper oxide films are taken from previous work on PE-PLD [2]. EDX was

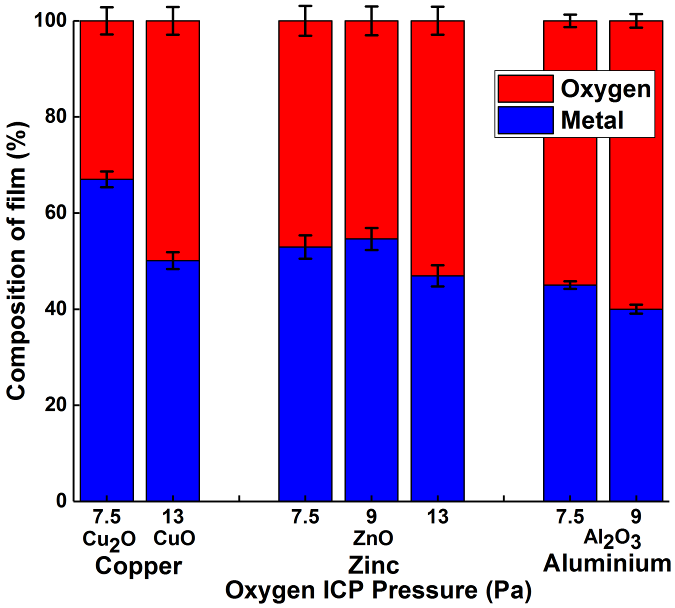

Figure 6.1: Composition of films deposited with PE-PLD under a varying pressures of ICP oxygen plasmas, with pure metal targets.

performed on films that were deposited for 1 hour, with a beam energy on 5 keV, which resulted in an $R_{KO}$ depth of approximately 100 nm, much smaller than the thickness of the film which was assumed to be 300 nm based on the 10 nm/min deposition rate; therefore no signal was obtained from the oxygen within the $SiO_2$, so no interference of the oxygen within the substrate would occur. Relevant emission lines analysed observable at this beam energy were the Oxygen $K_\alpha$ line at 0.52 keV, and the zinc $L_\alpha$ line at 1.01 keV [228], as shown in Figure (6.2). It can clearly be seen that the deposited zinc oxide films at 7.5 and 9 Pa take a 1:1 ratio between metal and oxygen within the uncertainties on each measurements, with the higher pressure of 13 Pa beginning to deviate from this ratio to be more oxygen rich. Uncertainties are taken from repeat measurements across multiple films and locations across each film.

Reasoning for zinc oxide forming this phase is under these conditions is two fold, firstly as mentioned being that there is only one stable phase of zinc oxide, being this observed 1:1 ratio of ZnO. Plus, when combined with the more readily ablatable nature of Zn under these conditions (see Section 4.1.1), there is sufficient density of both oxygen and metal atoms in the lower pressure conditions for sufficient reactions to take place and form the

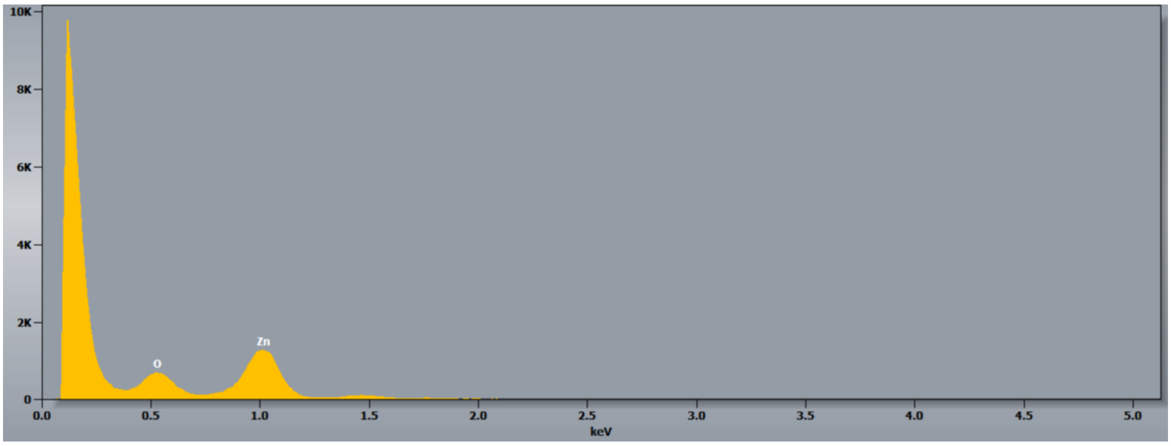

Figure 6.2: EDX spectra of ZnO film on $SiO_2$, deposited at 7.5 Pa, 500W, for 1 hour on $SiO_2$ substrate.

stable 1:1 phase. To note, there are other phases of zinc oxides that can form, namely zinc peroxide, $ZnO_2$, however these are highly unstable phases, typically observed in combustion and explosive environments [229], so it is highly unlikely these phases form and even if they do within the gas/plasma phase, do not survive long enough to successfully form a lattice within the film.

### 6.1.2 Structure

Structure for ZnO films deposited has been determined by the use of XRD, with these films deposited at 7.5 Pa, 500 W, for 1 hour, again resulting in approximately 300 nm thick films; These were deposited on substrates of $SiO_2$ as before, yet also single plane (1 0 0) Si to both gain a better understanding of how seeding layers/substrates effects film growth within PE-PLD, and also for application purposes due to the wide spread use of Si in the semiconductor and electronics industry. Results of these can be seen within Figure 6.3.

For the $SiO_2$ substrate plot, the substrate peak can clearly be seen as a wide, and therefore small grain size, peak centred around $21^o$, which corresponds to the well known (1 0 0) plane [231]. The sharper peak to its right at $56^o$ corresponds to the (1 1 0) plane of ZnO as seen on ICDD CARD 2300112 [230]. This (1 1 0) plane of ZnO is known to be a higher energy plane [232], seen in deposition techniques that result in high densities of precursors, such as other PLD based techniques [233, 234], some liquid based chemical processes [235, 236], and high pressure techniques [237]. This also matches what has been

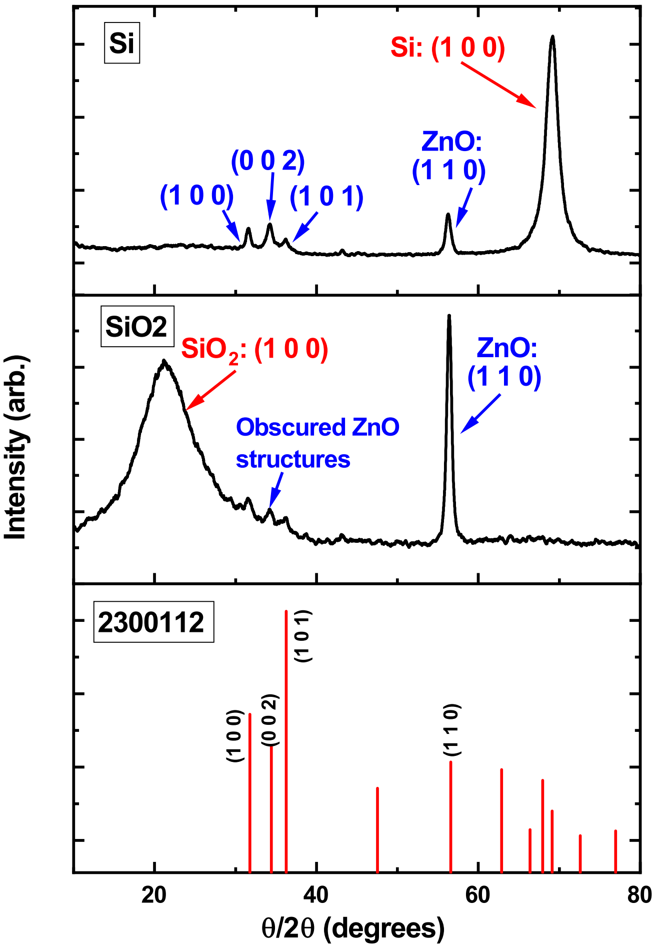

Figure 6.3: XRD spectra of ZnO deposited on different substrates, Top: $SiO_2$. Middle: Si. Bottom: ZnO ICDD card 2300112 [230].

seen with the copper oxide deposits from PE-PLD, where higher energy planes of CuO were seen [2]. Growth of such high energy planes is possible with PLD, as this high density of ablated material results in as a non-epitaxial deposition method (see Section 2.4). Therefore the deposited islands and grains will begin to form higher density planes before diffusion and bonding to substrates or sub-layers become dominant, which could reduce the likelihood of these high density planes forming.

This effect can be seen much more clearly within the deposits on single planar Si, also within Figure 6.3. The sharp Si peak at $69.1^o$, corresponding to (1 0 0) Si on card [238] from the substrate. Again, the high energy peak of (1 1 0) is seen at $56^o$ as before on $SiO_2$, however three additional peaks can be seen at $31.4^o$, $34.3^o$ and $36.2^o$, corresponding to the (1 0 0), (0 0 2), and (1 0 1) peaks of ZnO respectively; these peaks can also be somewhat seen on the $SiO_2$ substrate however are obscured by the peak of the substrate itself, therefore showing a polycrystalline film.

As discussed, such a polycrystalline structure comes as a result of the non-epitaxial nature of PE-PLD, due to the high density of material depositing onto the surface allowing the film to grow in a structure determined by itself and not the substrate. The size of these grains can be determined via the Scherrer equation, Equation 3.14, which has been calculated for each ZnO peak observed, and shown in Table 6.1. Here it can be seen each plane grows in grain sizes of approximately the same size of around 3 nm, yet what is interesting to note is that the higher energy plane (1 1 0) in both substrates were the largest of any observed plane, especially in the Si case, indicating somewhat preferential growth in this plane which is of high interest.

Table 6.1: Grain sizes of ZnO planes observed

| **Plane & material** | **Grain size (nm)** |
|---|---|
| (1 0 0), Si | 3.36 |
| (0 0 2), Si | 3.10 |
| (1 0 1), Si | 2.41 |
| (1 1 0), Si | 4.01 |
| (1 1 0), $SiO_2$ | 3.67 |

It is a possibility that some of these layers form within a transition layer between substrate and film, however due to the large disparity between the unit cells of ZnO and both the Si and $SiO_2$ substrates, this is somewhat unlikely. Unit cell basis for ZnO are shown in Figure 2.9, although summarised in Table 6.2 alongside the corresponding values for the substrates. What is perhaps most important to note is that this structure is being observed within the film without any form of substrate heating or post annealing, a practice which is common throughout industry and in some cases necessary for any form of crystalline film; it could indeed be considered that the structure of these films could change with post annealing, however this was not explored within this work.

Table 6.2: All unit cell sizes for fims and substrates of interest

| Material | a, Å | b, Å | c, Å |
|---|---|---|---|
| ZnO | 3.249 | 3.249 | 5.207 |
| $Cu_2O$ | 4.684 | 3.429 | 5.12 |
| Si [239] | 5.43 | 5.43 | 5.43 |
| SiO2 [239] | 4.913 | 4.913 | 5.405 |

## 6.2 Aluminium oxide films

These films were deposited and analysed for the use of Dr. D Shaw of the YPI during his PhD, however composition, structure, and deposition method were not of key interest during that study so will be discussed further here. Figure 6.1 shows the composition of $Al_2O_3$ films on steel substrates, deposited for 1 hour and analysed by EDX with a beam energy of 5 KeV, and Figure 6.4 shows a SEM image and photograph of an $Al_2O_3$ deposited at 9 Pa for 1 hour, alongside a blank steel substrate; note particulates seen in the SEM image are carbon clusters deposited for electron beam charge mitigation, and the $Al_2O_3$ and substrate is mounted to a stub for use in the SEM. The $R_{KO}$ depth of the beam within this sample is again approx. 100 nm, and an estimated film depth of approx. 300 nm, and therefore no interference from the substrate was observed, with the emission lines studied being the Oxygen $K_\alpha$ line at 0.52 KeV, and both the Aluminium lines of $K_\alpha$ at 1.48 and $K_\beta$ at 1.55 KeV. It was found that 9 Pa yielded the desired composition of 2:3.

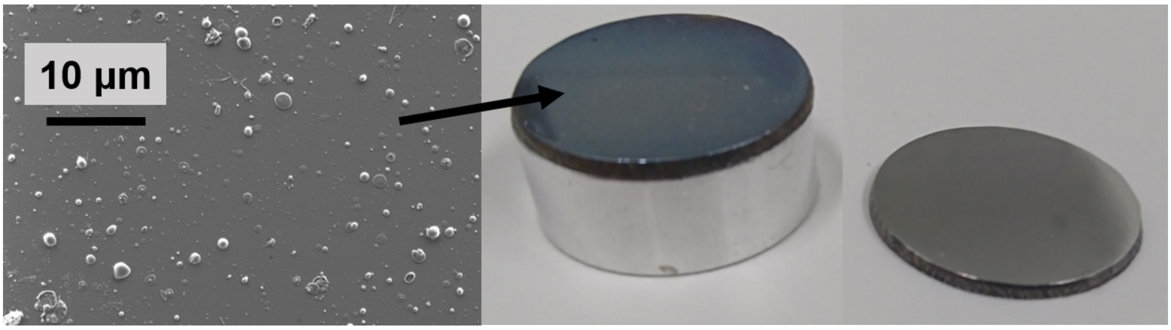

Figure 6.4: SEM image (left), and photograph of $Al_2O_3$ deposited on steel, compared to blank steel substrate.

Structure of these films were analysed via XRD, with the results shown in Figure 6.5. Four clear peaks were observed between $43^o$ and $75^o$, however these did not match any known planes of $Al_2O_3$, and after further investigation it was found that these were peaks from the underlying substrate. It was not known what specific form of steel was used and therefore extremely difficult to find a match to any known plane in literature or available databases, indicating amorphous $Al_2O_3$ has been deposited.

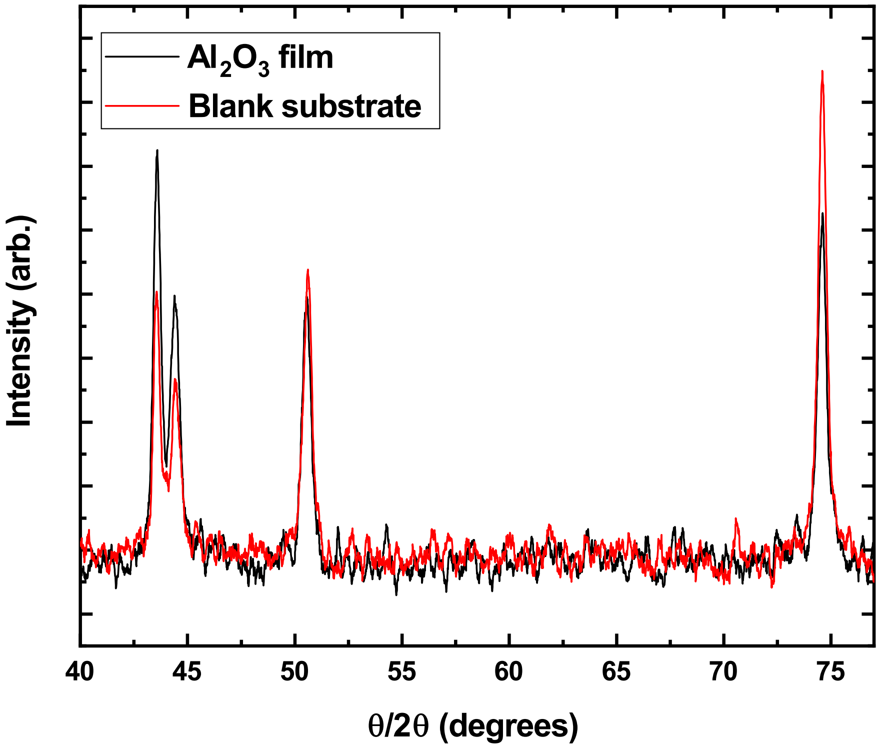

Figure 6.5: XRD spectra of $Al_2O_3$ deposited on steel.

However amorphous $Al_2O_3$ is commonly deposited by many deposition techniques [75, 76], and as a film has found further uses in such applications as MOSFETS [240]. Although different to the zinc and copper based which did exhibit some crystalline structure, much of the literature based on crystalline $Al_2O_3$ films heavily utilise post annealing and substrate biasing and heating or carefully controlled seeding layers [241–243]. Due to this, and a combination of the films being both sufficient for the work of Dr. Shaw, and the quality of the substrate being unknown, no further investigation was taken.

## 6.3 Composition as a function of depth

Although it has been proven that PE-PLD is able to deposit a variety of films on various of substrates, so far all analysis probes the nature of the bulk average of the film, with films analysed being quite thick in nature (i.e. on the order of microns). For PE-PLD to be a competitive technique within the semiconductor industry, films grown must also be able to be both thinner, and have consistent characteristics across the entire film depth. Therefore the composition as a function of the films depth has been determined via two different experimental means, as described in this section below:

### 6.3.1 TEM

$Cu_2O$ and CuO films deposited for 10 and 5 mins respectively have been analysed by TEM. This analysis was performed by Dr Jon Barnard and Dr Leonardo Lari of the York JOEL Nanocenter; Films were coated in protective layers of carbon, platinum, and palladium in order to withstand the heat imparted from etching by Ga ions, done so to etch of a lamella of a cross section of the film. Said materials were chosen as a coating due to their high heat conductivities, and also well known florescence to help distinguish from any detected signal. These lamella were then analysed via TEM, and can be seen in Figure 6.6.

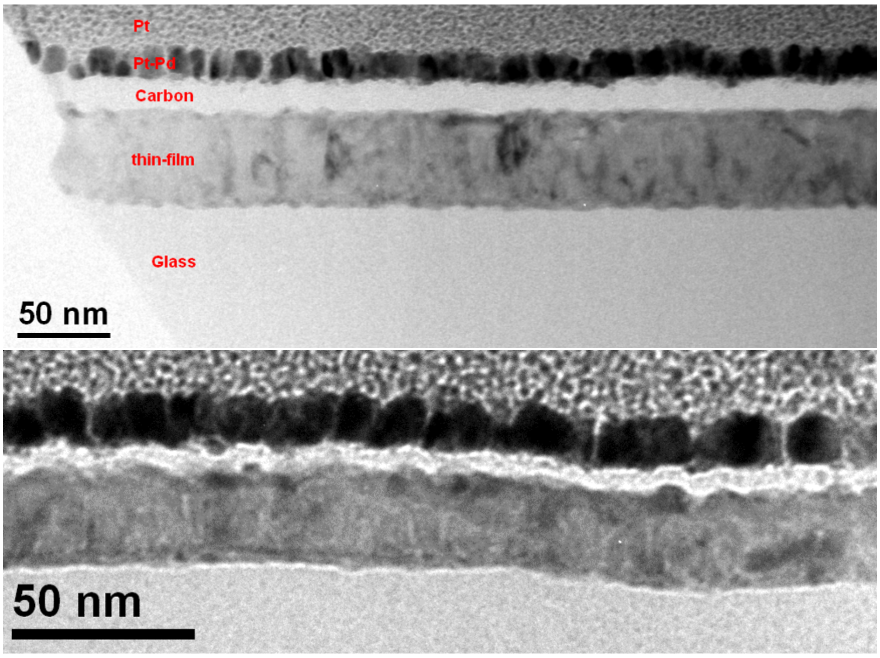

Figure 6.6: TEM images from lamella of, Top: $Cu_2O$, Bottom: CuO

The first observation within Figure 6.6 is indeed the thickness of the film itself, with the $Cu_2O$ film being $48.6 \pm 3$ nm thick after a 5 min deposit, and the CuO film being $26.0 \pm 1$ nm thick after 2.5 mins. This corresponds to a 10 nm/min deposition rate, matching the results from AFM analysis [2]. Uncertainties in these values have been determined from the standard deviation of multiple measurements across the film length, each of which taken at 30 locations. It is hard to tell structure from these images, therefore higher resolution, and dark field (DF) images were taken of each film, as seen in Figures 6.7 and 6.8. The $Cu_2O$ film can be seen to have columnar grains, growing along the axis of film growth, with a transition layer with the $SiO_2$ substrate of approx. 6 nm, as determined by the thickness of the discoloured region between film and substrate; And the CuO film has a grain structure of much more circular grains, and a transition layer with the substrate of around half that of the $Cu_2O$. The dashed patterns that can be seen on both the higher resolution images are Moire fringes, caused by the overlapping of films in the axis against film growth, and are not representative of any film structure.

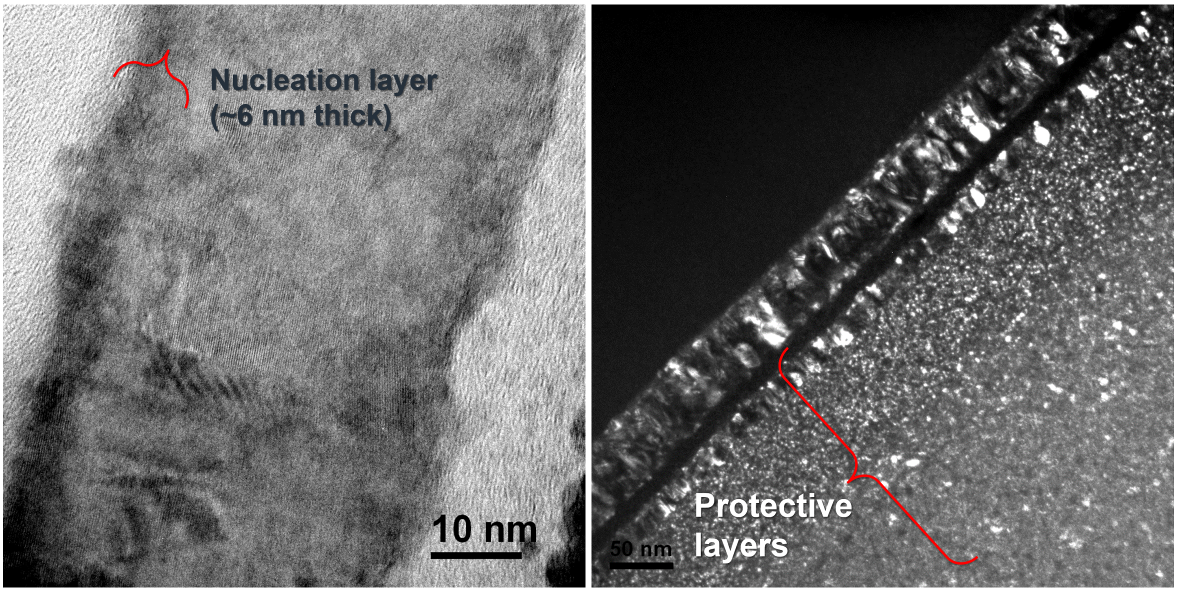

Figure 6.7: Left: Higher resolution image of $Cu_2O$ from TEM. Right: Dark field image of same film

Additionally EDX was performed on the $Cu_2O$ lamella in order to determine the atomic composition across the films depth; results of this can be seen in Figure 6.9, showing the two areas analysed and the corresponding counts, highlighted within the figure as to areas, a and b. Two regions have been analysed, as due the thick quartz under layer there was a high build

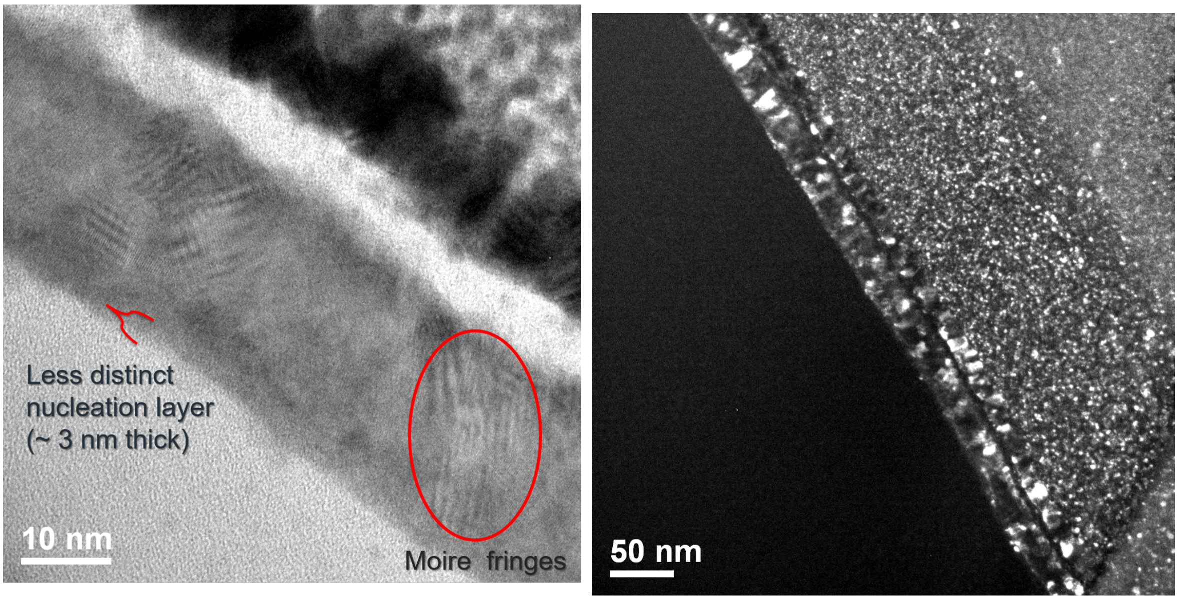

Figure 6.8: Left: Higher resolution image of CuO from TEM. Right: Dark field image of same film

| **Section** | **Cu** (%) | **Cu error** (%) | **O** (%) | **O error** (%) |
|---|---|---|---|---|
| A | 68.6 | 2 | 31.4 | 3 |
| B | 72.4 | 2 | 27.6 | 3 |

Table 6.3: Composition in two areas at various depths of a $Cu_2O$ film on quartz

up of charge due to insulated electrons, resulting in sensitive line profiles being not possible. Also within the counts it can be seen that there is Cu and O observed within the protective layers; O is likely present due to oxidation of the protective layers, and Cu comes from the mount used in the TEM being made of copper, and the highly luminescent Pt protective layer reflecting from its environments. Composition, determined from the integrated counts in both areas can be seen in Table 6.3. Area A, the section close to the substrate, show within error the expected 2:1 ratio determined from the EDX on the bulk films. Area B, close to the film surface/protective layers, show slightly more copper rich films, by roughly 2%. This is likely due to the luminescence of the adjacent reflective layers, as bulk EDX shows the 2:1 ratio, and cross section images show no difference in film structure.

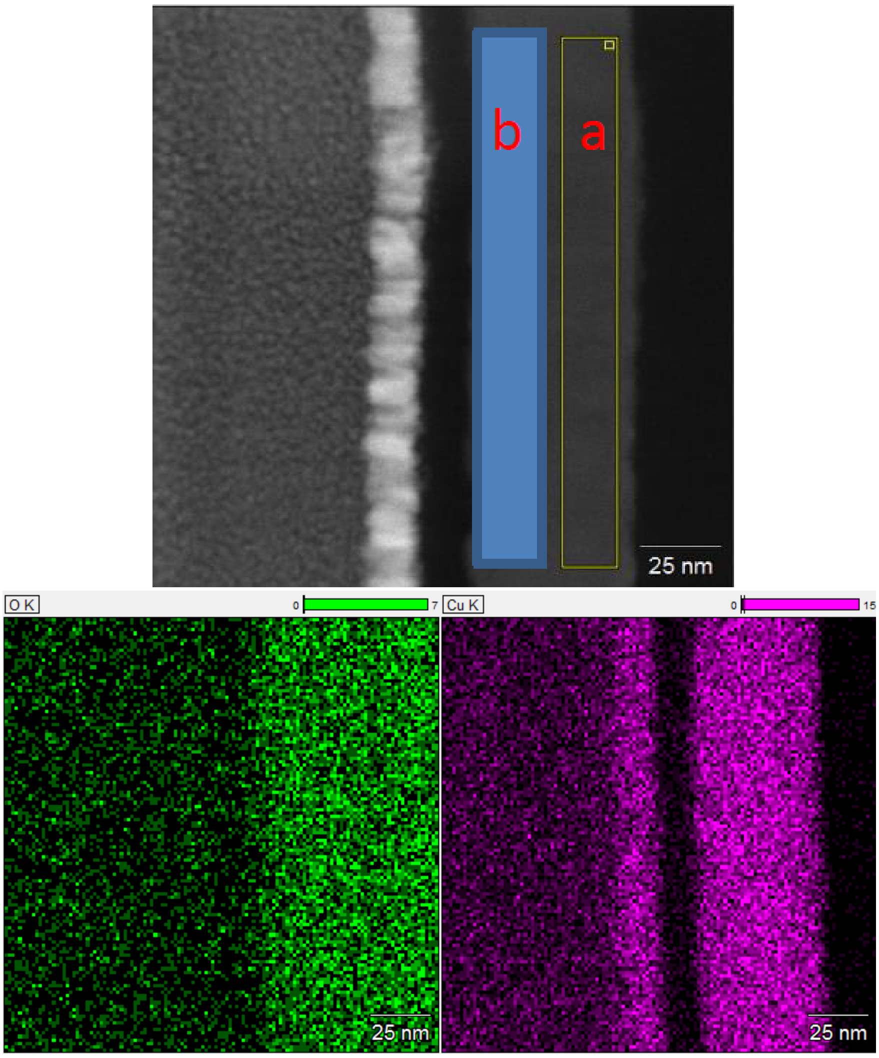

Figure 6.9: Areas at various depths of a $Cu_2O$ film on quartz, and for counts obtained from EDX.

### 6.3.2 MEIS

Alongside the TEM on cross sections, the non destructive technique MEIS was used; In addition to the advantages listed in this prior section, due to detection of $H^+$ ions there would be no confusion with the background or holders, like with the Cu in TEM, plus use of these films aided the understanding of this technique more, as will be discussed below. MEIS analysis was performed by Dr Andy Rossall of the University of Huddersfield. The list of all films analysed by MEIS is shown in Table 6.4, with analysis of films deposited on quartz substrates published in the following reference [244]. Figures 6.10 to 6.14 show MEIS analysis of these films.

For the case of $Cu_2O$ on $SiO_2$ deposited for 5 mins, i.e. very close to that of TEM

Table 6.4: List of PE-PLD samples analysed by MEIS

| **Film** | **Substrate** | **Deposition time (mins)** |
|---|---|---|
| ZnO | $SiO_2$ | 5 |
| ZnO | $SiO_2$ | 2.5 |
| $Cu_2O$ | $SiO_2$ | 5 |
| $Cu_2O$ | $SiO_2$ | 2.5 |
| CuO | Si | 2.5 |
| $Cu_2O$ | Si | 2.5 |
| ZnO | Si | 2.5 |

analysis, the trends match with those seen in the TEM lamellae, with a thickness matching roughly the 10 nm/min deposition rate. For all other films the ratio between elements within the film matched that exactly to EDX analysis of the bulk film, thus showing films of high uniformity across their depth. This is the case for both forms of copper oxide, as well as zinc oxide, on both substrates analysed.

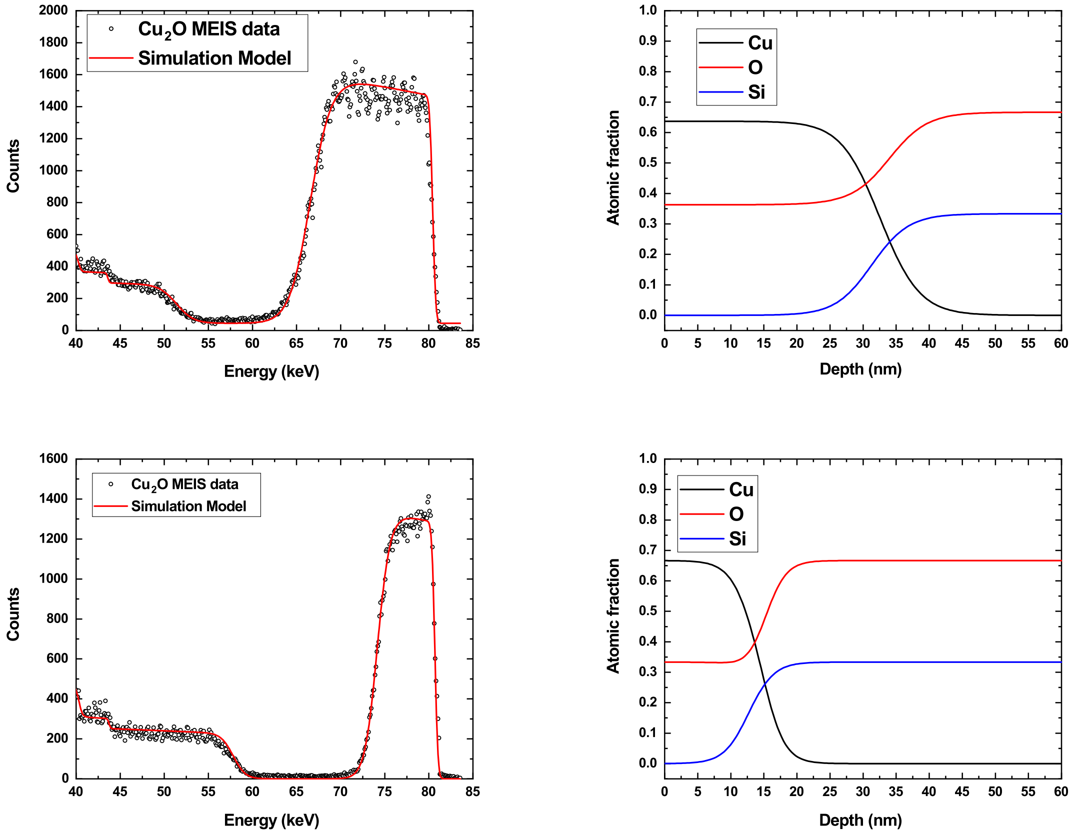

Figure 6.10: MEIS on $Cu_2O$ on $SiO_2$ for, Top: 5 mins, Bottom: 2.5 mins

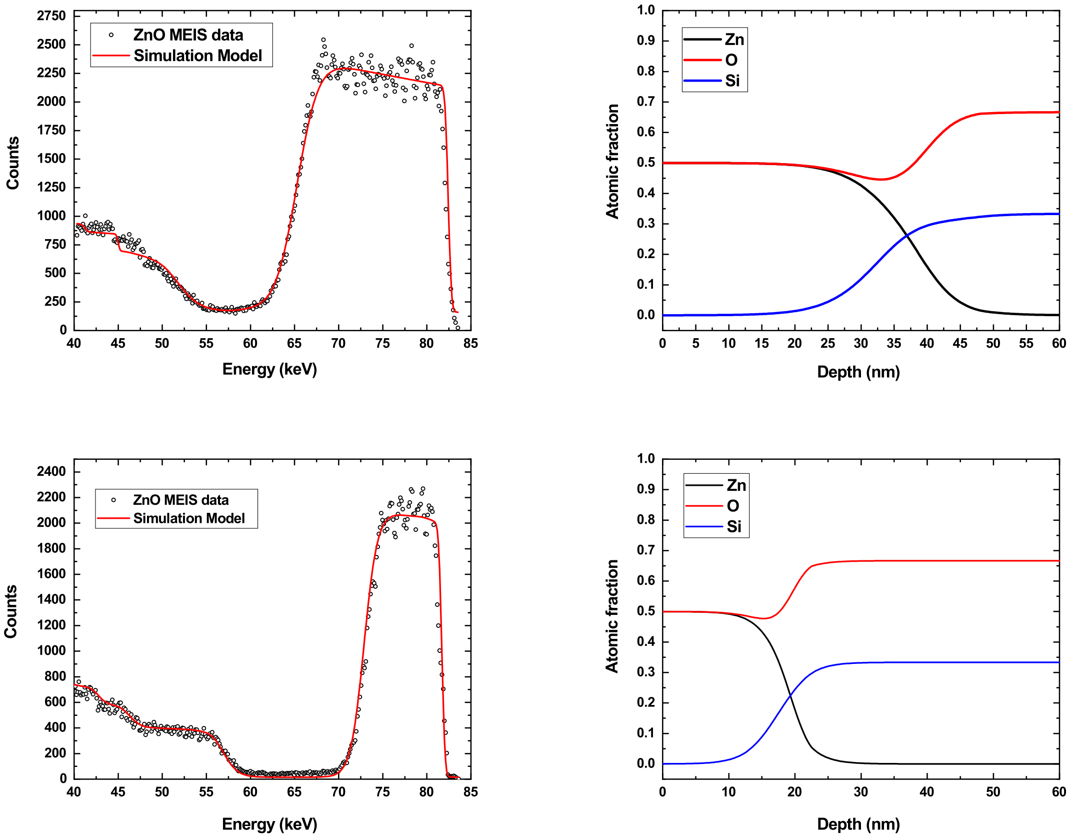

Figure 6.11: MEIS on ZnO on $SiO_2$ for, Top: 5 mins, Bottom: 2.5 mins

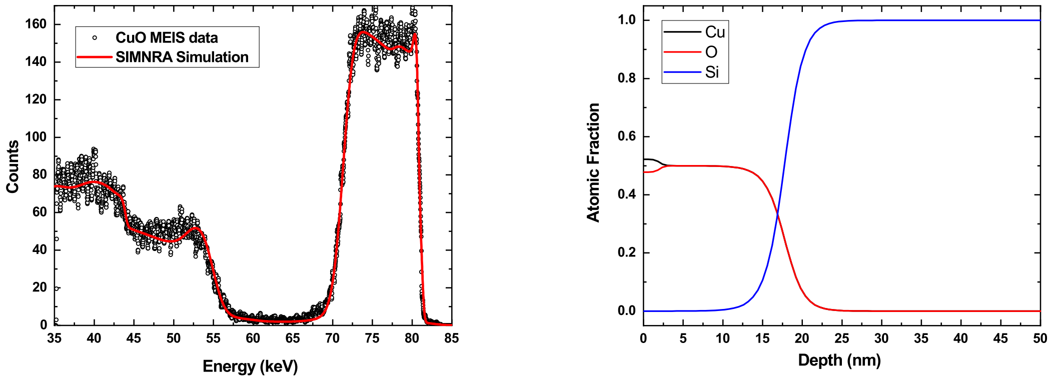

Figure 6.12: MEIS on CuO on Si for 2.5 mins

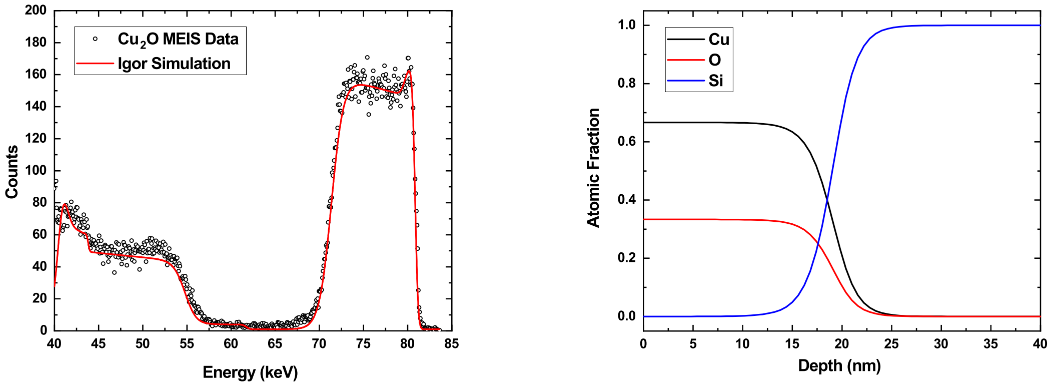

Figure 6.13: MEIS on $Cu_2O$ on Si for 2.5 mins

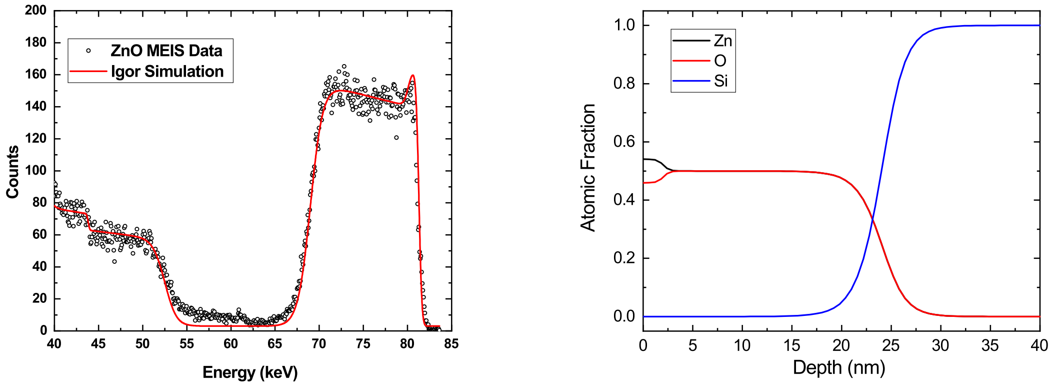

Figure 6.14: MEIS on ZnO on Si for 2.5 mins

However when comparing the MEIS analysis of $Cu_2O$ on $SiO_2$, Figure 6.10, to that of TEM in Figure 3.15, there is an overestimation of the transition layer, showing it to be roughly 16 nm for the 5 minute deposited, over double that seen from TEM. This comes from a key assumption made within MEIS, being that currently only single scattering of ions is taken into account, i.e. a $H^+$ ion only interacts with one atom within the target, being the event that scatters the ion back to the detector. Indeed this assumption may not be true, especially in the transition layer where the film does not have a well defined crystalline structure as seen from TEM. So with the use of this data, multi-scattering effects are currently under investigation within MEIS by a development of a new fitting package within the code SIMNRA. An example of which shown in Figure 6.15, which shows that although the transition depth is becoming smaller and matching TEM images closer, it is artificially stepped. As this investigation and development is still ongoing, with certain films such as CuO on Si as above in Figure 6.12 yielding physical profiles bar some artefacts on the film surface. All other MEIS analysis shown above is done via the use of the existing IGOR software, and therefore transition layers may not be accurate, however bulk compositions can be trusted.

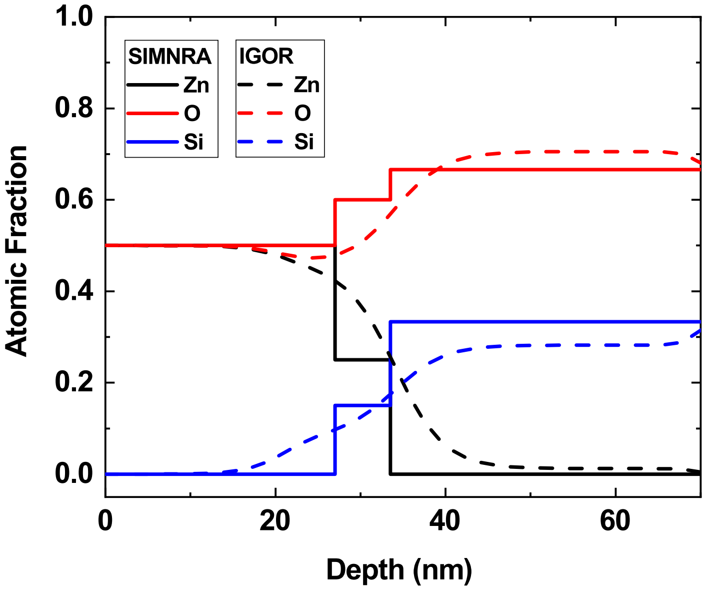

Figure 6.15: Initial SIMNRA analysis of ZnO film on $SiO_2$ compared to IGOR analysis.

## 6.4 Plastic substrates

One emerging trend within modern electronics is flexible technology, from entire tablets or computers that are flexible, to wearable technologies such as smart-watches and clothing, all of which use substrates that in some form or other comprise of some form of plastic or polymer. Current methods for deposition have typically focused around deposition of ITO and in some cases ZnO thin films onto plastic substrates, and are mostly based on CVD based techniques [245–247], or even printing from ink jet printers [248, 249]. These techniques still have drawbacks, such as the previously mentioned harmful precursors in CVD, and with the ink jet printers being a complex process with many parameters to control and a very slow deposition rate. As other commonly used methods such as sputtering and other forms of PLD require substrate heating and in come cases post annealing, they cannot be used with plastic substrates, as temperatures utilised are often many hundreds of degrees whereas plastics such as high density-polyethylene melting at just 105$^o$C.

Gas temperature measurements within Chapter 5 presented temperatures of up to 1500 K, yet also showed the nature of the heating during the pulse. So using the data from Figure 5.11, a simple model has been created in order to determine the corresponding substrate temperatures during the pulse. Said model is based on the known equation of the rate of heat flow, Equation (6.1), where $Q$ is the internal energy of the material, $t$ time within the pulse, $K$ the thermal conductivity coefficient of the substrate, $A$ and $x$ the substrate area and thickness, and $T$ temperature.

$$\frac{\Delta Q}{\Delta t} = -KA\frac{\Delta T}{x} \tag{6.1}$$

Then it is assumed that within an infinitesimal time that $Q$ will increase as outlined in Equation 6.2, where T$_i$ is the temperature at the previous time step, with this solved iteratively to determine the temperature increase over time. Additionally the thermal accommodation coefficient, $\alpha_e$, is introduced in order to account for the efficiency of temperature transfer, and as it was discussed in Section 5.4. A temperature is then calculated from this internal energy, $Q$, by the known specific heat capacity of the material, $c$. Values of constants used in this model for polyethylene (PE) are shown in Table 6.4.

$$\begin{gathered} Q = \frac{KA}{x}(T - T_i)\alpha \\ T_{sub} = \frac{Q}{c} \end{gathered} \tag{6.2}$$

For the case of 20 Pa, 500 W, as measured in Figure 5.11, which is the case measured closest to that during deposition in PE-PLD, this model has been applied and results shown in Figure 6.16. It can be seen that when assuming a perfectly efficient transfer of heat (i.e. $\alpha_e = 1$) that the plastic would reach its melting point at 10 ms, the pulse length within deposition in PE-PLD. Yet when altering $\alpha_e$ to values shown in Section 5.4 to result in matching gas temperatures, being 0.8 and 0.5, then the substrate temperature only surpasses the melting point after 10 ms. Although this is a first assumption, and effects such as losses to other areas such as the substrate holder are not taken into account, it was deemed safe to use plastics within the PE-PLD chamber during a plasma operation. Initial testing of depositions

| Constant | Value |
|---|---|
| K | 0.4 W/mK |
| A & x | $2.02\times10^{-3}$m (1 sq. inch) & $7\times10^{-5}$m |
| c | 1550 J/KgK |

Table 6.5: Constants of PE used in model. $K$ & $c$ are taken from [251]

proved this to be the case with plastic substrates not only surviving the conditions, yet showing no measurable deformation down to the measurable precision of 0.01 mm. So $Cu_2O$ and ZnO films have been deposited on PE and polytetrafluoroethylene (Teflon) substrates, with PE chosen due to being one of the most commonly used form of plastic, and Teflon known for its durability and resistance, including to plasma processes [250].

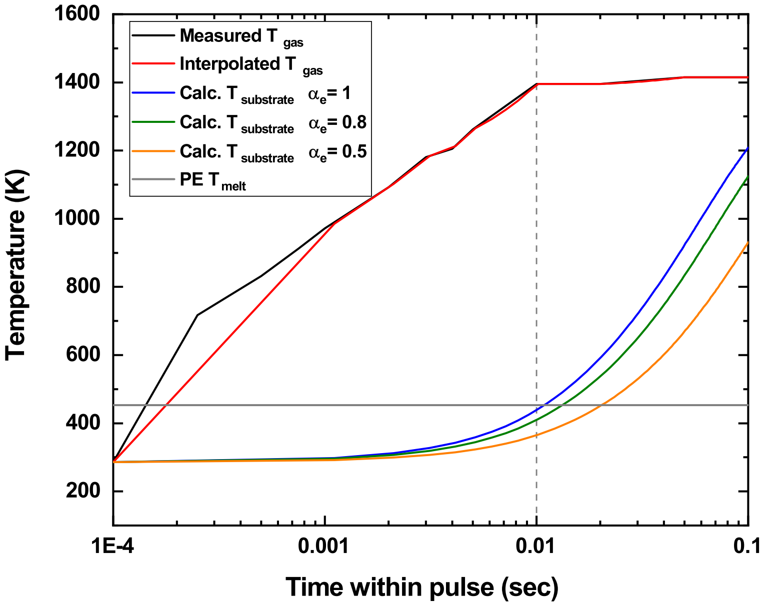

Figure 6.16: Calculated temperature of a polyethylene substrate

Figure 6.17 shows the composition of films analysed by EDX, deposited under the similar conditions as for $SiO_2$ and Si substrates, as highlighted in the figure caption. It is clearly seen that the composition of each film match that as when deposited on previous substrates, with the desired 1:1 ratio in the zinc based film, and 2:1 ratio for copper. A somewhat expected result due to the non-epitaxial nature of PE-PLD, yet it is again important to note that this composition has been created without any form of substrate bias or heating, and purely from

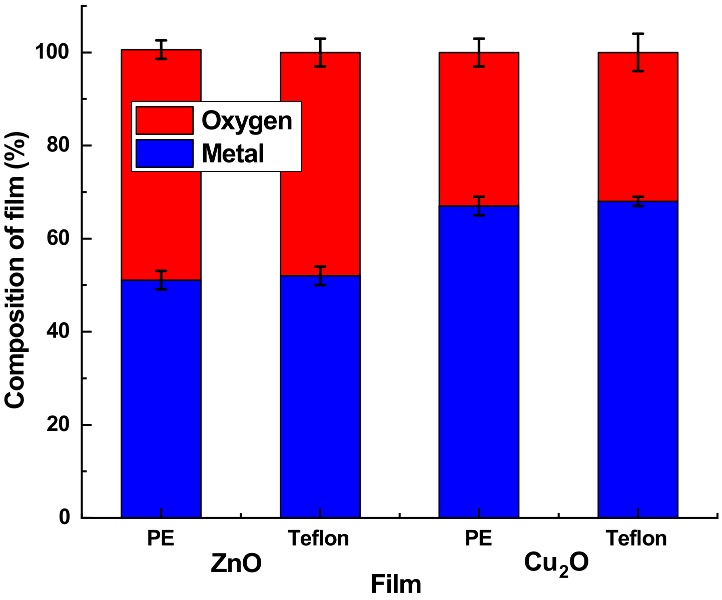

Figure 6.17: Mesaured composition of films deposited on plastic substrates. Both ZnO and $Cu_2O$ deposited for 1 hour, 7.5 Pa, 500 W.

control of the laser induced and RF plasmas. Although extensive analysis of deposition rate was not performed, there was no interference of the substrate during EDX analysis, so films were clearly over the $R_{KO}$ limit of approx. 100 nm, therefore the deposition rate can assumed to be the same as when other substrates. This deposition rate of 10 nm/min means PE-PLD is far quicker that some deposition techniques for the depositions of oxides on plastics, such as the above mentioned ink jet printing, which typically is 1 to 5 nm/min [249]. There are some techniques reported that quote quicker deposition techniques, such as the works of P Kelly et al [252], where $TiO_2$ was deposited of PET plastic at 22 nm/min; however in said work samples were required to be post annealed unlike here in PE-PLD, and the sputtering power supply used operated at 1.5 kW of power resulting in approximately $1.5\times10^{-2}$ nm/min/W, meaning PE-PLD is in fact more efficient only requiring 500 W of power, resulting in $2\times10^{-2}$ nm/min/W (plus additional efficiency from no required annealing). An SEM image and photograph of a $Cu_2O$ film deposited on a 2.54 cm sqaure PE substrate can be seen in Figure 6.18; note, ridges on SEM image are not intrinsic of film structures, as result from the morphology of the PE substrate.

XRD has been performed on all aforementioned combinations of oxides and plastics

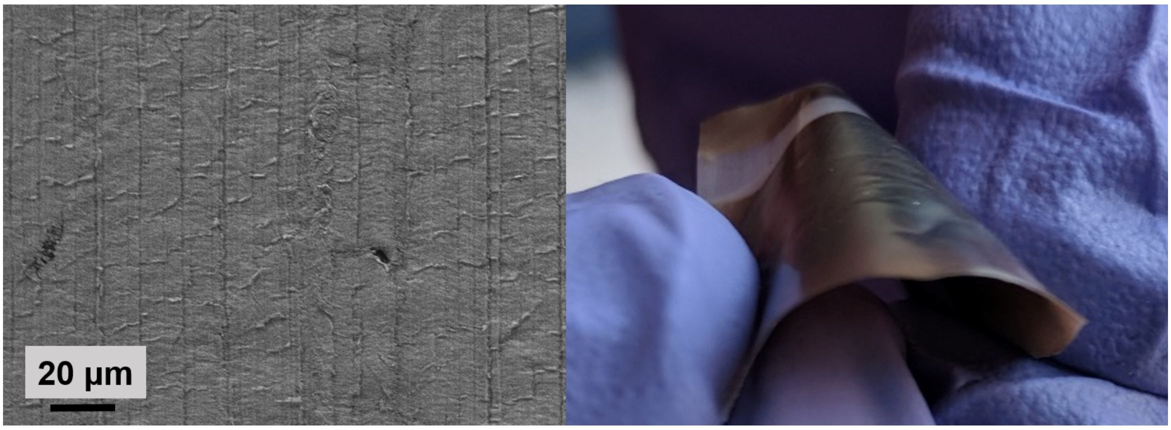

Figure 6.18: SEM (left) and photograph (right) of $Cu_2O$ on polyethylene, deposited for 1 hour, 7.5 Pa, 500 W.

substrates, and are shown within the Figures 6.20 and 6.21. Before discussing the results it is key to mention the method of which these deposits were performed, as in order to analyse a sample within XRD it is of key importance to have a flat sample as it is a highly sensitive reflection based technique, so a curved surface can effect the result. In order to maintain a flat surface during deposition and handling of the film during transport and XRD analysis, a sample of plastic was mounted to quartz discs by a thin layer of wax. Although there is some literature containing XRD on polymers, blank samples were analysed in order to aid distinguishing any observed signal, as shown in figure 6.19. The $SiO_2$ under layer can be seen

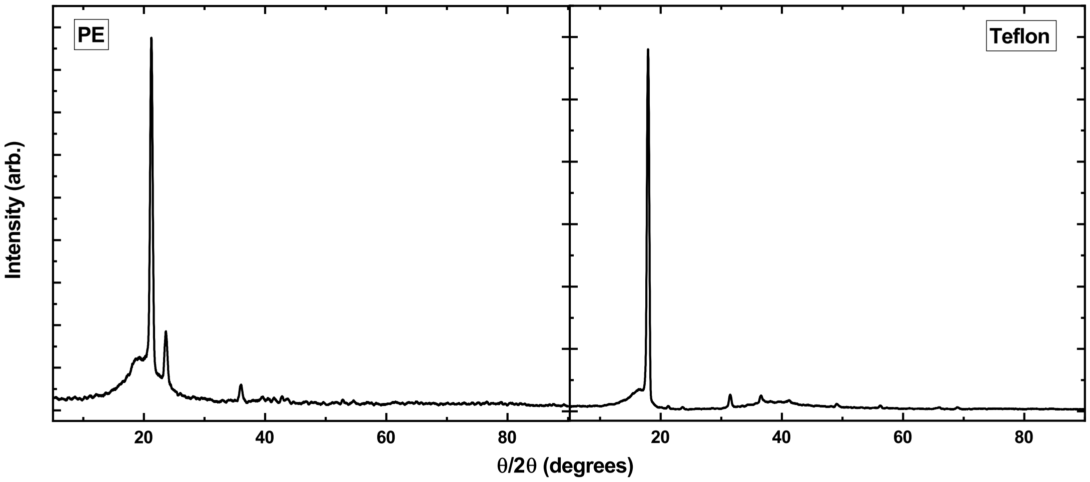

Figure 6.19: XRD of blank polymers mounted to $SiO_2$. Left: Polyethylene. Right: Teflon

as before at $21^o$, and with the Pe layer there are two sharp peaks at $21.5^o$ and $24^o$ matching that seen from XRD on PE in literature [253], with a smaller peak at $36^o$ which could either be the PE or perhaps the wax. The Teflon signal shows one sharp peak at $18^o$ and the smaller $36^o$ peak, and with a shallow bulge between $37^o$ and $50^o$ with some small peaks throughout. Said peaks in Figure 6.19 are used to help distinguish the structure observed in Figures 6.20 and 6.21.

It is clear from Figure 6.20 that the structure of the ZnO film is much less well defined as when on the Si and $SiO_2$ the substrates. On PE there are no noticeable peaks that are

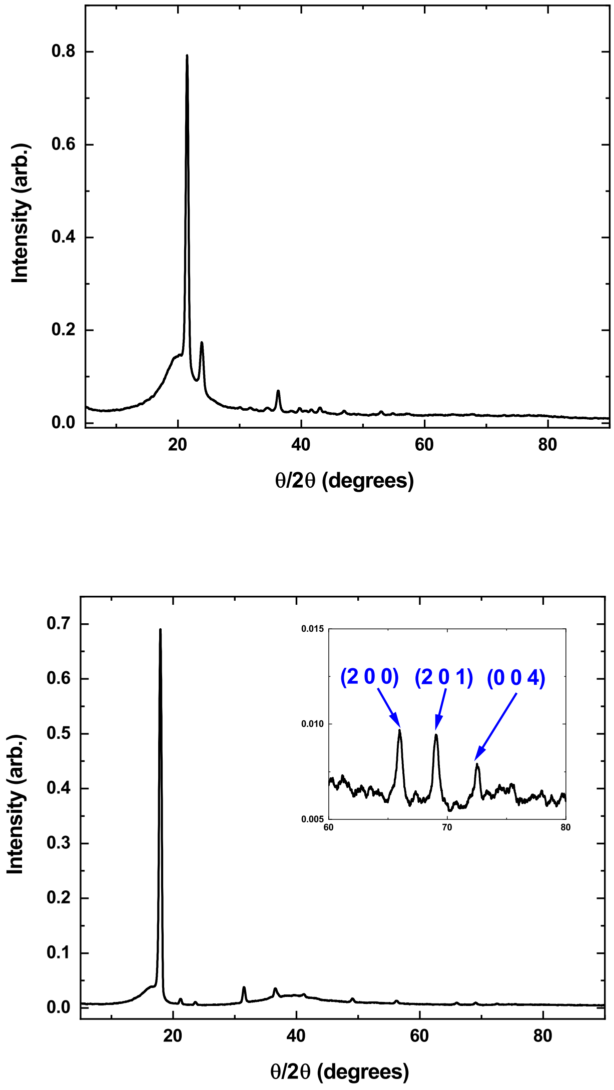

Figure 6.20: ZnO films deposited onto plastic substrates; Top: Polyethylene. Bottom: Teflon

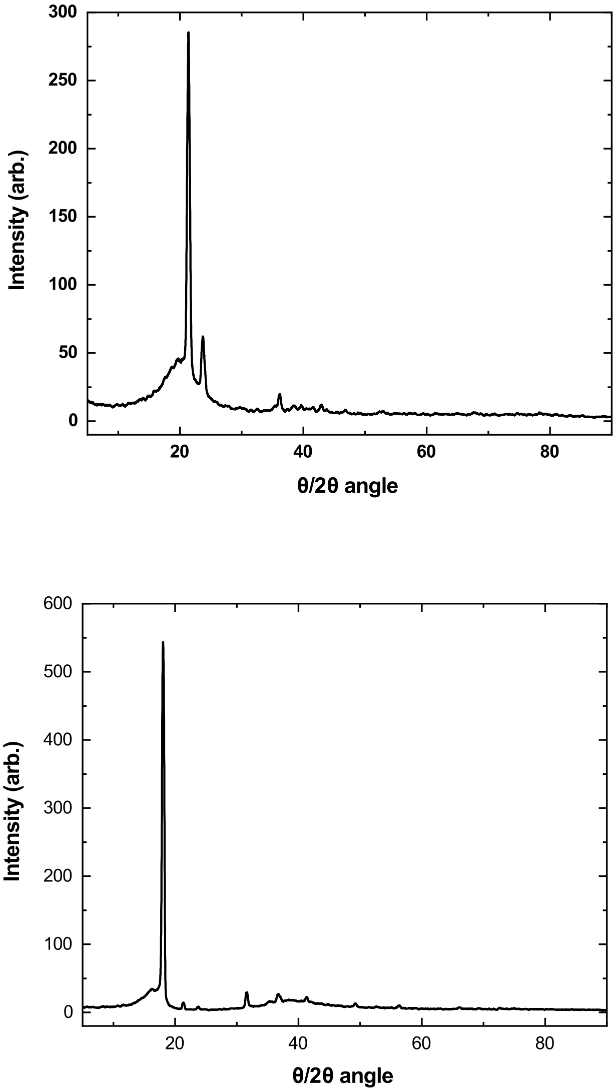

Figure 6.21: $Cu_2O$ films deposited onto plastic substrates; Top: Polyethylene. Bottom: Teflon

different from the substrate, meaning the film is purely amorphous; on Teflon however there are three peaks corresponding to three planes of ZnO, being (2 0 0), (2 0 1), and (0 0 4), at $66^o$, $69^o$, and $72.5^o$ respectively. However due to the relatively very small intensity of these peaks these planes must not be very prevalent throughout the film, likely in a polycrystalline layer somewhere within the mostly amorphous film formed as a result of the polycrystalline plastic under layer; which is also most likely the reason for amorphous nature of the film seen on the PE substrate.

The $Cu_2O$ films in figure 6.21 show no distinguishable features from those of XRD on simply the substrate, meaning there is a purely amorphous film. However it is worth to note than in existing literature, for films such as ITO on plastics, the crystal structure and XRD has not been a metric of success, with films tested in more specific means to their direct application such as piezoelectric or conductive properties.

## 6.5 Conclusion

This chapter has presented results based around further investigation into $Cu_2O$ and CuO films deposited by PE-PLD on $SiO_2$, and the deposition of other films such as ZnO and $Al_2O_3$ films on a variety of substrates. FIB-TEM analysis show that both forms of copper oxide deposited films that are of a uniform thickness across the substrate, and consistent structure across the films depth. This is in agreement with what is seen in the non-damaging MEIS analysis where copper oxide films are again seen to be uniform in composition, a trend that is also seen in ZnO films, and all types of films deposited on Si substrates. It has also been shown that PE-PLD is a highly adaptable technique, with the deposition of fusion-mirror proxies of $Al_2O_3$ on steel substrates, and semiconductor relevant films on plastic. Said $Cu_2O$ and ZnO films on polyethylene and polytetrafluoroethylene substrates are shown to have the exact same composition as before, yet with more amorphous structures as a result of the polycrystaline nature of the plastic.; however crystallinity is often not the determining factor for quality on films on plastic substrates, as it is often the case to perform more application-relevant testing (e.g. transmission curves, stress resistance etc.).

# Chapter 7

# Conclusions

The work presented in this thesis has focused around the thin film deposition technique, PE-PLD, with an investigation into each of the three key stages of this process; first, the nature of nanosecond laser ablation of metal targets, and the comparison to the behaviour of metal oxide targets, was explored via use of the code POLLUX. Secondly, absolute measurements of the gas temperature within the RF ICP utilised within PE-PLD, where three techniques were performed and benchmarked against each other, and the effect of pulsed operation of the plasma was investigated, alongside simulations of the gas temperature within HPEM. Lastly analysis of deposited metal oxides of a variety of substrates was performed, focusing on aspects such as the relative composition of elements as a function of depth, and the use of novel substrates such as plastics.

Simulations within POLLUX were benchmarked against experiment by two parameters deemed of key importance to film depositions, being the ablated mass and temperature of the plasma plume. Ablated masses from POLLUX from Zn and Cu targets were compared to masses obtained experimentally from craters produced on targets under PE-PLD like conditions. These masses matched within 35% for Zn and 22% for Cu, when the "full treatment" model was utilised which treats the phase change of the material in a classical manner. This means solid material must melt and further evaporate in order to enter the gas phase, which is the known behaviour under nanosecond pulse length ablation. When using the full treatment model for oxide targets however, the obtained masses were an order of magnitude lower than that of experiment. This is due to the different nature of the phase change of the oxide targets, as it is known that these oxides decompose when heated. When using a gaseous target as an analogy for how the oxygen atoms would behave during ablation by decomposition, the ablated mass matched experiment within 19% for ZnO and 17% for $Cu_2O$. This, when combined with determination of the internal thermal and kinetic energies of the plasma plume, highlights the importance of understanding how various targets behave under nanosecond pulsed laser ablation, relevant to PE-PLD.

Temperatures of an ablated Cu plume were compared to temperatures obtained by experiment from prior work of PE-PLD [2]. Here it was shown that at 50 ns, electron temperatures matched that of experiment, being approximately 1.4 eV, and at all times up to 100 ns were within 30% and exhibiting a similar trend. Furthermore, the nature of an artefact within the code, an artificial increase in temperatures at the leading edge, was explored in detail. Reasoning for this is determined to be artificial interaction with the background environment, and the lack of rigorous treatment of the plume expansion. However, it was also shown with comparison to experiments of the ablation of Si in a vacuum, that current models used to describe the adiabatic expansion of a plasma plume are currently insufficient. This was done by the use of data from POLLUX at early time-steps (20 ns), as an input into an existing model from the literature, that such existing model does not accurately predict the adiabatic expansion of the plume. This being due to assumptions made on the initial distribution temperatures and densities within the plume, which POLLUX is able to provide further detail on.

Absolute measurements of gas temperatures were shown to increase with both plasma pressure and power. The highest pressure case (50 Pa) was found to have a maximum of approximately 1750 K at 900 W, whereas the lowest pressure (5 Pa) reached a temperature between approximately 750 and 1500 K for the same powers. It was also seen in all pressure cases that as the ICP transitioned into H-mode, the gas temperatures increased by approximately a factor of 2. This has been linked to the increased dominance of dissociative heating, from the breaking of the bond within the $O_2$ molecule. With this relationship determined from the known increase in densities of plasma species (e, O etc.) within the H-mode.

Additionally, the importance of selection of an appropriate diagnostic technique has been highlighted, as different plasma conditions led to differences in the behaviour of each technique. The most desirable $O_2$ OES was successfully benchmarked to the other techniques within the E-mode operation, yet not suitable in the H-mode due to quenching of the upper state by atomic oxygen. $N_2$ OES was the only case to produce a signal in all plasma conditions, yet there was a deviation from Ar TDLAS measurements in the low pressure, high power conditions, most likely due to assumptions in the Boltzmann distribution of electrons within the upper molecular state not being valid. Lastly Ar TDLAS was not applicable in the highest pressure, low power conditions, due to the reduction in the densities of excited Ar species, from Penning reactions with the $O_2$ molecules, but was applicable in all other conditions.

Using $N_2$ OES at the higher pressures, the effect of pulsed power within H-mode operation, relevant to PE-PLD, was determined. The gas temperature in the 20 Pa pulsed case was found to increase at a fairly constant rate throughout the pulse, whereas the 50 Pa case maintained a fairly constant temperature until approx 2 ms, where a sharp increase was observed. This difference in behaviour is most likely due to the longer time required to obtain the sufficient electron density for H-mode operation in this case. However this could be as a result of the efficiency of the matching, a topic currently of high interest in the community. Plus of key relevance to PE-PLD, it can be shown from these measurements that the temperature within the off-time of the pulse returned to approximately room temperature, allowing for the use of materials within the chamber which otherwise would not survive the temperatures reached under continuous power conditions.

Lastly, films deposited by PE-PLD have been analysed by a variety of means. The composition as a function of depth of $Cu_2O$ deposited on $SiO_2$ has been determined by EDX on an lamella etched out by FIB, where it was seen that the composition was constant (within 4%) at two areas within the films depth. Plus, the depth profile of CuO, $Cu_2O$, and ZnO deposited on both $SiO_2$ and Si was determined via MEIS. Here it was seen that from fitting to the observed spectra, that the composition across the entire depth was constant, up until the transition layer of the substrate.

The polycrystalline structure of ZnO was also determined via XRD. Here it was seen that the (1 1 0) phase could be deposited on both $SiO_2$ and Si; with this phase known to be of high density and high surface energies, currently of interest in the semiconductor industry. Also it was shown that PE-PLD was able to deposit amorphous $Al_2O_3$ on steel substrates, relevant to hard protective coatings, and as a suitable and safe substitute to Be. Plus, with knowledge taken from the pulse temperature measurements, it was shown that heat sensitive, plastic substrates could be used within PE-PLD. Due to the non-epitaxial nature of PE-PLD, ZnO and $Cu_2O$ films of the same compositions as with Si and $SiO_2$ substrates could be deposited, with such films on plastics having relevance in flexible electronics. Yet films deposited on plastic were amorphous, however the crystal structure is not of key importance in many applications. With further testing on a case by case basis tailored to the films application, PE-PLD could still be an attractive technique for creating such films, due to its competitive deposition rate compared to existing techniques and lack of dangerous chemical precursors.

# Appendix A

# Expansion on POLLUX results from further modelling

As stated in Section (4.3), data from POLLUX, obtained from simulations performed by myself, was utilised as input with the model of Stapleton et al in order to eliminate many assumptions of the starting conditions of the plasma plume, which were present within the initial work where said model was presented [42] . This additional modelling was performed by Dr E. Wagenaars, and benchmarked against experimental data taken by Dr H. Liu and Prof. M. Ashfold of the university of Bristol, with this work recently accepted to the Journal of Applied Physics [207]. Here the key results of this modelling is presented, which shows how the existing model can not correctly predict the nature of both electron densities and temperatures simultaneously, yet can via the use of different assumptions of isothermic or isentropic behaviour.

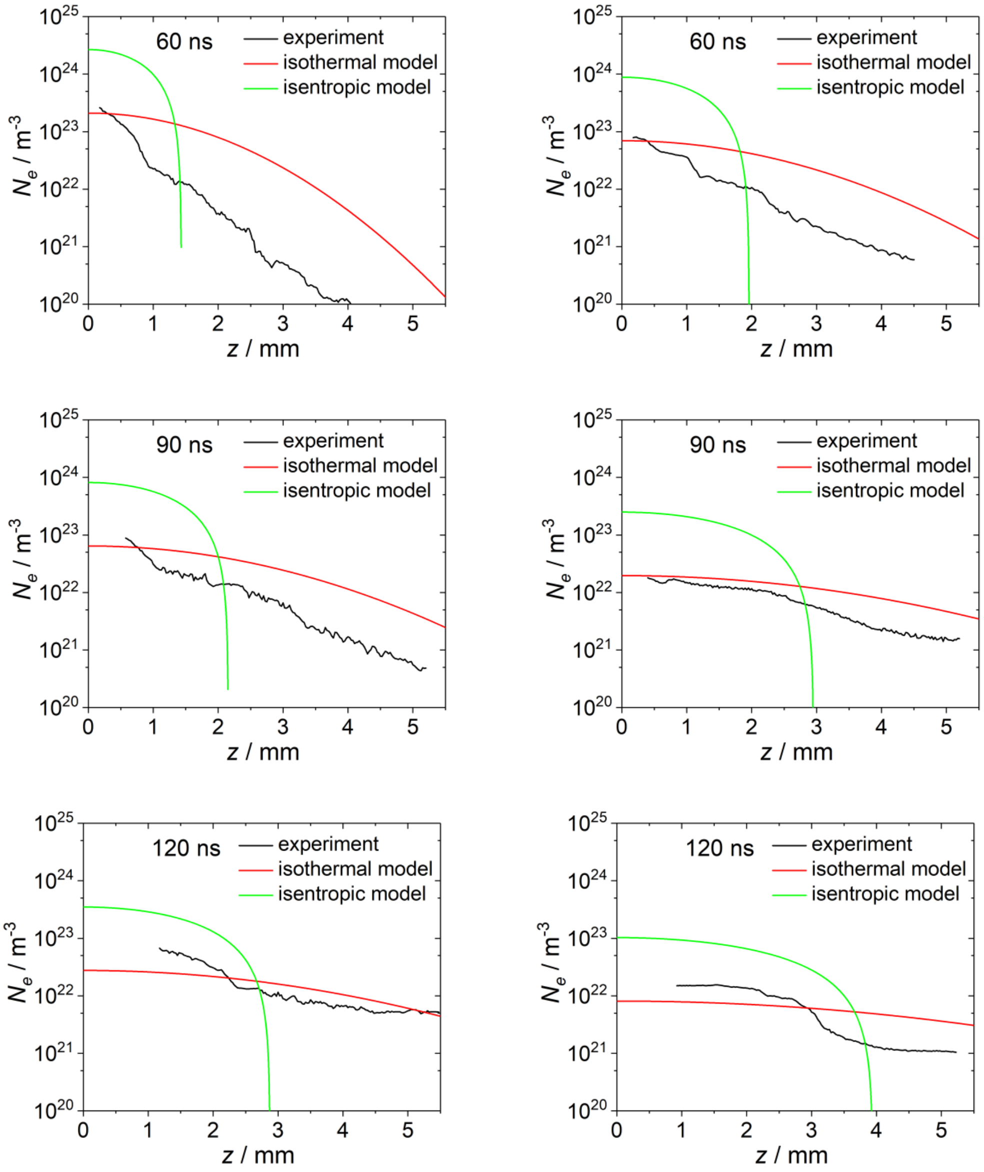

Figure A.1: Evolution of electron density over time, after laser ablation of a pure Si target determined from the model of Stapleton and the adiabatic and isentropic assumptions of said model, with inputs taken from POLLUX simulations. Left: 532 nm laser ablation. Right: 1064 nm. [207]

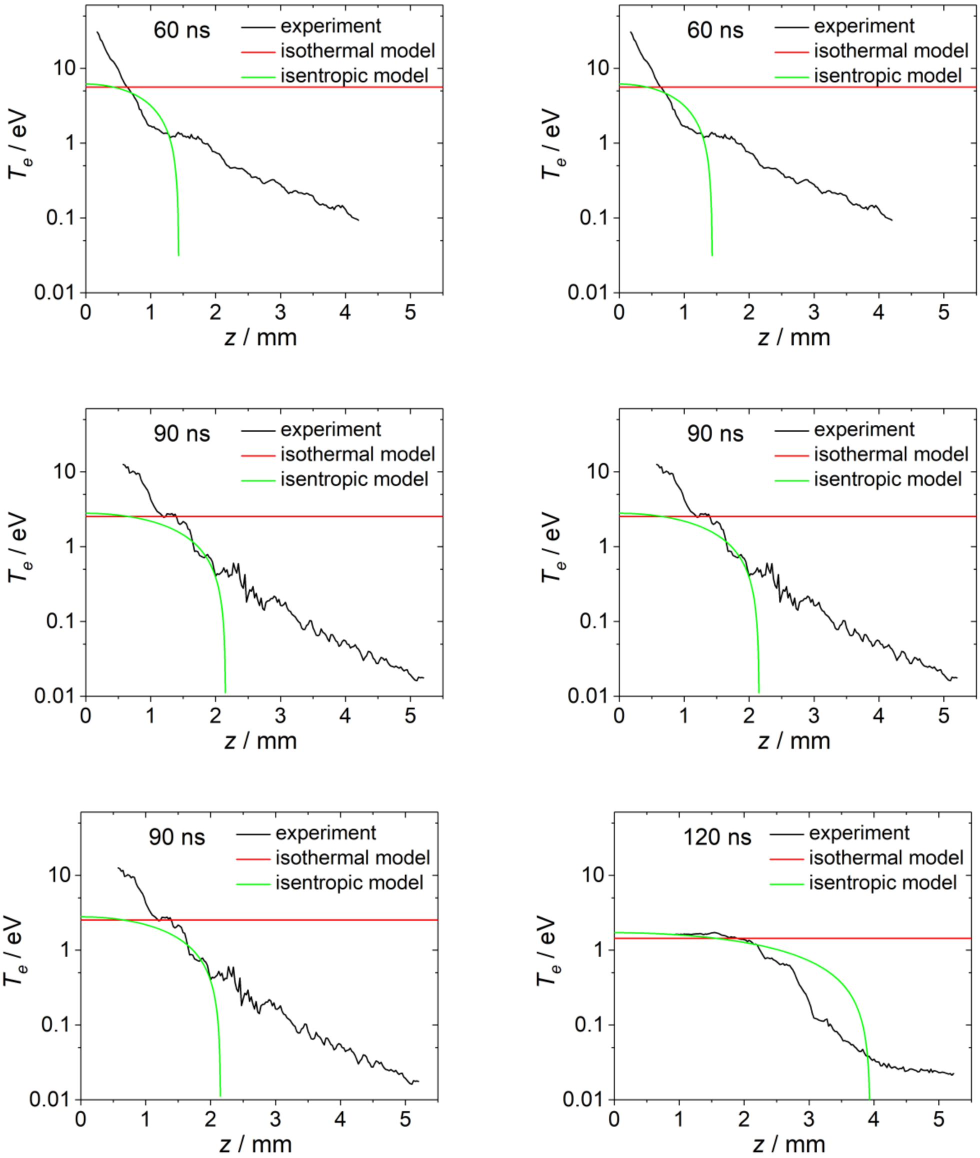

Figure A.2: Evolution of electron temperature at time, after laser ablation of a pure Si target determined from the model of Stapleton et al and the adiabatic and isentropic assumptions of said model, with inputs taken from POLLUX simulations. Left: 532 nm laser ablation. Right: 1064 nm. [207]

## Appendix B

# List of publications and communications

*Prior to the publication of this thesis, work contained has been presented in the following:*

**Publications**

- H. Liu, M. N. R. Ashfold, D. Meehan, E. Wagenaars. Wavelength-dependent variations of the electron characteristics in laser-induced plasmas: a combined hydrodynamic and adiabatic expansion modelling and time-gated, optical emission imaging study. *Journal of Applied Physics.* In review. (2019)
- A. K. Rossall, J. A. van den Berg, D. Meehan, S. Rajendiran, E. Wagenaars. Analysis of plasma enhanced pulsed laser deposition of transition metal oxide thin films using medium energy ion scattering. *Nuclear Inst. and Methods in Physics Research B*, In press, https://doi.org/10.1016/j.nimb.2018.06.023. (2018)

**Oral presentations**

- **E. Wagenaars**, D. Meehan, S. Rajendiran, A. K. Rossall. Plasma-Enhanced Pulsed Laser Deposition of metal-oxide thin films. $71^{st}$ *Gaseous Electronics Conference.*(2018)
- **D. Meehan**, S. Rajendiran, J. Barnard. A. K. Rossall, S. Schrøter, A. R. Gibson, E. Wagenaars. Plasma-Enhanced Pulsed Laser Deposition: Proof of concept & Gas temperature measurements of low pressure O2 plasmas. *International online plasma seminar series*(2018)

- **D. Meehan**, S. Rajendiran, J. Barnard, A. K. Rossall, E. Wagenaars. Comparisons between laser ablation of metal and oxide targets, and applications towards Plasma Enhanced-Pulsed Laser Deposition.20th *Workshop on the Exploration of Low-Temperature Plasma Physics.* (2017)

- **D. Meehan**, S. Rajendiran, A. K. Rossall, E. Wagenaars. Comparisons between laser ablation of metal and oxide targets, and applications towards Plasma Enhanced-Pulsed Laser Deposition.15th *Technological Plasma Workshop.*. (2017)

- **D. Meehan**, S. Rajendiran, E. Wagenaars. Laser ablation of metal and oxide targets, and applications towards Plasma Enhanced-Pulsed Laser Deposition.*IoP IPSI: Plasmas, Surfaces and Thin Films: Early Careers Researchers' Meeting.* (2017)

**Poster presentations**

- **D. Meehan**, S. Schrøter, A. R. Gibson, K. Niemi, E. Wagenaars. Gas temperature measurements in low pressure oxygen plasmas by the $O_2(b^1\Sigma_g^+, v = 0) \rightarrow_2 (X^3\Sigma_g^-, v = 0)$ band, with the effect of pulsing. 24th *Europhysics Conference on the Atomic and Molecular Physics of Ionized Gases.*(2018)

- **D. Meehan**, A. K. Rossall, J. A. van den Berg, S. Rajendiran, J. Barnard, L. Lari, E. Wagenaars. Composition of metal oxide films as a function of depth deposited by plasma enhanced pulsed laser deposition: comparison of MEIS and EDX. 24th *Europhysics Conference on the Atomic and Molecular Physics of Ionized Gases.*(2018)

- S. Rajendiran, D. Meehan, **E. Wagenaars**. Plasma- Enhanced Pulsed Laser Deposition: Proof-of-concept for copper oxide thin films. 24th *Europhysics Conference on the Atomic and Molecular Physics of Ionized Gases.*(2018)

- **D. Meehan**, S. Rajendiran, J. Barnard, L. Lari, A. K. Rossall, E. Wagenaars. Plasma Enhanced-Pulsed Laser Deposition: Proof Of Concept. 45th *IoP Plasma Physics Conference*(2018).

- **D. Meehan**, A. R. Gibson, K. Niemi, T. Gans, J. P. Booth, E. Wagenaars. Measuring atomic oxygen densities in an inductively coupled plasma for thin film deposition. 69th *Gaseous Electronics Conference.*(2016).

- **D. Meehan**, E. Wagenaars. Zinc Ablation for Plasma-Enhanced Pulsed Laser Deposition. *IoP IPSI: Plasmas, Surfaces and Thin Films: Early Careers Researchers' Meeting* (2016).

# List of References

[1] S. Rajendiran, A. Rossall, A. Gibson, and E. Wagenaars. Modelling of laser ablation and reactive oxygen plasmas for pulsed laser deposition of zinc oxide. *Surface and Coatings Technology*, 260:417-423, 2014.

[2] S. Rajendiran. Plasma enhanced pulsed laser deposition. *PhD Thesis, University of York*, 2017.

[3] Y. Zhang. ZnO nanostructures: Fabrication and Applications. *Wiley-VCH*, 2017.

[4] H. Morkoç and U. Özgur. Zinc oxide: Fundamentals, materials and device technology. *Wiley-VCH*, 2009.

[5] G. Papadimitropoulos, N. Vourdas, V. Vamvakas, and D. Davazoglou. Deposition and characterization of copper oxide thin films. *Journal of Physics: Conference Series*, 10:182-185, 2005.

[6] M. Al-Kuhaili. Characterization of copper oxide thin films deposited by the thermal evaporation of cuprous ($Cu_2O$). *Vacuum*, 82(6):623-629, 2008.

[7] A. Sayem Rahman, M. Islam, and K. Shorowordi. Electrodeposition and characterization of copper oxide thin films for solar cell applications. *Procedia Engineering*, 105:679-685, 2015.

[8] S. Nasser, M. Alsloum, and N. Hussain. Preparing of copper oxides thin films by chemical bath deposition (CBD) for using in environmental application. *Energy Procedia*, 74:1459-1465, 2015.

[9] R. Eason. Pulsed laser deposition of thin films: Applications-Led Growth of Functional Materials. *Wiley*, 2006.

[10] G. Hubler. Pulsed laser deposition. *MRS Bulletin*, 17(2), 1992.

[11] M. N. Ashfold, F. Claeyssens, G. M. Fuge, and S. J. Henley. Pulsed laser ablation and deposition of thin films. *Chemical Society Reviews*, 33(1):23-31, 2004.

[12] D. Smith. Thin-Film Deposition: Principles and Practice 1st Ed. *Mcgraw-Hill College Publishing*, 1994.

[13] H. M. Smith and A. Turner. Vacuum deposited thin films using a ruby laser. *Applied Optics*, 4(1):147-148, 1965.

[14] A. Moholkar, S. Shinde, A. Babar, K. Sim, Y. Kwon, K. Rajpure, B. C. Patil, P.S., and J. Kim. Development of CZTS thin films solar cells by pulsed laser deposition: Influence of pulse repition rate. *Solar Energy*, 85(7):1354-1363, 2011.

[15] K. Matsubara, P. Fons, K. Iwata, A. Yamada, K. Sakurai, H. Tampo, and S. Niki. ZnO transparent conducting films depostited by pulsed laser deposition for solar cell applications. *Thin Solid Films*, 431(1):431-432, 2003.

[16] H. Kim, A. Pique, H. Murata, Z. Kafafi, C. Gilmore, and D. Chrisey. Effect of aluminum doping on zinc oxide thin films grown by pulsed laser deposition for organic light-emitting devices. *Thin Solid Films*, 377:798-802, 2000.

[17] S. Tang, M. Lai, and L. Lu. Li-ion diffusion in highly (0 0 3) oriented $LiCoO_2$ thin film cathode prepared by pulsed laser deposition. *Journal of Alloys and Compounds*, 449(1):300-303, 2008.

[18] N. Kuwata, R. Kumar, K. Toribami, T. Suzuki, T. Hattoi, and J. Kawamura. Thin film lithium ion batteries prepared only by pulsed laser deposition. *Solid State Ionics*, 177(26):2827-2832, 2006.

[19] M. Park, G. Wang, H. Liu, and S. Dou. Electrochemical properties of Si thin film prepared by pulsed laser deposition for lithium ion micro-batteries. *Electrochimica Acta*, 51(25):5246-5249, 2006.

[20] B. Jin, S. Im, and S. Lee. Violet and UV luminescence emitted from ZnO thin films grown on sapphire by pulsed laser deposition. *Thin Solid Films*, 366(1):107-110, 2000.

[21] A. Singh, R. Mehra, N. Buthrath, A. Wakahara, and A. Yoshida. Highly conductive and transparent aluminum-doped zinc oxide thin films prepared by pulsed laser deposition in oxygen ambient. *Jounral of Applied Physics*, 90(11):5661-5665, 2001.

[22] E. Hecht. Optics, 5th ed. *Pearson Eduction*, 2017.

[23] H. J., J. W. Bartha, C. C. Poon, and A. C. Tam. Temperature dependence of the reflectivity of silicon with surface oxide at wavelengths 633 and 1047 nm. *Applied Physics Letters*, 75, 1999.

[24] T. T. D. Huynh and N. Semmar. In situ probing of pulsed laser melting and laser-induced periodic surface structures formation by dynamic reflectivity. *Surface Topography: Metrology and Properties*, 5(3):5003-5015, 2017.

[25] T. G. Mayerhöfer, H. Mutschke, and J. Popp. Employing theories far beyond their limits—the case of the (Boguer-) Beer-Lambert law. *Chem Phys Chem*, 17(13):1948-1955, 2016.

[26] D. Bäuerle. Laser Processing and Chemistry, 4th ed. *Springer*, 2011.

[27] S. Link, C. Burda, M. B. Mohamed, B. Nikoobakht, and M. A. El-Sayed. Laser photothermal melting and fragmentation of gold nanorods: Energy and laser pulse-width dependance. *Journal of Physical Chemistry A*, 103(9):1165-1170, 1999.

[28] B. N. Chichkov, C. Momma, S. Nolte, F. von Alvensleben, and A. Tünnermann. Femtosecond, picosecond and nanosecond laser ablation of solids. *Applied Physics A*, 63(2):109-115, 1996.

[29] A. Ng, D. Pasini, C. P., D. Parfeniuk, L. Da Silva, and J. Kwan. Ablation scaling in steady-state ablation dominated by inverse-bremsstrahlung absorption. *Applied Physics Letters*, 45(10):1046, 1984.

[30] J. F. Seely and E. G. Harris. Heating of a plasma by inverse bremsstrahlung. *Physical Review A*, 7(3):1064, 1974.

[31] G. J. Tallents. An introduction to the atomic and radiation physics of plasmas. *Cambridge Univeristy Press*, 2018.

[32] A. W. Miziolek, V. Palleschi, and I. Schechter. Laser induced breakdown spectroscopy. *Cambridge Univeristy Press*, 2006.

[33] G. Mainfra and C. Manus. Multiphoton ionization of atoms. *Reports on Progress in Physics*, 54(10):1333, 1991.

[34] T. Ando and N. Mori. Electro-optical-phon interaction in single and double heterostructures. *Physical Review B*, 40(9):6175, 1989.

[35] P. Chabert and N. Braithwaite. Physics of radio-frequency plasmas. *Cambridge Univeristy Press*, 2011.

[36] I. H. Hutchinson. Principles of plasma diagnostics. *Plasma Physics and Controlled Fusion*, 44(12):2603, 2002.

[37] R. Kelly and A. Miotello. Pulsed-laser sputtering of atoms and molecules. part I: Basic solutions for gas-dynamic effects. *Applied Physics B*, 57(2):145-158, 1993.

[38] R. Kelly and R. Dreyfus. On the effect of knudsen-layer formation on studies of vaporization, sputtering, and desorption. *Surface Science*, 198(1-2):263-276, 1988.

[39] T. Ytrehus. Theory and experiments on gas kinetics in evaporation. *Rarefied Gas Dynamics. Progress in Aeronautics*, 51:1197-1212, 1977.

[40] C. Cercignani. Strong evaporation of a polyatomic gas. *Progress in Astronautics and Aeronautics*, 74:305-320, 1981.

[41] S. Anisimov, B. Luk'Yanchuk, and A. Luches. An analytical model for three-dimensional laser plume expansion into vacuum in hydrodynamic regime. *Applied Surface Science*, 96:24-32, 1996.

[42] M. Stapleton, A. McKiernan, and J.-P. Mosnier. Expansion dynamics and equilibrium conditions in a laser ablation plume of lithium: Modeling and experiment. *Journal of Applied Physics*, 97(6):064904, 2005.

[43] S. Harilal, C. Bindhu, M. Tillack, F. Najmabadi, and A. Gaeris. Internal structure and expansion dynamics of laser ablation plumes into ambient gases. *Journal of Applied Physics*, 93(5):2380, 2003.

[44] K. Orsel, R. Groenen, H. M. Bastiaens, G. Koster, G. Rijnders, and K.-J. Boller. Spatial and temporal mapping of Al and AlO during oxidation in pulsed laser ablation of $LaAlO_3$. *Journal of Instrumentation*, 8(10):10021, 2013.

[45] P. Schaaf. Laser-Induced Breakdown Spectroscopy: $1^{st}$ Ed. *Singh, J. and Thakur, S.*, 2007.

[46] P. Barna and M. Adamik. Fundamental structure forming phenomena of polycrystalline films and the structure zone models. *Thin Solid Films*, 317(1):27-33, 1998.

[47] I. Petrov, P. Barna, L. Hultman, and J. Greene. Microstructural evolution during film growth. *Journal of Vacuum Science & Technology A: Vacuum, Surfaces, and Films*, 21(5):117-128, 2003.

[48] A. Y. Cho and J. R. Arthur. Molecular beam epitaxy. *Progress in Solid-State Chemistry*, 10(3):157-191, 1975.

[49] X. L. Li, C. X. Wang, and G. W. Yang. Thermodynamic theory of growth of nanosctructures. *Progress in Materials Science*, 64:121-199, 2014.

[50] M. Lieberman and A. Lichtenberg. Principles of plasma discharges and materials processing. *Wiley-Interscience*, 2nd Edition, 2005.

[51] J. Hopwood. Review of inductively coupled plasmas for plasma processing. *Plasma Sources Science and Technology*, 1(109):109-116, 1992.

[52] H. Conrads and M. Schmidt. Plasma generation and plasma sources. *Plasma Sources Science and Technology*, 9(4):441-454, 2000.

[53] C. Tendero, C. Tixier, P. Tristant, J. Desmaison, and P. Leprince. Atomsopheric pressure plasmas: A review. *Spectrochimica Acta Part B*, 61(1):2-30, 2006.

[54] S. N. Bathgate. Electrodless plasma thrusters for spacecraft: a review. *Plasma Science and Technology*, 19:083001, 2017.

[55] F. Paschen. Ueber die zum funkenübergang in luft, wasserstoff und kohlensäure bei verschiedenen drucken erforderliche potentialdifferenz. *Annalen der Physik*, 1889.

[56] J. C. Biswas and V. Mitra. High-frequency breakdown and paschen law. *Applied Physics*, 19(4):377-381, 1979.

[57] R. Massarczyk, P. Chu, C. Dugger, S. R. Elliott, K. Rielage, and W. Xu. Paschen's law studies in cold gases. *Journal of Instrumentation*, 12(6):06019, 2017.

[58] V. Lisovskiy, S. Yakovin, and V. Yegorenkov. Low-pressure gas breakdown in uniform dc electric field. *Journal of Physics D: Applied Physics*, 33(21):2722, 2000.

[59] U. Kortshagen, N. D. Gibson, and J. E. Lawler. On the E-H mode transition in RF inductive discharges. *Journal of Physics D: Applied Physics*, 29:1224, 1996.

[60] T. Wegner, C. Küllig, and J. Meichsner. On the EH transition in inductively coupled radio frequency oxygen plasmas: I. density and temperature of electrons, ground state and singlet metastable molecular oxygen. *Plasma Sources Science and Technology*, 26(2):025006, 2017.

[61] G. Cristoforetti, A. De Giacomo, M. Dell'Aglio, S. Legnaioli, E. Tognoni, V. Palleschi, and N. Omenetto. Local thermodynamic equilibrium in laser-induced breakdown spectroscopy: beyond the McWhirter criterion. *Spectrochimica Acta Part B: Atomic Spectroscopy*, 65(1):86-95, 2010.

[62] E. Fortunato, P. Barquinha, and R. Martins. Oxide semiconductor thin-film transistors: a review of recent advances. *Advanced Materials*, 24(22):2945-2986, 2012.

[63] H. Soonmin. A review on copper oxide thin films. *International Journal of Recent Scientific Research*, 7(6):11914-11918, 2008.

[64] L. Olsen, F. Addis, and W. Miller. Experimental and theoretical studies of $Cu_2O$ solar cells. *Solar Cells*, 7(3):247-279, 1982.

[65] K. Akimoto, S. Ishizuka, M. Yanagita, Y. Nawa, G. K. Paul, and T. Sakurai. Thin film deposition of $Cu_2O$ and application for solar cells. *Solar Energy*, 80(6):715-722, 2006.

[66] H. Al-Jawhari. A review of recent advances in transparent p-type $Cu_2O$-based thin film transistors. *Materials Science in Semiconductor Processing*, 40:241-252, 2015.

[67] S. Gražulis, D. Chateigner, R. T. Downs, A. Yokochi, M. Quirós, L. Lutterotti, E. Manakova, J. Butkus, P. Moeck, and A. Le Bail. Crystallography open database–an open-access collection of crystal structures. *Journal of Applied Crystallography*, 42(4):726-729, 2009.

[68] K. Momma and F. Izumi. Vesta: a three-dimensional visualization system for electronic and structural analysis. *Journal of Applied Crystallography*, 41(3):653-658, 2008.

[69] A. Ashrafi and C. Jagadish. Review of zincblende ZnO: Stability of metastable ZnO phases. *Journal of Applied Physics*, 102(7):4, 2007.

[70] A. Kołodziejczak-Radzimska and T. Jesionowski. Zinc oxide- From synthesis to application: A Review. *Materials*, 7(4):2833-2881, 2014.

[71] M. Girtan. Comparison of ITO/metal/ITO and ZnO/metal/ZnO characteristics as transparent electrodes for third generation solar cells. *Solar Energy Materials and Solar Cells*, 100:153-161, 2012.

[72] D. J. Cooke, A. Marmier, and S. C. Parker. Surface structure of (1010) and (1120) surfaces of ZnO with density functional theory and atomistic simulation. *The Journal of Physical Chemistry B*, 110(15):7985-7991, 2006.

[73] P. Mark, S. Chang, W. Creighton, and B. Lee. A comparison of some important surface properties of elemental and tetrahedrally coordinated compound semiconductors. *Critical Reviews in Solid State and Material Sciences*, 5(2):189-229, 1975.

[74] K. Fujimoto, T. Oku, T. Akiyama, and A. Suzuki. Fabrication and characterization of copper oxide-zinc oxide solar cells prepared by electrodeposition. *Journal of Physics: Conference Series*, 433(1):012024, 2013.

[75] D. Stoychev, P. Stefanov, D. Nikolova, A. Aleksandrova, G. Atanasova, and T. Marinova. Preparation of $Al_2O_3$ thin films on stainless steel by electrochemical deposition. *Surface and Coatings Technology*, 180:441-445, 2004.

[76] J. Masalski, J. Gluszek, J. Zabrzeski, K. Nitsch, and P. Gluszek. Improvement in corrosion resistance of the 316l stainless steel by means of $Al_2O_3$ coatings deposited by the sol-gel method. *Thin Solid Films*, 349(1-2):186-190, 1999.

[77] L. Marot, C. Linsmeier, B. Eren, L. Moser, R. Steiner, and E. Meyer. Can aluminium or magnesium be a surrogate for beryllium: A critical investigation of their chemistry. *Fusion Engineering and Design*, 88(9):1718-721, 2013.

[78] D. Ivanova, et al. An overview of the comprehensive first mirror test in JET with ITER-like wall. *Physica Scripta*, 2014(159):014011, 2014.

[79] L. Moser, L. Marot, B. Eren, R. Steiner, D. Mathys, F. Leipold, R. Reichle, and E. Meyer. Towards plasma cleaning of ITER first mirrors. *Nuclear Fusion*, 55(6):063020, 2015.

[80] D. Shaw. *Removal of fusion-relevant deposits from metallic surfaces using low-temperature plasmas*. Ph.D. thesis, University of York, 2018.

[81] H. Oechsner. Sputtering - a review of some recent experimental and theoretical aspects. *Applied Phsyics*, 8(3):185198, 1975.

[82] P. J. Kelly and R. D. Arnell. Magnetron sputtering; a review of recent developments and applications. *Vacuum*, 56(3):159-172, 2000.

[83] K. Choy. Chemical vapour deposition of coatings. *Progress in Materials Science*, 48(2):57-170, 2003.

[84] D. L. Plata, A. J. Hart, C. M. Reddy, and P. M. Gschwend. Early evaluation of potential environmental impacts of carbon nanotube synthesis by chemical vapor deposition. *Environmental Science & Technology*, 43(21):8367-8373, 2009.

[85] O. G. Griffiths, J. P. O'Byrne, L. Torrente-Murciano, M. D. Jones, D. Mattia, and M. C. McManus. Identifying the largest environmental life cycle impacts during carbon nanotube synthesis via chemical vapour deposition. *Journal of Cleaner Production*, 42:180-189, 2013.

[86] J. Perrin, J. Schmit, C. Hollenstein, A. Howling, and L. Sansonnens. The physics of plasma-enhanced chemical vapour deposition for large-area coating: Industrial application to flat panel displays and solar cells. *Plasma Physics Control Fusion*, 42, 2000.

[87] K. Sarakinos, J. Alami, and S. Konstantinidis. High power pulsed magnetron sputtering: A review on scientific and engineering state of the art. *Surface & Coatings Technology*, 204(11):1661-1684, 2010.

[88] A. De Giacomo, V. Shakhatov, G. Senesi, and S. Orlando. Spectroscopic investigation of the technique of plasma assisted pulsed laser deposition of titanium dioxide. *Spectrochimica Acta Part B: Atomic Spectroscopy*, 56(8):1459-1472, 2001.

[89] S. Huang, Y. Chou, C. Chou, and V. Hsiao. Room temperature radio-frequency plasma-enhanced pulsed laser deposition of ZnO thin films. *Applied Surface Science*, 266:194-198, 2013.

[90] N. Scarisoreanu, D. Matei, G. Dinescu, G. Epurescu, C. Ghica, L. Nistor, and M. Dinescu. Properties of ZnO thin films prepared by radio-frequency plasma beam assisted laser ablation. *Applied Surface Science*, 247(1):518-525, 2005.

[91] L. Nistor, C. Ghica, D. Matei, G. Dinescu, M. Dinescu, and G. Van Tendeloo. Growth and characterization of a-axis textured ZnO thin films. *Journal of Crystal Growth*, 277(14):26-31, 2005.

[92] P. Miller, G. Hebner, K. Greenberg, P. Pochan, and B. Aragon. An inductively coupled plasma source for the gaseous electronics conference rf reference cell. *Journal of Research of the Natlional Institute of Standards and Technology*, 100(2):427-439, 1995.

[93] S. Gomez, P. Steen, and W. Graham. Atomic oxygen surface loss coefficient measurements in a capacitive/inductive radio-frequency plasma. *Applied Physics Letters*, 81(1):19-21, 2002.

[94] C. Corr, S. Gomez, and W. Graham. Discharge kinetics of inductively coupled oxygen plasmas: experiment and model. *Plasma Sources Science and Technology*, 21(5):055024, 2012.

[95] A. R. Gibson, M. Foucher, D. Marinov, P. Chabert, T. Gans, M. J. Kushner, and J.-P. Booth. The role of thermal energy accommodation and atomic recombination probabilities in low pressure oxygen plasmas. *Plasma Physics and Controlled Fusion*, 59(2):024004, 2017.

[96] M. Abdel-Rahman, T. Gans, V. Schulz-Von Der Gathen, and H. Döbele. Space and time resolved rotational state populations and gas temperatures in an inductively coupled hydrogen rf discharge. *Plasma Sources Science and Technology*, 14(1):51, 2005.

[97] H. Abada, P. Chabert, J. P. Booth, J. Robiche, and G. Cartry. Gas temperature gradients in a $CF_4$ inductive discharge. *Journal of Applied Physics*, 92(8):4223-4230, 2002.

[98] J.-P. Booth, D. Marinov, M. Foucher, O. Guaitella, D. Bresteau, L. Cabaret, and C. Drag. Gas temperature measurements in oxygen plasmas by high-resolution two-photon absorption laser-induced fluorescence. *Journal of Instrumentation*, 10(11):C11003, 2015.

[99] C. J. Sansonetti, M. L. Salit, and J. Reader. Wavelengths of spectral lines in mercury pencil lamps. *Applied Optics*, 35(1):74-77, 1996.

[100] J. Noxon. Observation of the $(\mathrm{b}^1\Sigma_g^+ \rightarrow a^1\Delta_g)$ transition in $\mathrm{O}_2$. *Canadian Journal of Physics*, 39(8):1110-1119, 1961.

[101] M. Touzeau, M. Vialle, A. Zellagui, G. Gousset, M. Lefebvre, and M. Pealat. Spectroscopic temperature measurements in oxygen discharges. *Journal of Physics D: Applied Physics*, 24(1):41-47, 1991.

[102] P. Veis and G. Cernogora. Study of oxygen recombination with a double pulse discharge. *Czechoslovak Journal of Physics*, 48(1):75-87, 1998.

[103] S. Zyryanov and D. Lopaev. Measurements of the gas temperature in an oxygen plasma by spectroscopy. *Plasma Physics Reports*, 33(6):510-520, 2007.

[104] G. Herzberg. Molecular Structure and Molecular Spectra I. Spectra of Diatomic Molecules. *Van Nostrand, New York*, 1950.

[105] R. Schlapp. Fine structure in the $\Sigma^3$ ground state of the oxygen molecule, and the rotational intensity distribution in the atmospheric oxygen band. *Physical Review*, 51(5):342, 1937.

[106] C. M. Western. PGOPHER: A program for simulating rotational, vibrational and electronic spectra. *Journal of Quantitative Spectroscopy and Radiative Transfer*, 186:221-242, 2017.

[107] A. Wijaikhum, D. Schröder, S. Schröter, A. R. Gibson, K. Niemi, J. Friderich, A. Greb, V. Schulz-von der Gathen, D. O'Connell, and T. Gans. Absolute ozone densities in a radio-frequency driven atmospheric pressure plasma using two-beam UV-LED absorption spectroscopy and numerical simulations. *Plasma Sources Science and Technology*, 26(11):115004, 2017.

[108] P. Bruggeman, N. Sadeghi, D. Schram, and V. Linss. Gas temperature determination from rotational lines in non equilibrium plasmas: a review. *Plasma Sources Science and Technology*, 23(2):023001, 2014.

[109] F. Roux, F. Michaud, and M. Vervloet. High-resolution fourier spectrometry of $^{14}N_2$ violet emission spectrum: extensive analysis of the $\mathrm{C}^3\Pi_u \rightarrow B^3\Pi_g$ system. *Journal of Molecular Spectroscopy*, 158(2):270-277, 1993.

[110] Q. Wang, F. Doll, V. M. Donnelly, D. J. Economou, N. Sadeghi, and G. F. Franz. Experimental and theoretical study of the effect of gas flow on gas temperature in an atmospheric pressure microplasma. *Journal of Physics D: Applied Physics*, 40(14):4202, 2007.

[111] V. Donnelly and M. Malyshev. Diagnostics of inductively coupled chlorine plasmas: Measurements of the neutral gas temperature. *Applied Physics Letters*, 77(16):2467-2469, 2000.

[112] G. Herzberg. Molecular spectra and molecular structure. I. Spectra of diatomic molecules. *American Journal of Physics*, 19(6):390-391, 1951.

[113] I. Kovacs. Formulae for rotational intensity distribution of triplet transitions in diatomic molecules. *The Astrophysical Journal*, 145:634, 1966.

[114] A. Schadee. Theory of first rotational lines in transitions of diatomic molecules. *Astronomy and Astrophysics*, 41:203, 1975.

[115] S. Pellerin, K. Musiol, O. Motret, B. Pokrzywka, and J. Chapelle. Application of the (0, 0) Swan band spectrum for temperature measurements. *Journal of Physics D: Applied Physics*, 29(11):2850, 1996.

[116] S. Reuter, J. S. Sousa, G. D. Stancu, and J.-P. H. van Helden. Review on VUV to MIR absorption spectroscopy of atmospheric pressure plasma jets. *Plasma Sources Science and Technology*, 24(5):054001, 2015.

[117] D. O'Connell, T. Gans, D. Crintea, U. Czarnetzki, and N. Sadeghi. Neutral gas depletion mechanisms in dense low-temperature argon plasmas. *Journal of Physics D: Applied Physics*, 41(3):035208, 2008.

[118] S. Schröter, H. Bahre, M. Böke, and J. Winter. The role of argon metastables in an inductively coupled plasma for treatment of pet. *Plasma Processes and Polymers*, 11(3):239-246, 2014.

[119] B. Clarenbach, B. Lorenz, M. Krämer, and N. Sadeghi. Time-dependent gas density and temperature measurements in pulsed helicon discharges in argon. *Plasma Sources Science and Technology*, 12(3):345, 2003.

[120] K. Niemi, S. Reuter, L. Graham, J. Waskoenig, N. Knake, V. Schulz-Von Der Gathen, and T. Gans. Diagnostic based modelling of radio-frequency driven atmospheric pressure plasmas. *Journal of Physics D: Applied Physics*, 43(12):124006, 2010.

[121] P. Tian and M. J. Kushner. Controlling VUV photon fluxes in pulsed inductively coupled Ar/$Cl_2$ plasmas and potential applications in plasma etching. *Plasma Sources Science and Technology*, 26(2):024005, 2017.

[122] J. T. Gudmundsson and E. Thorsteinsson. Oxygen discharges diluted with argon: dissociation processes. *Plasma Sources Science and Technology*, 16(2):399, 2007.

[123] A. Bogner, P.-H. Jouneau, G. Thollet, D. Basset, and C. Gauthier. A history of scanning electron microscopy developments: towards "wet-STEM" imaging. *Micron*, 38(4):390-401, 2007.

[124] D. McMullan. Scanning electron microscopy 1928-1965. *Scanning*, 17(3):175-185, 1995.

[125] D. Krinsley. Advanced scanning electron microscopy and X-ray microanalysis. *Eos Transactions American Geophysical Union*, 69(35):821-821, 1988.

[126] K. Kanaya and S. Okayama. Penetration and energy-loss theory of electrons in solid targets. *Journal of Physics D: Applied Physics*, 5(1):43, 1972.

[127] D. B. Williams and C. B. Carter. The transmission electron microscope. *Transmission Electron Microscopy*, page 3-17, 1996.

[128] www.wavemetrics.com. IGOR Pro. accessed Jan. 2019.

[129] J. F. Ziegler, M. D. Ziegler, and J. P. Biersack. SRIM–the stopping and range of ions in matter (2010). *Nuclear Instruments and Methods in Physics Research Section B: Beam Interactions with Materials and Atoms*, 268(11-12):1818-1823, 2010.

[130] R. Tromp. Practical surface analysis. *Ion and Neutron Spectroscopy*, 2:577, 1992.

[131] T. Gustafsson, H. Lu, B. Busch, W. Schulte, and E. Garfunkel. High-resolution depth profiling of ultrathin gate oxides using medium-energy ion scattering. *Nuclear Instruments and Methods in Physics Research Section B: Beam Interactions with Materials and Atoms*, 183(1-2):146-153, 2001.

[132] J. v. d. Berg, G. Carter, D. Armour, M. Werner, R. Goldberg, E. Collart, P. Bailey, and T. Noakes. Damage profiles of ultrashallow B implants in Si and the Kinchin-Pease relationship. *Applied Physics Letters*, 85(15):3074-3076, 2004.

[133] D. Dorset. X-ray diffraction: a practical approach. *Microscopy and Microanalysis*, 4(5):513-515, 1998.

[134] R. Jenkins, T. Fawcett, D. Smith, J. Visser, M. Morris, and L. Frevel. JCPDS—international centre for diffraction data sample preparation methods in X-ray powder diffraction. *Powder Diffraction*, 1(2):51-63, 1986.

[135] A. Patterson. The scherrer formula for X-ray particle size determination. *Physical Review*, 56(10):978, 1939.

[136] G. Pert. Two-dimensional hydrodynamic models of laser-produced plasmas. *Journal of Plasma Physics*, 41(2):263-280, 1989.

[137] G. Pert. Models of Laser-Plasma Ablation. *Journal of Plasma Physics*, 35(1):43-74, 1986.

[138] G. Pert. Models of laser-plasma ablation. Part 2. Steady-state theory: self-regulating flow. *Journal of Plasma Physics*, 36(3):415-446, 1986.

[139] G. Pert. Models of laser-plasma ablation. Part 3. Steady-state theory: deflagration flow. *Journal of Plasma Physics*, 39(2):241-276, 1988.

[140] G. Pert. The hybrid model and its application for studying free expansion. *Journal of Fluid Mechanics*, 131:401-426, 1983.

[141] A. Rossall and D. Meehan. Pollux description. *Univeristy of York: Internal technical notes*, 2014-Ongoing.

[142] G. Pert. Quasi-lagrangian rezoning of fluid codes maintaining an orthogonal mesh. *Journal of Computational Physics*, 49(1):1-43, 1983.

[143] R. Courant, K. Friedrichs, and H. Lewy. Über die partiellen differenzengleichungen der mathematischen physik. *Mathematische Annalen*, 100(1):32-74, 1928.

[144] S. L. Thompson. ANEOS analytic equations of state for shock physics codes input manual. *SANDIA REPORT SAND*, page 892-951, 1990.

[145] C. H. Lupis. Chemical thermodynamics of materials. *Elsevier Science Publishing Co., Inc., 1983*, page 581, 1983.

[146] G. Pert. Approximations for the rapid evaluation of the Thomas-Fermi equation. *Journal of Physics B: Atomic, Molecular and Optical Physics*, 32(2):249, 1999.

[147] R. Latter. Temperature behavior of the Thomas-Fermi statistical model for atoms. *Physical Review*, 99(6):1854, 1955.

[148] J. McDougall and E. C. Stoner. The computation of Fermi-Dirac functions. *Physical Transactions of the Royal Society of London A*, 237(773):67-104, 1938.

[149] L. Spitzer Jr and R. Härm. Transport phenomena in a completely ionized gas. *Physical Review*, 89(5):977, 1953.

[150] J. P. Boris and D. L. Book. Flux-corrected transport. III. minimal-error FCT algorithms. *Journal of Computational Physics*, 20(4):397-431, 1976.

[151] J. P. Boris and D. L. Book. Flux-corrected transport. I. SHASTA, a fluid transport algorithm that works. *Journal of Computational Physics*, 11(1):38-69, 1973.

[152] D. L. Book, J. P. Boris, and K. Hain. Flux-corrected transport II: Generalizations of the method. *Journal of Computational Physics*, 18(3):248-283, 1975.

[153] D. S. Kershaw. The incomplete Cholesky-conjugate gradient method for the iterative solution of systems of linear equations. *Journal of Computational Physics*, 26(1):43-65, 1978.

[154] M. J. Kushner. Hybrid modelling of low temperature plasmas for fundamental investigations and equipment design. *Journal of Physics D: Applied Physics*, 42(19):194013, 2009.

[155] A. J. Lofthouse, L. C. Scalabrin, and I. D. Boyd. Velocity slip and temperature jump in hypersonic aerothermodynamics. *Journal of Thermophysics and Heat Transfer*, 22(1):38-49, 2008.

[156] J. F. Richardson and J. M. Coulson. *Chemical Engineering.: Fluid Flow, Heat Transfer and Mass Transfer.* Butterworth-Heinemann, 1999.

[157] E. Kemaneci, J.-P. Booth, P. Chabert, J. Van Dijk, T. Mussenbrock, and R. P. Brinkmann. A computational analysis of the vibrational levels of molecular oxygen in low-pressure stationary and transient radio-frequency oxygen plasma. *Plasma Sources Science and Technology*, 25(2):025025, 2016.

[158] D. Toneli, R. Pessoa, M. Roberto, and J. T. Gudmundsson. A volume averaged global model study of the influence of the electron energy distribution and the wall material on an oxygen discharge. *Journal of Physics D: Applied Physics*, 48(49):495203, 2015.

[159] S. Tinck and A. Bogaerts. Computer simulations of an oxygen inductively coupled plasma used for plasma-assisted atomic layer deposition. *Plasma Sources Science and Technology*, 20(1):015008, 2011.

[160] P. Cosby. Electron-impact dissociation of oxygen. *The Journal of Chemical Physics*, 98(12):9560-9569, 1993.

[161] S. Lawton and A. Phelps. Excitation of the b $^1\Sigma_g^+$ state of $O_2$ by low energy electrons. *The Journal of Chemical Physics*, 69(3):1055-1068, 1978.

[162] A. Phelps. Phelps database, LXCAT. *fr.lxcat.net*, Accessed Jan. 2019.

[163] M. Tashiro, K. Morokuma, and J. Tennyson. R-matrix calculation of electron collisions with electronically excited $O_2$ molecules. *Physical Review A*, 73(5):052707, 2006.

[164] Y. Itikawa and A. Ichimura. Cross sections for collisions of electrons and photons with atomic oxygen. *Journal of Physical and Chemical Reference Data*, 19(3):637, 1990.

[165] R. Hall and S. Trajmar. Scattering of 4.5 eV electrons by ground ($X^3\Sigma_g^-$) state and metastable ($a^1\Delta_g$ ) oxygen molecules. *Journal of Physics B: Atomic and Molecular Physics*, 8(12):L293, 1975.

[166] P. Burrow. Dissociative attachment from the $O_2$ (a $^1\Delta_g$) state. *The Journal of Chemical Physics*, 59(9):4922-4931, 1973.

[167] R. R. Laher and F. R. Gilmore. Updated excitation and ionization cross sections for electron impact on atomic oxygen. *Journal of Physical and Chemical Reference Data*, 19(1):277-305, 1990.

[168] H. Deutsch, P. Scheier, K. Becker, and T. Märk. Calculated cross-sections for the electron-impact detachment from negative ions using the Deutsch–Märk (DM) formalism. *Chemical Physics Letters*, 382(1-2):26-31, 2003.

[169] R. Peverall, et al. Dissociative recombination and excitation of $\mathrm{O}_2^+$: Cross sections, product yields and implications for studies of ionospheric airglows. *The Journal of Chemical Physics*, 114(15):6679-6689, 2001.

[170] A. Florescu-Mitchell and J. Mitchell. Dissociative recombination. *Physics Reports*, 430(5-6):277-374, 2006.

[171] J. Gudmundsson. A critical review of the reaction set for a low pressure oxygen processing discharge. *Technical Report*, RH-17-2004.

[172] S. G. Ard, J. J. Melko, B. Jiang, Y. Li, N. S. Shuman, H. Guo, and A. A. Viggiano. Temperature dependences for the reactions of $\mathrm{O}_2^-$ and $\mathrm{O}^-$ with N and O atoms in a selected-ion flow tube instrument. *The Journal of Chemical Physics*, 139(14):144302, 2013.

[173] A. Midey, I. Dotan, S. Lee, W. Rawlins, M. A. Johnson, and A. Viggiano. Kinetics for the Reactions of $\mathrm{O}^-$ and $\mathrm{O}_2^-$ -with $\mathrm{O}_2$ (a$\Delta_g$) Measured in a Selected Ion Flow Tube at 300 K. *The Journal of Physical Chemistry A*, 111(24):5218-5222, 2007.

[174] N. Aleksandrov. Electron detachment from $\mathrm{O}^-$ and $\mathrm{O}_2^-$ ions in excited molecules in an air discharge. *Soviet Physics-Technical Physics*, 23:806-808, 1978.

[175] M. Ziółkowski, G. C. Schatz, A. Viggiano, A. Midey, and I. Dotan. $\mathrm{O}_2$ (X $^3\Sigma_g^-$) and $\mathrm{O}_2$ (a $^1\Delta_g$) charge exchange with simple ions. *The Journal of Chemical Pysics*, 140(21):214307, 2014.

[176] I. Dotan. Rate constants and branching ratios for the reactions of $^{18}O^+$ and $^{18}O^{18}O^+$ ions with $^{16}O^{16}O$ measured at relative kinetic energies 0.04–eV. *Chemical Physics Letters*, 75(3):509-512, 1980.

[177] V. J. Abreu, J.-H. Yee, S. C. Solomon, and A. Dalgarno. The quenching rate of O (1D) by O (3P). *Planetary and Space Science*, 34(11):1143-1145, 1986.

[178] R. Atkinson, D. Baulch, R. Cox, J. Crowley, R. Hampson, R. Hynes, M. Jenkin, M. Rossi, and J. Troe. Evaluated kinetic and photochemical data for atmospheric chemistry: volume I-gas phase reactions of Ox, HOx, NOx and SOx species. *Atmospheric Chemistry and Physics*, 4:1461-1738.

[179] G. Streit, C. J. Howard, A. Schmeltekopf, J. Davidson, and H. Schiff. Temperature dependence of O (1 D) rate constants for reactions with $O_2$, $N_2$, $CO_2$, $O_3$, and $H_2O$. *The Journal of Chemical Physics*, 65(11):4761-4764, 1976.

[180] L. Lee and T. Slanger. Observations on O (1 D→3 P) and $O_2$ (b $^1\Sigma_g^+ \rightarrow X^3\Sigma_g^-$) following $O_2$ photodissociation. *The Journal of Chemical Physics*, 69(9):4053-4060, 1978.

[181] I. Clark and R. Wayne. The reaction of $O_2(1\Delta_g)$ with atomic nitrogen and with atomic oxygen. *Chemical Physics Letters*, 3(6):405-407, 1969.

[182] J. Burkholder, S. Sander, J. Abbat, J. Barker, R. Huie, C. Kolb, M. Kurylo, V. Orkin, D. Wilmouth, and P. Wine. Chemical kinetics and photochemical data for use in atmospheric studies. *JPL Publication*, (18), 2015.

[183] R. F. Heidner III, C. E. Gardner, T. El-Sayed, G. Segal, and J. Kasper. Temperature dependence of $O_2$ (1Δ)+ $O_2$ (1Δ) and I (2 P 1/2)+ $O_2$ (1Δ) energy pooling. *The Journal of Chemical Physics*, 74(10):5618-5626, 1981.

[184] J. Ihlemann, B. Wolff, and P. Simon. Nanosecond and femtosecond excimer laser ablation of fused silica. *Applied Physics A*, 54(4):363-368, 1992.

[185] S. H. Kim, I.-B. Sohn, and S. Jeong. Ablation characteristics of aluminum oxide and nitride ceramics during femtosecond laser micromachining. *Applied Surface Science*, 255(24):9717-9720, 2009.

[186] M. Qaisar and G. Pert. Laser ablation of Mg, Cu, and Pb using infrared and ultraviolet low-fluence lasers. *Journal of Applied Physics*, 94(3):1468-1477, 2003.

[187] U. Rossler. Semiconductors, II-VI and I-VII compounds: Semimagnetic compounds, vol 41b. *Landolt-Bornstein New Series, Group III*, 1999.

[188] A. Soon, M. Todorova, B. Delley, and C. Stampfl. Thermodynamic stability and structure of copper oxide surfaces: A first-principles investigation. *Physical Review B*, 75(12):125420, 2007.

[189] W. M. Haynes. *CRC Handbook of Chemistry and Physics*. CRC press, 2014.

[190] V. Coleman and C. Jagadish. Zinc oxide bulk, thin films and nanostructures. *UK, Elsevier*, page 1-5, 2006.

[191] C. Ho, R. Powell, and P. Liley. Thermal conductivity of the elements: A comprehensive review. *Jounral of physical and chemical reference data*, 3(1), 1974.

[192] M. Singh and M. Singh. Thermal expansion in zinc oxide nanomaterials. *Nanoscience and Nanotechnology Research*, 1(2):27-29, 2013.

[193] L. A. Neely, E. M. See, H. D. Robinson, and V. Kochergin. Thermal expansion of Cu (II) O nano-and micro-particles and composites at cryogenic temperatures. *Physica Status Solidi (B)*, 249(9):1698-1703, 2012.

[194] J. Hallberg and R. Hanson. The elastic constants of cuprous oxide. *Physica Status Solidi (B)*, 42(1):305-310, 1970.

[195] J. McCreary and R. Thorn. Enthalpy of sublimation of zinc and cadmium; correlation of $\Delta H^o$ vs $\Delta S^o$; comparison of Torsional and Knudsen vapor pressures. *The Journal of Chemical Physics*, 50(9):3725-3733, 1969.

[196] N. Simon, E. Drexler, and R. Reed. Properties of copper and copper alloys at cryogenic temperatures. *NIST Monograph*, 177, 1992.

[197] J. F. Shackelford, Y.-H. Han, S. Kim, and S.-H. Kwon. *CRC Materials Science and Engineering Handbook*. CRC press, 2016.

[198] A. Krivtsov and V. Kuz'kin. Derivation of equations of state for ideal crystals of simple structure. *Mechanics of Solids*, 46(3):387, 2011.

[199] S. Blackwell, R. Smith, S. D. Kenny, J. M. Walls, and C. F. Sanz-Navarro. Modelling the growth of ZnO thin films by PVD methods and the effects of post-annealing. *Journal of Physics: Condensed Matter*, 25(13):135002, 2013.

[200] Filmetrics. Filmetrics: Profilm 3D, www.filmetrics.com/profilometers/profilm3d. Accessed Jan. 2019.

[201] J. Dean. Properties of atoms, radicals, and bonds. *Lange's Handbook of Chemistry*, 15(4), 1999.

[202] J. Bilello, D. Dew-Hughes, and A. Pucino. The surface energy of zinc. *Journal of Applied Physics*, 54(4):1821-1826, 1983.

[203] J. Sugar and A. Musgrove. Energy levels of copper, Cu I through Cu XXIX. *Journal of Physical and Chemical Reference Data*, 19(3):527-616, 1990.

[204] M. A. Liberman and A. L. Velikovich. Physics of shock waves in gases and plasmas. *Springer Verlag Springer Series on Electrophysics*, 19, 1986.

[205] A. K. Rossall, V. Aslanyan, G. J. Tallents, I. Kuznetsov, J. J. Rocca, and C. S. Menoni. Ablation of submicrometer holes using an extreme-ultraviolet laser. *Physical Review Applied*, 3(6):064013, 2015.

[206] A. Bogaerts, Z. Chen, R. Gijbels, and A. Vertes. Laser ablation for analytical sampling: what can we learn from modeling? *Spectrochimica Acta Part B: Atomic Spectroscopy*, 58(11):1867-1893, 2003.

[207] H. Liu, M. N. Ashfold, D. Meehan, and E. Wagenaars. Wavelength-dependent variations of the electron characteristics in laser-induced plasmas: a combined hydrodynamic and adiabatic expansion modelling and time-gated, optical emission imaging study. *Journal of Applied Physics*, 125(8):083304, 2019.

[208] O. Madelung, U. Rossler, and S. M. Silicon (Si), Debye temperature, heat capacity, density, hardness, melting point. *Group IV Elements, IV-IV and III-V Compounds. Part B - Electronic, Transport, Optical and Other Properties*, 41:1-16, 2002.

[209] R. K. Singh and J. Narayan. Pulsed-laser evaporation technique for deposition of thin films: Physics and theoretical model. *Physical Review B*, 41(13):8843, 1990.

[210] W. Wiese, J. Brault, K. Danzmann, V. Helbig, and M. Kock. Unified set of atomic transition probabilities for neutral argon. *Physical Review A*, 39(5):2461, 1989.

[211] R. Zaplotnik, A. Vesel, and M. Mozetic. Transition from E to H mode in inductively coupled oxygen plasma: Hysteresis and the behaviour of oxygen atom density. *EPL (Europhysics Letters)*, 95(5):55001, 2011.

[212] O. Braginskiy, A. Vasilieva, K. Klopovskiy, A. Kovalev, D. Lopaev, O. Proshina, T. Rakhimova, and A. Rakhimov. Singlet oxygen generation in $O_2$ flow excited by RF discharge: I. homogeneous discharge mode: $\alpha$-mode. *Journal of Physics D: Applied Physics*, 38(19):3609, 2005.

[213] I. Kossyi, A. Y. Kostinsky, A. Matveyev, and V. Silakov. Kinetic scheme of the non-equilibrium discharge in nitrogen-oxygen mixtures. *Plasma Sources Science and Technology*, 1(3):207, 1992.

[214] T. Slanger and G. Black. Interactions of $O_2$ (b $^1\Sigma_g^+$) with O (3 P) and $O_3$. *The Journal of Chemical Physics*, 70(7):3434-3438, 1979.

[215] K. Becker, H. Engels, and T. Tatarczyk. Lifetime measurements of the c $^3\Pi^u$ state of nitrogen by laser-induced fluorescence. *Chemical Physics Letters*, 51(1):111-115, 1977.

[216] C. Smith, J. Brandon, S. Shannon, P. Tian, M. Kushner, and S.-K. Nam. Self-consistent circuit model for pulsed inductively coupled plasmas. *Bulletin of the American Physical Society*, 2018.

[217] C. Qu, S. Lanham, P. Tian, C. Smith, K. Ford, J. Brandon, S. Shannon, and M. J. Kushner. Consequences of EH transitions in impendence matching of pulsed inductively coupled plasmas. *Bulletin of the American Physical Society*, 2018.

[218] P. Macko and P. Veis. Time resolved $O_2$ (b) rotational temperature measurements in a low-pressure oxygen pulsed discharge. simple and quick method for temperature determination. *Journal of Physics D: Applied Physics*, 32(3):246, 1999.

[219] M. Hübner, D. Marinov, O. Guaitella, A. Rousseau, and J. Röpcke. On time resolved gas temperature measurements in a pulsed dc plasma using quantum cascade laser absorption spectroscopy. *Measurement Science and Technology*, 23(11):115602, 2012.

[220] G. Cartry, X. Duten, and A. Rousseau. Atomic oxygen surface loss probability on silica in microwave plasmas studied by a pulsed induced fluorescence technique. *Plasma Sources Science and Technology*, 15(3):479, 2006.

[221] V. Guerra. Analytical model of heterogeneous atomic recombination on silicalike surfaces. *IEEE Transactions on Plasma Science*, 35(5):1397-1412, 2007.

[222] V. Guerra and D. Marinov. Dynamical Monte Carlo methods for plasma-surface reactions. *Plasma Sources Science and Technology*, 25(4):045001, 2016.

[223] E. Sartori, L. Brescaccin, and G. Serianni. Simulation of diatomic gas-wall interaction and accommodation coefficients for negative ion sources and accelerators. *Review of Scientific Instruments*, 87(2):02A502, 2016.

[224] Z. Liang, W. Evans, and P. Keblinski. Equilibrium and nonequilibrium molecular dynamics simulations of thermal conductance at solid-gas interfaces. *Physical Review E*, 87(2):022119, 2013.

[225] G. Fan and J. Manson. Calculations of the energy accommodation coefficient for gas-surface interactions. *Chemical Physics*, 370(1-3):175-179, 2010.

[226] H. A. Michelsen. Derivation of a temperature-dependent accommodation coefficient for use in modeling laser-induced incandescence of soot. *Applied Physics B*, 94(1):103, 2009.

[227] A. Giri and P. E. Hopkins. Analytical model for thermal boundary conductance and equilibrium thermal accommodation coefficient at solid/gas interfaces. *The Journal of Chemical Physics*, 144(8):084705, 2016.

[228] J. A. Bearden and A. Burr. Reevaluation of X-ray atomic energy levels. *Reviews of Modern Physics*, 39(1):125, 1967.

[229] W. Chen, Y. Lu, M. Wang, L. Kroner, H. Paul, H.-J. Fecht, J. Bednarcik, K. Stahl, Z. Zhang, and U. Wiedwald. Synthesis, thermal stability and properties of $ZnO_2$ nanoparticles. *The Journal of Physical Chemistry C*, 113(4):1320-1324, 2009.

[230] H. Ahsbahs and H. Sowa. High-pressure x-ray investigation of zincite ZnO single crystals using diamond anvils with an improved shape. *Journal of Applied Crystallography*, 39(2):169-175, 2006.

[231] L. Levien, C. T. Prewitt, and D. J. Weidner. Structure and elastic properties of quartz at pressure. *American Mineralogist*, 65(9-10):920-930, 1980.

[232] Z. Fan and J. G. Lu. Zinc oxide nanostructures: synthesis and properties. *Journal of Nanoscience and Nanotechnology*, 5(10):1561-1573, 2005.

[233] J. Wei, B. Zhang, N. Yao, X. Wang, H. Ma, and S. Wang. Pulsed laser deposition of zinc oxide luminescent thin films. *Journal of Vacuum Science & Technology B: Microelectronics and Nanometer Structures Processing, Measurement, and Phenomena*, 19(3):1082-1084, 2001.

[234] A. J. Ghazai, W. J. Aziz, and N. T. Yassen. Effect of laser pulses and energy on the structural properties of ZnO thin film prepared using PLA technique. *Condensed Matter Physics*, 2017.

[235] M. Oves, M. Arshad, M. S. Khan, A. S. Ahmed, A. Azam, and I. M. Ismail. Antimicrobial activity of cobalt doped zinc oxide nanoparticles: Targeting water borne bacteria. *Journal of Saudi Chemical Society*, 19(5):581-588, 2015.

[236] V. Koutu, L. Shastri, and M. Malik. Effect of NaOH concentration on optical properties of zinc oxide nanoparticles. *Materials Science Poland*, 34(4):819-827, 2016.

[237] S. Desgreniers. High-density phases of ZnO: Structural and compressive parameters. *Physical Review B*, 58(21):14102, 1998.

[238] J. Kasper and S. Richards. The crystal structures of new forms of silicon and germanium. *Acta Crystallographica*, 17(6):752-755, 1964.

[239] C. Kittel. *Introduction to Solid State Physics*, volume 8. Wiley New York, 1976.

[240] R. Y. Khosa, E. Thorsteinsson, M. Winters, N. Rorsman, R. Karhu, J. Hassan, and E. Ö. Sveinbjörnsson. Electrical characterization of amorphous $Al_2O_3$ dielectric films on n-type 4H-SiC. *AIP Advances*, 8(2):025304, 2018.

[241] P. Lamparter and R. Kniep. Structure of amorphous $Al_2O_3$. *Physica B: Condensed Matter*, 234:405-406, 1997.

[242] L. Zhang, H. Jiang, C. Liu, J. Dong, and P. Chow. Annealing of $Al_2O_3$thin films prepared by atomic layer deposition. *Journal of Physics D: Applied Physics*, 40(12):3707, 2007.

[243] S. Prokes, M. Katz, and M. Twigg. Growth of crystalline $Al_2O_3$ via thermal atomic layer deposition: Nanomaterial phase stabilization. *APL Materials*, 2(3):032105, 2014.

[244] A. K. Rossall, J. A. van den Berg, D. Meehan, S. Rajendiran, and E. Wagenaars. Analysis of plasma enhanced pulsed laser deposition of transition metal oxide thin films using medium energy ion scattering. *Nuclear Instruments and Methods in Physics Research Section B: Beam Interactions with Materials and Atoms*, 2018.

[245] S. Yamabi and H. Imai. Growth conditions for wurtzite zinc oxide films in aqueous solutions. *Journal of Materials Chemistry*, 12(12):3773-3778, 2002.

[246] M. Boehme and C. Charton. Properties of ITO on PET film in dependence on the coating conditions and thermal processing. *Surface and Coatings technology*, 200(1-4):932-935, 2005.

[247] C. S. Oh, S. M. Lee, E. H. Kim, E.-W. Lee, and L. S. Park. Electro-optical properties of index matched ITO-PET film for touch panel application. *Molecular Crystals and Liquid Crystals*, 568(1):32-37, 2012.

[248] S. Chung, S. O. Kim, S.-K. Kwon, C. Lee, and Y. Hong. All-inkjet-printed organic thin-film transistor inverter on flexible plastic substrate. *IEEE Electron Device Letters*, 32(8):1134-1136, 2011.

[249] W. Smaal, et al. Complementary integrated circuits on plastic foil using inkjet printed n-and p-type organic semiconductors: Fabrication, characterization, and circuit analysis. *Organic Electronics*, 13(9):1686-1692, 2012.

[250] M. Keidar, I. D. Boyd, and I. I. Beilis. On the model of Teflon ablation in an ablation-controlled discharge. *Journal of Physics D: Applied Physics*, 34(11):1675, 2001.

[251] R. Zeller and R. Pohl. Thermal conductivity and specific heat of noncrystalline solids. *Physical Review B*, 4(6):2029, 1971.

[252] P. Kelly, P. Barker, S. Ostovarpour, M. Ratova, G. West, I. Iordanova, and J. Bradley. Deposition of photocatalytic titania coatings on polymeric substrates by HiPIMS. *Vacuum*, 86(12):1880-1882, 2012.

[253] T. Furukawa, H. Sato, Y. Kita, K. Matsukawa, H. Yamaguchi, S. Ochiai, H. W. Siesler, and Y. Ozaki. Molecular structure, crystallinity and morphology of polyethylene/polypropylene blends studied by raman mapping, scanning electron microscopy, wide angle X-ray diffraction, and differential scanning calorimetry. *Polymer Journal*, 38(11):1127-1136, 2006.